

PERFORMANCE OF A CARBON NANOTUBE FIELD EMISSION X-RAY SOURCE
ARRAY FOR STATIONARY DIGITAL BREAST TOMOSYNTHESIS

Emily Morgan Gidcumb

A dissertation submitted to the faculty at the University of North Carolina at Chapel Hill in
partial fulfillment of the requirements for the degree of Doctor of Philosophy in the
Department of Applied Physical Sciences (Materials Science).

Chapel Hill
2014

Approved by:

Otto Zhou

Alfred Kleinhammes

Yueh Z. Lee

Jianping Lu

Sean Washburn

© 2014
Emily Morgan Gidcumb
ALL RIGHTS RESERVED

ABSTRACT

Emily Morgan Gidcumb: Performance of a carbon nanotube field emission X-ray source array for stationary digital breast tomosynthesis
(Under the direction of Otto Zhou and Jianping Lu)

This work describes the performance of a stationary digital breast tomosynthesis (s-DBT) X-ray tube based on carbon nanotube (CNT) cathodes, and the imaging system developed around it. The s-DBT system has the potential to improve the detection and diagnosis of breast cancer over commercially available digital breast tomosynthesis (DBT) systems. DBT is growing in popularity in the United States, and around the world, as a potential replacement for traditional 2D mammography. The main advantage of DBT over 2D mammography lies in the pseudo-3D nature of the technique allowing the removal of overlapping breast tissue within the image. s-DBT builds on this advantage by removing blur from focal spot motion.

Introductions to breast imaging techniques and the DBT modality are given, followed by an introduction to carbon nanotube field emission, the foundation of the s-DBT technology. Details of the s-DBT X-ray tube design and system integration are discussed including specific design parameters, system requirements, and the development process. Also included are summaries of the X-ray tube and system performance over time, and results from characterization measurements.

Specific focus is given to the development and completion of a fabrication procedure for tungsten gate mesh, characterization of the CNT cathodes, and improving the system's

spatial resolution with use of the focusing electrodes. The tungsten gate mesh is an essential component for extracting electrons from CNTs. A successful deep reactive ion etching fabrication procedure was developed, and the improved gate mesh allowed for higher cathode current and longer pulse widths to be employed in the s-DBT system.

Characterization of the CNT cathodes revealed their high-current capacity and the ability to produce relatively long pulse widths, mimicking a 2D imaging modality. This work confirmed that the cathodes are well suited for the task of breast imaging, and explored possible improvements. Lastly, it was shown that by employing and optimizing the focusing electrodes, spatial resolution of the s-DBT system improved, with a tradeoff in loss of transmission rate. This work has contributed to the development and evaluation of the s-DBT technology from the laboratory research stage through clinical trials on human tissue and patients.

Let the words of my mouth and the meditation of my heart be acceptable in your sight, O
Lord, my rock and my redeemer.
Psalm 19:14

ACKNOWLEDGEMENTS

This research was funded through the National Cancer Institute (R01-CA134598) and the Carolina Center of Cancer Nanotechnology Excellence, also funded by the National Cancer Institute, through grant U54-CA151652.

I would first like to thank my advisors, Dr. Otto Zhou and Dr. Jianping Lu. Dr. Zhou, you have been amazing in guiding and redirecting me over the years. The support and understanding you have shown have been invaluable to me. I truly would not have been able to participate in this great work without you. Dr. Lu, I really appreciate your patience and help with my questions over the years, and your advice on the direction and content of my work. It was a pleasure working with you.

In addition, I must thank the rest of my wonderful committee: Dr. Sean Washburn, Dr. Yueh Lee, and Dr. Alfred Kleinhammes. Sean, you have been a big support for me since our relationship began in Mechanics I, spring semester 2007. I really admire you and think you are an amazing professor. Thank you for your help, support these many, many years, and never giving up on me. Dr. Lee, you opened up the world of medical research to me. I've loved the clinical experiences you have made available to me. I really admire your passion and energy for research. Alfred, I thank you not only for the support you have given me throughout the graduate school process, but the support you have given to my family. You have helped the Gidcumb household in many ways, and I'm extremely thankful.

Thank you to all those who helped in the editing and proofreading of this thesis:
Lance Gidcumb, Sean Washburn, Allison Hartman, and Shaun Gidcumb.

I would like to acknowledge Dr. Bo Gao and Ai Leen Koh for their collaborations on published works. It was a joy working with both of you. Also, I give a big thank you to Derrek Spronk for all your practical help and assistance over the years. I always appreciated your willingness to help.

Thanks to all of my lab members, past and present. Xiomara Calderòn-Colòn and Shabana Sultana, we did not work together long but I treasured that time and value the relationships we have continued since. Xin Qian, you taught me so much when I started in the lab. Christy Inscoc, there is not enough space to list all of the ways you have been a help to me, in addition to the help you gave me in my research. I do not believe I would have gotten to this point had you not been a part of my life. Lei Zhang, I'm so lucky to have found one of my dearest friends in a lab mate. You have made this whole experience better in innumerable ways. I would like to specially thank those who worked with me on the breast tomosynthesis project: Andrew Tucker and Jabari Calliste. It was a lot of work, but we had a lot of fun along the way, too. Jing Shan and Pavel Chtcheprov, I want to thank you both for help on various portions of my research over the years. Marci Potuzko, Allison Hartman, and Gongting Wu, thanks for making the lab more fun. It has been great getting to know and work with you all.

My amazing family has been a source of support throughout this process, without which I would not have succeeded. My dear husband, Shaun Gidcumb, I love you more every day and wouldn't be here without you. My parents, Don and Patsy Morgan, have been a constant support my entire life. Thanks for all your love and never giving up on me. I

would also like to thank my brother, Andrew Morgan; my in-laws, Lance and Candy Gidcumb; my cousins, Anna Stout and Rand Allingham; and my grandparents, James and Jenny Case and Doris Morgan. I love you all more than words can say, and space would allow.

Finally, I want to thank my dear friends who were involved in my graduate life. Soo Yeon Sim and Hanlin Luo, we began as classmates but I know we will remain friends forever. Jamie Stiller, Jenn Rice, and Becca Miller, thank you so much for attending my defense. It meant so much to me, but not as much as your love and friendship. I truly treasure your presence in my life.

PREFACE

Portions of several chapters in this work have been previously published in other locations, with my participation as an author or co-author. All reused portions are noted, as they appear, throughout this work.

Chapter 5, titled “Initial Performance of CNT X-ray Source for Stationary Digital Breast Tomosynthesis”, contains text and figures from Qian, X. *et al.*, “High resolution stationary digital breast tomosynthesis using distributed carbon nanotube x-ray source array”, *Med. Phys.*, **39** (2012); as well as Gidcumb, E. *et al.*, “Carbon nanotube electron field emitters for X-ray imaging of human breast cancer”, *Nanotechnology* **25** (2014). Other portions of Gidcumb, E. *et al.*, “Carbon nanotube electron field emitters for X-ray imaging of human breast cancer”, *Nanotechnology* **25** (2014) appear in Chapter 6, titled “Long Pulse Width Field Emission Testing of Cathodes”, and in Chapter 7, titled “s-DBT System Performance”. Chapter 6 also includes a portion of the work by Koh, A. L *et al.*, “Observations of Carbon Nanotube Oxidation in an Aberration-Corrected Environmental Transmission Electron Microscope”, *ACS Nano* **7**, 2566-2572 (2013). Furthermore, Chapter 7 includes work from Tucker, A. W. *et al.* in *Medical Imaging 2013: Physics of Medical Imaging*. (SPIE, 2013).

Other work in Chapter 7 has been reused, with permission, from Tucker, A. W., Lu, J. & Zhou, O. “Dependency of image quality on system configuration parameters in a stationary digital breast tomosynthesis system”, *Med. Phys.* **40** (2013); and Tucker, A. W. *et*

al. “Increased microcalcification visibility in lumpectomy specimens using a stationary digital breast tomosynthesis system” (SPIE, 2014). Where applicable, other figures that were previously published have been reused with proper permissions obtained from the publisher and author.

TABLE OF CONTENTS

LIST OF TABLES	xviii
LIST OF FIGURES	xxi
LIST OF ABBREVIATIONS AND SYMBOLS	xxxi
CHAPTER 1: INTRODUCTION	1
1.1 Importance of breast imaging	1
1.2 Motivation for improving breast imaging	2
1.3 Mammography	3
1.3.1 Mammographic features	3
1.3.1.1 Masses	3
1.3.1.2 Calcifications	7
1.3.2 Non-radiographic imaging modalities used with mammography	9
1.3.2.1 Ultrasound	9
1.3.2.2 Magnetic resonance imaging	12
1.3.3 Current state of X-ray mammography	15
1.3.3.1 The physics of X-ray imaging	15
1.3.3.1.1 Electromagnetic radiation	15
1.3.3.1.2 Production of X-rays	16
1.3.3.1.3 Interaction of X-rays with matter	19

1.3.3.1.4	X-ray attenuation.....	21
1.3.3.1.5	Absorption of X-ray energy	22
1.3.3.2	Technique	24
1.3.3.2.1	Equipment	24
1.3.3.2.2	Positioning.....	31
1.3.3.3	Goals, trends, and limitations	33
1.4	Digital breast tomosynthesis.....	36
1.4.1	Main principles	36
1.4.2	Technique and current systems.....	39
1.4.3	Advantages over FFDM.....	43
1.4.4	FDA approval.....	47
1.5	REFERENCES	1
CHAPTER 2: MOTIVATIONS FOR AND FOUNDATIONS OF STATIONARY DIGITAL BREAST TOMOSYNTHESIS		3
2.1	Limitations of current DBT methods.....	3
2.2	Basic idea and proposed advantages of s-DBT.....	6
2.3	Materials science of s-DBT	8
2.3.1	Theory of field emission	8
2.3.2	Field emission versus thermionic emission for X-ray production	10
2.3.3	CNT properties as field emitters.....	15
2.3.4	Altered CNTs and other materials for field emission	23
2.3.5	Development of carbon nanotube cathodes for s-DBT.....	26

2.4	REFERENCES	29
CHAPTER 3: DESIGN AND DEVELOPMENT OF THE STATIONARY DIGITAL BREAST TOMOSYNTHESIS SYSTEM		36
3.1	Tube design.....	36
3.1.1	Electrode structure	36
3.1.2	Tube layout and properties.....	42
3.2	System design and build challenges	48
3.2.1	Overall system information.....	48
3.2.2	X-ray tube construction.....	50
3.2.3	Tube and system evaluation.....	50
3.2.4	Electronic controls integration and system summary	52
3.2.5	Reconstructions.....	54
3.2.6	FDA requirements.....	54
3.3	Other CNT X-ray sources	55
3.4	REFERENCES	58
CHAPTER 4: FABRICATION OF TUNGSTEN METAL GATE MESH.....		60
4.1	Introduction.....	60
4.1.1	Various gate mesh used in CNT X-ray sources	60
4.1.2	Deep reactive ion etching.....	63
4.1.3	Tungsten etching alternatives	65
4.2	Methods.....	67
4.2.1	Determining optimal etch process	67

4.2.2	Complete procedure for tungsten gate mesh fabrication	68
4.3	Results.....	72
4.4	Discussion.....	76
4.5	Conclusion	78
4.6	REFERENCES	80
CHAPTER 5: INITIAL PERFORMANCE OF CNT X-RAY SOURCE FOR STATIONARY DIGITAL BREAST TOMOSYNTHESIS		81
5.1	Argus 3.0 performance characterization.....	81
5.1.1	Anode heat capacity.....	81
5.1.2	Current characteristics of CNT cathodes	83
5.1.3	Focal spot sizes	86
5.1.4	Spatial resolution	87
5.1.5	Phantom imaging	89
5.2	Additional tomosynthesis accelerated lifetime tests.....	91
5.2.1	Motivation and methods	92
5.2.2	Results.....	93
5.2.3	Conclusions.....	97
5.3	REFERENCES	99
CHAPTER 6: LONG PULSE WIDTH FIELD EMISSION TESTING OF CATHODES		100
6.1	Introduction.....	100
6.1.1	Motivation.....	100
6.1.2	Different types of nanotubes.....	101

6.1.3	Differences in nanotube fabrication.....	103
6.1.3.1	FWNTs with thermal CVD.....	103
6.1.3.2	MWNTs with arc discharge.....	104
6.2	Methods.....	104
6.3	Results.....	108
6.3.1	Initial I-V curves.....	108
6.3.2	FWNT results.....	110
6.3.2.1	4 s pulses.....	110
6.3.2.2	3 s pulses.....	113
6.3.2.3	2 s pulses.....	115
6.3.3	MWNT results.....	117
6.3.3.1	4 s pulses.....	117
6.3.3.2	3 s pulses.....	118
6.3.3.3	2 s pulses.....	119
6.3.4	SEM images of cathodes.....	122
6.3.4.1	FWNT cathodes.....	122
6.3.4.2	MWNT cathode.....	125
6.3.5	Optical microscope images of gate mesh.....	127
6.3.5.1	FWNT cathodes' gate mesh.....	127
6.3.5.2	MWNT cathode's gate mesh.....	130
6.4	Discussion.....	131

6.5	Conclusion	133
6.6	REFERENCES	135
CHAPTER 7: s-DBT SYSTEM PERFORMANCE.....		136
7.1	Optimization study results	136
7.1.1	Artifact spread function	136
7.1.2	Modulation transfer function	138
7.2	System operation over time	139
7.2.1	Cathode voltage over time	140
7.2.2	Transmission rate over time.....	142
7.2.3	Summary	144
7.3	Specimen study results.....	144
7.3.1	Lesion characterization versus 2D imaging.....	145
7.3.2	Microcalcification visibility versus CTM DBT	147
7.4	Patient images	150
7.5	REFERENCES	153
CHAPTER 8: FOCUSING VOLTAGE OPTIMIZATION.....		154
8.1	Introduction.....	154
8.1.1	Focal spot size and the focusing electrodes	154
8.1.2	Modulation transfer function	157
8.2	Purpose.....	160
8.3	Methods.....	160
8.3.1	Experimental setup and MTF measurement	160

8.3.2	Tested range of focusing voltages.....	164
8.3.3	Transmission rate measurements	167
8.4	Results.....	168
8.4.1	One-beam projection data using cathode P11.....	168
8.4.2	Fifteen-beam projection and reconstruction data.....	173
8.4.2.1	Transmission rates	173
8.4.2.2	Projection results	173
8.4.2.3	Reconstruction results.....	176
8.5	Discussion.....	177
8.5.1	Trends over focusing voltages	177
8.5.2	Optimal focusing settings and focal spot size.....	179
8.5.3	Transmission rate tradeoff	180
8.6	Conclusion	182
8.7	REFERENCES	184
CHAPTER 9: CONCLUSIONS AND FUTURE DIRECTIONS		185
9.1	Conclusions.....	185
9.2	Future directions	187

LIST OF TABLES

Table 1.1 Specifications of current commercial and prototype DBT systems. Adapted from Sechopoulos, 2013, Part I.	41
Table 2.1 Table of field emission results from high and low density CNT films from Neupane, 2012.	22
Table 2.2 Field emission properties of alternate CNT materials. The blank fields were not discussed in the study. The turn-on field corresponds to $10 \mu\text{A}/\text{cm}^2$, and threshold field to $1 \text{ mA}/\text{cm}^2$	23
Table 2.3 Field emission properties of non-CNT materials. The blank fields were not discussed in the study. The turn-on field corresponds to $10 \mu\text{A}/\text{cm}^2$, and threshold field to $1 \text{ mA}/\text{cm}^2$, unless otherwise noted.	24
Table 2.4 Summary of CNT cathode development over time.	27
Table 3.1 Key properties of the s-DBT tube, Argus 3.0.	47
Table 3.2 Key, integrated s-DBT system parameters.	53
Table 3.3 Leakage radiation results. Directions are relative to facing the system from the front, as a patient.	55
Table 4.1 Initial method parameters and results used by Xiomara Calderòn-Colòn for etching tungsten gate mesh.	67
Table 4.2 Table summarizing the process parameters used for DRIE of tungsten gate mesh for the s-DBT X-ray tube.	71
Table 4.3 Etch rates for tungsten gate mesh fabricated by DRIE.	73
Table 4.4 Data summary of measurements collected on etched mesh's bar widths and space widths. Pitch was calculated by the sum of bar and space widths.	75
Table 5.1 Testing summary and percent increases with respect to initial electric field. Reprinted from Emily Gidcumb <i>et al.</i> 2014 <i>Nanotechnology</i> 25 245704.	96
Table 6.1 Electric field values at various cathode currents corresponding to the initial I-V curves. Results conflict with other experiments due to uncertainty in gate-cathode distances in these experiments.	109
Table 6.2 Summary of all field emission measurements on both cathode types.	121

Table 7.1 Transmission rate data summary. Reprinted from Gidcumb <i>et al.</i> 2014 <i>Nanotechnology</i> 25 245704.	143
Table 7.2 MC area and FWHM of the ASF for each of the 12 MCs, for both imaging modalities. DBT refers to the CTM DBT system. Reprinted with permission from SPIE. Tucker <i>et al.</i> , Increased microcalcification visibility in lumpectomy specimens using a stationary digital breast tomosynthesis system, <i>Proc. of SPIE</i> , 2014.....	149
Table 8.1 Dimensions for initial testing chamber focal spot size measurements. The long side dimension is listed first. The electrodes had elliptical apertures. Reused with permission from S. Sultana, PhD thesis, 2010.	156
Table 8.2 10 % MTF results from various DBT systems using the wire method. The MTF values are system values given from reconstructed images. Pixel sizes vary due to different detector binning and reconstructions between the systems. Siemens and Hologic data are for 0 mm above detector surface.	159
Table 8.3 10 % MTF results comparing Hologic Selenia Dimensions and s-DBT. The MTF values are from central projection images, and do not incorporate effects of the reconstruction. Pixel sizes are identical.	159
Table 8.4 Relative focusing voltages when both F1 and F2 grounded. Cathode voltages are reported for 43 mA cathode current. Note: $V_{\text{Appl, F1}} = V_{\text{Appl, F2}}$, and $V_{\text{Rel, F1}} = V_{\text{Rel, F2}}$	166
Table 8.5 Tested ranges corresponding to Figure 8.5, for both the applied and relative focusing voltages. The relative values, as noted in the table, are in reference to the initial I-V data of the 15 beams.....	167
Table 8.6 Results from P11 of the best settings, chosen for 15-projection imaging. Ground refers to the setting $F1 = F2 = 0$ V, where F1 and F2 refers to the electrode on which the voltage is applied.	172
Table 8.7 Transmission rate results for 15-beam imaging and the percentage difference from the grounded setting. TR error is the standard deviation between all 15 beams.	173
Table 8.8 MTF results in both directions for the 15-beam imaging and percentage difference from the grounded setting. Error is the standard deviation in the measurement between all 15 beams.....	174
Table 8.9 MTF product results for 15-beam imaging and the percentage difference from the grounded setting. Error was calculated from the standard deviation in the MTF measurements, in each direction.	175

Table 8.10 In-focus plane, reconstructed MTF product results and percentage difference from the grounded setting. Error was calculated from the standard deviation in the MTF measurements in each direction.....	177
Table 8.11 In-focus plane, reconstructed MTF results for each direction, and percentage difference from the grounded setting. Error is the standard deviation in the MTF measurements.	177
Table 8.12 Table displaying the number of projections, pulse width, and exposure required for imaging different compressed breast thicknesses. The total acquisition time assumes a detector integration time of 0.1 s.	182

LIST OF FIGURES

Figure 1.1 Illustration of various mass shapes (upper row) and types of mass margins (lower row). Adapted from Kopans, 2007.	4
Figure 1.2 MLO view of a round mass with pleomorphic calcifications adjacent to smaller, round masses. Ultrasound images, taken afterward, indicated cancer.	5
Figure 1.3 Slightly lobulated, circumscribed, round mass simulating fibroadenoma that biopsy showed to be invasive ductal cancer.	6
Figure 1.4 Image (H) shows a vague round mass that was shown in the magnification view (I) to have indistinct borders; a biopsy revealed invasive ductal cancer.	7
Figure 1.5 Illustration of many calcification types that are observed with mammography. Adapted from Kopans, 2007.	8
Figure 1.6 X-ray examples of calcifications typical of ductal carcinoma in situ. Left: Granular type. Right: Pleomorphic type.	9
Figure 1.7 (A) Photograph of an ultrasound unit used in a mammography clinic. (B) Close-up of a transducer used for imaging.	10
Figure 1.8 Ultrasound image of a multilobulated mass that is invasive ductal cancer, but appeared round on a mammogram.	11
Figure 1.9 Dedicated MRI breast coil, with the coil detail shown in (B).	13
Figure 1.10 MRI breast image sequence of invasive lobular carcinoma in the left breast.	14
Figure 1.11 Illustration of a typical Bremsstrahlung radiation spectrum for the case of a 40 kV acceleration potential.	17
Figure 1.12 Illustration of a complete X-ray spectrum characteristic of a silver metal target and acceleration potential of 40 kV.	18
Figure 1.13 Illustration of a mammography unit with major components labeled. Adapted from Ikeda, 2011.	25
Figure 1.14 Photograph of a mammography unit built by GE.	26
Figure 1.15 Cross-section of a mammography unit showing the details of the X-ray tube and collimation, as well as the breast support area and image receptor housing. Adapted from Bushberg, 2002.	27

Figure 1.16 Direction lines for the CC and MLO views used in breast imaging.	31
Figure 1.17 A CC-view set of X-rays placed back-to-back. The images for each breast are placed back to back. Attribution: © Nevit Dilmen	32
Figure 1.18 Right and left MLO X-rays back-to-back. Attribution: © Nevit Dilmen.....	33
Figure 1.19 X-ray images of right MLO views of two different women with fatty breasts. The left image (C) is an SFM image, and the right image (A) is a DM image.....	34
Figure 1.20 Illustration of a DBT system with major components labeled. Example tube trajectory during imaging is indicated by the curved arrow. There is one tube head, black, that moves to different projection locations, illustrated by the gray tube head images.	37
Figure 1.21 Illustration of the shift-and-add method for image reconstruction whose principle is the basis for more complex reconstruction methods used in DBT. This image shows how a plane would be constructed so that the burst shape comes into focus.....	38
Figure 1.22 Comparison of a 2D DM projection and a DBT slice for DCIS. The spiculation and MCs are hidden in the DM image, but clearly seen in the DBT image.....	45
Figure 1.23 Photograph of a Hologic Selenia Dimensions DBT system in a laboratory setting.....	47
Figure 2.1 Illustration of a proposed s-DBT system with many X-ray sources housed in one X-ray tube. The "x" markers indicate X-ray source locations within the tube, corresponding to projection locations that will form the tomosynthesis reconstruction.	6
Figure 2.2 Illustration comparing the difference between a stationary focal spot (s-DBT), and a blurred focal spot (DBT). The DBT focal spot gets stretched in the direction of tube travel. This illustration assumes a tube travel of 1.65 mm during an exposure in which the whole acquisition would total 100 mAs.	8
Figure 2.3 Potential energy diagram at the surface of a metal under the influence of an external electric field.....	9
Figure 2.4 Simple schematic of a thermionic X-ray tube. Adapted from Johns, 1974.	12
Figure 2.5 Simplified schematic of a field emission X-ray tube.	13

Figure 2.6 Illustration of a Spindt field emitter array. The left image is a cross-section view, and the right image is a top view, showing the circular gate openings. Adapted from Zhu, 2001.....	14
Figure 3.1 The left photograph in this figure shows three CNT cathodes of the type placed in the s-DBT system. On the right, in the red box, is a TEM image of the type of FWNTs deposited on the cathodes.....	37
Figure 3.2 On the left is a magnified photograph of a gate mesh immediately after fabrication. The right photograph shows an example of a gate frame with gate mesh welded over the individual openings. This gate frame was not for the s-DBT tube, but the gate mesh are very similar.....	38
Figure 3.3 Optical microscope images of a tungsten gate mesh. The bar thickness and spacing size are labeled. Also, the curved bar edges can be seen.	39
Figure 3.4 Illustration of the complete electron configuration in the s-DBT tube including simulated electron trajectories in the left-hand image. The two views are different cross-sections of the structure. Adapted with permission from Sultana, 2010.	40
Figure 3.5 Complete electrode structure from the SolidWorks drawing of the s-DBT tube.....	41
Figure 3.6 Photographs of an s-DBT X-ray tube with key features labeled. The orientation used in breast imaging is shown in the right photograph, with the X-ray window facing downward toward the detector.....	42
Figure 3.7 Schematic illustrating the difference in the real, or actual, focal spot size and the effective focal spot size.	44
Figure 3.8 Schematic of the geometric configuration determining effective anode angle with tube tilt and positioning on the gantry incorporated.....	45
Figure 3.9 Dose rate measurements comparing the Hologic Selenia Dimensions system to the s-DBT system. Data taken by Dr. Andrew Tucker.	47
Figure 3.10 (A) Hologic Selenia Dimensions system, with a red arrow indicating the tube motion path. (B) The s-DBT tube integrated with the Hologic gantry. Reprinted from Gidcumb <i>et al</i> 2014 <i>Nanotechnology</i> 25 245704.....	48
Figure 3.11 Photograph of the completely integrated s-DBT system including the Hologic and s-DBT controls.	49
Figure 3.12 Simplified electronic communication flow diagram of the integrated system.	53

Figure 4.1 Illustration of woven and linear tungsten-wire gate mesh. Adapted with permission from Sultana, 2010.....	61
Figure 4.2 Optical microscope images. Left: Woven tungsten mesh. Middle: Molybdenum with a grid of circular openings. Right: Etched, linear tungsten mesh. Images reused with permission of Xiomara Calderòn-Colòn.....	61
Figure 4.3 Pictures of various gate materials investigated for s-DBT. The silicon and tungsten (straight bars) images were used with permission from Xiomara Calderon-Colon. Stainless steel and molybdenum images are from XinRay Systems.	63
Figure 4.4 Illustration of the Bosch process. Adapted from Fransilla, 2010.....	65
Figure 4.5 Photograph of the corner paste configuration that allowed for successful mesh etching.....	74
Figure 4.6 Photographs comparing the appearances between a failed sample, due to photoresist damage, to a successful one. There was some photoresist damage even on the successful sample, but it did not reach the critical area containing the tungsten bars. The top of the left-most mesh in the successful etch example was not fully etched, but the other two were.....	74
Figure 4.7 10x magnification optical microscope images of tungsten gate mesh corresponding to the MRT sample data presented in Table 4.4.....	76
Figure 4.8 Optical microscope images comparing the surface roughness of DRIE mesh and wet-etched mesh. Images taken by Derrek Spronk.	79
Figure 5.1 Temperature simulation results at the center of the s-DBT tungsten anode during one X-ray pulse. The settings are for various anode currents and pulse widths, all at 38 kV anode voltage. The insert is an image of the simulated anode showing the temperature distribution at the end of a pulse with settings of: 250 ms, 28 mA anode current, and 38 kV anode voltage. Reprinted with permission from Qian et al., Med. Phys., 39, 2094, (2012). Copyright 2012, American Association of Physicists in Medicine.	83
Figure 5.2 Accelerated lifetime test data using a testing module, simulating the electrode configuration of the s-DBT X-ray tube. (A) 27 mA anode current, 250 ms pulse width, 5 % duty cycle. Inset: Shows an example cathode current pulse. (B) 38 mA anode current, 183 ms pulse width, 0.6 % duty cycle. Reprinted with permission from Qian et al., Med. Phys., 39, 2095, (2012). Copyright 2012, American Association of Physicists in Medicine.	84

Figure 5.3 Cathode-gate voltages required to produce an average of 42.6 ± 0.4 mA for the 31 CNT cathodes in the s-DBT X-ray tube. Reprinted with permission from Qian et al., <i>Med. Phys.</i> , 39, 2096, (2012). Copyright 2012, American Association of Physicists in Medicine.	86
Figure 5.4 Results of focal spot size measurements using focusing settings to achieve the smallest focal spot sizes. Reprinted with permission from Qian et al., <i>Med. Phys.</i> , 39, 2096, (2012). Copyright 2012, American Association of Physicists in Medicine.	87
Figure 5.5 (A) The projection MTFs of the stationary and rotating gantry DBT systems along the scanning direction. (B) The system MTFs obtained using the in-focus reconstruction slice. Reprinted with permission from Qian et al., <i>Med. Phys.</i> , 39, 2097, (2012). Copyright 2012, American Association of Physicists in Medicine.	88
Figure 5.6 (A) Photograph of the CIRS breast biopsy phantom. (B) - (D) Reconstructed slices of the CIRS phantom from the s-DBT system. The depths of the slices are (B) 1 cm, (C) 2.5 cm, and (D) 4 cm from the phantom's surface. Reprinted with permission from Qian et al., <i>Med. Phys.</i> , 39, 2097, (2012). Copyright 2012, American Association of Physicists in Medicine.	90
Figure 5.7 (A) Photograph of the ACR phantom. (B) Illustration of the objects imbedded within the ACR phantom. The yellow box indicates 0.54 mm specs, the green box indicates 0.4 mm specs, and the blue box indicates 0.32 mm specs. (C) - (E) s-DBT system reconstruction slices at (C) 0.7 cm, (D) 1.4 cm, and (E) 2 cm from the top of the phantom. (F) - (H) s-DBT reconstruction slices at 1.4 cm for the three MC spec sizes indicated by the colored boxes. (I) - (K) The same images as (F) - (H) for the Hologic system. Reprinted with permission from Qian et al., <i>Med. Phys.</i> , 39, 2097-98, (2012). Copyright 2012, American Association of Physicists in Medicine.	91
Figure 5.8 Plots of cathode current and electric field data during field emission testing with 0.1 Hz frequency. Cathode current settings were (A) 27 mA, (B) 41 mA, (C) 60 mA, (D) 80 mA, and (E) 78 mA. The experimental data for (A) through (D) was gathered sequentially on a single cathode using 250 ms pulse widths. The data in (E) was performed with a second cathode, and 125 ms pulse widths. Reprinted from Emily Gidcumb <i>et al.</i> 2014 <i>Nanotechnology</i> 25 245704.	94
Figure 6.1 (A) SEM image of a CNT cathode. (B) Raman spectroscopy data of a CNT sample representative of those deposited on the FWNT cathodes tested throughout this study. Data provided by Dr. Bo Gao. Reprinted from Gidcumb <i>et al.</i> 2014 <i>Nanotechnology</i> 25 245704.	102

Figure 6.2 (A) High-magnification TEM images of (A) CVD-grown CNTs and (B) arc-discharge CNTs. Scale bar represents 5 nm. Reprinted with permission from Koh et al., ACS Nano, 7, 2567, (2013). Copyright 2013 American Chemical Society.	103
Figure 6.3 Illustration of the experimental setup, not drawn to scale. The tube housing contained three cathode-anode pairs, an example of only one is shown here. Reprinted from Gidcumb <i>et al.</i> 2014 <i>Nanotechnology</i> 25 245704.....	105
Figure 6.4 I-V curves for both the MWNT and FWNT cathode. Both current and current density are shown plotted versus electric field. FWNT data reprinted from Gidcumb <i>et al.</i> 2014 <i>Nanotechnology</i> 25 245704.....	109
Figure 6.5 FWNT field emission results for the 4 s pulse width testing, for both 50 mAs and 75 mAs targets. (A) and (B) plot different quantities for the same pulses; same for (C) and (D). (A) Raw cathode current and voltage data for the 50 mAs target. Inset: One, 4 s pulse of cathode current averaging 27.6 mA, producing 61 mAs. (B) Calculated anode exposure and electric field data for the 50 mAs testing. The green lines demarcate the region considered the target exposure region. The vertical dotted lines in (A) and (B) indicate when anode voltage changed during the experiments. (C) Cathode current and voltage data for the 75 mAs testing. Inset: One, 4 s pulse of 33.5 mA cathode current, equaling 74 mAs. (D) Calculated anode exposure and electric field data for the 75 mAs testing, also with green dotted lines indicating the target region. All data in (C) and (D) was taken at 35 kV. Cathode current and applied electric field data, as well as the inset in (A) are reprinted from Gidcumb <i>et al.</i> 2014 <i>Nanotechnology</i> 25 245704.	111
Figure 6.6 Field emission data for the FWNT cathode producing 3 s pulse widths with a target of 50 mAs. (A) Plots of measured cathode current and cathode voltage. (B) Plots of calculated anode exposure and applied electric field, with the target exposure region outlined with green dotted lines.....	114
Figure 6.7 Field emission results for 2 s pulses. All data was taken at 35 kV. (A) and (B) show the results for cathode 1 (FW 1); (C) and (D) show the results for cathode 2 (FW 2). An example 2 s pulse is shown in the inset of (C). The pulse had an average current of 44.5 mA, equaling an exposure of 49 mAs. It can be seen that the anode exposure in (B) never reached the target region, outlined by the green dotted lines.	116
Figure 6.8 Field emission data for 4 s pulses produced from the MWNT cathode. The data was taken at various anode voltages, as indicated by the vertical dotted black lines. (A) Cathode current and voltage, and	

anode current measurements. (B) Anode exposure and applied electric field calculations, with the target exposure region outlined with green horizontal lines. The inset in (B) shows an anode current pulse 4 s long, averaging 13.7 mA, totaling 50 mAs. 118

Figure 6.9 Field emission results for the 3 s experiments done with the MWNT cathode. (A) Cathode and anode current data, as well as cathode voltage data. (B) Calculated anode exposure and applied electric field data. Inset: A 3 s anode-current pulse averaging 18.3 mA, equaling 50 mAs. 119

Figure 6.10 Field emission results for the 2 s, 50 mAs testing done with a MWNT cathode. (A) Measured cathode current, anode current, and cathode voltage data for each pulse. (B) Calculated anode exposure and applied electric field for each pulse. Inset: An example 2 s pulse with an average anode current of 24.2 mA, totaling an exposure of 49 mAs..... 120

Figure 6.11 SEM images of cathode FW 1 after use in field emission experiments. (A) and (B) are profile images, where the SEM sample was tilted approximately 90°. (C) and (D) are top-view images, looking straight on the cathode surface..... 122

Figure 6.12 SEM images of cathode FW 2 after being removed from the testing chamber, where it underwent conditioning and 2 s pulse testing. (A) and (B) are profile views, and (C) and (D) are top views. 123

Figure 6.13 SEM images of the third FWNT cathode in the testing chamber that only underwent conditioning. (A) and (B) are side-view images. (C) and (D) are top-view images. (D) is a low magnification image showing unusual pock marks or melting..... 124

Figure 6.14 (A) SEM image of surface damage of the third FWNT cathode. Pink outline indicates where the EDS spectrum was taken. The scale bar represents 80 μm . (B) EDS spectrum from the area in (A), taken at 20 kV and 12 mm working distance. 125

Figure 6.15 SEM images of the MWNT cathode before it was used for field emission measurements. (A) and (B) are profile views. (C) and (D) are top views. The scale bar in (D) is 3 μm 126

Figure 6.16 SEM images of the MWNT cathode after it was used for field emission measurements. (A) and (B) are profile views. (C) and (D) are top views. 127

Figure 6.17 Optical microscope images of the gate mesh above cathode FW 1 during field emission measurements..... 128

Figure 6.18 Optical microscope images of the gate mesh above cathode FW 2.....	129
Figure 6.19 Optical microscope images of the gate mesh above the third FWNT cathode in the testing chamber, only used during conditioning.	130
Figure 6.20 Optical microscope images of the gate mesh above the MWNT cathode used in field emission experiments.....	131
Figure 7.1 Plot of the ASF of a 14° angular span (red) and of a 28° angular span (blue). Number of projection images and total entrance dose were held constant. Reprinted with permission from Tucker et al., Med. Phys., 40, 031917-8, (2013). Copyright 2013, American Association of Physicists in Medicine.	137
Figure 7.2 FWHM of ASF data at various angular spans. Reprinted with permission from Tucker et al., Med. Phys., 40, 031917-8, (2013). Copyright 2013, American Association of Physicists in Medicine.	138
Figure 7.3 MTF of the s-DBT system for two different detector pixel sizes. Reprinted with permission from Tucker et al., Med. Phys., 40, 031917-8, (2013). Copyright 2013, American Association of Physicists in Medicine.	139
Figure 7.4 Cathode voltages required to produce approximately 39 mA cathode current, for each of the 31 s-DBT system cathodes, at two different points measured in Dec. 2010 and Nov. 2012. This data demonstrates that all 31 cathodes in a working s-DBT tube can reliably operate for several years. Dec. 2010 data provided by Derrek Spronk. Reprinted from Gidcumb <i>et al.</i> 2014 <i>Nanotechnology</i> 25 245704.....	141
Figure 7.5 Plot of the transmission rate, in fraction form, for each cathode in the s-DBT prototype X-ray tube at various dates. The legend entry contains the date the data was taken in month and year, followed by the cathode current. Sept. 2011 data provided by Andrew Tucker. Reprinted from Gidcumb <i>et al.</i> 2014 <i>Nanotechnology</i> 25 245704.....	143
Figure 7.6 (A) Reconstructed slice from the s-DBT system of a breast specimen with a suspicious mass. (B) 2D magnification image of the same breast specimen. Reprinted with permission from SPIE. Tucker et al., Comparison of the diagnostic accuracy of stationary digital breast tomosynthesis to digital mammography with respect to lesion characterization in breast tissue biopsy specimens: a preliminary study, Proc. of SPIE, Vol. 8668, 2013.....	146
Figure 7.7 (A) Reconstruction slice of a specimen with a large cluster of MCs using the s-DBT system. (B) The same cluster imaged with the CTM	

DBT system. (C) Zoomed-in area of the MC cluster as indicated by the blue box in (A). (D) Zoomed-in area of the same MC cluster imaged with the CTM DBT system. Reprinted with permission from SPIE. Tucker et al., Increased microcalcification visibility in lumpectomy specimens using a stationary digital breast tomosynthesis system, Proc. of SPIE, 2014..... 148

Figure 7.8 Regions of interests around the first 6 chosen MCs. The s-DBT images are in the top row, and the CTM DBT images are in the bottom row. Reprinted with permission from SPIE. Tucker et al., Increased microcalcification visibility in lumpectomy specimens using a stationary digital breast tomosynthesis system, Proc. of SPIE, 2014..... 149

Figure 7.9 Reconstructed CC image slices of Patient 1 at heights of (A) 13.5 mm and (B) 26.5 mm. The red and yellow boxes illustrate different objects coming into focus at different heights. The red box shows a mass marked by a metal biopsy clip, and the yellow box shows a microcalcification cluster. Total exposure was 91 mAs over 15 projections, with a peak voltage of 34 kVp. 151

Figure 7.10 A reconstructed MLO slice from Patient 1, at 16.5 mm, with the same areas highlighted in yellow and red as in Figure 7.9. Total exposure was 97 mAs over 15 projections, with a peak voltage of 38 kVp. 152

Figure 8.1 Representative beam profile exhibiting shift in focal plane along the axial direction with change in Focus 2 aperture. Figure reprinted with permission from S. Sultana, PhD thesis, 2010¹. 155

Figure 8.2 Illustration showing directional naming conventions. The short and long side of the cathode gave rise to the terms short and long side of the focal spot size. The short side corresponds to the scanning direction, and the long side corresponds to the non-scanning direction. The right side of the picture is a top-view of the detector plane. 157

Figure 8.3 Photos of the experimental setup. (A) Top-view of the MTF cross-wire phantom attached to the breast compression paddle. A line pair phantom is also present. (B) Side-view of the setup showing the display on the gantry, used for relocating the paddle after each image. (C) Front-view showing the phantom suspended below the compression paddle. (D) ACR phantom, after the top and wax insert were removed, was used to level the compression paddle so that it was parallel to the detector surface. 161

Figure 8.4 Example image taken during the experiments, with each item labeled. The chest wall side of the image is the right side, and the x and y coordinates have been labeled according to the conventions of Figure 8.1.

The orange box shows the region of wire used to measure MTF in the x-direction, and the blue box is that for MTF in the y-direction.	162
Figure 8.5 Example data analysis of the image shown in Figure 8.3 from beam P11 for MTF in the x-direction. (A) The resultant oversampled LSF produced from many LSFs along the wire ROI and adjusted for wire angle. (B) MTF resulting from the FT of the oversampled LSF in (A), with a 10 % value of 7.6 cycles/mm.	164
Figure 8.6 Plot of all applied focusing settings tested using beam P11 to narrow down an area to test the 15-beam set. The point outlined in orange is the grounded setting. The purple-outlined points were selected for testing all 15 beams.	167
Figure 8.7 MTF product results for all settings from P11 images. MTF product is in (cycles/mm) ² and plotted versus V _{Appl} on F2. (A) Results for the most negative V _{Appl} settings on F1. (B) Results for more positive settings on F1. Results were separated for better data visualization.....	169
Figure 8.8 Color figures giving 2D distribution of MTF magnitudes over applied focusing voltages. (A) MTF product results. (B) X-direction only. (C) Y-direction only. Color bars to the right provide scaling information.	170
Figure 8.9 Transmission rate results for beam P11 at all tested focusing voltages. (A) and (B) separate the results according to more negative and positive V _{Appl} settings on F1, respectively. (C) 2D color distribution of TR results, with the magnitude scale bar to the right.	171
Figure 8.10 MTF product results. Results for each cathode/projection are given for each setting. Coloring from green to red indicates the settings with the highest to the lowest all-beam average MTF product.....	176
Figure 8.11 Simulation results showing FSS area to be weakly dependent on F1 voltage. Anode voltage was 30 kV, gate voltage was 1250 V producing 20 mA. Data reprinted with permission from Shabana Sultana ¹	178
Figure 8.12 Simulation of projection MTF curves based on focal spot size. The blue curve results from a focal spot of 0.985 mm, and the purple curve corresponds to a focal spot size of 0.6 mm. All other settings are the same, and are the parameters used in these experiments. The 10 % MTF results are displayed next to their respective curves.....	180

LIST OF ABBREVIATIONS AND SYMBOLS

2D	Two-dimensional
3D	Three-dimensional
Å	angstrom
a-Se	Amorphous selenium
a	Constant in the Fowler-Nordheim equation
A	ampere
AC	Alternating current
AEC	Automatic exposure control
Ag	silver
Al	aluminum
Ar	argon
ART	Algebraic reconstruction technique
ASF	Artifact spread function
b	Constant in the Fowler-Nordheim equation
B	boron
Be	beryllium
BI-RADS	Breast Imaging-Reporting and Data System
Br	bromine
c	Speed of light
C	Coulomb or carbon
CC	craniocaudal
CCD	Charge coupled device

CHANL	Chapel Hill Analytical and Nanofabrication Laboratory
Cl	chlorine
cm	centimeter
CNT	Carbon nanotube
Co	cobalt
c_p	Temperature-dependent heat capacity
CR	Computed radiography
CsI	Cesium iodide
CT	Computed tomography
CTM	Continuous tube motion
Cu	copper
CVD	Chemical vapor deposition
d	Distance from cathode to gate
D	dose
D_{air}	Dose in air
DBT	Digital breast tomosynthesis
DC	Direct current
DM	Digital mammography
DMIST	Digital Mammography Imaging Screening Trial
DQE	Detective quantum efficiency
DRIE	Deep reactive ion etching
DRR	Dynamic Reconstruction and Rendering
e	exponential

E	energy or effective focal spot length
E_{eff}	Effective field at CNT tip
E_{macro}	Macroscopic electric field
ECM	Electro-chemical machining
EDS	Energy-dispersive X-ray spectroscopy
EPD	Electrophoretic deposition
ESF	Edge spread function
ETEM	Environmental transmission electron microscope
f	Spatial frequency
F	Applied electric field or fluorine
F1	Focusing 1
F2	Focusing 2
FBP	Filtered backprojection
FDA	Food and Drug Administration
Fe	iron
FFDM	Full field digital mammography
FT	Fourier transform
FWHM	Full width at half maximum
FWNT	Few-wall nanotube
g	gram
Gy	gray
H	hydrogen
He	helium

hr	hour
HV	High voltage
Hz	Hertz
I	Intensity of monoenergetic X-rays exiting a material or emission current
I_0	Initial monoenergetic intensity
ITO	Indium tin oxide
J	Joule or current density
k	Boltzmann constant or emitter shank variable
K	Kelvin
keV	kiloelectronvolt
kg	kilogram
kVp	Kilovolt peak
lb	pound
Li	lithium
LSF	Line spread function
lp	Line pairs
m	meter
mA	milliamperere
mAs	Unit current in mA times unit time in seconds
MC	microcalcification
MeV	megaelectronvolt
mg	milligram
Mg	magnesium

mGy	milligray
min	minute
MITS	Matrix inversion tomosynthesis
mL	milliliter
MLEM	Maximum likelihood expectation maximization method
MLO	Mediolateral oblique
mm	millimeter
Mo	molybdenum
MQSA	Mammography Quality Standards Act
mR	milliRoentgen
MRI	Magnetic resonance imaging
MRT	Microbeam radiation therapy
MTF	Modulation transfer function
MTF _x	MTF in the x-direction
MTF _y	MTF in the y-direction
MWNT	Multi-wall nanotube
n	Number of photons removed
N	Number of incident photons or number of transmitted photons or nitrogen
N ₀	Number of incident photons
nA	nanoampere
Ni	nickel
nm	nanometer
NMP	N-methylpyrrolidinone

NMR	Nuclear magnetic resonance
O	oxygen
ODD	Object-to-detector distance
P_{in}	Input power
P_{rad}	Output power from blackbody radiation
PCM	Photochemical machining
PET	Positron emission tomography
pm	picometer
PSF	Point spread function
r	emitter radius
R	Roentgen or emitter-gate distance or real focal spot length
rad	Radiation absorbed dose
RF	Radio frequency
Rh	rhodium
RIE	Reactive ion etching
ROI	Region of interest
rpm	Revolutions per minute
RTT	Real Time Tomography
s	second
S	sulfur
S_0	Initial polyenergetic spectrum
sccm	Standard cubic centimeters per minute
s-DBT	Stationary digital breast tomosynthesis

SART	Simultaneous algebraic reconstruction technique
SDNR	Signal difference-to-noise ratio
SFM	Screen film mammography
SI	International System of Units
Si	silicon
SID	Source-to-image receptor distance
SIRT	Simultaneous iterative reconstruction technique
SNR	Signal-to-noise ratio
SOD	Source-to-object distance
SSM	Step-and-shoot motion
SWNT	Single-wall nanotube
t	time
T	temperature
T_m	Melting temperature
TEM	Transmission electron microscopy
Ti	titanium
TR	Transmission rate
U.S.	United States
US	ultrasound
UNC	University of North Carolina at Chapel Hill
UV	ultraviolet
V	Applied voltage or Volt
V_{Appl}	Applied focusing voltage

V_{Cath}	Cathode voltage
V_{Rel}	Relative focusing voltage
W	tungsten or Watt
x	thickness or distance
X	exposure
z	Focal plane location
Z	Atomic number
Zn	zinc
λ	Wavelength of electromagnetic radiation
ν	Frequency of electromagnetic radiation
h	Planck's constant
μ	Linear attenuation coefficient or Fermi level
Δx	Small, discrete unit of length or thickness
ρ	density
Ψ	Energy fluence
$\frac{\mu_{en}}{\rho_0}$	Mass energy absorption coefficient
Φ	fluence
ϕ	Work function
β	Field enhancement factor
μm	micrometer
μA	microampere
θ	Anode angle
\vec{x}	Position vector

∇	gradient
Ω	Ohm
μ_{bkg}	Average value of background pixels
\bar{x}	Average value of parameter x
δx	Error of parameter x
$ x $	Magnitude of parameter x

CHAPTER 1: INTRODUCTION

1.1 Importance of breast imaging

The lifetime risk for a woman in the United States of being diagnosed with breast cancer is one in eight¹. In 2013, in the United States, invasive female breast cancer accounted for 29 % of all new cancer cases and 14 % of all cancer related deaths². In addition to the estimated 232,340 new invasive breast cancer cases, 64,640 in situ diagnosed cancer cases were estimated in 2013. In situ cancers only have cells at the initial cancer site, whereas invasive cancerous cells have moved beyond the initial tissue layer². It is hoped that, through screening efforts, cancers can be detected while in situ, before the cancer begins spreading¹.

Breast cancer screening, comprised of a clinical breast exam and mammography for women aged 40 and over, helps save lives by catching cancers as early as possible². There is a positive correlation between cancer stage at the time of diagnosis and the 5-year relative survival rate of cancer patients to people without cancer¹. If the cancer is localized at the time of diagnosis, the survival rate is 99 %. But, if the cancer is distant from the original site, the 5-year relative survival rate lowers to 24 %. From the 1980's to the 1990's breast cancer screening caused the breast cancer incidence rate to increase, but have since then stabilized. Over the 20 years from 1990 to 2010, mortality decreased by 34 % due to a combination of early detection and improved treatments¹. Breast cancer screening does save lives, but cancer survival depends on many other factors as well, including age, race, socioeconomic status, family history, and personal health history^{1,2}.

In addition to screening, diagnostic imaging is a very important part of breast imaging. Effective patient care must include both the accurate detection and diagnosis of cancer. The main purpose of screening is to detect the presence of disease, but diagnosis is needed to determine whether the disease is malignant or benign³. Typically, if cancer is detected through mammography, biopsies are done in order to properly diagnose the cancer. The role of breast imaging is to clearly confirm the presence of a suspicious lesion, but it can only aid in diagnosis if the lesion presents with visual indications of being benign or malignant. For example, certain calcification arrangements can be such an indicator. Breast imaging plays an important role in both effectively detecting cancer and helping to rule out malignancy, in order to reduce the number of breast biopsies returning negative results³.

1.2 Motivation for improving breast imaging

Although mammography is a powerful tool in saving lives, there are notable drawbacks. Today, mammography is primarily dominated by X-ray imaging. Unfortunately, it is not 100 % accurate, and accuracy is worse for women with dense breasts². Women who may never get cancer in their lifetime are subject to regular screenings, and many will go through false alarms¹. Studies find varying rates, of up to 30 %, of the over diagnosis of cancers that would not have progressed and report the rate of biopsies corresponding to false positives at 19 %¹. In Europe, about 200 out of 1,000 patients receive false positives⁴ possibly inducing negative consequences such as anxiety⁴ and increased monetary cost, through further imaging and biopsies⁵. Worse than false positives are false negatives, they possibly allow cancer to go undiagnosed. It is also possible to miss a cancer that begins between screenings⁵.

In addition to X-ray mammography, magnetic resonance imaging (MRI) and ultrasound (US) are used to supplement the screening and diagnosis of breast cancer for some patients. Both of these modalities have their own advantages and drawbacks. A study of 617 patients in the Czech Republic showed that results from preoperative workups, including all three modalities plus core needle biopsy, were significantly different than postoperative histology findings for tumor size, multifocality, and suspicious lymph node status⁶. Current mammographic techniques and procedures have greatly increased breast cancer survival rates, but there are many drawbacks that make further improvements necessary.

Among the three imaging modalities of X-ray, MRI, and US, X-ray imaging remains the most heavily used method for evaluating breast cancer and is the application that is the focus of this work. The motivation for improving X-ray mammography lies in helping to increase accuracy, resulting in lowering treatment costs and improving the patient's quality of life.

1.3 Mammography

1.3.1 Mammographic features

Mammographic features of interest for determining the presence of breast cancer include masses, calcifications, architectural distortions, asymmetries, and any changes in those since previous images were taken³.

1.3.1.1 Masses

There are five distinct mass shapes of varying complexity, and the more irregularly shaped masses indicate a higher chance of malignancy³. Important characteristics to be observed for masses include their shape, margin type, size, attenuation, location, and how

they affect surrounding tissues³. Figure 1.1 gives an illustration of the various types of mass shapes as well as various types of margins masses can have.

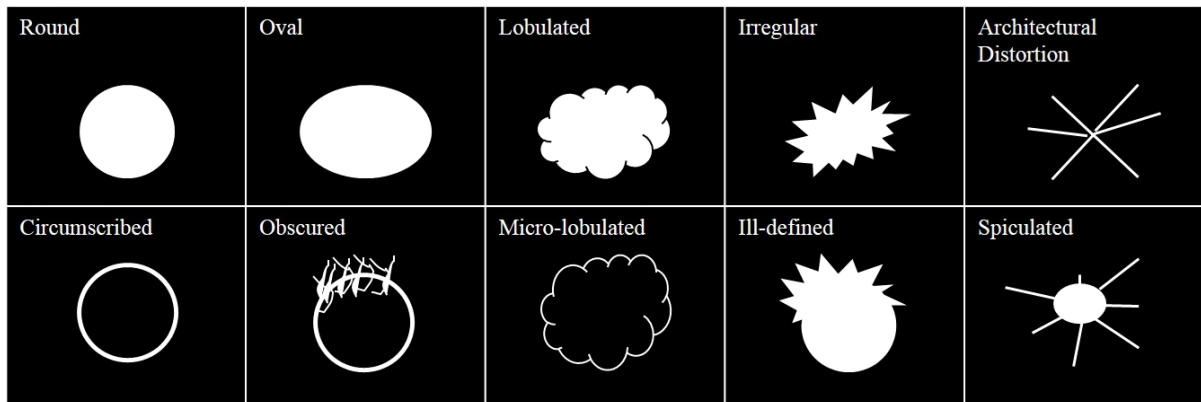


Figure 1.1 Illustration of various mass shapes (upper row) and types of mass margins (lower row). Adapted from Kopans, 2007.

Round, oval, and lobulated masses tend to have circumscribed margins that are sharp and clear³. Benign lesions tend to be round and circumscribed. Less than 10 % of breast cancers have smooth shapes and margins. An example of a cancerous, round mass can be seen in Figure 1.2^{1 7}. The mass required US for diagnosis, highlighting the diagnostic limitations of 2D X-ray mammography. Benign lesions tend to be fibroadenoma, cyst, abscesses from infection, Phyllodes Tumors, papilloma, or fat-containing masses, and are very rarely cancers including metastasis from another cancer elsewhere in the body^{3,7}.

The appearance of normal lymph nodes on a mammogram are usually oval and fatty, but an abnormal lymph node that would indicate cancer spreading would be larger, rounder, and non-fatty⁷. Typically, benign lymph nodes, cysts, and scars are left un-biopsied if

¹ This image was published in Breast Imaging: The Requisites, 2nd Edition, Debra M. Ikeda, Chapter 4, Page 115, Copyright Elsevier (2011).

margins can be clearly identified as regular shaped, and well circumscribed⁷. Therefore, having good spatial resolution in imaging is important to clearly define the edges of structures, such as masses and lymph nodes.



Figure 1.2 MLO view of a round mass with pleomorphic calcifications adjacent to smaller, round masses. Ultrasound images, taken afterward, indicated cancer.

Malignant lesions are defined as those that invade the surrounding tissue, and therefore tend to have irregular shapes and margins⁷. Obscured margins usually end up being biopsied because, due to overlapping tissue, it is unclear whether the mass shape is regular or irregular^{3,7}. Lobulated masses have a high probability of being benign, but a micro-lobulated margin, where the shape irregularities are on the order of millimeters, could be the result of a growing cancer, as shown in Figure 1.3^{2,3}. Ill-defined or indistinct margins suggest that a malignancy is spreading to surrounding tissue, and requires biopsy^{3,7}. Finally, spiculated margins indicate the growth of cancer cells into the surrounding tissues, and is a key

² This image was published in *Breast Imaging: The Requisites*, 2nd Edition, Debra M. Ikeda, Chapter 4, Page 115, Copyright Elsevier (2011).

indicator for malignancy⁷. Types of cancers that present with spiculated margins include invasive ductal cancer, invasive lobular carcinoma, and tubular cancer. Other lesions can appear with spiculations, but may not be cancer, such as scars and fat necrosis⁷.

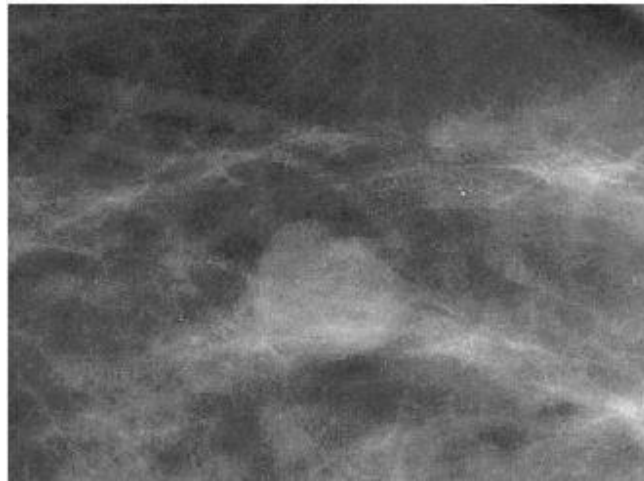


Figure 1.3 Slightly lobulated, circumscribed, round mass simulating fibroadenoma that biopsy showed to be invasive ductal cancer.

Being able to clearly see the outline of a mass is a very important part of breast cancer screening and may require additional views, as shown in Figure 1.4³. Overlapping tissue can blur lesion margins, and spiculated or irregularly shaped masses could have fine details that need to be differentiated in an image. Therefore, mammographic image quality and the ability to remove surrounding tissue overlap is very important for determining the presence of cancer.

³ This image was published in *Breast Imaging: The Requisites*, 2nd Edition, Debra M. Ikeda, Chapter 4, Page 116, Copyright Elsevier (2011).

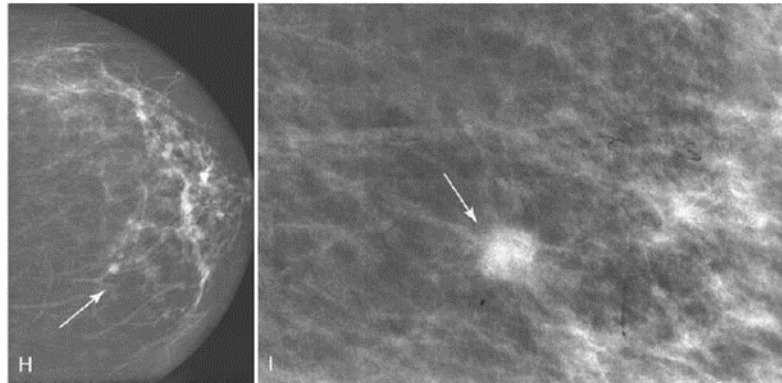


Figure 1.4 Image (H) shows a vague round mass that was shown in the magnification view (I) to have indistinct borders; a biopsy revealed invasive ductal cancer.

1.3.1.2 Calcifications

Another key feature that radiologists look for in a mammogram is calcifications, examples are illustrated in Figure 1.5. Most calcifications that form in the breast are benign, but 50 % – 80 % of all cancers are associated with calcifications and are sometimes the only visible sign of cancer on the mammogram⁷. Cancerous calcifications develop from tumor center necrosis or secretions from malignant cells. Important factors to look for are the individual shape of a calcification, and the shape and location of the calcification cluster. In general, calcifications that are located in the breast ducts, lobules, and inside tumors are malignancy indicators⁷. A mass that has other malignant indicators has an increased chance of being cancerous if calcifications are also present³. If the calcifications are located within interlobular stroma, outside of ducts, or in the blood vessels, fat, muscle, nipple, or skin, they are typically benign⁷.

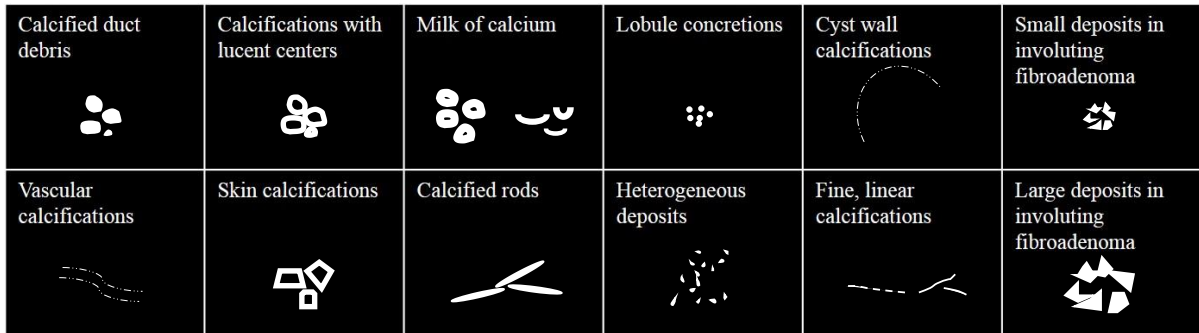


Figure 1.5 Illustration of many calcification types that are observed with mammography. Adapted from Kopans, 2007.

Calcifications that are easily labeled as benign are any with lucent centers, that are less X-ray absorbent, and include those found in fat necrosis or in the skin³. Other benign calcifications are those found in cysts, either egg-shell type on a cyst wall or those referred to as milk of calcium. Any calcifications formed into rods due to secretory disease or present in involuting fibroadenoma are benign. Typically, benign calcifications are calcified debris in ducts, concretions in dilated lobules, and vascular calcifications. If duct debris begins to form a spherical cluster over time, they could be a cause for concern³.

Cancerous calcifications are typically less than or equal to 0.5 mm in size, irregularly shaped, and vary in shape and size within a cluster³. Heterogeneous deposits, also known as pleomorphic or granular deposits, are not typical of anything but are suspicious if they meet the qualifications for cancerous calcifications. An example of these calcifications is shown in Figure 1.6⁴, where they were indicative of ductal carcinoma in situ. Fine, linear calcifications, less than 1 mm in size, are usually present in necrotic tumors. They are thin, irregularly shaped, and made up of discrete, discontinuous calcifications³. Therefore, spatial

⁴ This image was published in *Breast Imaging: The Requisites*, 2nd Edition, Debra M. Ikeda, Chapter 3, Page 87, Copyright Elsevier (2011).

resolution and image quality for mammograms are very important because cancerous calcifications are generally smaller and more difficult to see.

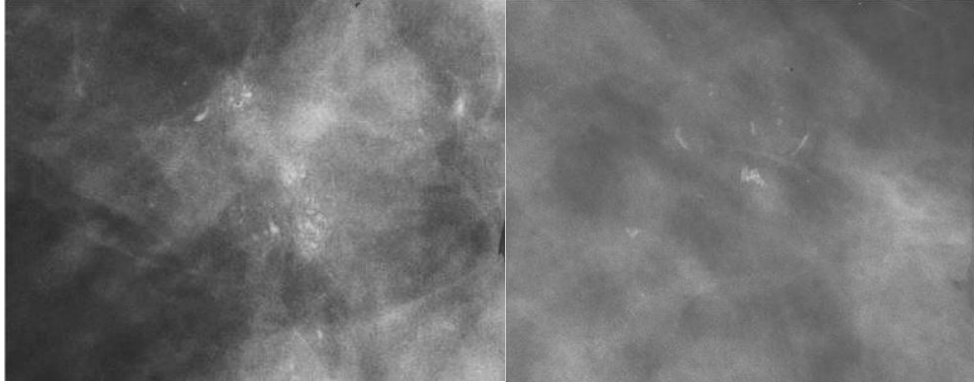


Figure 1.6 X-ray examples of calcifications typical of ductal carcinoma in situ. Left: Granular type. Right: Pleomorphic type.

1.3.2 Non-radiographic imaging modalities used with mammography

Although neither ultrasound nor MRI are recommended for general breast cancer screening at this time, there are many uses for both modalities to supplement current mammography practices⁷.

1.3.2.1 Ultrasound

Ultrasound (US) imaging combines the properties of high-frequency sound waves and the acoustic properties of the body⁸. A transducer is used to emit short ultrasound pulses into the tissue it is physically in contact with, as shown in Figure 1.7. The sound waves interact with the tissue which reflects an echo back to the transducer, especially at object surfaces and internal structures. The echoes are detected along linear paths over different angles in the area being imaged, known as sector scanning. The images produced are on a gray scale proportional to the echo amplitude detected, and depth of the object can be determined by the time difference between when the echo is measured and when the original pulse was

produced. Two-dimensional (2D) tomographic images, or three-dimensional (3D) images can be produced through US⁸.

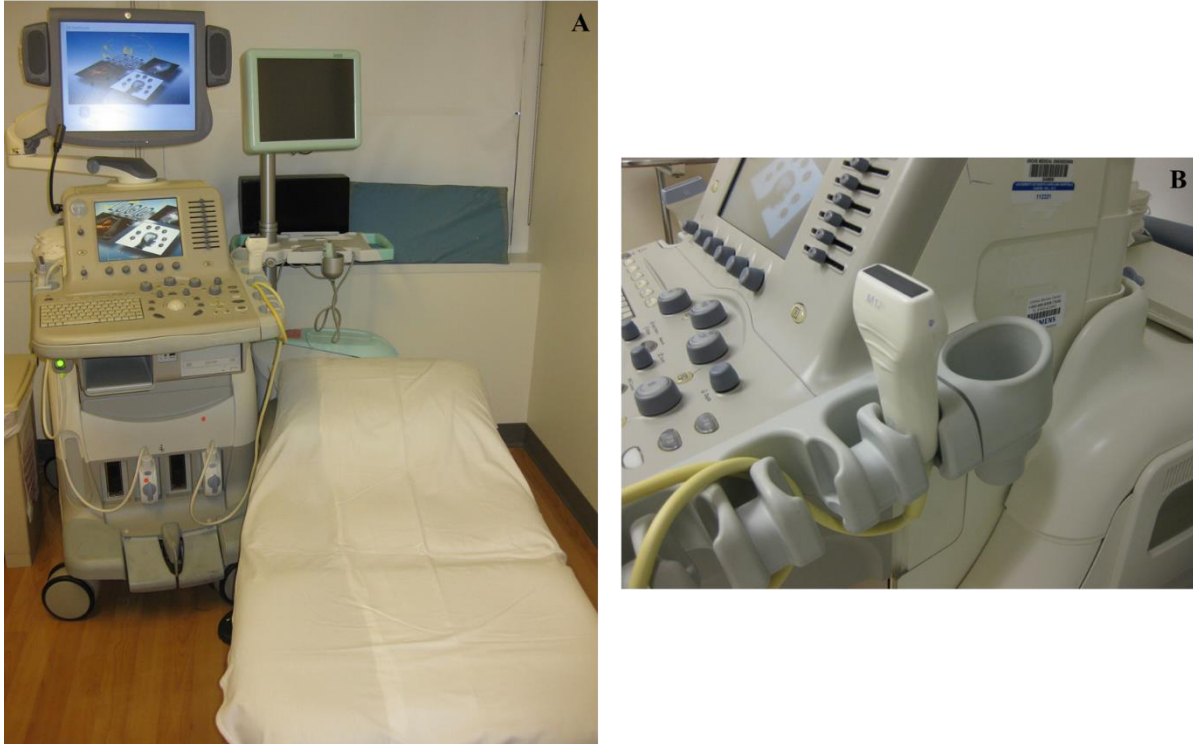


Figure 1.7 (A) Photograph of an ultrasound unit used in a mammography clinic. (B) Close-up of a transducer used for imaging.

If a clinical breast exam or screening mammography return abnormal findings, US can be used in a follow-up exam, as in the Figure 1.8⁵, used to follow up on the lesions shown in Figure 1.2⁹. For example, US could be used to further evaluate calcifications found on a mammogram to see if there is a mass associated with the calcifications that was invisible to X-rays⁷. Screening is done with ultrasound for women younger than 30 if they have a palpable mass and for women of any age with dense breasts⁷. For women who have dense

⁵ This image was published in Breast Imaging: The Requisites, 2nd Edition, Debra M. Ikeda, Chapter 4, Page 115, Copyright Elsevier (2011).

breasts, US can be useful to remove the obstruction from overlying tissues that would be a problem in digital mammography¹⁰. It has been shown that using whole breast screening US in combination with mammography can increase the detection of cancers in women with dense breasts by 55 %⁹. One major use for US is in differentiating solid masses from cysts^{7,11}. Cysts make up about 25 % of all detected breast lesions¹¹, but are benign⁷. However, a solid mass could be either benign or malignant⁷. To evaluate the presence of cancer in a solid mass, US is used to determine the mass shape, margins, thickness of the echogenic rim, duct extension, how the mass affects surrounding tissue, if it is taller than wide, and its acoustic properties. If a mass is taller than it is wide, that indicates the mass is growing outside of its initial tissue plane, and is a sign of malignancy⁷. Other main uses of US include image guidance for percutaneous needle biopsies⁷ and decision making for surgery and therapy planning¹⁰.

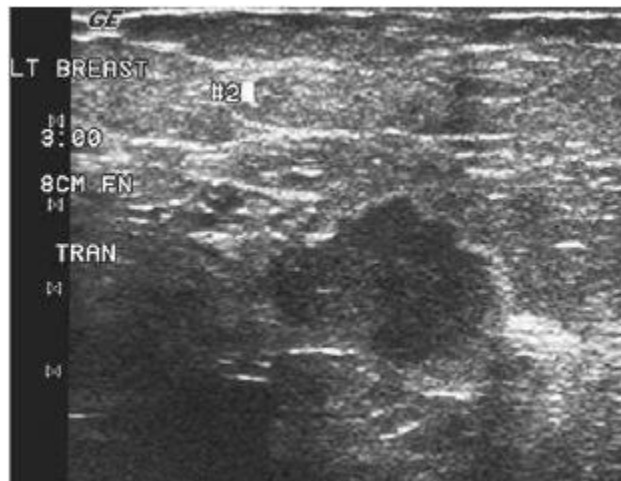


Figure 1.8 Ultrasound image of a multilobulated mass that is invasive ductal cancer, but appeared round on a mammogram.

Additionally, ultrasound is very useful because it is a fast and easy method that can be carried out with handheld transducer devices⁷. It does not involve ionizing radiation; only

employs moderate compression, if any; and is widely available⁷. However, there is currently not enough evidence to prove that US alone is adequate for general breast cancer screening⁹. Although some lesions that are missed in mammography can be seen with US, there are lesions, both cancerous and non-cancerous, that cannot be seen with US⁷. Ultrasound is also limited in its effectiveness for fatty breasts and for visualizing most calcifications⁷.

1.3.2.2 Magnetic resonance imaging

MRI generates images by localizing nuclear magnetic resonance (NMR) signals using magnetic field gradients⁸. NMR signals originate from the magnetic properties inherent to the nuclei of atoms with nonzero nuclear magnetic moments. When the nuclei are placed in a strong, external magnetic field and exposed to radiofrequency (RF) pulse sequences, they absorb and emit a characteristic energy that is used to identify the location and quantity of the particular nuclei of interest. An example of a dedicated MRI coil for the breast can be seen in Figure 1.9⁶. The characteristic energy signals are then reconstructed into MR images with high levels of soft tissue contrast, adjustment made possible through the development of increasingly complex pulse sequences. The images are 3D and viewed as sets of tomographic slices through the imaged portion of the body. Due to their different local magnetic properties, MRI can differentiate materials such as fat, brain matter, fluids, and cancer⁸.

⁶ Reprinted from *Magnetic Resonance Imaging*, 31, Bertine L. Stehouwer, Dennis W.J. Klomp, Mies A. Korteweg, Helena M. Verkooijen, Peter R. Luijten, Willem P.Th.M. Mali, Maurice A.A.J. van den Bosch, Wouter B. Veldhuis, *Resonance Imaging of invasive ductulolobular carcinoma: First clinical experience*, Page 614, Copyright (2013), with permission from Elsevier.

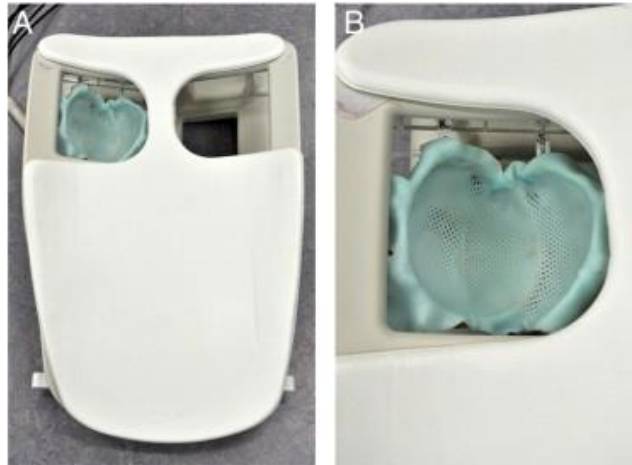


Figure 1.9 Dedicated MRI breast coil, with the coil detail shown in (B).

MRI is primarily used in breast cancer screening for women who are at a higher risk of breast cancer for reasons such as having a family history of breast cancer⁹, testing positive for the BRCA1 and BRCA2 genetic mutations⁹, women with a history of Hodgkin disease⁷, and women with a greater than 20 % lifetime risk of developing cancer⁷. Women with silicon breast augmentation are also screened with MRI⁷, because the silicon does not cause extensive artifacts in MRI nor prohibit imaging the surrounding breast tissue as it does with mammography.

Certain lesions are only visible on MRI⁷, such as some cases of ductal carcinoma in situ and some cases of multifocal disease¹⁰; and it is the most accurate and sensitive for evaluating tumor extent¹⁰. With a 93 % sensitivity rate, it is also the most sensitive modality for the preoperative staging of invasive lobular carcinoma¹⁰. Invasive lobular carcinomas that cannot be seen with mammography can generate a high signal intensity in MRI when using contrast agents⁷, giving information on the lesion's vascularization¹⁰. An example of an MRI

image showing invasive lobular carcinoma can be seen in Figure 1.10⁷. Other main uses of MRI for the breast include image-guided core biopsies and needle localization for surgery. It is also used to evaluate patients' response to chemotherapy and to evaluate the recurrence of cancers⁷.

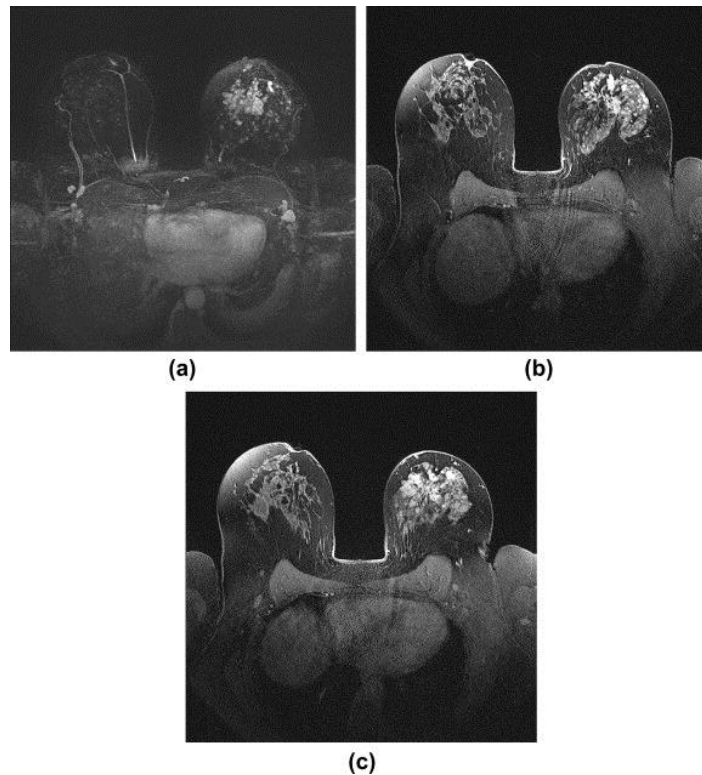


Figure 1.10 MRI breast image sequence of invasive lobular carcinoma in the left breast.

One of the main drawbacks of MRI is its cost, playing a large part in its infrequent use in breast screening in general⁷. Another issue is the tendency of MRI to overestimate a lesions' malignancy, giving it a large specificity range of 39 % to 95 %. These false positives

⁷ Reprinted from Clinical Radiology, 69, M. Muttalib, R. Ibrahim, A.S. Khashan, M. Hajaj, Prospective MRI assessment for invasive lobular breast cancer. Correlation with tumour size at histopathology and influence on surgical management, Page 27, Copyright (2014), with permission from Elsevier.

can be due to lesions that, in MRI, mimic ductal carcinoma in situ or invasive carcinoma. Some of the types of lesions that cause issues are fibroadenoma and papilloma. MRI is also subject to many types of artifacts, including motion of the patient and motion from cardiac and respiratory processes⁷. In addition to the imaging shortcomings due to the modality itself, and even with its high sensitivity, MRI would not be used for general population screening because of the expense and limited access relative to X-ray imaging⁹.

1.3.3 Current state of X-ray mammography

Before going into the details of X-ray mammography, a summary of the physical principles of X-rays will be given.

1.3.3.1 The physics of X-ray imaging

1.3.3.1.1 Electromagnetic radiation

X-rays are a type of electromagnetic radiation that originate outside an atom's nucleus and are known as ionizing radiation⁸. Ionizing radiation has enough energy in each photon to be able to remove electrons from their atomic orbits. All types of electromagnetic radiation can behave either as waves having a wavelength, frequency, and amplitude, or as particles of a specific energy, known as photons. The wavelength of an X-ray is determined by its speed and frequency according to the equation:

$$\lambda = \frac{c}{\nu}$$

where λ is the wavelength in meters (m), c is the speed of light defined as 3.0×10^8 m/s, and ν is frequency in hertz (Hz)⁸. The energy of a photon is defined as:

$$E = h\nu$$

where E is the photon energy in Joules (J), and h is Planck's constant equal to 6.626×10^{-34} J·s¹².

X-rays have high frequencies, short wavelengths, and range in energy from the keV to the MeV range¹². For imaging, wavelengths range from 10 pm – 100 pm and energies range from 12.4 keV – 124 keV¹³.

1.3.3.1.2 Production of X-rays

X-rays are produced when electrons interact with matter so that some of the kinetic energy of the electron is lost⁸. The lost kinetic energy is converted to electromagnetic radiation in the form of X-rays. For this process to occur there must be an electron source, a vacuum environment, a target material, and an energy source to accelerate the electrons toward the target material⁸.

Bremsstrahlung

Bremsstrahlung means “breaking radiation”⁸. This type of X-ray can have any energy up to the energy of the accelerating power supply. As an electron passes through the target material it will encounter nuclei at different distances. The interaction causes a loss of kinetic energy from the electron because of the Columbic forces between it and the atomic nuclei. An X-ray is emitted of energy equal to the loss in kinetic energy, and the electron path is altered. The closer the electron is to the nucleus of an atom at the time of interaction, the higher the energy of the resultant X-ray will be. Since it is more likely for an electron to interact with nuclei at a large distance, most X-rays produced are at lower energies. An example Bremsstrahlung spectrum is shown in Figure 1.11. More often than not, however, an electron will collide with another electron and lose its kinetic energy as heat. The efficiency of X-ray production is very low relative to the amount of heat produced, usually less than 1 %⁸.

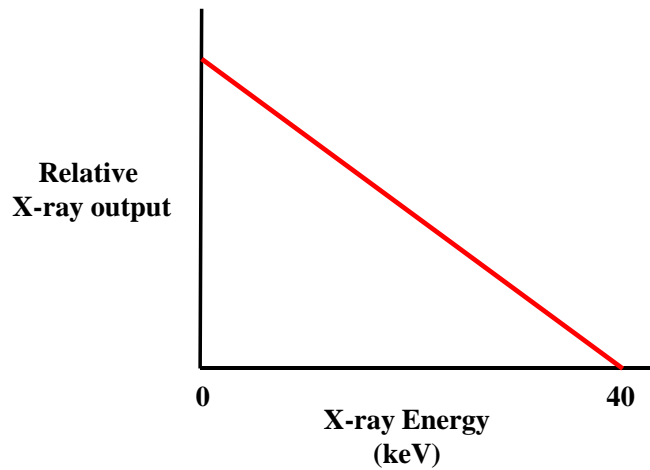


Figure 1.11 Illustration of a typical Bremsstrahlung radiation spectrum for the case of a 40 kV acceleration potential.

Characteristic radiation

Electrons surrounding atomic nuclei are ordered according to binding energies and are labeled according to different energy shells⁸. Going from highest binding energy and closest to the nucleus, to lower binding energy farther away, the shells are labeled K, L, M, and N. Each element has characteristic energy levels for each of their electron shells, revealing the source of the name characteristic radiation. If an electron or Bremsstrahlung X-ray has an energy higher than the binding energies of the target material, there is the opportunity for characteristic radiation to be produced by ejecting an electron from its orbit⁸.

Upon ejection from its energy shell, an electron leaves an unstable “hole” in the electron cloud that is quickly filled by an electron from a shell of lower binding energy⁸. As the electron moves to a shell with higher binding energy, energy is lost by the electron via a characteristic X-ray. The energy of the X-ray is equal to the difference in the binding energies of the final and initial shells. These X-rays show up on the X-ray spectrum as peaks

located at the energies characteristic to the electron shell transitions. For the energy ranges relevant to imaging, the peaks seen are usually K-shell peaks⁸.

Figure 1.12 shows an illustration of a spectrum from a silver target with an accelerating potential of 40 kV. In the figure, the Bremsstrahlung radiation is filtered by the X-ray window of the tube, aluminum for example. Some energies are completely absorbed by the window, explaining why there are no X-rays at the lowest energies. Two characteristic K peaks can be seen adding on top of the Bremsstrahlung radiation. If, for example, the target material was tungsten, the K-peaks would not be visible because the binding energy of the tungsten K-shell is higher than that of a 40 kV accelerating potential. Because the acceleration potential is 40 kV, this spectrum would be referred to as a 40 kVp spectrum. The spectrum contains a wide range of energies, but peaks at 40 kV.

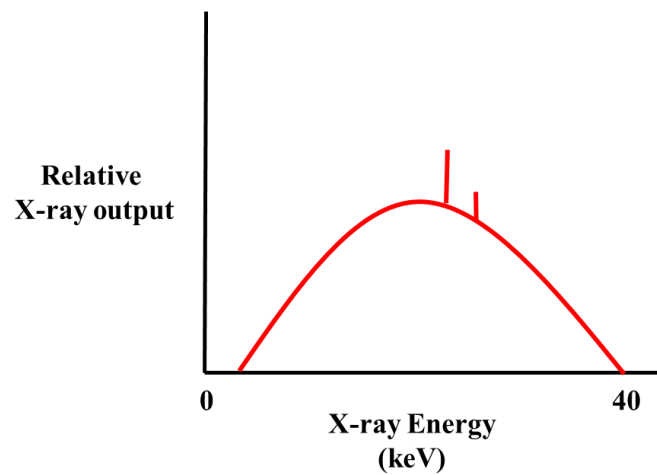


Figure 1.12 Illustration of a complete X-ray spectrum characteristic of a silver metal target and acceleration potential of 40 kV.

1.3.3.1.3 Interaction of X-rays with matter

Once X-rays are produced in a medical imaging device, they are directed toward the patient, where the X-rays will interact with body tissues. There are three main ways that X-rays of energies relevant for breast imaging interact with matter: Compton scattering, Rayleigh scattering, and the photoelectric effect^{8,12}.

Compton scattering

Compton scattering occurs when an X-ray photon interacts with an individual valence electron, ionizing the atom by knocking the electron out of its orbit^{8,12}. The incident photon is scattered at some angle and changes direction¹². The scattered photon energy is the difference between the incident photon energy and the scattered electron's kinetic energy, and is dependent on the photon scattering angle^{8,12}. This type of interaction dominates the others within the diagnostic imaging range, and leads to image degradation⁸. At breast imaging energies, most of the energy stays with the scattered photon, reducing attenuation contrast from the primary photons. The probability of forward scattering, which impacts image quality most, is increased at higher energies⁸.

Rayleigh scattering

Rayleigh scattering occurs when an incident X-ray photon excites all of an atom's electrons into a coherent oscillation that mimics the oscillation of its electric field^{8,13}. Each of the electrons quickly emit radiation of the same wavelength as the incident X-ray. Those emitted X-rays combine into one scattered X-ray photon of the same wavelength traveling at a different angle relative to the incident photon. During this process the atom does not become ionized, and no energy is lost to kinetic energy^{8,13}. The chance of this type of scattering to occur is 12 % at 30 keV⁸, and decreases as photon energy increases¹³. This

scattering can cause image degradation by slightly increasing the width of the X-ray beam¹³, especially in the mammography energy range of 15 keV – 30 keV⁸.

Photoelectric effect

The photoelectric effect is a process by which atoms become ionized when a photon of energy slightly greater than or equal to the binding energy of an electron transfers that energy to the electron, ejecting it from the atom⁸. This electron is called a photoelectron. The kinetic energy of the photoelectron is the energy of the incident photon minus the electron's binding energy. Because there are no scattered photons produced, the photoelectric effect does not negatively impact image quality. Characteristic radiation can be produced when electrons of lower binding energy fill the "hole" left by a photoelectron, but this is very infrequent. The probability of the photoelectric effect occurring is proportional to Z^3/E^3 , where Z is the atomic number of the ionized atom and E is the incident photon energy. This shows that the effect occurs more at low energies and in heavier elements. Tissue is a relatively low Z material, so the probability of characteristic radiation being produced in the body during imaging is low. Below energies of 50 keV the photoelectric effect actually improves image contrast because it highlights the differences between tissues having slightly different Z values⁸.

The photoelectric effect is an important factor only up to 50 keV¹³. For water, it makes up the highest percentage of matter interactions between 10 keV – 20 keV, making up 92 % – 81 % of all interactions. Compton scattering is the dominant matter interaction for energies 30 keV and above. At 10 keV Compton scattering is only 3 % of all interactions, but increases to 51 % at 30 keV. Rayleigh scattering is never the dominant interaction, but peaks at 30 keV, at 13 % of all interactions. At 60 keV, the photoelectric effect has lowered in

percentage from 92 % at 10 keV, to being approximately equal to Rayleigh scattering at about 7 %¹³.

1.3.3.1.4 X-ray attenuation

Attenuation of X-rays is the source of image contrast in mammography. In the breast, there are different types of materials such as calcifications, fat, and glandular tissue. Each of these has a different density and effective atomic number, causing them to attenuate X-rays differently⁸. Different amounts of X-ray attenuation will show up as lighter or darker areas on an X-ray image, providing contrast.

X-ray attenuation is caused by the removal of photons⁸. Removal of photons occurs by absorption or scattering in a material. In the energy range used for imaging, the linear attenuation coefficient results from the combined attenuation from all scattering types and the photoelectric effect as:

$$\mu = \mu_{Rayleigh\ scattering} + \mu_{photoelectric\ effect} + \mu_{Compton\ scattering}$$

where μ is the symbol for the linear attenuation coefficient⁸. It is the fraction of photons that are lost to the material, n , per unit length or thickness, Δx , of the material^{8,12}; as follows:

$$\mu = \frac{n/N}{\Delta x}$$

where N is the number of incident photons⁸. In general, μ decreases with increasing energy, except at materials' K-edges at which the photon energy is approximately equal to the binding energy of the electrons in the K-shell. It also increases with increasing density of the material. Normalizing the linear attenuation coefficient by a materials' density gives the mass attenuation coefficient as μ/ρ , with units of cm^2/g ⁸.

Taking the equation for μ as continuous we can write it as a differential equation:

$$\frac{dN}{N} = -\mu dx$$

and solved to obtain the fundamental photon attenuation law

$$N = N_0 e^{-\mu x}$$

where N_0 is the number of incident photons, N is the number of transmitted photons, and x is thickness¹². The number of photons is proportional to the intensity of the X-ray beams, and for monoenergetic beams the intensity is simply

$$I = I_0 e^{-\mu x}$$

where I is the resultant intensity and I_0 is initial intensity. This equation, however, assumes that μ is uniform over the x -direction, which it may not necessarily be. To take into account an inhomogeneous material the equation becomes,

$$I(x) = I_0 e^{-\int_0^x \mu(x') dx'}$$

taking the integral over the thickness of the material. Mammography is not done with a monoenergetic beam, but instead a polyenergetic spectrum, as in Figure 1.12. To take the inhomogeneity of the material and the polyenergetic spectrum into account, the final equation of the resulting intensity after attenuation is

$$I(x) = \int_0^\infty S_0(E') E' e^{-\int_0^x \mu(x'; E') dx'} dE'$$

where S_0 is the original, polyenergetic spectrum. However, this calculation is not typically carried out because the equation for μ tends to be complex, and is instead often estimated¹².

1.3.3.1.5 Absorption of X-ray energy

Another important aspect of medical imaging is knowing the radiation dose given to the patient and how that relates to the X-ray output of the mammography system.

Absorbed dose

Absorbed dose is the amount of energy from X-rays that is deposited per unit of mass of material⁸. The SI unit of absorbed dose, or dose, is the gray (Gy). One Gy is equal to 1 J/kg. The traditional unit for dose is the rad, equal to 10 mGy. Dose (D) can be calculated by multiplying the mass energy absorption coefficient by the energy fluence, according to

$$D = \Psi \left(\frac{\mu_{en}}{\rho_0} \right)_E.$$

Ψ is energy fluence, defined as fluence (Φ) times energy per photon, in keV/cm², written as

$$\Psi = \Phi \cdot E.$$

Fluence is defined as the number of photons per unit area. The mass energy absorption coefficient, represented as $\frac{\mu_{en}}{\rho_0}$, is the mass attenuation coefficient multiplied by the percentage of initial photon energy that was converted to kinetic energy⁸.

Exposure

Exposure (X) is a measure that is directly related to the output of an X-ray tube⁸. It is defined as the amount of electric charge produced from the X-rays in matter, per unit of mass. The unit for exposure is the roentgen, R, equivalent to 2.58×10^{-4} C/kg⁸. The output intensity of an X-ray machine is X divided by unit current multiplied by unit time (mAs). This measure is also specific to the kVp, source-to-image receptor distance (SID), and filtration in use¹².

The amount of electric charge produced, or ionization, in air can be measured directly with use of an ion chamber. The amount of ionization in air is very similar to that which would be present in soft tissue. Therefore, a relationship can be made between measured exposure and the dose a patient will receive. This conversion is specific to the particular photon energy and material being measured, and for air is written as

$$D_{air} = 8.76 \times X$$

where dose (D_{air}) is in mGy, and exposure (X) is in roentgens⁸.

1.3.3.2 Technique

Mammography practices and equipment are regulated by the United States Food and Drug Administration (FDA), according to the Mammography Quality Standards Act (MQSA)⁷. The MQSA changes as technology advances, and also determines a lot of the characteristics equipment must have. There are two main types of mammography units in use today, and the difference lies in how the image is captured. Originally all units were screen film units (SFM) that captured images on film which required developing⁷. Over time, SFM began being replaced by full field digital mammography (FFDM). The transition from SFM to FFDM began around 2005 when the Digital Mammographic Screening Trial (DMIST) study was published, comparing the two modalities¹⁴. As of May 2010, two-thirds of all mammography systems in the United States were digital⁷. Most remaining SFM units are slowly being replaced¹⁴.

1.3.3.2.1 Equipment

Figure 1.13 illustrates the main components common to all mammography systems, and Figure 1.14 shows an example mammography unit manufactured by GE. All mammography units have an X-ray source and image receptor that are fixed relative to one another by a rotating C-arm. The C-arm allows the unit to rotate in either direction in order to obtain different views of the breast. The SID is usually 65 cm to 70 cm, but must be at least 55 cm⁷.

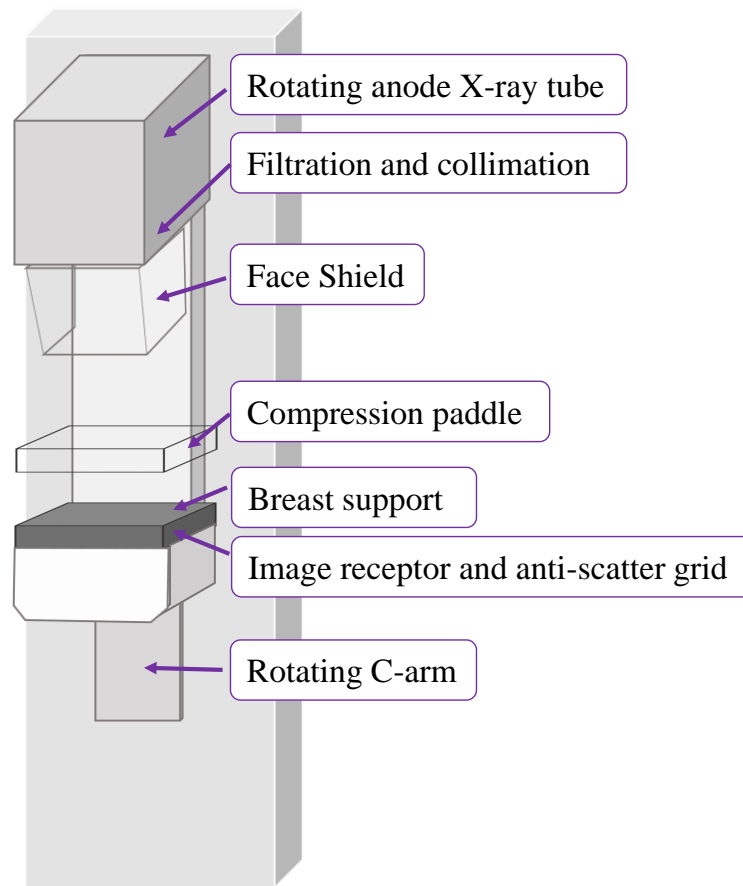


Figure 1.13 Illustration of a mammography unit with major components labeled. Adapted from Ikeda, 2011.



Figure 1.14 Photograph of a mammography unit built by GE.

X-ray tube

More detail of the tube head, containing the X-ray source, filtration, and collimation; and the image receptor lying below the breast support and anti-scatter grid, can be seen in Figure 1.15. Electrons are produced at the cathode and travel toward the anode. In the X-ray tube, the cathode is on the chest wall side in order for the maximum intensity of X-rays to be directed toward the thickest part of the breast. Intensity changes across the field of view due to the Heel effect inside the anode⁸. Some electrons must travel through thicker parts of the anode before they are emitted, lowering the beam intensity. The anode rotates in order to dissipate heat from the electron interactions with the material, preventing it from melting.

The area of the anode that receives electrons is known as the focal spot. There are generally two sizes used, 0.3 mm and 0.1 mm⁷. The larger focal spot is used for normal imaging tasks. When magnification is used the breast is moved closer to the X-ray source and the smaller focal spot is employed to limit geometric blurring⁷.

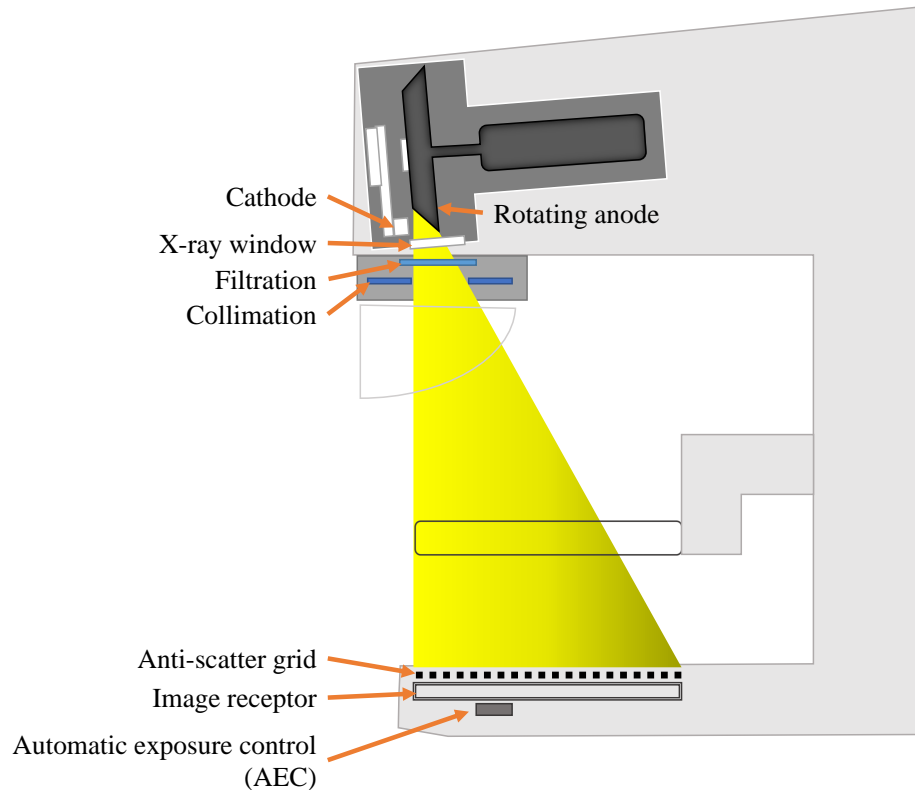


Figure 1.15 Cross-section of a mammography unit showing the details of the X-ray tube and collimation, as well as the breast support area and image receptor housing. Adapted from Bushberg, 2002.

The X-ray generator provides power to the X-ray tube⁷. It is required to be able to provide 24 kVp – 32 kVp, and 5 mA – 300 mA of current. When using a molybdenum anode, 24 kVp – 32 kVp is typically used. For rhodium or tungsten targets, 26 kVp – 35 kVp is the range used⁷.

If there is no magnification, an X-ray tube generally operates with 100 mA of current on the anode⁷. But, the specific current used depends on breast thickness and can range from 10 mA to several hundred milliamperes. The average breast is usually defined as being 5 cm thick. To image an average breast, the tube would output 100 mA at 26 kVp for 1.5 s, giving a tube output of 150 mAs⁷.

Filtration

After X-rays are produced at the anode, they leave the X-ray tube through the X-ray window, usually beryllium metal, 1.5 mm thick or less¹⁵. After the X-rays leave the X-ray tube, the spectrum is filtered to optimize it for imaging. There are several combinations of anode and filter materials typically found in mammography X-ray tubes. The combination Mo/Mo (where Mo stands for molybdenum) is the most common, with a Mo anode and filter⁷. It is also the choice used for women with thinner breasts defined as having a compressed breast thickness of less than or equal to 5 cm. The anode/filter combination Mo/Rh penetrates deeper into tissue and is used for thicker breasts. Other combinations include Rh/Rh, W/Rh, W/Ag, and W/Al. These are appropriate for breasts thicker than 5 cm, denser breasts, and for use in combination with higher kVp settings⁷.

Collimation

After the X-ray beam is filtered, it then passes through a collimator. The collimator determines the shape and size of the area covered by X-rays⁷. It serves to protect tissue that is not in the image, and conforms to the shape of the image receptor. MQSA regulations state that the X-ray beam is not allowed to enter into the chest wall more than 2 % of the SID⁷.

Compression

The breast compression plate lies within the collimated beam, but it is transparent to X-rays and does not impact the image. The role of the compression plate is to provide enough force to immobilize the breast between itself and the breast support plate, which sits above the image receptor.⁷ It must be able to maintain 25 lb – 45 lb of pressure for at least 1 min. The compression plate must have a lip perpendicular to the chest wall, at least 3 cm in height. This lip prevents unwanted tissue from getting imaged. Compression improves imaging in a couple of ways. Firstly, it spreads out fibroglandular tissue which can occlude lesions, allowing increased visualization of cancer. Secondly, it decreases breast thickness. Thinner compressed thicknesses require less exposure time and lower dose. This reduces dose to the patient and reduces the chance of patient motion interfering with image quality⁷.

Image receptors and resolution requirements

Whether SFM or digital mammography (DM), there is an anti-scatter grid above the image receptor that removes scattered photons before they are detected⁷. The grid is able to retract, and is not used in magnification images. Typically the grid is made up of lead strips, with a set strip height to pitch ratio. For a detector area of 18 cm × 24 cm it is 3.5:1, and for 24 cm × 30 cm it is 5:1. In addition to being able to retract, it also moves around during imaging so that the image of the lead strips is evenly blurred out and does not show up on the image. The grid does absorb a significant amount of primary X-rays in addition to scattered X-rays. Therefore, to get good image quality the exposure must be double that without the grid in place⁷.

In SFM systems the image receptor is a film cassette⁷. The cassette usually consists of a single emulsion film above an intensifying screen. To see the image, the film must be developed. The film is placed into an auto processor where it goes through a liquid developer

that amplifies the latent image by deionizing silver atoms. Generally the resolution ranges from 18 lp/mm – 21 lp/mm. The unit of resolution, lp/mm, stands for line pairs per millimeter. As it sounds, it is a measure of how many line pairs can be distinguished in 1 mm by a given imaging system. For a 0.3 mm focal spot, an SFM system is required to have specific resolution levels in both in-plane directions. It must be 11 lp/mm or 13 lp/mm if it is being measured perpendicular to the long direction of the focal spot, or parallel to it, respectively. The limiting factor for resolution in SFM is actually the focal spot size, not the film itself⁷.

In DM, there are four different types of digital detectors: indirect, direct, photoconductive¹⁴, and CR⁷. Indirect detectors convert X-rays into visible light photons, usually with CsI fluorescent screens. The visible light photons are detected with either amorphous silicon or charge-coupled devices (CCDs). Direct detectors are able to detect the X-rays themselves, and count them, to form an image. Photoconductive detectors, usually amorphous selenium, absorb X-rays and store information as ionization charges. A laser or silicon diode array is used to read out the charge distribution. CR, or computed radiography, detectors use cassettes as in an SFM system. X-rays are absorbed by a photostimulable phosphor made out of barium fluorobromide doped with europium. The absorption of X-rays into the crystal promotes its electrons into higher energy levels. The crystal is read by a red laser light, releasing the stored electrons. The release of electrons emits a blue light proportional to exposure that is then read. The resolution of DM detectors is limited by pixel size, and ranges between 5 lp/mm to 10 lp/mm⁷.

In both SFM and DM systems, underneath the image receptor is a D-shaped sensor called the automatic exposure control (AEC) sensor⁷. AEC is used to detect the densest part

of the breast, and helps to tailor the X-ray output in such a way as to make the optical density on film as uniform as possible⁷. It allows the appropriate amount of dose to be determined for proper DM image quality while not overdosing the patient. It also employs a safety feature allowing it to shut off the system after 4 s to 6 s, and it limits tube output to between 300 mAs and 750 mAs, for tube safety⁷.

1.3.3.2.2 Positioning

The two most common mammographic views are the craniocaudal (CC) and mediolateral oblique (MLO) views^{7,15}, the directions of both are illustrated in Figure 1.16.

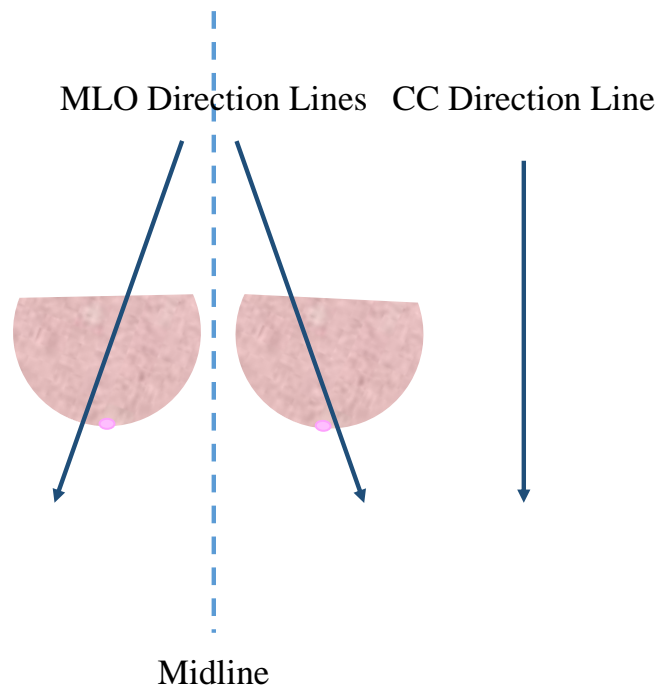


Figure 1.16 Direction lines for the CC and MLO views used in breast imaging.

The CC view is taken without any tilt from the C-arm, and the X-rays travel in the direction from the head through the breast. An example set of CC X-rays is shown in Figure

1.17. It is desired that a CC image include the medial portion of the breast which is the area nearest the midline of the body, the outer regions of the breast, and a portion of the pectoralis muscle. Inclusion of the medial region is very important because viewing this portion in a CC view may be the only way to catch certain breast lesions.

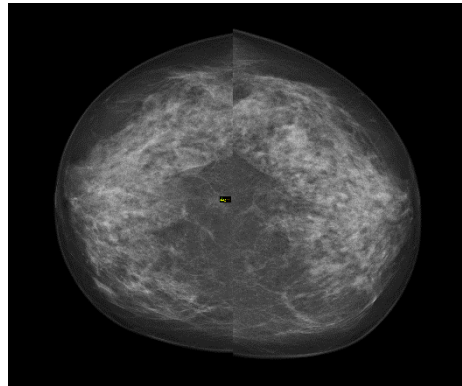


Figure 1.17 A CC-view set of X-rays placed back-to-back. The images for each breast are placed back to back. Attribution: © Nevit Dilmen

The MLO view, shown in Figure 1.18, is taken with the C-arm tilted at an angle, the direction dependent on which breast is being imaged at the time. The detector should be positioned parallel to the pectoralis muscle, and the X-rays travel from above the body midline down through the breast at an angle. The pectoralis muscle should be in the image, appearing convex in shape, with some fat visible between it and the fibroglandular. At the bottom of the image, the upper portion of the abdominals should be visible. There should be as much tissue near the chest wall as possible^{7,15}.

A screening session will include at least one CC and MLO view per breast, or four images total. The mean glandular dose, defined as the absorbed dose to the fibroglandular

tissue, is usually 2 mGy per exposure in SFM⁷. A complete SFM screening would total at least 8 mGy mean glandular dose to the patient.

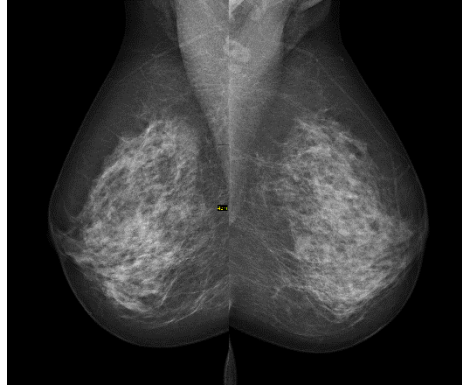


Figure 1.18 Right and left MLO X-rays back-to-back. Attribution: © Nevit Dilmen

In order to see a certain portion of the breast more clearly, magnification views would be used⁷. This technique is especially useful for imaging calcifications more clearly. The breast is raised on a magnification stand so that it is closer to the X-ray tube. The smaller focal spot is used, and current output is lowered to 25 mA – 40 mA. MQSA requires that any mammography unit must be able to provide magnification factors between 1.4 and 2⁷.

1.3.3.3 Goals, trends, and limitations

One of the main goals of screening mammography is to detect cancer at the earliest stage possible, so that treatment can be effective in reducing mortality¹⁴. It is desired that a screening technique would have both high sensitivity and high specificity, meaning that it successfully detects cancers and allows for the correct diagnosis of those cancers without recalling patients unnecessarily. To lower the risk of radiation exposure, these goals need to be achieved while exposing patients to the least amount of dose possible¹⁴.

Figure 1.19⁸ compares an SFM and a DM image of two patients with fatty breasts, side-by-side for visual comparison. FFDM has been shown to increase cancer detection rate. More cancers are found through a higher number of referrals, or recalls, for diagnostic imaging when cancer is then confirmed. However, overdiagnosis rates also increase with FFDM over SFM. Some studies in the United States have shown that FFDM accuracy is increased over SFM for younger women, women with denser breasts, and premenopausal women¹⁶. The DMIST study from 2005 made a large impact in the acceptance of DM¹⁴. That study compared results between SFM and DM for 50,000 women. The overall statistics suggested that there is no significant difference between the two methods, except in a specific subset of women. DM was more accurate in breast cancer diagnosis for women that were younger than 50 years old and had dense breasts¹⁴. The trial also showed that mean glandular dose is reduced with the use of FFDM by 22 %⁷.

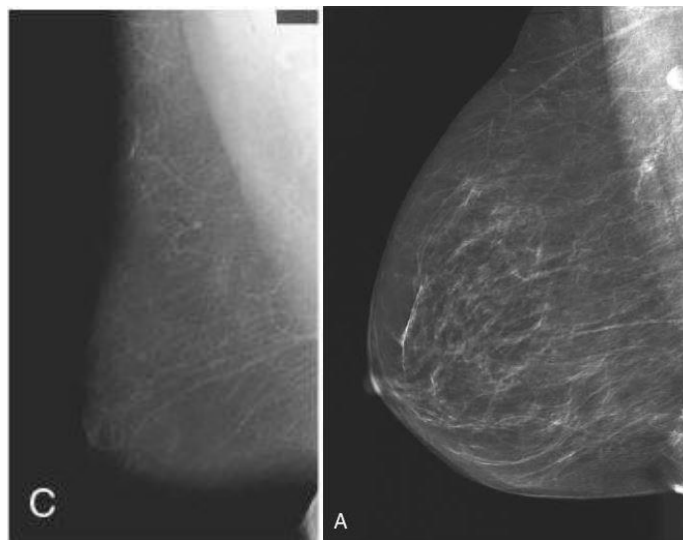


Figure 1.19 X-ray images of right MLO views of two different women with fatty breasts. The left image (C) is an SFM image, and the right image (A) is a DM image.

⁸ These images were published in Breast Imaging: The Requisites, 2nd Edition, Debra M. Ikeda, Chapter 1, Pages 7 and 13, Copyright Elsevier (2011).

It has been shown that, in general, CR detectors perform worse than the other three DM detection methods¹⁴. Factors that affect image quality performance in mammography include spatial resolution, the effective focal spot size, relative motion between the patient and the gantry, and detector resolution. Detector resolution is negatively affected in different ways for SFM and DM systems. In SFM, blurring occurs from light spreading out in the phosphor screen. In DM, different types of detectors lose resolution from different mechanisms as well. CR detectors have light spreading in the phosphor crystals, and photoconductive detectors are limited by the size of the detector element. Direct detectors' spatial resolution is only limited by the pixel size¹⁴. Another advantage of DM over SFM is that digital images have the ability to be altered after acquisition⁷. In general DM suffers from lower spatial resolution, but post processing helps to make up for that deficit⁷.

Signal to noise ratio is another important factor to take into account, and it is desired to be as high as possible¹⁴. Noise levels are increased through quantum noise, competing energy conversions in the detector, film granularity, and electronic noise. CR detectors additionally suffer primary signal loss of 75 %, and cannot undergo flat-field correction. Flat-field or gain correction helps to make the detector image uniform by correcting fixed pattern noise that is present in digital detectors¹⁴.

The last major limitation of mammography is one inherent to the technique, and that is the presence of masking artifacts¹⁴. Fibroglandular tissue in the breast creates a complex anatomical background, which is worse in dense breasts. The complex background makes the detection of breast cancer much more difficult. All tissue that is above or below a lesion gets superimposed on it in the 2D image. This can have the effect of completely hiding a lesion, or creating the appearance of a lesion that is not really there¹⁴.

1.4 Digital breast tomosynthesis

1.4.1 Main principles

Tomosynthesis is defined as the process of generating arbitrary image slices, or tomograms, after acquiring a limited number of projection images¹⁷. This definition was first given by D.G. Grant in 1972, who was the first person to create a 3D image projector based on a circular image acquisition. The theory of tomosynthesis was around longer, dating back to 1917 by Radon, and using it in medical imaging was introduced by Zeides des Plantes in 1932¹⁷. The idea of tomosynthesis was around decades before it could be technically realized. Until digital mammography was developed, the detector technology necessary to implement tomosynthesis was not available¹⁸. The advances in digital detectors made it possible to build tomosynthesis systems for clinical use and led to the introduction of one of the newest mammographic techniques, digital breast tomosynthesis (DBT).

DBT is an emerging clinical technology that has the capability to improve on digital mammography by reducing the blur and obstruction from overlapping anatomical noise that can mask or even mimic breast cancer lesions^{3,17,18}. Figure 1.20 illustrates the general system components and operating mechanism. Most DBT systems are modified from current FFDM systems, and therefore look very similar. Just like FFDM, they use rotating anode X-ray tubes, face shields, compression paddles, and digital detectors. A specific system will have a designated angular range over which the X-ray tube will travel. While it traverses its trajectory, projection images are acquired at specific locations at set intervals¹⁷. The projection images are low dose because the total exposure that would normally be used for a 2D acquisition is divided among the multiple projections¹⁹. After acquisition of the set of projection images is complete, they are reconstructed into a quasi-3D image volume¹⁹. The

resulting reconstructed image is quasi-3D because not all of frequency space is imaged with tomosynthesis, as in computed tomography.

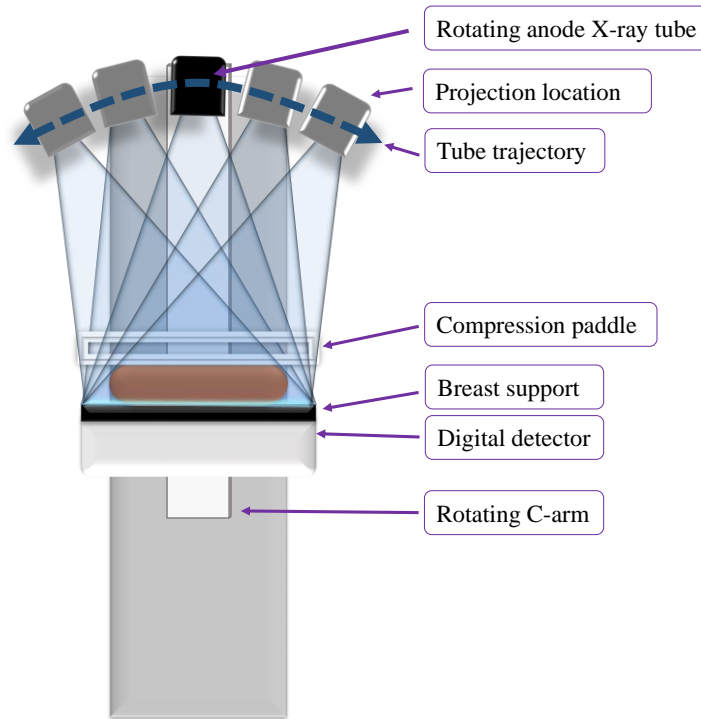


Figure 1.20 Illustration of a DBT system with major components labeled. Example tube trajectory during imaging is indicated by the curved arrow. There is one tube head, black, that moves to different projection locations, illustrated by the gray tube head images.

The general principle for how the reconstructed image is formed is illustrated in Figure 1.21, and is termed the shift-and-add method^{3,8,17}. The figure gives an example image acquisition in which three projection views are obtained, labeled “1”, “2”, and “3”. The object being imaged contains two horizontally aligned shapes, a lightning bolt and a burst shape. The positions of the shapes in the original images are shown below the acquisition illustration. In this example, it is desired to reconstruct the plane that the burst shape is in, to see it clearly and not blocked by the lightning bolt. First, the images are shifted so that the

position of the burst shape lines up in all three, as shown in the right side of the illustration. After being aligned, the images are added together. The resulting image has the burst shape in focus, while the contribution from the lightning bolt is blurred across the image³. To make a reconstructed image set, this process would be repeated for every plane in the breast volume. Each plane would contain an image in which the structures located at that height appear clear and in focus, and the overlying and underlying structures are blurred out³.

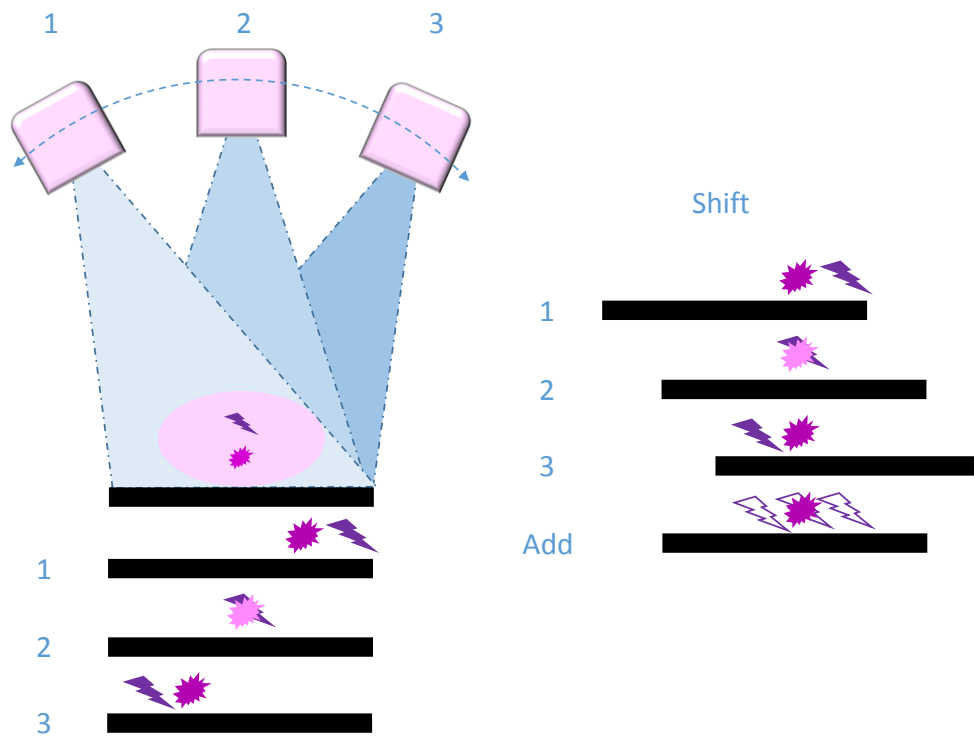


Figure 1.21 Illustration of the shift-and-add method for image reconstruction whose principle is the basis for more complex reconstruction methods used in DBT. This image shows how a plane would be constructed so that the burst shape comes into focus.

1.4.2 Technique and current systems

Reconstruction

The shift-and-add method is a very simplified version of how projection images are actually reconstructed. The projection images must be preprocessed before they can be reconstructed. One main step is performing a logarithmic transform on the projections, because the intensity of detected X-rays is an exponential equation¹⁷. Doing this allows the image intensity to be linearly related to the absorption coefficients instead of exponentially. Afterwards, the images can then be easily added or subtracted to either bring a certain object into focus on a plane, or remove blur from objects out of the plane¹⁷.

The two main types of DBT reconstruction are filtered back projection (FBP) and iterative reconstruction algorithms. Back projection is a method also used in computed tomography that imitates the geometric tomography process, but in reverse¹⁷. X-rays are projected from their location on the detector, back through the object in their original direction, for each projection³. This allows the determination of attenuation and location of different tissues and objects by showing where the rays overlap³. Filtered back projection applies different types of filters to improve the reconstruction image quality and remove blur. One of the most common filters used is a ramp filter, or some variation thereof²⁰.

Iterative reconstruction algorithms tend to be more complex, and strive to reduce artifacts caused by FBP³. The general idea is to make a model reconstruction volume and projection slices, then compare those to the actual projection images. The model is adjusted and the comparison process is repeated until sufficient image quality is obtained³. Some examples of these algorithms include simultaneous iterative reconstruction technique (SIRT), algebraic reconstruction technique (ART), simultaneous algebraic reconstruction technique

(SART), matrix inversion tomosynthesis (MITS), and the maximum likelihood expectation maximization method (MLEM)²⁰. Extensive studies have been done on each of these methods, and many more, but will not be discussed here as reconstruction methods are not the main focus of this work.

Equipment and techniques

The digital detector is one of the most important parts of a DBT system. Usually there are specific adjustments that need to be made to DM detectors to make them acceptable for use in DBT¹⁹. There must be a fast readout time in order to keep the total acquisition time as low as possible. The readout time is the time that the detector needs between each projection acquisition to read out and store the data before a new image is taken. The amorphous selenium (a-Se) detector used on Hologic's Selenia Dimensions system has a reduced readout time due to replacing a layer that was dielectric, with one that is conductive. That meant there was less stored charge to read out, and the acquisition time for the system was able to lower to 3.7 s, as can be seen in Table 1.1¹⁹. To prevent artifacts, there must be minimal ghosting, or latent images burned on the detector from previous exposures, and no lag, or signal carry over, due to needing to take successive images^{19,21}. The detective quantum efficiency (DQE) must be maintained at low exposures because, as already mentioned, DBT projections are each relatively low-dose images¹⁹.

Table 1.1 lists many detector characteristics of the major DBT systems available, or in development, today: detector pixel size, detector type, detector size, and detector motion. Detector pixel size is important in order to get maximum spatial resolution. The detector types tend to be direct a-Se detectors. Detector motion is an interesting characteristic, and tends to either be static or rotating. That means that while the tube moves to different

projection locations, the detector either remains fixed or angles slightly in the direction of the X-ray source. This rotation is not visible, if it does occur, but is hidden by the breast support plate and detector housing.

Table 1.1 Specifications of current commercial and prototype DBT systems. Adapted from Sechopoulos, 2013, Part I.

	Hologic Selenia Dimensions	Siemens MAMMOMAT Inspiration	GE Essential	IMS Giotto TOMO	Phillips MicroDose	Planned Nuance Excel DBT
Development stage	Commercial system	Commercial system	Prototype	Commercial system	Prototype	Prototype
X-ray tube motion	Continuous	Continuous	Step-and-shoot	Step-and-shoot	Continuous	Continuous
Scan time (s)	3.7	20	7	12	3 – 10	20
Angular range (deg)	15 or 30	46	25	40	11	30
Number of projections	15	25	9	13	21	15
Detector pixel size (μm)	70 (2×2 binning)	85	100	85	50 (perpendicular to motion)	85
Detector type	Full field – direct (a-Se)	Full field – direct (a-Se)	Full field – indirect	Full field – direct (a-Se)	Linear slit scan – spectral photon counting (Si)	Full field – direct (a-Se)
Detector size (cm)	24×29	24×30	24×30	24×30	24×30	24×30
Detector motion	Rotating	Static	Static	Static	Continuous slit scan	Rotating during exposure
Reconstruction method	FBP	FBP	Iterative	Iterative with total variation regularization	Iterative	Iterative
X-ray tube target	W	W	Mo or Rh	W	W	W
X-ray tube filtration	0.7 mm Al	0.05 mm Rh	0.03 mm Mo or 0.025 mm Rh	0.05 mm Rh or 0.5 mm Ag	0.5 mm Al	0.075 mm Ag or 0.06 mm Rh
FDA approval	Yes	No	No	No	No	No

All of the systems in Table 1.1 use rotating anode X-ray tubes, very similar to or those exactly found in DM systems. Most of the tubes have tungsten targets, except for the

GE Essential, probably due to the fact that DBT uses higher kilovolt peak values than DM does. DBT systems are also more likely than DM systems to use aluminum filtration. The signal-to-noise ratio (SNR) of DBT systems is increased by using a slightly higher kilovolt peak range, but an optimized range for DBT has not yet been determined¹⁹.

Many of the optimization parameters are not yet fixed for DBT, as can be noted by all of the varying system specifications in Table 1.1, such as: X-ray tube motion, number of projections, angular range, and exposure distribution (not listed). There are two major types of X-ray tube motion, continuous tube motion (CTM) and step-and-shoot motion (SSM). CTM moves the X-ray tube continuously through the entire acquisition, whether the X-rays are on or off. SSM stops at each projection location, takes the image, and then moves to the next location. SSM has less motion blur than CTM during the image acquisition, but tends to take longer¹⁸.

The number of projections used, as listed in Table 1.1, can range from 9 to 25. The total number of projections is limited by the amount of dose given to the patient, because it must be divided amongst each projection but still be high enough to get a decent image¹⁹. Lower exposure per projection increases the amount of quantum noise, and possibly electronic noise, lowering the SNR. But, studies have shown that, in general, more projections is better for increasing image quality. There is a point, however, at which the law of diminishing returns kicks in. Artifact spread function (ASF) is a measure of vertical resolution in DBT images, and should be kept as low as possible. After increasing the number of projections to about 13, the reduction in ASF becomes statistically insignificant¹⁹.

Angular range also has a tradeoff. Larger angular range increases the angle of X-ray incidence on the detector, degrading spatial resolution¹⁹. On the other hand, it has been

shown that increasing angular range improves the detection of lesions in the breast. Overall, it seems that wider angular range has been shown to improve image quality, but it is possible that for high frequency objects like microcalcifications, a narrower range would be best¹⁹.

It is desired in tomosynthesis to maintain a dose level similar to what a patient would receive in one or two, 2D images. That is why the dose is low for each projection. The distribution of the X-ray exposure amongst projections is one of the subjects of optimization studies for DBT systems. For the most part, it has been shown that an even distribution among all projections performs better than an uneven one¹⁹. Uneven distributions may be useful for small structures, such as microcalcifications. The uneven distributions used tend to weight the exposure more heavily among the middle projections, when the tube angle is closest to zero. The Italian system, IMS Giotto TOMO, available for use outside the U.S., has a built in option to use 50 % of total exposure on the central projection, and the rest evenly distributed amongst all others¹⁹. It is clear that there are many variables undergoing extensive study for optimization, and this trend is likely to continue as DBT gains wider acceptance and undergoes more clinical trials and studies.

1.4.3 Advantages over FFDM

DBT's ability to remove tissue overlap leads to improved lesion detection¹⁷, especially in dense and heterogeneous breasts^{3,17}, often leading to a lower recall rate for benign lesions³. Compared to FFDM, DBT has increases in both sensitivity, the detection of cancer, and specificity, the correct categorization of cancer³.

The problem of overlapping tissue makes certain structures appear suspicious, that if seen clearly, would easily be identified as benign or normal tissue, such as: focal asymmetries, architectural distortions, and masses¹⁸. Also, the overlapping tissue could hide

cancerous lesions, as shown in Figure 1.22⁹. For cysts and fibroadenomas DBT presents clearer margins, helping to identify their benign nature. Oval and lobulated masses with well circumscribed margins are typically benign, but usually obscured by other tissue in 2D imaging. It is possible that this issue could be avoided with DBT, but further study is required. Malignant lesions are also more easily detected with DBT because the distinct cancer characteristics of indistinct and spiculated margins are more easily visualized without tissue overlap and noise. For calcifications, benign calcifications tend to be larger and can be easily seen. Malignant calcifications tend to be smaller, referred to as microcalcifications (MCs), and can be detected, but further study is needed to show how reliable it is¹⁸. Spangler et al. found that FFDM is slightly more sensitive for calcifications than DBT, but it is hoped that improved reconstruction algorithms could change that²². Overall, DBT did not negatively affect the diagnostic performance of microcalcifications, but did not improve it either²². It is possible that there is some benefit to knowing the 3D morphology of calcifications, provided only by DBT¹⁸.

⁹ Reprinted from Clinical Radiology, 68, M. Alakhras, R. Bourne, M. Rickard, K.H. Ng, M. Pietrzyk, P.C. Brennan, Digital tomosynthesis: A new future for breast imaging?, Page e232, Copyright (2013), with permission from Elsevier.

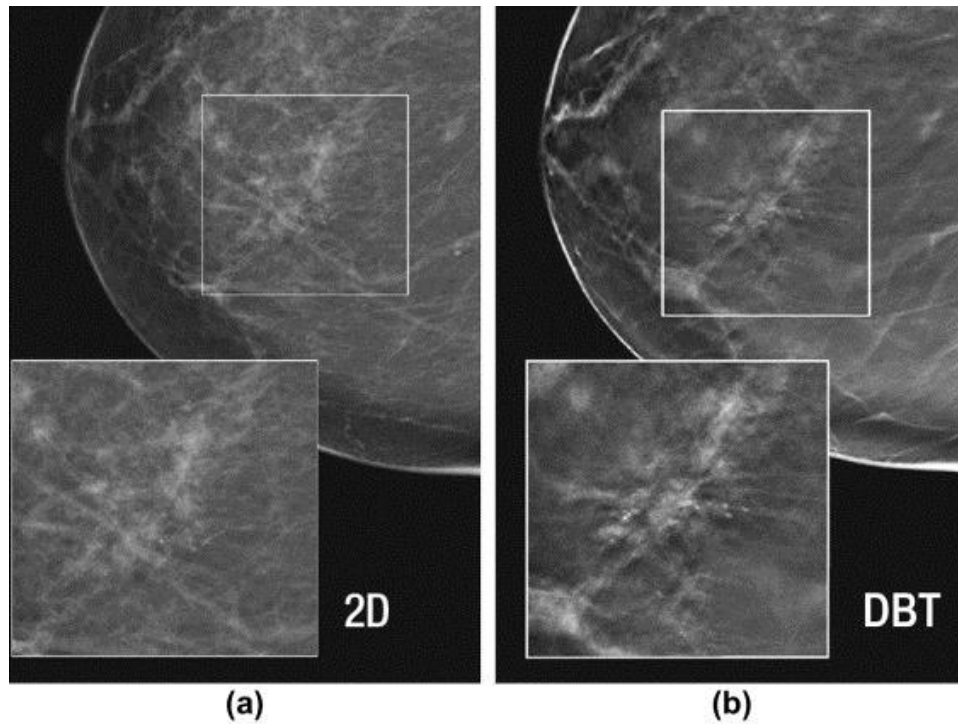


Figure 1.22 Comparison of a 2D DM projection and a DBT slice for DCIS. The spiculation and MCs are hidden in the DM image, but clearly seen in the DBT image.

Other than improved detection of specific lesions, removing tissue overlap helps with understanding the geometric relationship between a mass and corresponding calcifications, as well as evaluating the need for a biopsy of a specific lesion¹⁷. Due to the 3D information available with DBT, it is possible to get depth localization of lesions which is not possible with FFDM screening¹⁷. In the future, it could be possible to fuse the data from DBT with other 3D data sets, such as positron emission tomography (PET)³.

Current screening practice for DM is to perform both CC and MLO views for each breast. It is possible that DBT could perform screening only using the MLO view³, which would add many benefits to the patient. Taking only the MLO view would reduce the dose to the patient and reduce discomfort from compression. For the radiologist, image-reading time

would be decreased by only having one view to assess. It was shown at Massachusetts General Hospital that only 0.8 % of cancers are not visible in the MLO view, and an additional 1 % were only partially imaged by the MLO view³. Waldherr et al. compared the clinical performance of the MLO DBT view to the 2-view DM screening²³. It was shown that DBT with only an MLO view had better sensitivity and negative predictive value in both fatty breast and dense breast cases. Only 11 % of the DBT images indicated a need for more imaging, compared to 23 % of FFDM images²³.

When patients are recalled for more imaging, it is typically referred to as diagnostic imaging even though mammography does not have diagnostic capabilities in the strict definition of the word. Diagnostic imaging is used to see if a spotted lesion is a real lesion and not the effect of overlapping tissue, to locate a lesion, or to decide the malignancy likelihood and resultant management of a suspicious lesion³. DBT is able to reduce the need for diagnostic imaging, if used for screening, in all of these cases. Usually 25 % of diagnostic imaging shows that suspicious areas are overlapping tissue, which DBT removes. The 3D location of lesions is easily determined by knowing the depth of a reconstructed plane, as well as the x and y coordinates of a lesion. Lastly, margins are more easily seen, making the determination of malignancy likelihood easier³.

Another result of removing tissue overlap is the potential of compression reduction, because there is less need for spreading out the fibrous breast tissue¹⁸. A simulation study has shown that, for the same dose, reducing compression by one-eighth does not affect lesion visibility^{18,19}. Another clinical study researched the effect of reducing compression by one-half^{18,19}. From a patient point of view, half compression was much preferred. It was found not to affect the ability to detect lesions, and actually improved visualization of glandular

structures and fibrous strands. Additional advantages from reducing compression is scatter reduction, currently DBT does not use scatter grids, reduction in dose, reduced motion artifacts, and increased amount of tissue visible in the detector field of view¹⁹.

1.4.4 FDA approval

In 2011, the FDA approved Hologic's Selenia Dimensions system, pictured in Figure 1.23, for use in the United States for mammography screening²⁴. The approval was only for use in combination mode, where it is required that a complete image acquisition has both 2D and 3D images. This requirement causes much more dose to be delivered to the patient than if 3D could be used exclusively. No other commercial system listed in Table 1.1 is approved for use in the United States.



Figure 1.23 Photograph of a Hologic Selenia Dimensions DBT system in a laboratory setting.

REFERENCES

- 1 Breast Cancer Facts & Figures 2013-2014. 0-40 (American Cancer Society, Atlanta, GA, 2013).
- 2 Cancer Facts & Figures 2013. 0-64 (American Cancer Society, Atlanta, GA, 2013).
- 3 Kopans, D. B. *Breast Imaging*. 3rd edn, (Lippincott Williams & Wilkins, 2007).
- 4 Bolejko, A., Zackrisson, S., Hagell, P. & Wann-Hansson, C. A roller coaster of emotions and sense - coping with the perceived psychosocial consequences of a false-positive screening mammography. *J Clin Nurs* **23**, 2053-2062, doi:10.1111/jocn.12426 (2014).
- 5 Greif, J. M. Mammographic screening for breast cancer: An invited review of the benefits and costs. *Breast* **19**, 268-272, doi:10.1016/j.breast.2010.03.017 (2010).
- 6 Kolarik, D. *et al.* Breast cancer characteristics-comparison of preoperative and postoperative values. *Pathology, research and practice* **209**, 433-440, doi:10.1016/j.prp.2013.04.011 (2013).
- 7 Ikeda, D. M. *Breast Imaging: The Requisites*. 2nd edn, (Mosby Inc., 2011).
- 8 Bushberg, J. T., Seibert, J. A., Leidholdt, E. M. & Boone, J. M. *The Essential Physics of Medical Imaging*. 2nd edn, (Lippincott Williams & Wilkins, 2002).
- 9 Lee, W. & Peters, G. Mammographic screening for breast cancer: A review. *Journal of Medical Radiation Sciences* **60**, 35-39, doi:10.1002/jmrs.6 (2013).
- 10 Luparia, A. *et al.* Accuracy of tumour size assessment in the preoperative staging of breast cancer: comparison of digital mammography, tomosynthesis, ultrasound and MRI. *Radiol med* **118**, 1119-1136, doi:10.1007/s11547-013-0941-z (2013).
- 11 Mohey, N. & Hassan, T. A. Value of mammography and combined grey scale ultrasound and ultrasound elastography in the differentiation of solid breast lesions. *The Egyptian Journal of Radiology and Nuclear Medicine* **45**, 253-261, doi:10.1016/j.ejrn.2013.11.002 (2014).
- 12 Prince, J. L. & Links, J. M. *Medical Imaging Signals and Systems*. (Pearson Education, Inc., 2006).
- 13 Johns, H. E. & Cunningham, J. R. *The physics of radiology*. (Charles C Thomas, 1974).

- 14 Yaffe, M. J. *et al.* Comparative performance of modern digital mammography systems in a large breast screening program. *Med Phys* **40**, 121915, doi:10.1118/1.4829516 (2013).
- 15 A Guide to Mammography and Other Breast Imaging Procedures. (National Council on Radiation Protection and Measurements, 2004).
- 16 Nederend, J. *et al.* Impact of the transition from screen-film to digital screening mammography on interval cancer characteristics and treatment - a population based study from the Netherlands. *Eur J Cancer* **50**, 31-39, doi:10.1016/j.ejca.2013.09.018 (2014).
- 17 Dobbins J T III & Godfrey, D. J. Digital x-ray tomosynthesis: current state of the art and clinical potential. *Phys. Med. Biol.* **48**, R65-R106 (2003).
- 18 Baker, J. A. & Lo, J. Y. Breast tomosynthesis: state-of-the-art and review of the literature. *Acad Radiol* **18**, 1298-1310, doi:10.1016/j.acra.2011.06.011 (2011).
- 19 Sechopoulos, I. A review of breast tomosynthesis. Part I. The image acquisition process. *Med Phys* **40**, 014301, doi:10.1118/1.4770279 (2013).
- 20 Sechopoulos, I. A review of breast tomosynthesis. Part II. Image reconstruction, processing and analysis, and advanced applications. *Med Phys* **40**, 014302, doi:10.1118/1.4770281 (2013).
- 21 Bloomquist, A. K., Yaffe, M. J., Mawdsley, G. E., Hunter, D. M. & Beideck, D. J. Lag and ghosting in a clinical flat-panel selenium digital mammography system. *Med Phys* **33**, 2998-3005 (2006).
- 22 Spangler, M. L. *et al.* Detection and classification of calcifications on digital breast tomosynthesis and 2D digital mammography: a comparison. *AJR. American journal of roentgenology* **196**, 320-324, doi:10.2214/AJR.10.4656 (2011).
- 23 Waldherr, C. *et al.* Value of one-view breast tomosynthesis versus two-view mammography in diagnostic workup of women with clinical signs and symptoms and in women recalled from screening. *AJR. American journal of roentgenology* **200**, 226-231, doi:10.2214/AJR.11.8202 (2013).
- 24 Lee, C. I. & Lehman, C. D. Digital breast tomosynthesis and the challenges of implementing an emerging breast cancer screening technology into clinical practice. *Journal of the American College of Radiology : JACR* **10**, 913-917, doi:10.1016/j.jacr.2013.09.010 (2013).

CHAPTER 2: MOTIVATIONS FOR AND FOUNDATIONS OF STATIONARY DIGITAL BREAST TOMOSYNTHESIS

2.1 Limitations of current DBT methods

While DBT does have many advantages over digital mammography, the systems suffer from limitations in image acquisition time, spatial resolution, visualization of microcalcifications, and other technical aspects that need development as they emerge in the clinic.

Relative to digital mammography, image acquisition time is much longer for DBT, resulting from taking many projection images. Long scanning time is due to limits on the X-ray tube travel velocity, for both CTM and SSM systems. The result of a long scanning time is an increased likelihood of patient motion either from compression discomfort or random movements as total acquisition time increases^{1,2}. Patient motion is a problem because it causes blurring artifacts that can make objects appear larger, especially calcifications².

Factors that contribute to lowering the spatial resolution of DBT systems include blurring from focal spot motion³⁻⁶, oblique incidence of X-rays on the detector^{7,8}, and limited angular sampling⁹. In 2008, Zhao and Zhao showed that CTM caused image blur from the focal spot travel during exposure³, which for Hologic's Selenia Dimensions is 2.48 mm⁴. Focal spot blur on an image is an order of magnitude larger than focal spot enlargement due to tube motion⁴. Objects farther above the detector surface are blurred more than objects closer to the detector^{2,3}. The effect was more pronounced in central projections⁶, for small objects⁵, and when the detector was in full resolution because it could not be masked by pixel

binning^{3,4}. Blur lowers system spatial resolution and reduces DQE by 50%³. Focal spot blur is worse with less projections and higher tube velocity³, longer exposure time, shorter total acquisition time, and larger angular range⁴. Bissonette et al. found that increasing total acquisition time to 39 s completely removes the effect of focal spot blur, but the tradeoff between longer scan time and increased patient motion remains². SSM does not suffer from focal spot motion blur if all vibration ceases during exposure⁵. Because of this, SSM has 8% to 9 % higher peak contrast for MCs, 1 % to 2 % higher peak contrast for masses, and 27 % higher modulation transfer function (MTF) than CTM. MTF is a measure of in-plane spatial resolution⁵. SSM acquisitions are longer than CTM acquisitions, making patient motion a problem.

One limitation of DBT that is due to the relative motion of the X-ray tube and the detector is obliquity of X-rays hitting the detector. Oblique incidence above 20° on a stationary detector⁷ reduces MTF by 25 % to 30 %⁸, with outer projections suffering more than central ones⁷. The effect differs at high and low spatial frequencies, respectively decreasing or increasing DQE⁸. Oblique incidence can lead to misregistration and increased noise, possibly reversible with post processing⁷. Resolution in the z-direction, or out-of-plane direction, is limited by the angular range which can make small structures, like microcalcifications, appear stretched⁹.

Visualizing microcalcifications is troublesome in DBT. DBT images are viewed in slices, so calcification clusters look different than how radiologists are used to viewing them on 2D images⁹. They may not appear clustered if sufficiently spread over enough slices⁹. Viewing only a few MCs per slice makes clusters difficult to assess, but stacking and viewing slices as slabs could somewhat alleviate that problem^{10,11}. Factors that lead to

blurring MCs include tube motion, longer acquisition time, detector pixel pitch, detector noise, and detector binning¹¹. Hu et al. showed that MC visibility can be increased with more dose in the central projection⁶. Radiologists are not yet well-trained at viewing DBT images of MCs¹⁰. Generally, radiologists prefer viewing MCs with FFDM, and FFDM has higher sensitivity for calcifications. However, diagnostic performance is not statistically different for DBT. FFDM may be better overall for detecting and viewing MCs, but these problems could be overcome with DBT technology development¹⁰.

Other areas of development include scatter rejection and biopsy capabilities. With any type of X-ray imaging, scatter is a problem. In DM, scatter grids are used to combat the reduction of image quality caused by scatter. However, it is not possible to use the current grids in DBT because the varying tube position would allow too many primary photons to be absorbed and would sacrifice exposure⁸. The effect of scatter on clinical performance is unknown, but it does reduce lesion contrast by 30 %, signal difference-to-noise ratio (SDNR) by 60 %, and reconstructed attenuation accuracy by 28 %⁸.

One factor that led to the acceptance of DM over SFM was the ability to perform stereotactic needle biopsy¹¹. As of yet there is no widely available method for performing breast tomosynthesis-guided needle biopsy¹¹, and concepts remain in the patent stage^{12,13}.

In addition to technological developments, further training for and acceptance by radiologists is needed. It takes longer to interpret DBT images than DM images¹¹. With the typical slice thickness of 1 mm, an average 5 cm breast image set would contain 50 slices for each view, per breast. Viewing a set of DBT images takes 70 % longer than DM images – 2 min versus 1.2 min¹¹. Viewing time can be reduced somewhat if it is determined that MLO views alone are sufficient with use of DBT⁹. However, not all cancers are visible in an MLO

view. The percentage of cancers visible only in the CC view ranges from 1 %⁹ to 9 %¹¹. The necessity of the CC view still requires further study¹¹.

Although there is no significant difference between the diagnostic capabilities of DBT and DM, digital mammography has been shown to have a slightly higher calcification sensitivity, 90 % compared to 80 %¹¹. More study is needed to confirm if this difference is constant, clinically significant, or insurmountable through technology development.

2.2 Basic idea and proposed advantages of s-DBT

Stationary digital breast tomosynthesis (s-DBT) development began during 2006, at UNC¹⁴. The main difference between s-DBT and other DBT systems is the substitution of a moving X-ray tube with a stationary one. Tomosynthesis acquisition with use of a stationary X-ray tube does not physically translate a single X-ray source, but fires fixed X-ray sources combined in one X-ray tube. The basic setup is illustrated in Figure 2.1.

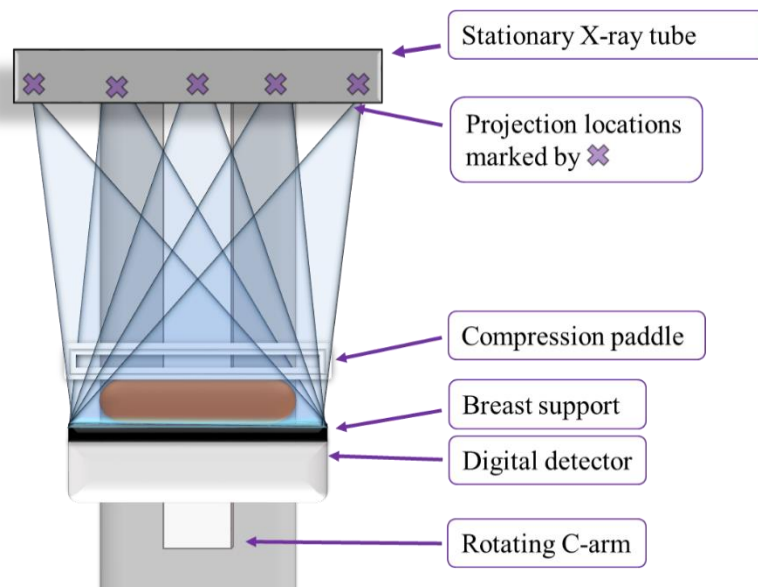


Figure 2.1 Illustration of a proposed s-DBT system with many X-ray sources housed in one X-ray tube. The "x" markers indicate X-ray source locations within the tube, corresponding to projection locations that will form the tomosynthesis reconstruction.

Having a single X-ray tube containing many focal spots is only possible if the technology used to create the focal spots was very small. Therefore, the basis of s-DBT is carbon nanotube (CNT) nanotechnology. CNTs are deposited onto metal cathodes, 2.5 mm × 13 mm in size, creating an electron beam through field emission. The current iteration of s-DBT houses 31 CNT cathodes. They are equally spaced, covering a 30° angular range. Each cathode has a corresponding anode, creating an individual X-ray focal spot. It is also possible to build X-ray tubes with cathodes in non-linear configurations, or in linear configurations of different lengths and containing different numbers of cathodes.

Each cathode-anode pair is controlled electronically. Field emission occurs once a sufficient electric field is applied above the cathode. Electronic switching allows for each cathode, and consequently each X-ray beam, to be programmed to turn on and off in sequence. The beams can turn on one at a time, multiple at a time, sequentially down a line, or in random order. The beam quickly turns on and off, making imaging possible in a very short period of time.

s-DBT will overcome current DBT systems' low spatial resolution and long total acquisition time. As discussed earlier, focal spot blur lowers image quality through a loss in spatial resolution. Figure 2.2 illustrates how the focal spot gets elongated along the direction of X-ray tube motion. The figure shows that X-ray tube motion extends the focal spot size in the scanning direction. This loss in spatial resolution negatively affects imaging microcalcifications the most, because they are the smallest objects of interest in the breast. Eliminating the need to translate the X-ray focal spot removes the negative effects of focal spot blur. This should increase the sharpness of microcalcifications, a current problem in DBT systems.

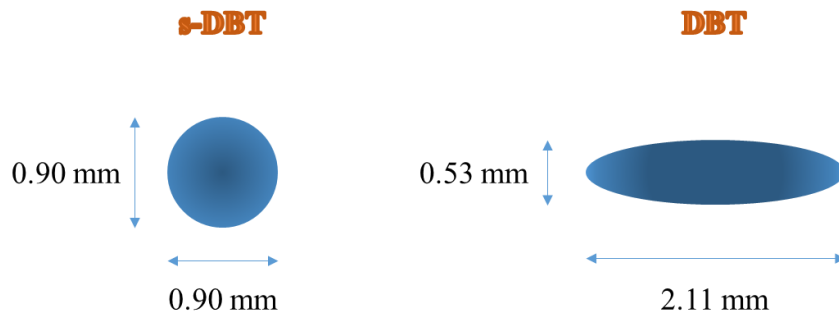


Figure 2.2 Illustration comparing the difference between a stationary focal spot (s-DBT), and a blurred focal spot (DBT). The DBT focal spot gets stretched in the direction of tube travel. This illustration assumes a tube travel of 1.65 mm during an exposure in which the whole acquisition would total 100 mAs.

DBT acquisitions take longer than 2D mammography imaging because of the acquisition of more images, the allowed X-ray tube velocity, and the digital detector readout time per projection. A stationary tube that can quickly turn on and off fixed focal spots can potentially shorten total acquisition time. s-DBT removes the need to move the X-ray tube. Therefore, the same or more projection images can be taken in a certain period of time than with traditional X-ray sources. Limitations from detector readout time can only be overcome by improving digital detector technology.

2.3 Materials science of s-DBT

2.3.1 Theory of field emission

Field emission is the process of ejecting electrons from the surface of a solid, typically into a vacuum environment¹⁵. This type of electron emission occurs under the influence of a strong external electrostatic field. A potential energy diagram is given in Figure 2.3. Field emission occurs when electrons tunnel through the lowered effective

potential barrier. The effective potential barrier is the result of the barrier potential due to the metal surface, the applied electrostatic field, and the image potential¹⁵.

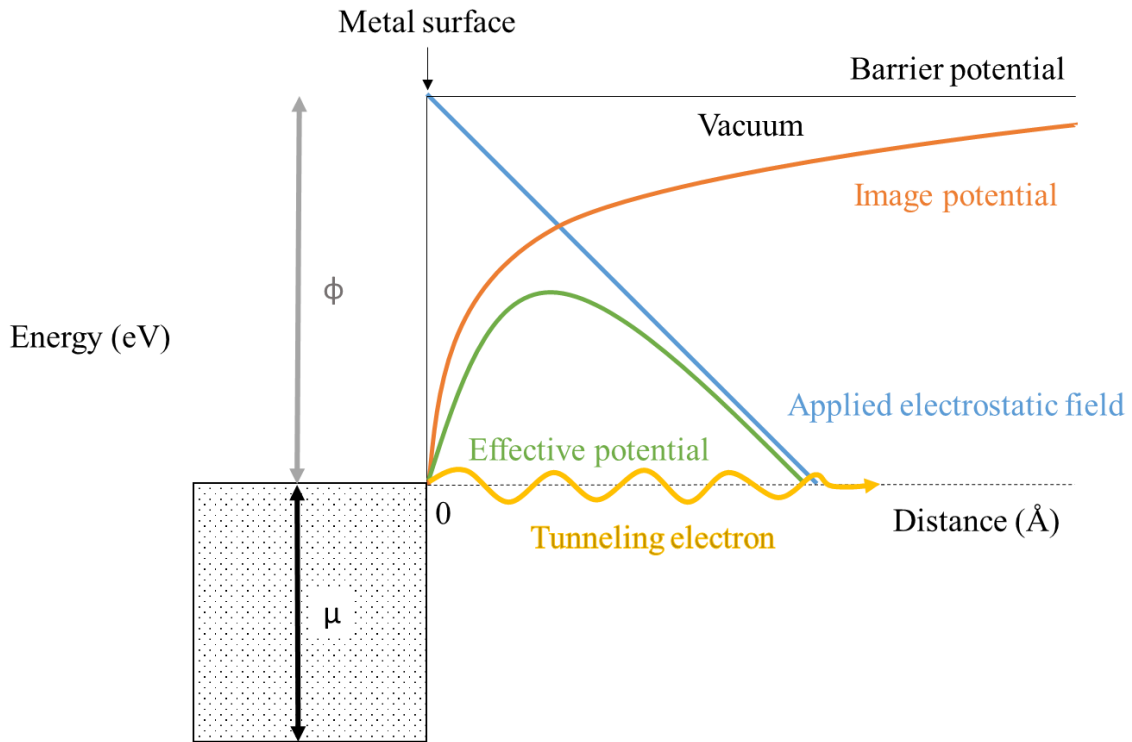


Figure 2.3 Potential energy diagram at the surface of a metal under the influence of an external electric field.

Assuming the electrons behave according to the free electron model, atomic outer electrons of the metal or semiconductor atoms will form bands¹⁵. Electrons organize themselves in conduction bands according to Fermi statistics, with 2 electrons per level. After all of the electrons have filled into levels, the highest energy filled is the Fermi level, μ ¹⁵.

Another important property in field emission is the work function, ϕ . The work function is defined as the difference between the energy of a field-free vacuum near the material surface, and the Fermi level¹⁵. The work function arises because electrons inside the

material have a different energy than those in vacuum, due to density, temperature, etc., and from electrostatic effects from the material's surface structure¹⁵.

The equation used to describe the current density emitted from a metal surface through field emission is the Fowler-Nordheim equation. It results from multiplying the probability that an electron traveling toward the barrier will pass through and not return by the arrival rate of those electrons to the surface, and then integrating over electron kinetic energies from 0 to μ ¹⁵. The resulting equation derived by Fowler and Nordheim in 1928 is as follows

$$J = 6.2 \times 10^{-6} \frac{\mu^{1/2}}{(\phi + \mu)\phi^{1/2}} F^2 e^{-2.1 \times 10^8 \phi^{3/2}/F}$$

where J is current density in A/cm² and F is the applied electric field¹⁶. A more simplistic version of the Fowler-Nordheim equation relevant to CNT field emission is

$$I = aV^2 e^{-b\phi^{3/2}/\beta V}$$

where I is emission current, V is applied voltage, β is the field enhancement factor, and a and b are constants¹⁷.

2.3.2 Field emission versus thermionic emission for X-ray production

Thermionic emission theory

Conventional X-ray tubes that are used in today's commercial mammography and DBT systems today emit electrons via thermionic emission. Thermionic emission occurs when electrons' kinetic energies are increased so that they pass over the energy barrier at the material-vacuum interface¹⁵. This is accomplished by heating metal until the kinetic energy is greater than or equal to $\mu + \phi$. The equation for thermionic current density, in A/cm², is

$$J = 120T^2 e^{-\phi/kT}$$

where T is temperature and k is the Boltzmann constant¹⁵, equal to 1.38×10^{-16} J/K¹⁸. For high melting-temperature metals, the work function ranges from 4 V to 5 V, requiring temperatures above 1,500 K to induce thermionic emission¹⁵.

Thermionic X-ray tubes

A thermionic X-ray tube has some significant differences from a field-emission tube. The cathode block of a thermionic X-ray tube consists of a focusing cup and a filament¹⁹. The filament is a tungsten wire coil connected to a filament circuit. The filament circuit provides current that heats the filament through resistive heating, creating thermionic emission. The tube current is adjusted by changing the filament current and temperature. Typically up to 10 V is applied to the filament, producing up to 7 A in current. In a mammography tube there is a small filament and a large filament. The large filament creates a 0.3 mm focal spot, and 100 ± 25 mA tube current, whereas the small filament creates a 0.1 mm focal spot, and 25 ± 10 mA tube current¹⁹.

A simplified schematic of a thermionic X-ray tube is shown in Figure 2.4. High voltage is applied between the cathode and the anode, with the anode held at a positive potential relative to the cathode. The tube voltage is controlled by rectifying circuits (not shown), converting lower AC voltage to higher DC voltage¹⁹. The voltage waveform controls the X-ray exposure waveform, as well as controlling the cathode current waveform. The more phases in the rectifying circuit, the less voltage ripple in the voltage waveforms¹⁹.

Electrons emitted from the filament are attracted to the anode. The role of the focusing cup is to concentrate the electrons onto the anode²⁰. The tube current is the amount of electrons boiled off the filament that reach the anode. The width of the focal spot on the

anode is determined by the focusing cup voltage. Voltage applied to the focusing cup creates electric field lines that focus the electron beam²⁰.

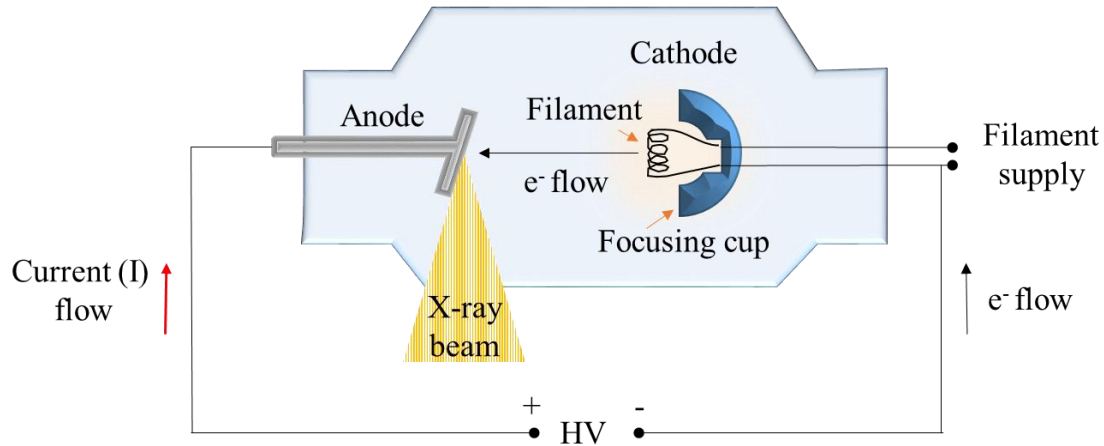


Figure 2.4 Simple schematic of a thermionic X-ray tube. Adapted from Johns, 1974.

The relationship between tube current and tube voltage is different in a thermionic X-ray tube than in a field emission X-ray tube. Tube voltage in a thermionic tube is the high voltage (HV) applied between the cathode block and the anode. Tube current is the current flowing from the cathode filament to the anode through vacuum. Below 40 kVp, the space charge effect at the filament limits the amount of tube current that can be produced¹⁹. There is an electron cloud that forms around the filament, even when the voltage is set to zero. This repels emitted electrons back to the filament, unless the applied voltage is high enough to overcome the repulsion²⁰. In the mammographic imaging range, the space charge effect is significant and the current is saturated at a lower level than at higher voltages. At higher voltages, maximum current can increase before saturation because the space charge effect is more effectively overcome. Higher tube currents are produced from the applied high voltage and filament emission, whereas lower tube currents result only from filament emission²⁰.

Cold cathodes for X-ray production

In contrast to thermionic X-ray tubes, the cathodes in a field emission tube are cold cathodes. Under the application of an electric field, electrons are emitted at room temperature²¹. The electrons are extracted by a gate electrode placed very close to the cathode, on the order of microns to hundreds of microns. It creates the electric field that extracts the electrons, and lowers the voltage required for field emission. The cathode is a conducting material with atomically sharp tips able to concentrate the electric field, allowing for field emission. The development of microfabrication allowed the creation of gates and cathodes of the proper sizes and geometries needed for field emission²¹. An illustration of a field emission X-ray tube is shown in Figure 2.5.

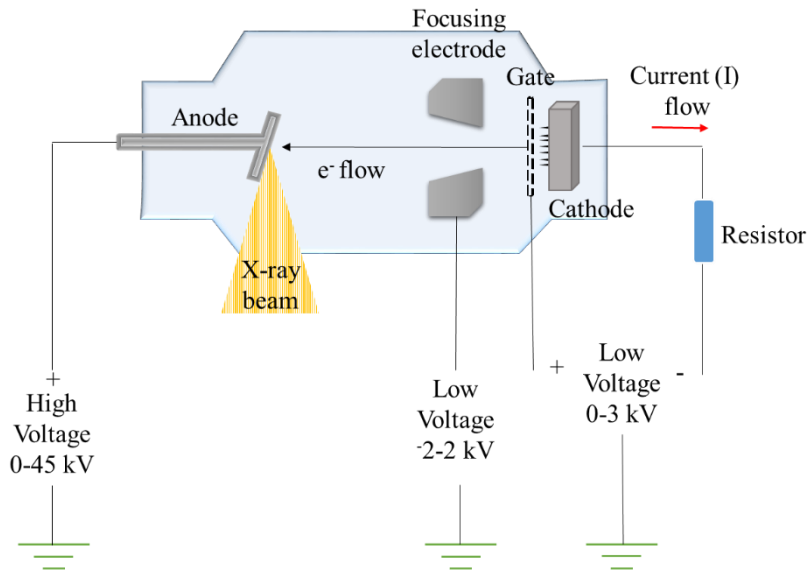


Figure 2.5 Simplified schematic of a field emission X-ray tube.

The anode in a field emission tube need not be different than in a thermionic tube. One or a series of additional electrodes, called focusing electrodes, can be added between the gate and anode. The focusing electrodes are similar to the focusing cup in a thermionic tube.

Depending on the voltage applied, they focus the electron beam into a focal spot on the anode. Often, resistors are placed on the cathodes in order to stabilize current among many field emitters and to protect against damage.

One of the very first types of cold cathodes were Spindt cathodes, developed in 1968²¹. An illustration of these field emitters is shown in Figure 2.6. They are fabricated through microfabrication techniques. The cathodes are molybdenum tips formed by etching processes, approximately 200 Å in radius and 1 μm tall. They are attached to a molybdenum base that acts as a conducting electrode. The gate electrode is the molybdenum gate film, separated from the base electrode by silicon dioxide insulation. The openings in the gate film are about 0.5 μm, and the density of emitters is 10⁷ emitters/cm². The gate voltage required for operation is approximately 100 V²¹.

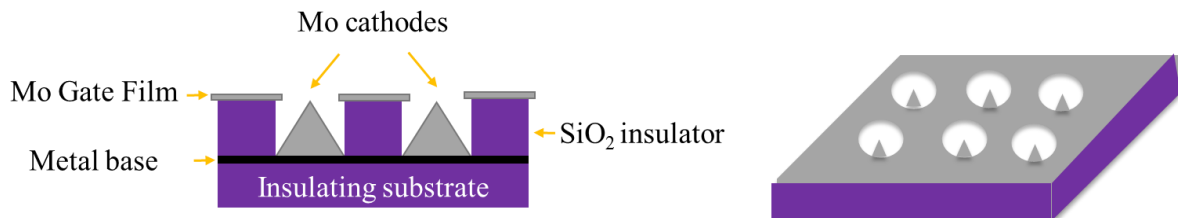


Figure 2.6 Illustration of a Spindt field emitter array. The left image is a cross-section view, and the right image is a top view, showing the circular gate openings. Adapted from Zhu, 2001.

The sharpness of the emitter tip is key for successful field emitters, incorporated in the Fowler-Nordheim current equation as the field enhancement factor, β , which deals with the effect of emitter geometry²¹. To maximize field emission current, the material should have a small work function, large emission area, and large field enhancement. Field enhancement is achieved by decreasing the emitter radius, r , and can be approximated by:

$$\beta = \frac{R}{kr(R-r)} \approx \frac{1}{kr} \text{ for } r \ll R$$

where R is the distance between the emitter tips and the gate electrode, and k accounts for the effect of the emitter shank²¹.

Spindt emitters were one of the first field emission cathodes, but many other materials and emitters have been developed over time. One of the most heavily evaluated materials for field emission are carbon nanotubes (CNTs), which were chosen for the s-DBT system's cathodes.

2.3.3 CNT properties as field emitters

Carbon nanotubes

Carbon nanotubes are a type of carbon fullerene with atoms arranged in a trigonal planar formation with sp^2 bonds²², arranged in graphitic cylindrical sheets²¹. A nanotube made of a single sheet is known as a single-wall nanotube (SWNT). One made of many concentric sheets is known as a multi-wall nanotube (MWNT)²¹⁻²³, where the interlayer spacing ranges from 0.330 nm – 0.344 nm²⁴. The surface of the nanotubes is a honeycomb lattice, with carbon atoms in repeating hexagon formations²³. The size of the repeating structure and the density of electronic states is determined by the nanotube diameter²³. Diameters of nanotubes range from 1 nm for SWNTs, and up to 50 nm for MWNTs²⁴. The length of carbon nanotubes is on the order of microns²¹. The electronic nature of individual CNTs is determined by their chiral indices, which describes how the hexagonal unit repeats along the tube. Chiral SWNTs tend to be semiconducting, non-chiral tubes tend to be metallic²⁵, and MWNTs tend to be semi-metallic²⁶. Most samples of CNTs have a 2:1 ratio of metallic and semiconducting nanotubes²⁵.

The list of unique properties that CNTs possess making them appealing for field emission is extensive:

- 1) High aspect ratio^{21,23}, leading to low turn-on fields^{24,25}
- 2) Structural integrity²³
- 3) High mechanical^{21,25} and tensile strength²²
- 4) High chemical^{23,25} and environmental stability²¹
- 5) High electrical conductivity^{22,23} and current-carrying capacity^{24,25}
- 6) Low-cost mass production²⁵
- 7) Field emission stability²⁴
- 8) Instantaneous response to electric field variation²⁴
- 9) Resistance to temperature fluctuations^{22,24}

High aspect ratio and electric field enhancement

The aspect ratio is defined as length divided by diameter²², and for CNTs can be greater than 1,000²¹. The large aspect ratio causes the applied electric field to be concentrated at the tip of the CNT. Although the work function of CNTs is relatively high, approximately 5 eV, the field enhancement at the tip allows electrons to be emitted at low voltages. The field enhancement factor, β , can range from $10^2 - 10^3$, thus better than metal tip field emitter arrays²¹.

In the Fowler-Nordheim equation, V is the voltage creating the electric field, E_{macro} , set up between the cathode and the extraction electrode. The extraction electrode could be the gate or anode depending on if the electrode structure is triode or diode, respectively. The macroscopic field is defined as

$$E_{macro} = V/d$$

where d is the cathode-gate distance²². The effective field, E_{eff} , is the local field at the nanotube tip, defined as

$$E_{eff} = \beta \times E_{macro}^{22}$$

The effective field at the emitter tip depends on the voltage between the nanotube and the gate, the nanotube, and the nanotube length. It can be up to 1,200 times larger than the macroscopic electric field²³.

The field enhancement factor is experimentally determined from the slope of a Fowler-Nordheim plot, a linear curve plotting $\log(I/V^2)$ versus $1/V$. At larger currents joule heating can cause deviation from the linear curve, but is still accurate within 10% without altering the equation, due to the curvature of the nanotube tip²⁵. In addition to experimental measurements, there is work being done on equating β in terms of nanotube and electrode geometry^{22,27}, the details of which will not be discussed here.

Electrostatic screening and optimal spacing

Electric field enhancement at the tips of carbon nanotubes can be reduced by electrostatic screening if the nanotubes are placed too closely together. Jeong et al. reported that the emitted current and field enhancement factor of carbon nanotubes were greater on the edges of patterned CNT arrays because there was less electrostatic screening²⁸. Field enhancement is reduced if the spacing is less than 2 times the nanotube height²⁴. As the spacing between nanotubes increases, the field enhancement factor maximizes at approximately 10^6 tubes/cm² or when spacing is one-half²⁷, equal to^{22,29}, or twice the nanotube height³⁰. The range of optimal nanotube spacing differs between various numerical and experimental methods, but is generally agreed to be roughly on the order of nanotube height.

Current emission characteristics

Many CNT physical characteristics are anisotropic²², leading to electron emission occurring from the tips of the nanotubes²¹. The tips of nanotubes have a 30 times higher density of states than along the cylindrical portion of the nanotube²³. An individual nanotube can produce 1 μA ²¹ (SWNT) to 100 μA (MWNT) routinely, but can output up to 0.2 mA (MWNT). However, resistive heating is likely to destroy the nanotube at that point because it is nearing the theoretical output limit²³. Randomly oriented films of carbon nanotubes have been shown to produce 1 $\text{A}/\text{cm}^2 - 4 \text{A}/\text{cm}^2$ without damage, which is the highest current density among any carbon-based emitter²¹.

Carbon nanotube current emission behavior, or I-V characteristics, has three distinct regions²¹. The first, at low current and voltage, is Fowler-Nordheim tunneling. As current and voltage increase there is a region of current saturation, where the current output is more stable. This is the range of about 100 mA/cm^2 for a group of nanotubes. As current and voltage increase higher, Fowler-Nordheim tunneling returns. Various explanations for the current saturation region include space charge effects as in thermionic tubes, interactions between neighboring nanotubes, localized electronic states at nanotube tips that are non-metallic, and the presence of surface adsorbates^{21,25}. If a tube is “dirty” with surface adsorbates, the current can increase by 2 to 4 orders of magnitude^{21,31}. The adsorbates perturb the electronic states, causing a drop in field enhancement creating a current plateau²¹. As the current reaches about 1 μA per tube, adsorbates are removed through self-heating²¹. Tubes without adsorbates never saturate, even up to 2 μA ³¹.

As carbon nanotubes begin to fail, the voltage supplied must be significantly increased to maintain the same current level²⁴. For SWNTs, failure can occur in the 300 nA

to 1 μA range as the nanotube begins to evaporate. MWNTs are still stable from 1 μA to 10 μA . Over time MWNTs shorten, and at higher currents the outer walls begin to be removed or peeled back. If a single MWNT emits more than 0.1 mA it can undergo irreversible damage in less than 1 ms²⁴.

Environmental stability

Even when carbon nanotubes are “dirty” from adsorbate states, the emitters are not destroyed from sputtering or oxidation²¹. Compared to other carbons, CNTs are more stable and durable due to low number of defects, small sputtering yield, and low carbon-atom mobility. In the presence of hydrogen or argon gases there is no effect on CNT field emission. When water is adsorbed, current is increased until the water is removed by ion bombardment. CNTs are susceptible to oxygen gas which can decrease current output due to C-O dipole formation. SWNTs degrade more quickly than MWNTs²¹ because they are less resistant to oxygen degradation²⁵.

Thermal stability

Carbon nanotubes emit stable current at temperatures up to 1,600 K, where metal tip emitters would melt²⁵. In the microampere range, current is increased at high temperatures because of “self-cleaning”, recrystallization removing defects, and initiating thermally-assisted field emission^{25,32}. This non-destructive phenomenon occurs at increased tube temperature resulting from current heating in the tube²⁵.

At higher currents and higher temperatures, CNTs do experience problems. CNTs shorten at extreme currents, but evaporation does not occur until about 1,900 K (SWNTs)²⁵. The tip of a MWNT can reach 2,000 K at 1 μA from Joule heating along the length of the tube³², but does not result in failure as for SWNTs. Longer nanotubes suffer more from

heating effects than shorter nanotubes²⁹. At high currents, shorter nanotubes perform better because heat dissipates more quickly. High temperatures at the tips of the nanotubes dissipate through the junction at the substrate²⁹.

Requirements for good CNT field emission cathodes

Single nanotube emission is different than attempting to create stable field emission from a group or film of nanotubes. A single MWNT could emit 200 μA , but 10,000 CNTs in 0.1 mm^2 may not even produce 1 A³³. It is difficult to create a high-density emitter environment that would allow each nanotube to perform well. The CNTs must be high quality. This means taking into account purity, desiring no amorphous carbon; diameter; aspect ratio, higher is better; chirality, semiconducting CNTs have 200 times more resistance than metallic ones; and, defects in the crystalline structure. Another way to improve performance is to reduce the work function of CNTs by applying an alkali metal coating or to increase the field enhancement factor without causing CNT degradation³³.

Optimizing the electric field distribution on the surface of an entire emitter is possible by controlling the surface density of CNTs. Attempts include directly growing patterned CNTs onto the substrate, dispersing pre-fabricated CNTs in solution before deposition, and post-treating prepared films³³.

One major problem for CNT field emission cathodes is the junction between the cathode and conducting substrate. Junctions need to be highly conductive and very strong. If there is high electrical and/or thermal resistance at the junction, the CNTs can be damaged or removed from the substrate. It is important to pick suitable junction and substrate materials. Even improving 1 % of a cathode's junctions would drastically increase current performance.

The junctions need to be strong, even at high temperatures. If not, Coulomb repulsion forces remove CNTs from the substrate and high temperatures break or crack the junctions³³.

Lastly, the vacuum environment the emitter is in should be optimized for current performance. Lower residual gas pressure is better. Gas present during field emission can become ionized or dissociated, and that destroys emission points and changes the CNT composition. The species present is important, with hydrogen gas being most desirable³³.

Recent study results

Milne et al., in 2006, developed aligned CNT films for microwave amplifiers. They grew the nanotubes on a TiN substrate using Ni catalyst dots. These films produced a maximum of 2.5 mA – 3 mA; a current density of 1 A/cm²³⁴.

Wang et al. made a thin Ti-based film of MWNTs purchased from Xintek, where taping was used to align the nanotubes. In DC mode, 1 A/cm² was produced at 5 V/μm – 6 V/μm. They measured β between 1,100 and 1,500³⁵.

In 2011, Kim et al. made a cathode by using a CNT paste of hyperbranched polymers. The polymers create cracks, exposing the nanotube tips. The turn-on field (current density not specified) was 0.5 V/μm. The maximum current reached was 20 mA, corresponding to a current density of 25.5 mA/cm² at 2 V/μm³⁶. Also in 2011, Jo et al. made a thermally stable CNT emitter with paste containing acrylate binders and inorganic fillers. The maximum current density achieved was 30 mA/cm² at 2.1 V/μm³⁷.

Neupane et al, in 2012, used Ni nanodots as catalysts to grow vertically aligned CNTs on a Cu substrate. The difference between high and low density films were studied. The turn-on field was defined as that needed to produce 1 μA/cm², and the threshold field was for 1

mA/cm^2 . The results are shown Table 2.1, below³⁸. At high density, the threshold field was not reached.

Table 2.1 Table of field emission results from high and low density CNT films from Neupane, 2012.

Density	Turn-on field (V/μm)	Threshold field (V/μm)	β
High	7.96	N/A	460
Low	5.19	9.89	1,680

Lee et al. made a field emitter from cut CNT yarn produced through chemical vapor deposition (CVD). The turn-on field, in this case defined as the field needed to produce $10 \mu\text{A}/\text{cm}^2$, was $0.33 \text{ V}/\mu\text{m}$. The threshold field was $0.48 \text{ V}/\mu\text{m}$. Stable current density was $2.13 \text{ mA}/\text{cm}^2$, and β was calculated as 19,141³⁹.

In 2013, Shahi et al. measured CVD-grown CNTs and found that maximum current is produced when there is the most edge length in the pattern design because shielding by neighboring nanotubes at edges is decreased. The turn-on field was $2.3 \text{ V}/\mu\text{m}$, and β equal to 4,560. The maximum current density of $14.53 \text{ mA}/\text{cm}^2$ was reached at $5 \text{ V}/\mu\text{m}$ ⁴⁰.

Huang et al. measured the field emission properties of aligned Ti-coated CNTs in a honeycomb configuration on a glass substrate. The maximum current density was $7 \text{ mA}/\text{cm}^2$ at $2.5 \text{ V}/\mu\text{m}$ ⁴¹.

Sun et al. built a microfabricated Spindt-type cathode with CNTs instead of a Mo metal tip. It was able to produce $550 \mu\text{A}$ at 40V and a current density of $275 \text{ mA}/\text{cm}^2$, equivalent to $0.26 \mu\text{A}/\text{CNT}$ ⁴².

It is difficult to compare these results with one another because the methods and CNTs used were different. One common result was very high field enhancement factors, as

predicted by theory. Most field values required to produce low currents were relatively low. Current density measurements varied more widely. They are difficult to compare because if the tested area is very small, the current density will be high even though total produced current may be small. Most field emission cathodes are intended for field emission displays, which have lower current requirements.

2.3.4 Altered CNTs and other materials for field emission

Recent studies on CNTs that have been coated or made into composites explore other possibilities for good field emitters, hoping to improve upon plain CNT emission performance. These methods include titanium decoration⁴³, diamond coating⁴⁴, ZnO composites⁴⁵, lithium coating⁴⁶, titanium dioxide composites⁴⁷, molybdenum composites⁴⁸, and cobalt composites⁴⁹. Results of these studies are summarized in Table 2.2.

Table 2.2 Field emission properties of alternate CNT materials. The blank fields were not discussed in the study. The turn-on field corresponds to 10 $\mu\text{A}/\text{cm}^2$, and threshold field to 1 mA/cm^2 .

Material	Turn-on field (V/μm)	Threshold field (V/μm)	Maximum current	Field at maximum current (V/μm)	β
Ti-decorated, aligned CNTs	0.63	1.06	23 mA/cm^2	1.80	$\sim 7,000$ - $\sim 12,000$
B-doped, diamond-coated, MWNT “teepee”	3.0	-	~ 0.8 mA/cm^2	-	-
ZnO-CNT composites	0.31	-	~ 95 $\mu\text{A}/\text{cm}^2$	~ 1.25	18,800
Li-coated CNTs on tip-type substrates	0.65	-	618 μA	1.2	4,200
CNT/TiO_2 composites	1.3	-	~ 7 mA/cm^2	~ 4.6	10,000

Material	Turn-on field (V/μm)	Threshold field (V/μm)	Maximum current	Field at maximum current (V/μm)	β
MoS₂/MWNT composites	2.7 for 1 $\mu\text{A}/\text{cm}^2$	5.3	-	-	-
Co/MWNT composites	2.7 – 3.8	-	-	-	-

In general, CNT composite materials have higher field enhancement factors than plain CNTs. The low turn-on fields are comparable to those of normal CNT materials.

However, the maximum current densities are much lower than those of the “normal” CNTs.

In addition to CNT-type alternatives, many other materials are being explored as field emitters. A review article by Fang et al.⁵⁰ goes into detail on several field emission materials: ZnO, ZnS, Si, WO₃, AlN, and SiC. Table 2.3 summarizes some of the efforts over the last 14 years in developing various field emission cathode materials.

Table 2.3 Field emission properties of non-CNT materials. The blank fields were not discussed in the study. The turn-on field corresponds to 10 $\mu\text{A}/\text{cm}^2$, and threshold field to 1 mA/cm^2 , unless otherwise noted.

Material	Turn-on field (V/μm)	Threshold field (V/μm)	Maximum current	Field at maximum current (V/μm)	β
Ti-O materials					
Reduced TiO nanotubes ⁵¹	1.51	2.96	5.00 mA/cm^2	4.03	-
Fe-doped TiO ₂ nanotubes ⁵²	12	-	12 mA/cm^2	19	455 \pm 136
TiO ₂ nanorods ⁵³	1.78 – 6.46	3.15 – 10.5	2 mA/cm^2	3.3	961 – 4,757
TiO ₂ /Ti nanotubes ⁵⁴	7.8	-	3.4 mA/cm^2	19.7	870

Material	Turn-on field (V/μm)	Threshold field (V/μm)	Maximum current	Field at maximum current (V/μm)	β
TiO ₂ nanotubes ⁵⁵	-	~ 1.8	~4.0 mA/cm ²	~2.4	~8,363
WO materials					
Nanotips ⁵⁶	~2.0	~4.37 (10 mA/cm ²)	1,200 μA	-	-
Nanowires ⁵⁷	-	11.9	1,120 μA , 4.9 mA/cm ²	16.2	6,932
Mo nanowalls ⁵⁸	4.0	7.6 (10 mA/cm ²)	57.5 mA/cm ²	-	817
Si materials					
Si nanowires on C cloth ⁵⁹	0.3	0.7	~1.1 mA/cm ²	~0.7	61,000
SiC nanowires ⁶⁰	0.7 – 1.5	2.5 – 3.5 (10 mA/cm ²)	-	-	-
C-coated Si nanowires ⁶¹	-	-	0.3 μA	5.7	11,010
N-doped SiC nanoarrays ⁶²	1.90 – 2.65	2.53 – 3.51	~2 mA/cm ²	~2.5	1,710
ZnO materials					
Nanotubes ⁶³	7.0 (0.1 $\mu\text{A}/\text{cm}^2$)	17.8	-	-	910
Nanorods ⁶⁴	4.6 (1 $\mu\text{A}/\text{cm}^2$)	-	420 $\mu\text{A}/\text{cm}^2$	8.89	~1,700
Aligned nanowires ⁶⁵	6 (5 $\mu\text{A}/\text{cm}^2$)	-	50 mA/cm ² (unstable)	-	50
Well-aligned nanowires ⁶⁶	6.0 (0.1 $\mu\text{A}/\text{cm}^2$)	11.0	-	-	~847
Graphene edge ⁶⁷	3.34 (1 $\mu\text{A}/\text{cm}^2$)	-	~6 μA	~1325 V	-
BN nanotubes ⁶⁸	150 V	-	0.02 μA	~70 V	-

From Table 2.3, it is difficult to make direct comparisons among studies because of the wide variety of materials, ranges of parameters reported, and the definition of those parameters. Overall, it appears that titanium oxide materials, especially titanium dioxide nanotubes, have the highest stable current levels. The study by Alivov et al.⁵⁵ was the only

one exploring materials for X-ray generation, and was a titanium dioxide nanotube study. The field enhancement factors were not as high as the alternative CNT materials, except for Si materials. Even within the same material family, experimental results varied widely.

Most of these materials were not seriously investigated for X-ray applications. Most applications were for field emission displays, microwave amplifiers, sensors, etc. These data shows that research in developing new field emission sources is an active one. However, current results do not present a competitive alternative to plain CNTs.

2.3.5 Development of carbon nanotube cathodes for s-DBT

Originally, the CNTs used for field emission cathodes at UNC were SWNTs, as can be seen in Table 2.4. The SWNTs were made through laser ablation⁶⁹. The SWNTs self-assembled into hydrophilic bundles⁷⁰. These bundles were formed into inks that with electrophoretic deposition (EPD), were made into the cathodes. The ink consisted of 1 mg of SWNTs, 200 mL of alcohol, and MgCl₂. MgCl₂ was used as a charger salt that directed the CNT solution toward the cathode of the EPD setup⁷¹. Mg²⁺ ions were absorbed on the nanotube surface that had been treated with a mixture of nitric and sulfuric acid, functionalizing the CNTs with COOH groups⁷¹⁻⁷³. In EPD, particles suspended in a liquid (in this case SWNTS) surround two electrodes – a cathode and an anode – that have voltage applied between them. The charged SWNTs migrate toward the cathode and form a film composite on the surface⁷². The rate of deposition depends on the CNT suspension concentration, the charger concentration, and the current⁷⁰. The composite density is determined by the nanotube length, shorter nanotubes creating a more dense composite⁷⁰, and the CNT concentration in the EPD ink⁷⁴. The deposited film thickness depends on the deposition time and the voltage applied between the anode and cathode⁷⁴. One of the first

results of a CNT field emission cathode made with this method produced a current density of 67 mA/cm² for 6 hours⁷¹.

Table 2.4 Summary of CNT cathode development over time.

Cathode used	Turn-on field	Threshold field	Max current
SWNTs on stainless steel substrate ⁷¹			67 mA/cm ²
SWNTs on flat metal disc with Fe interlayer ⁶⁹		2 V/μm (1 mA/cm ²)	28 mA, 140 mA/cm ²
SWNT cathode, 4 mm diameter ⁷⁰			32 mA/cm ² (11.3 V/μm)
SWNTs in organic solvent sprayed into film (no EPD) ⁷⁵			3.3 kA, 51.6 A/cm ² (330 kVp)
SWNTs on glass ⁷³	6 V/μm (1 mA/cm ²)	8 V/μm (10 mA/cm ²)	
SWNTs on W tip ¹⁴	~1,000 V (5 μA)		2.5×10 ⁵ A/cm ²
MWNTs/FWNTs on glass substrate ⁷⁶			<u>Small cathode:</u> 1,900 mA/cm ² (~8 V/μm) <u>Larger cathode:</u> ~700 mA/cm ² (~8.5 V/μm)

In 2002, Yue et al. published results of a miniature X-ray source. This was a triode experiment with a Cu anode, metal grid for the gate electrode, and a 0.2 cm² metal disc for the cathode. A maximum cathode current of 28 mA (140 mA/cm²) was produced with a transmission rate of 80 %. For 10 hr in DC mode, 2 mA were produced with a 2 % – 4% fluctuation. In pulsed mode, 6 mA were stably produced equaling 30 mA/cm²⁶⁹. It was reported that the 4 mm diameter SWNT cathode was able to produce 16 mA (32 mA/cm²) at an electric field value of 11.3 V/μm⁷⁰.

In 2004, the photolithography patterning of cathodes was described by Oh et al. The deposition area shape and size was patterned with UV photolithography, and the exposed

areas removed. The CNTs were deposited with EPD on either ITO glass or Ag-coated glass. Post processing included soft baking, removal of remaining photoresist, and vacuum annealing. These cathodes showed good adhesion of the CNT composite to the glass because of the strong interaction between hydrophilic CNTs and metals and bonding promoted by Mg^{2+} charger ions. The cathodes had an emitter density of $\sim 5 \times 10^5$ emitters/cm² ⁷³.

The work done by Dr. Xiomara Calderòn-Colòn led to the most current cathode design used for s-DBT today ^{72,74,76}. Main changes made to the EPD ink for these cathodes included using MWNTs produced by thermal CVD, also known as FWNTs ⁷⁷, and adding a glass powder or frit, SCB-13. The substrates for the FWNT cathodes are metal plates, instead of metal-coated glass. The substrate goes through the photolithography process, or shadow masking if a larger cathode area is needed ¹⁴. After the area is patterned, CNTs are deposited with EPD. First, a glass suspension layer is deposited to promote adhesion, followed by CNT ink deposition ⁷². After deposition, the cathode is vacuum annealed and activated by taping. This allows a larger portion of CNT tips to protrude from the composite surface ⁷⁴. Taping also semi-aligns the randomly arranged CNTs. Film thickness is about 15 μ m. As can be seen in Table 2.4, smaller cathodes are able to produce higher current density than larger ones. For s-DBT, larger cathodes of ~ 2.5 mm \times ~ 13 mm are used to produce more current, although the current density is lower.

REFERENCES

- 1 Ren, B. *et al.* in *Medical Imaging 2011: Physics of Medical Imaging*. (eds Norbert J. Pelc, Ehsan Samei, & Robert M. Nishikawa) 79615F-79615F-79612 (SPIE Proceedings).
- 2 Acciavatti, R. J. & Maidment, A. D. A. in *Medical Imaging 2012: Physics of Medical Imaging*. (eds Norbert J. Pelc, Robert M. Nishikawa, & Bruce R. Whiting) 831306-831301-831312 (SPIE Proceedings).
- 3 Zhao, B. & Zhao, W. Imaging performance of an amorphous selenium digital mammography detector in a breast tomosynthesis system. *Med Phys* **35**, 1978-1987, doi:<http://dx.doi.org/10.1118/1.2903425> (2008).
- 4 Marshall, N. W. & Bosmans, H. Measurements of system sharpness for two digital breast tomosynthesis systems. *Phys Med Biol* **57**, 7629-7650, doi:10.1088/0031-9155/57/22/7629 (2012).
- 5 Shaheen, E., Marshall, N. & Bosmans, H. in *Medical Imaging 2011: Physics of Medical Imaging*. (eds Norbert J. Pelc, Ehsan Samei, & Robert M. Nishikawa) 79611E-79611E-79619 (SPIE Proceedings).
- 6 Hu, Y. H. & Zhao, W. The effect of angular dose distribution on the detection of microcalcifications in digital breast tomosynthesis. *Med Phys* **38**, 2455-2466, doi:<http://dx.doi.org/10.1118/1.3570580> (2011).
- 7 Mainprize, J. G., Bloomquist, A. K., Kempston, M. P. & Yaffe, M. J. Resolution at oblique incidence angles of a flat panel imager for breast tomosynthesis. *Medical Physics* **33**, 3159, doi:10.1118/1.2241994 (2006).
- 8 Sechopoulos, I. A review of breast tomosynthesis. Part I. The image acquisition process. *Med Phys* **40**, 014301, doi:10.1118/1.4770279 (2013).
- 9 Kopans, D. B. *Breast Imaging*. 3rd edn, (Lippincott Williams & Wilkins, 2007).
- 10 Spangler, M. L. *et al.* Detection and classification of calcifications on digital breast tomosynthesis and 2D digital mammography: a comparison. *AJR. American journal of roentgenology* **196**, 320-324, doi:10.2214/AJR.10.4656 (2011).
- 11 Baker, J. A. & Lo, J. Y. Breast tomosynthesis: state-of-the-art and review of the literature. *Acad Radiol* **18**, 1298-1310, doi:10.1016/j.acra.2011.06.011 (2011).
- 12 Defreitas, K. F. *et al.* Breast biopsy and needle localization using tomosynthesis systems. (2013).

- 13 Girgenti, J., Defreitas, K. F. & DeYoung, T. W. Breast Biopsy Lateral Arm System. (2013).
- 14 Yang, G. *Carbon nanotube based stationary X-ray tomosynthesis scanner for detection of breast cancer [electronic resource]*, University of North Carolina at Chapel Hill, (2008).
- 15 Gomer, R. *Field Emission and Field Ionization*. (American Institute of Physics, 1993).
- 16 Fowler, R. H. & Nordheim, L. Electron Emission in Intense Electric Fields. *Proceedings of the Royal Society of London. Series A, Containing Papers of a Mathematical and Physical Character* **119**, 173-181, doi:10.2307/95023 (1928).
- 17 Cheng, Y. & Zhou, O. Electron field emission from carbon nanotubes. *Comptes Rendus Physique* **4**, 1021-1033, doi:10.1016/s1631-0705(03)00103-8 (2003).
- 18 Modinos, A. *Field, Thermionic, and Secondary Electron Emission Spectroscopy*. (Plenum Press, 1984).
- 19 Bushberg, J. T., Seibert, J. A., Leidholdt, E. M. & Boone, J. M. *The Essential Physics of Medical Imaging*. 2nd edn, (Lippincott Williams & Wilkins, 2002).
- 20 Johns, H. E. & Cunningham, J. R. *The physics of radiology*. (Charles C Thomas, 1974).
- 21 Zhu, W. *Vacuum Micro-electronics*. (John Wiley & Sons, Inc., 2001).
- 22 Ren, Z. & Lan, Y. *Aligned Carbon Nanotubes: Physics, Concepts, Fabrication and Devices*. (Springer, 2013).
- 23 Dresselhaus, M. S., Dresselhaus, G. & Avouris, P. *Carbon Nanotubes: Synthesis, Structure, Properties, and Applications*. Vol. 80 (Springer-Verlag Berlin Heidelberg, 2001).
- 24 Hamanaka, M. H. M. O., Mammana, V. P. & Tatsch, P. J. Review of Field Emission from Carbon Nanotubes: Highlighting Measuring Energy Spread. *NanoCarbon 2011: Selected Works from the Brazilian Carbon Meeting* **3**, 1-32, doi:10.1007/978-3-642-31960-0_1 (2013).
- 25 Saito, Y. *Carbon Nanotube and Related Field Emitters: Fundamentals and Applications*. (WILEY-VCH Verlag GmbH & Co., 2010).
- 26 Milne, W. I. *et al.* Carbon nanotubes as field emission sources. *Journal of Materials Chemistry* **14**, 933-943, doi:10.1039/B314155C (2004).

- 27 Bel'skii, M. D., Bocharov, G. S., Elets'kii, A. V. & Sommerer, T. J. Electric field enhancement in field-emission cathodes based on carbon nanotubes. *Tech. Phys.* **55**, 289-295, doi:10.1134/s1063784210020210 (2010).
- 28 Jeong, H. J., Lim, S. C., Kim, K. S. & Lee, Y. H. Edge effect on the field emission properties from vertically aligned carbon nanotube arrays. *Carbon* **42**, 3036-3039, doi:10.1016/j.carbon.2004.07.005 (2004).
- 29 Patra, S. K. & Mohan Rao, G. Field emission current saturation of aligned carbon nanotube—Effect of density and aspect ratio. *Journal of Applied Physics* **100**, 024319, doi:10.1063/1.2219082 (2006).
- 30 Cai, D. & Liu, L. The screening effects of carbon nanotube arrays and its field emission optimum density. *AIP Advances* **3**, 122103, doi:10.1063/1.4841275 (2013).
- 31 Dean, K. A. & Chalamala, B. R. Current saturation mechanisms in carbon nanotube field emitters. *Applied Physics Letters* **76**, 375, doi:10.1063/1.125758 (2000).
- 32 Purcell, S. T., Vincent, P., Journet, C. & Binh, V. T. Hot nanotubes: stable heating of individual multiwall carbon nanotubes to 2000 k induced by the field-emission current. *Phys Rev Lett* **88**, 105502 (2002).
- 33 Kato, S. & Noguchi, T. in *Carbon Nanotube and Related Field Emitters: Fundamentals and Applications* (ed Yahachi Saito) Ch. High-Current-Density Field Emission Electron Source, 373-388 (WILEY-VCH Verlag GmbH & Co., 2010).
- 34 Milne, W. I. *et al.* Aligned carbon nanotubes/fibers for applications in vacuum microwave amplifiers. *J. Vac. Sci. Technol. B* **24**, 345 (2006).
- 35 Wang, G., Noguchi, T. & Kato, S. in *Vacuum Nanoelectronics Conference, 2009. IVNC 2009. 22nd International.* 289-290.
- 36 Kim, Y. C. *et al.* Activation-free printed carbon nanotube field emitters. *Nanotechnology* **22**, 435601, doi:10.1088/0957-4484/22/43/435601 (2011).
- 37 Jo, A. R., Kim, D. I. & Kim, D. J. in *Nanotechnology Materials and Devices Conference (NMDC), 2011 IEEE.* 315-317.
- 38 Neupane, S. *et al.* Synthesis and field emission properties of vertically aligned carbon nanotube arrays on copper. *Carbon* **50**, 2641-2650, doi:10.1016/j.carbon.2012.02.024 (2012).
- 39 Lee, J. *et al.* High-performance field emission from a carbon nanotube carpet. *Carbon* **50**, 3889-3896, doi:10.1016/j.carbon.2012.04.033 (2012).

- 40 Shahi, M. *et al.* Effect of purity, edge length, and growth area on field emission of multi-walled carbon nanotube emitter arrays. *Journal of Applied Physics* **113**, 204304, doi:10.1063/1.4807916 (2013).
- 41 Huang, Y.-J. *et al.* Field emission characteristics of vertically aligned carbon nanotubes with honeycomb configuration grown onto glass substrate with titanium coating. *Materials Science and Engineering: B* **182**, 14-20, doi:10.1016/j.mseb.2013.11.022 (2014).
- 42 Sun, Y., Yeow, J. T. & Jaffray, D. A. Design and fabrication of carbon nanotube field-emission cathode with coaxial gate and ballast resistor. *Small* **9**, 3385-3389, doi:10.1002/smll.201300553 (2013).
- 43 Zuo, Y., Ren, Y., Wang, Z., Han, X. & Xi, L. Enhanced field emission and hysteresis characteristics of aligned carbon nanotubes with Ti decoration. *Organic Electronics* **14**, 2306-2314, doi:10.1016/j.orgel.2013.05.027 (2013).
- 44 Zou, Y., May, P. W., Vieira, S. M. C. & Fox, N. A. Field emission from diamond-coated multiwalled carbon nanotube “teepee” structures. *Journal of Applied Physics* **112**, 044903, doi:10.1063/1.4748336 (2012).
- 45 Su, C.-H. & Huang, C.-M. Field emission characteristics study for ZnO–CNTs composites by the microwave plasma jet chemical vapor deposition system. *Materials Letters* **111**, 140-142, doi:10.1016/j.matlet.2013.07.130 (2013).
- 46 Kim, J.-P., Chang, H.-B., Kim, B.-J. & Park, J.-S. Enhancement of electron emission and long-term stability of tip-type carbon nanotube field emitters via lithium coating. *Thin Solid Films* **528**, 242-246, doi:10.1016/j.tsf.2012.08.060 (2013).
- 47 He, K.-X., Su, J., Guo, D.-Z., Xing, Y.-J. & Zhang, G.-M. Mechanical fabrication of carbon nanotube/TiO₂ nanoparticle composite films and their field-emission properties. *physica status solidi (a)* **208**, 2388-2391, doi:10.1002/pssa.201084202 (2011).
- 48 Zhang, Q. *et al.* Synthesis of a MoS₂@MWNT nanostructure with enhanced field emission and electrochemical properties. *RSC Advances* **3**, 10994, doi:10.1039/c3ra41239c (2013).
- 49 Arai, S. & Miyagawa, K. Field emission properties of cobalt/multiwalled carbon nanotube composite films fabricated by electrodeposition. *Applied Surface Science* **280**, 957-961, doi:10.1016/j.apsusc.2013.05.117 (2013).
- 50 Fang, X., Bando, Y., Gautam, U. K., Ye, C. & Golberg, D. Inorganic semiconductor nanostructures and their field-emission applications. *Journal of Materials Chemistry* **18**, 509, doi:10.1039/b712874f (2008).

- 51 Zhu, W.-D., Wang, C.-W., Chen, J.-B. & Zhang, X.-q. Low temperature synthesis of reduced titanium oxide nanotube arrays: Crystal structure transformation and enhanced field emission. *Materials Research Bulletin* **50**, 79-84, doi:10.1016/j.materresbull.2013.10.030 (2014).
- 52 Wang, C. C., Wang, K. W. & Perng, T. P. Electron field emission from Fe-doped TiO₂ nanotubes. *Applied physics letters* **96** (2010).
- 53 Li, D. S. *et al.* Aligned rutile TiO₂ nanorods: Facile synthesis and field emission. *Superlattices and Microstructures* **59**, 187-195, doi:10.1016/j.spmi.2013.04.010 (2013).
- 54 Chen, J.-B. *et al.* Field emission from the structure of well-aligned TiO₂/Ti nanotube arrays. *Thin Solid Films* **517**, 4390-4393, doi:10.1016/j.tsf.2009.01.088 (2009).
- 55 Alivov, Y., Klopfer, M. & Molloy, S. TiO₂ nanotubes as a cold cathode for x-ray generation. *Applied Physics Letters* **96**, 243502, doi:10.1063/1.3454244 (2010).
- 56 Zhou, J. *et al.* Growth and field-emission property of tungsten oxide nanotip arrays. *Applied Physics Letters* **87**, doi:10.1063/1.236006 (2005).
- 57 Yue, S. *et al.* Amazing ageing property and in situ comparative study of field emission from tungsten oxide nanowires. *Nanotechnology* **22**, 115703, doi:10.1088/0957-4484/22/11/115703 (2011).
- 58 Shen, Y. *et al.* Highly conductive vertically aligned molybdenum nanowalls and their field emission property. *Nanoscale Res Lett* **7**, 463, doi:10.1186/1556-276X-7-463 (2012).
- 59 Zeng, B. Q. *et al.* Field emission of silicon nanowires grown on carbon cloth. *Applied Physics Letters* **90**, doi:10.1063/1.242854 (2007).
- 60 Pan, Z. *et al.* Oriented Silicon Carbide Nanowires: Synthesis and Field Emission Properties. *Advanced Materials* **12**, 1186-1190, doi:10.1002/1521-4095(200008)12:16<1186::aid-adma1186>3.0.co;2-f (2000).
- 61 Das, N. S., Banerjee, D. & Chattopadhyay, K. K. Enhancement of electron field emission by carbon coating on vertically aligned Si nanowires. *Applied Surface Science* **257**, 9649-9653, doi:10.1016/j.apsusc.2011.06.091 (2011).
- 62 Chen, S. *et al.* Growth of flexible N-doped SiC quasisaligned nanoarrays and their field emission properties. *Journal of Materials Chemistry C* **1**, 4779, doi:10.1039/c3tc30752b (2013).
- 63 Wei, A. *et al.* Stable field emission from hydrothermally grown ZnO nanotubes. *Applied Physics Letters* **88**, 213102, doi:10.1063/1.2206249 (2006).

- 64 Wang, L. L., Gong, S. D., Wu, L. H. & Li, X. J. Field emission from zinc oxide nanorod bundles grown on silicon nanoporous pillar array. *Applied Surface Science* **270**, 124-127, doi:10.1016/j.apsusc.2012.12.136 (2013).
- 65 Semet, V., Vu Thien, B., Pauporte, T., Joulaud, L. & Vermersch, F. J. in *Vacuum Nanoelectronics Conference (IVNC), 2010 23rd International*. 3-4.
- 66 Lee, C. J. *et al.* Field emission from well-aligned zinc oxide nanowires grown at low temperature. *Applied Physics Letters* **81**, 3648, doi:10.1063/1.1518810 (2002).
- 67 Tsai, J. T., Chu, T. Y., Shiu, J. Y. & Yang, C. S. Field emission from an individual freestanding graphene edge. *Small* **8**, 3739-3745, doi:10.1002/sml.201200880 (2012).
- 68 Cumings, J. Field emission properties of boron nitride nanotubes. *Aip Conf Proc* **591**, 577-580, doi:10.1063/1.1426935 (2001).
- 69 Yue, G. Z. *et al.* Generation of continuous and pulsed diagnostic imaging x-ray radiation using a carbon-nanotube-based field-emission cathode. *Applied Physics Letters* **81**, 355, doi:10.1063/1.1492305 (2002).
- 70 Zhou, O. *et al.* Materials Science of Carbon Nanotubes: Fabrication, Integration, and Properties of Macroscopic Structures of Carbon Nanotubes. *Accounts of Chemical Research* **35**, 1045-1053, doi:10.1021/ar010162f (2002).
- 71 Gao, B. *et al.* Fabrication and Electron Field Emission Properties of Carbon Nanotube Films by Electrophoretic Deposition. *Advanced Materials* **13**, 1770-1773, doi:10.1002/1521-4095(200112)13:23<1770::aid-adma1770>3.0.co;2-g (2001).
- 72 Calderón-Colón, X. *Fabrication, characterization and integration of carbon nanotube cathodes for field emission x-ray source* PhD thesis, University of North Carolina at Chapel Hill, (2009).
- 73 Oh, S. J., Zhang, J., Cheng, Y., Shimoda, H. & Zhou, O. Liquid-phase fabrication of patterned carbon nanotube field emission cathodes. *Appl. Phys. Lett.* **87**, 3738 (2004).
- 74 Zhou, O. & Calderon-Colon, X. in *Carbon Nanotube and Related Field Emitters: Fundamentals and Applications* (ed Yahachi Saito) Ch. Carbon nanotube based field emission x-ray technology, 417-438 (WILEY-VCH Verlag GmbH & Co., 2010).
- 75 Shiffler, D., Zhou, O., Bower, C., LaCour, M. & Golby, K. A High-Current, Large-Area, Carbon Nanotube Cathode. *IEEE Transactions on Plasma Science* **32**, 2152-2154, doi:10.1109/tps.2004.835519 (2004).

- 76 Calderon-Colon, X. *et al.* A carbon nanotube field emission cathode with high current density and long-term stability. *Nanotechnology* **20**, 325707, doi:10.1088/0957-4484/20/32/325707 (2009).
- 77 Qian, C. *et al.* Fabrication of small diameter few-walled carbon nanotubes with enhanced field emission property. *J Nanosci Nanotechnol* **6**, 1346-1349, doi:10.1166/Jnn.2006.140 (2006).

CHAPTER 3: DESIGN AND DEVELOPMENT OF THE STATIONARY DIGITAL BREAST TOMOSYNTHESIS SYSTEM

3.1 Tube design

3.1.1 Electrode structure

The electrode structure of the s-DBT tube consists of five main electrodes: cathode, gate, focusing 1 (F1), focusing 2 (F2), and anode.

Cathodes

The current iteration of the s-DBT tube is called Argus 3.0. There were two previous designs of the tube that will not be discussed here. In Argus 3.0, there are 31 CNT cathodes made from molybdenum metal substrates that are 7.25 mm tall. The CNT deposition area on the top of the substrate is 0.325 cm², with dimensions 2.5 mm × 13 mm. An example of these cathodes is shown in Figure 3.1. Because the deposition area is relatively large for higher current capacity in the s-DBT application, the CNT deposition area was marked off with a mask. The CNTs were deposited through the EPD method described in Chapter 2¹. The CNTs used in the EPD ink were produced through thermal CVD, termed few-wall nanotubes (FWNTs)².

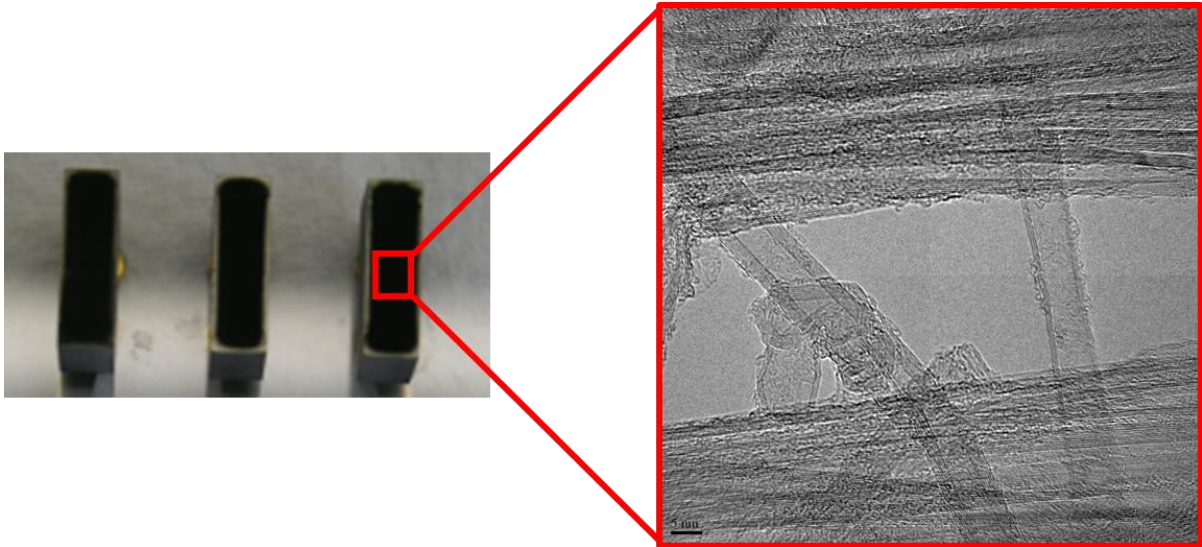


Figure 3.1 The left photograph in this figure shows three CNT cathodes of the type placed in the s-DBT system. On the right, in the red box, is a TEM image of the type of FWNTs deposited on the cathodes.

Gate

The gate is made up of two parts: the gate frame, and the gate mesh. The gate frame is a 2 mm thick stainless steel electrode that spans the length of the X-ray tube with elliptical holes (3 mm \times 17 mm) cut out over each cathode. Each cathode has a corresponding gate mesh welded to the gate frame across the opening, as shown in Figure 3.2. The gate mesh were made from tungsten metal sheets 50 μm or 60 μm in thickness, depending on where they were made. If they were made at UNC they are 50 μm , and if ordered from Elcon Precision LLC (San Jose, CA) they are 60 μm . Metal bars were etched into the tungsten that are 50 μm wide and separated by spaces that are 200 μm wide. Therefore, the bar pitch is 250 μm . The bars are curved on the ends to protect against breakage from thermal expansion. Optical microscope images in Figure 3.3 show the detail of the gate mesh.

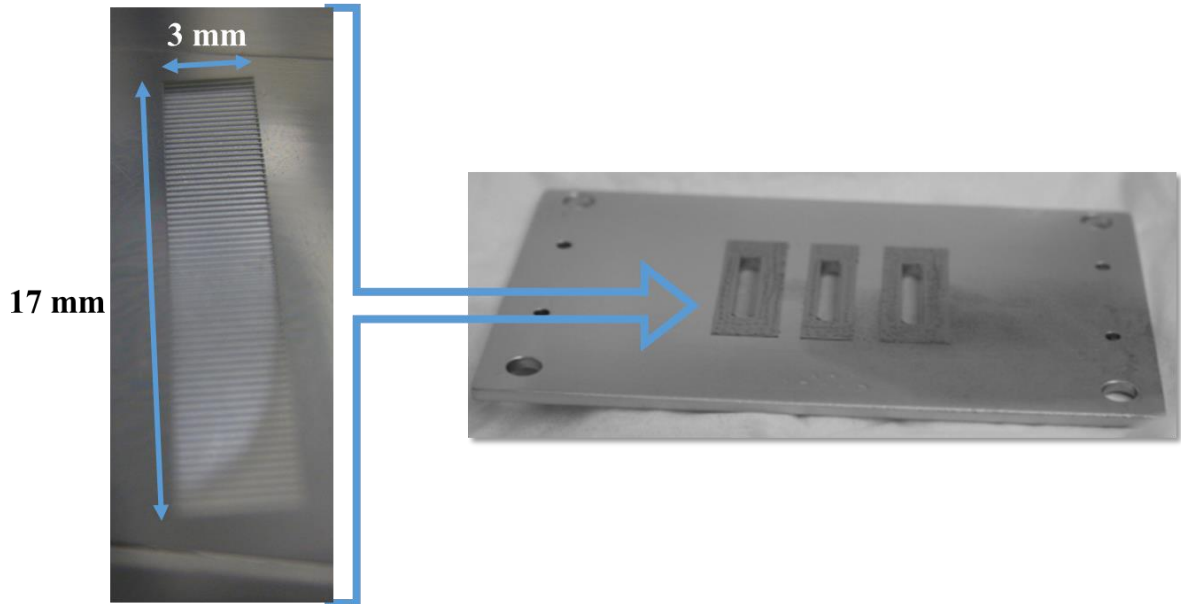


Figure 3.2 On the left is a magnified photograph of a gate mesh immediately after fabrication. The right photograph shows an example of a gate frame with gate mesh welded over the individual openings. This gate frame was not for the s-DBT tube, but the gate mesh are very similar.

The purpose of the gate is to create the electric field that will induce field emission from the CNTs. The distance from the top of the cathode to the gate frame is $280\ \mu\text{m}$. The exact distance to the gate mesh would be $280\ \mu\text{m}$ minus the thickness of the gate mesh, because the gate mesh is welded on the side of the gate frame closest to the cathode. Applied electric field is calculated by dividing the potential difference between the gate and cathode, by the distance between the cathode and the gate mesh.

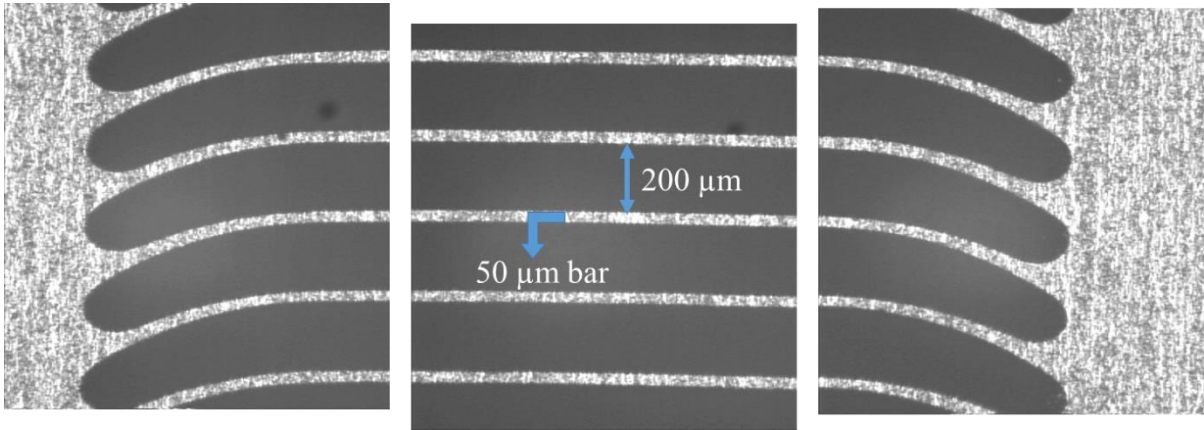


Figure 3.3 Optical microscope images of a tungsten gate mesh. The bar thickness and spacing size are labeled. Also, the curved bar edges can be seen.

The use of a gate mesh makes this a triode setup as opposed to a diode setup having only an anode and a cathode. A triode setup increases the turn-on electric field due to a non-uniform electric field above the cathode¹. It also lowers the rate of electron transmission to the anode from the cathode because some electrons are blocked by the gate. Current loss is dependent on the percentage of open space in the mesh. The focal spot size is also affected by the gate mesh because it alters the electron beam. Misalignment of cathodes to their individual gate openings can cause non-uniform field emission behavior between cathodes¹. Optimizing the gate mesh is a very important part of tube design.

Focusing electrodes

The focusing structure used in the s-DBT system, shown in Figure 3.4, was designed and optimized by Dr. Sultana³. The purpose of the focusing electrodes is to narrow the electron beam after it passes through the gate mesh into the desired focal spot size on the anode. The focal spot size can be altered by changing the voltage on the focusing electrodes. However, applying different voltages can also lower the percentage of the electron beam that is transmitted through the focusing to the anode. Typical s-DBT operation uses both focusing

electrodes grounded to the same potential as the gate frame to maximize the transmission rate.

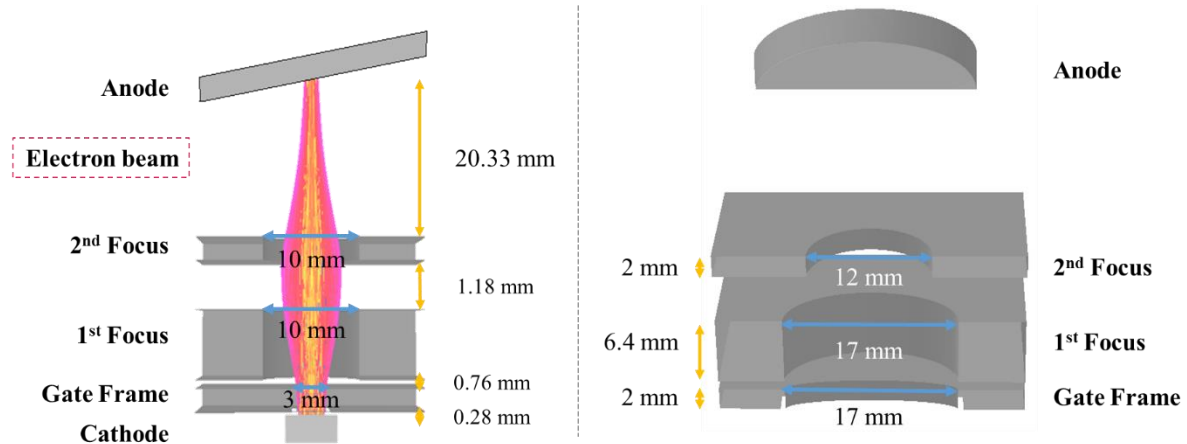


Figure 3.4 Illustration of the complete electron configuration in the s-DBT tube including simulated electron trajectories in the left-hand image. The two views are different cross-sections of the structure. Adapted with permission from Sultana, 2010.

As can be seen from Figure 3.4, the focusing structure is made of two Einzel type electrostatic focusing lenses. The openings in the focusing structures are elliptical. Focusing 1 (F1) is lower, closer to the gate electrode. Focusing 2 (F2) is the higher of the two, nearer to the anode. The opening in F1 is larger than that of F2, 17 mm versus 12 mm. The F1 electrode is also much thicker than F2. The distance between the two electrodes is 1.18 mm.

Both F1 and F2 are stainless steel electrodes that, like the gate electrode, traverse the entire length of the X-ray tube. There is an opening in each electrode per cathode. Since the electrode is common amongst all cathodes, it is not practical to change the focusing voltages for each cathode as they are turned on and off sequentially. Therefore, when a focusing voltage is applied to one cathode, it will be held constant for all of the cathodes.

Anode

The anode is the final electrode in the five-electrode structure. A more realistic illustration of the complete electrode configuration, as designed for the prototype s-DBT tube, is shown in Figure 3.5. As the electron beam bombards the anode, X-rays are created. The anode material in the s-DBT tube is tungsten. Unlike most imaging X-ray tubes, the anode is stationary. This limits the usable focal spot size to prevent melting the anode material. One of the reasons tungsten was chosen for the anode is its high melting temperature. The anode is tilted so that the electron beam intersects with the anode over a larger area to reduce heating while maintaining good spatial resolution.

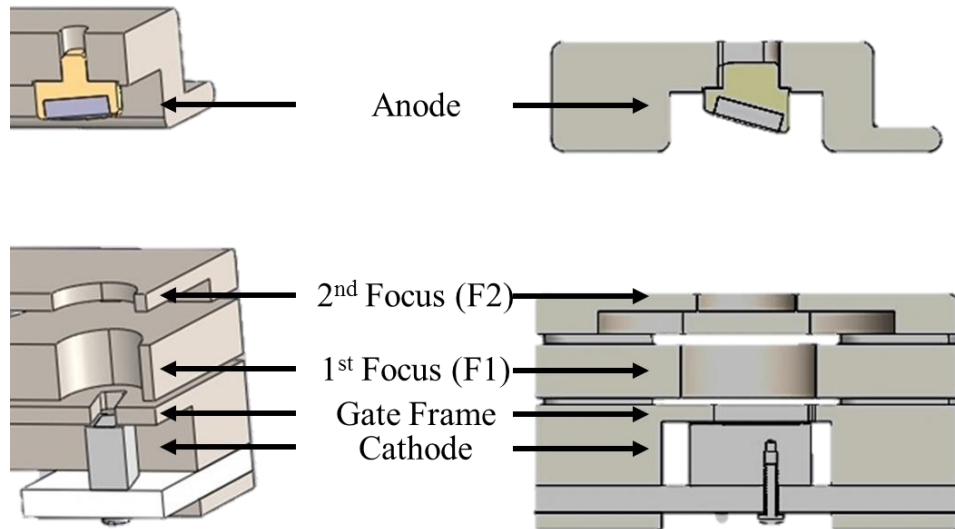


Figure 3.5 Complete electrode structure from the SolidWorks drawing of the s-DBT tube.

A high positive voltage is applied to the anode to accelerate the electrons toward it. The X-ray spectrum peaks at the energy corresponding to the net difference of the anode and cathode voltages. The voltage used for breast imaging can range from 25 kV to 40 kV.

Although there are 31 individual anodes in the s-DBT tube, the same voltage is applied to all of them during imaging.

3.1.2 Tube layout and properties

Figure 3.6 shows photographs of a complete s-DBT tube, designed to be compatible with the Hologic Selenia Dimensions DBT system. The X-ray window on the tube is 1 mm thick aluminum. The tube has two ion pumps, used to maintain a vacuum of approximately 10^{-7} torr. The external collimator's attachment points can be seen in the left image of Figure 3.6, and the collimator is mounted below the X-ray window in the right image. There are two high voltage focusing feedthroughs on top of the tube, one for F1 and for F2. Thirty-one high voltage cathode feedthroughs are lined along the top of the tube, one per cathode. There is no gate electrode feedthrough because it is permanently grounded to the tube housing. Voltage between the gate and cathode for electron extraction is applied to the cathode, and is a negative voltage on the order of 1 kV – 2 kV.

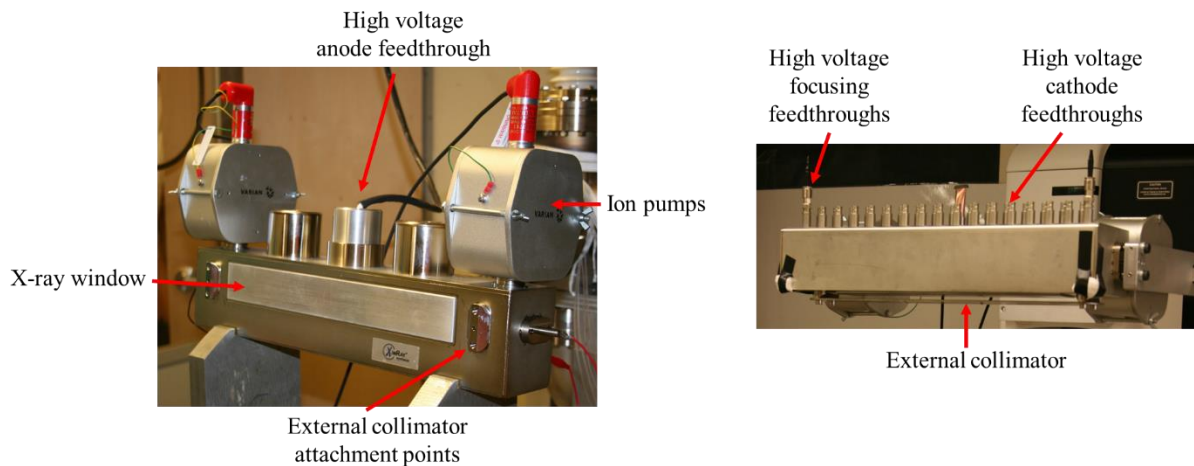


Figure 3.6 Photographs of an s-DBT X-ray tube with key features labeled. The orientation used in breast imaging is shown in the right photograph, with the X-ray window facing downward toward the detector.

Linear focal spot configuration

The cathode-anode pairs such that the angular separation between each projection is 1° , and the total angular range is 30° . Therefore, the angular spacing of the projections is uniform, but the linear spacing of the cathodes is not. The cathode-anode pairs angle inward toward the central location to create an imaging isocenter 5 cm above the detector surface. Internal collimation is also present within the tube in order to control the beam width leaving the X-ray window. This restricts X-rays from falling too far outside of the detector area. The outermost beams are collimated to an angle of 23.4° . The external collimator restricts the beam from penetrating too far into the patient's chest wall.

Effective focal spot size

The focal spot size can be described in two ways: the actual focal spot size, and the effective focal spot size. The actual focal spot size is the area of electron bombardment on the angled surface of the anode. The effective focal spot size is the area of the actual focal spot size projected onto the detector and is dependent on anode angle and the measurement location on the detector.

With both focusing electrodes grounded, the effective focal spot size was measured to be $0.9 \text{ mm} \times 0.9 \text{ mm}$. Due to the anode angle tilt, the real focal spot size is larger than the effective focal spot size. This only affects the focal spot dimension corresponding to the long side of the cathode, as illustrated in Figure 3.7.

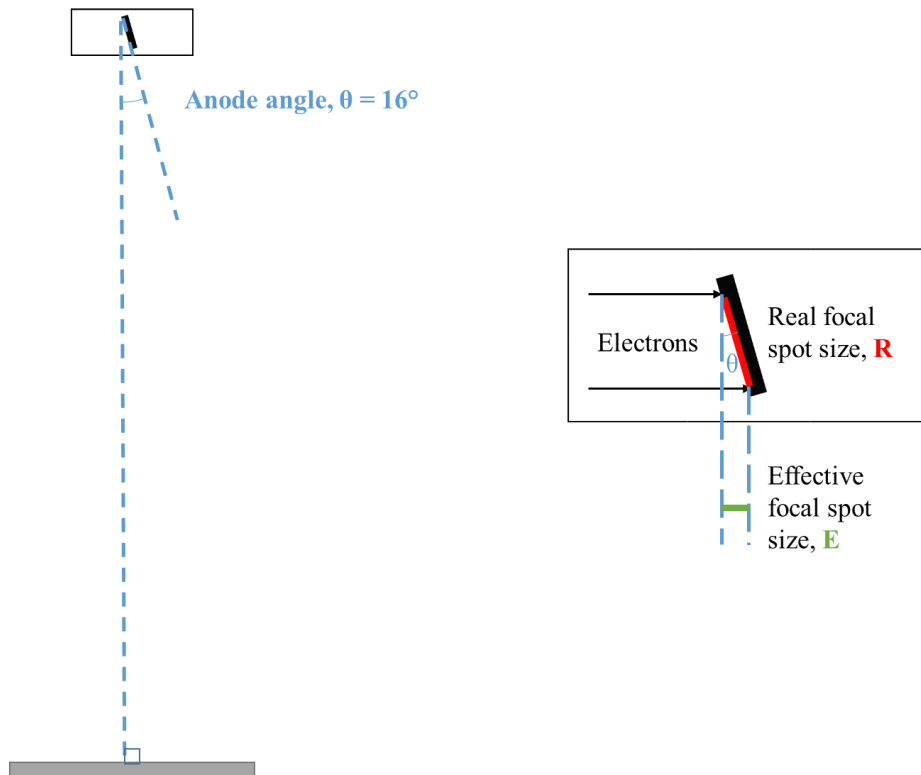


Figure 3.7 Schematic illustrating the difference in the real, or actual, focal spot size and the effective focal spot size.

In the s-DBT tube the anode is tilted by 16° . Keeping with the definitions in Figure 3.7, the relationship for the effective focal spot size is: $E = \sin\theta \cdot R$. Knowing that the measured effective focal spot was 0.9 mm and the anode angle is 16° , the length R is calculated to be 3.26 mm. To calculate the height of the electron beam, B , one would use $B = R \cdot \cos\theta$. The height of the electron beam is then 3.13 mm. The original cathode dimension in that direction is 13 mm. The gate and focusing electrodes, when grounded, reduced the electron beam to approximately one-fourth of its original length. In the short cathode dimension of 2.5 mm, the anode angle does not reduce the electron beam size. Therefore, the 0.9 mm measured size is due completely to the electrode structure focusing the electron beam to approximately one-third of its original size.

The s-DBT tube is mounted onto the gantry 70 cm above the detector and is tilted to make the X-ray intensity more uniform across the detector surface. The effective focal spot size changes depending on where it is measured on the detector. A schematic illustrating how this changes the effective anode angle at the center of a 23 cm long detector is shown in Figure 3.8.

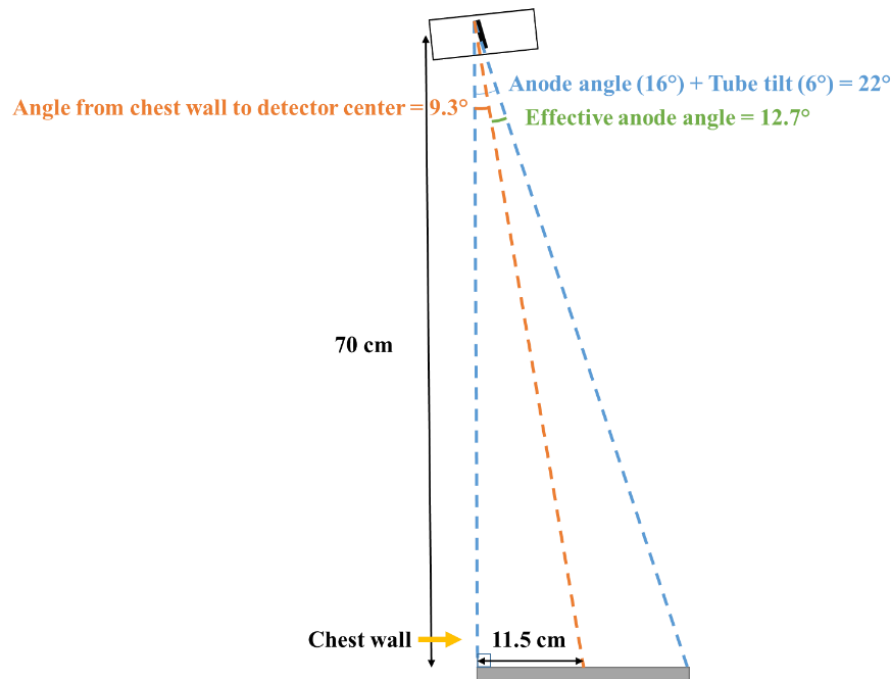


Figure 3.8 Schematic of the geometric configuration determining effective anode angle with tube tilt and positioning on the gantry incorporated.

Transmission rate and anode exposure

Transmission rate (TR) is defined as the percentage of cathode current that reaches the anode: $TR = \frac{\text{Anode current}}{\text{Cathode current}}$. Averaging over all 31 cathodes with grounded focusing, the s-DBT tube transmission rate is $61 \pm 4\%$. Transmission rate can be affected by focusing voltage and gate mesh design. It is important to know the transmission rate to extrapolate the cathode current required for a desired anode exposure.

Anode exposure is anode current multiplied by cathode pulse width. It can be estimated if the cathode current, which can be programmed electronically, and transmission rate are known. The anode exposure for a tomosynthesis acquisition is designed to approximately equal one 2D mammography exposure, but divided among many projections. For the Hologic Selenia Dimensions system the anode exposure, determined by AEC, ranges from 36 mAs to 72 mAs, depending on compressed breast thickness⁴. Assuming for a 100 mAs total exposure example with fifteen projections, each projection must produce 6.67 mAs, where the current is the anode current and the time is the pulse width.

Anode exposure is important because it is proportional to the dose that a patient will receive, as discussed in Chapter 1. The exposure produced on the anode, in units of mAs, is not the same as the exposure that leaves the X-ray tube because of filtration by the tube window. The ratio of dose to anode exposure is defined here as the dose rate. Figure 3.9 compares the dose rate of the s-DBT tube to Hologic's Selenia Dimensions DBT system; the s-DBT system producing less dose for each anode exposure level. The difference is due to X-ray filtration differences between the systems, with s-DBT using 1 mm Al and Hologic using 0.7 mm Al plus 0.63 mm Be. The absorbed dose to the patient in mGy is proportional to exposure, as was discussed in Chapter 1. The average mean glandular dose to a patient of average breast thickness (5 cm) is approximately 2 mGy when using a Hologic Selenia Dimensions system⁴.

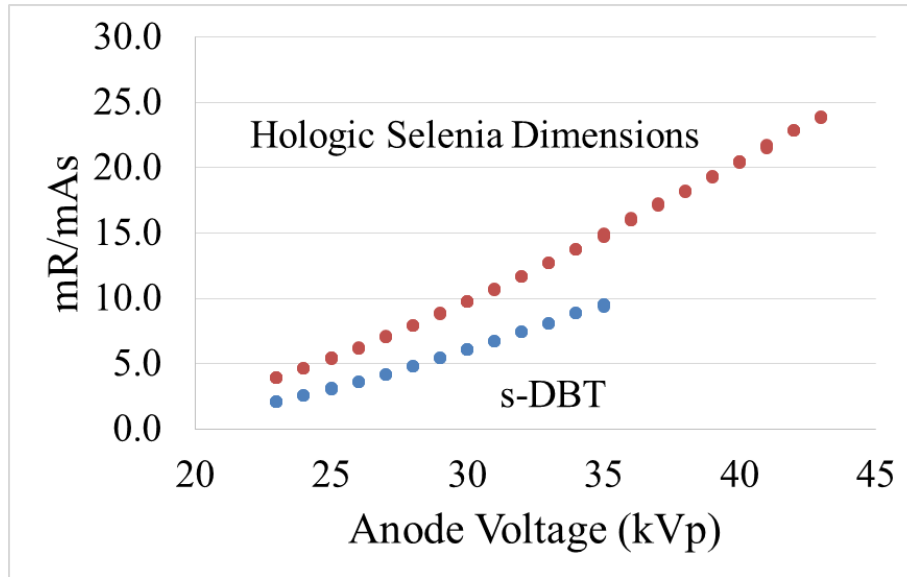


Figure 3.9 Dose rate measurements comparing the Hologic Selenia Dimensions system to the s-DBT system. Data taken by Dr. Andrew Tucker.

To summarize, key properties of the s-DBT tube are listed in Table 3.1.

Table 3.1 Key properties of the s-DBT tube, Argus 3.0.

Tube property	Value for Argus 3.0
Number of cathodes	31
CNT deposition area	2.5 mm × 13 mm
Gate electrode-to-cathode distance	280 μm
X-ray window	1 mm Al
Average TR	61 ± 4 %
Average vacuum pressure	10 ⁻⁷ torr
Angular spacing between projections	1°
Total angular coverage	30°
Focal spot size, focusing grounded	0.9 mm × 0.9 mm
Anode angle	16°

3.2 System design and build challenges

3.2.1 Overall system information

The s-DBT system is an integration of the Argus 3.0 CNT X-ray source into the Hologic Selenia Dimensions system, as shown in Figure 3.10 and Figure 3.11. The X-ray tube is mounted 70 cm above the detector surface, a distance known as the source-to-image receptor distance (SID). The detector size is 29 cm × 23 cm. The readout time for the detector is 0.1 ms. The anode voltage range, limited by the tube, is 45 kV or less, with typical operation ranging from 26 kV to 36 kV.

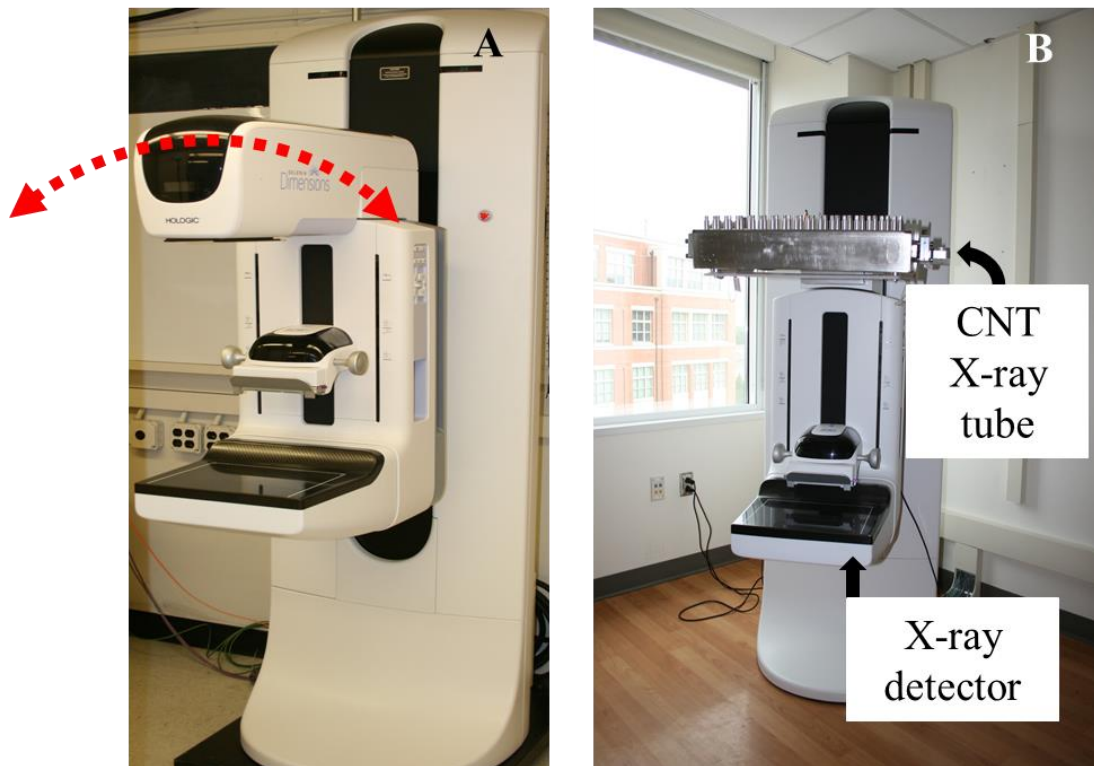


Figure 3.10 (A) Hologic Selenia Dimensions system, with a red arrow indicating the tube motion path. (B) The s-DBT tube integrated with the Hologic gantry. Reprinted from Gidcumb *et al* 2014 *Nanotechnology* **25** 245704.

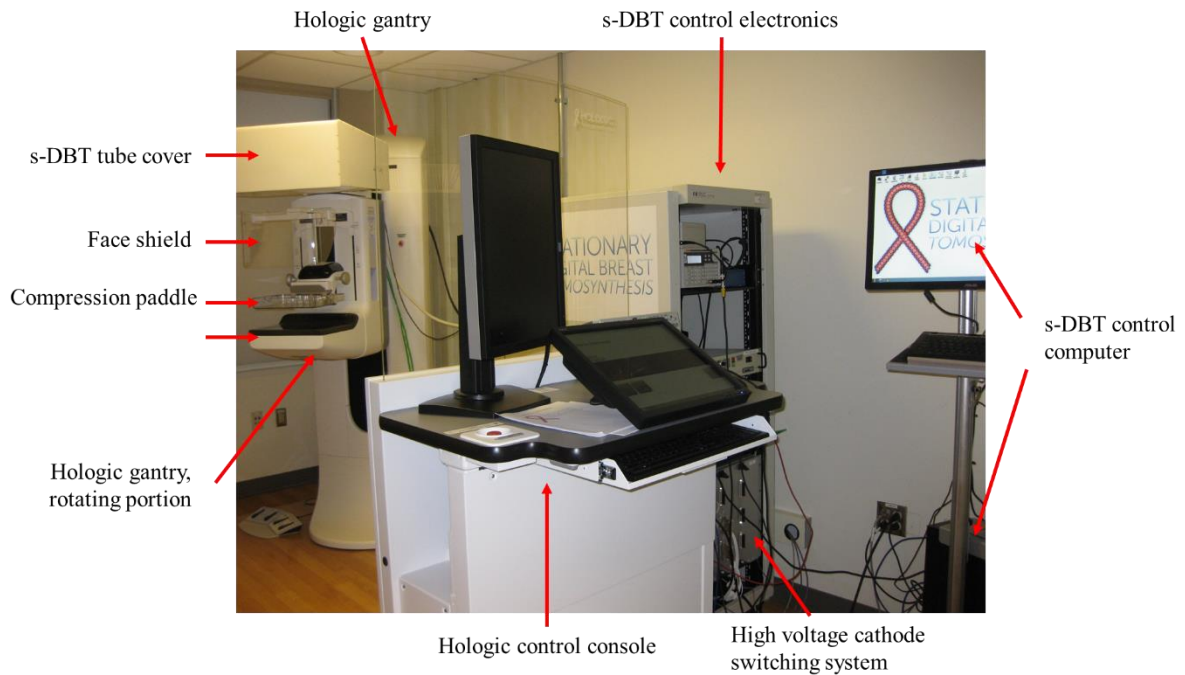


Figure 3.11 Photograph of the completely integrated s-DBT system including the Hologic and s-DBT controls.

Basic tube operation requires interaction with both the s-DBT control computer and the Hologic console. Imaging protocol is set by and initiated with the s-DBT control computer. The s-DBT control computer programs the high voltage cathode switching system. The switching system regulates the cathode current and turns on each beam as desired. The detector communicates with the control console to indicate it is ready for imaging. The imaging is triggered through interlock handles on the Hologic console. After the interlocks are activated, the projection images are acquired synchronizing detector acquisition with the cathode current control of the switching system. Settings for a particular image acquisition are dependent on breast thickness, which is read from the Hologic gantry via the compression paddle height.

3.2.2 X-ray tube construction

After the tube was designed, there were some challenges that needed to be overcome for the tube to be built. One main problem to be solved was the design and fabrication of the gate mesh. Prior to the first tube's construction, no suitable gate mesh had been found. Thus, it was necessary to develop and optimize a gate mesh design and fabrication procedure over the course of 2 to 3 months. A deep reactive ion etching (DRIE) technique was developed utilizing the CHANL facilities at UNC, which will be discussed in Chapter 4. The DRIE mesh was the first source of the gate mesh, later followed by ordering them from Elcon Precision LLC who employed a wet etching technique.

When all of the necessary components were ready, the electrode structure had to be put together by XinRay Systems (Cedar Fork, NC). The tube and parts were next flown to Germany to be permanently sealed by Siemens, then flown back to the United States.

3.2.3 Tube and system evaluation

Because there are 31 individual cathodes in the X-ray tube, there is variation in the performance between one cathode and the next. For a certain current setting, the gate voltage required can vary approximately 400 V among all cathodes. The initial way of dealing with non-uniform cathode current behavior was to use a resistor box to compensate for the voltage differences. Building a resistor box was challenging. It required finding high-power components and housing large enough for the components of 31 cathodes. In addition, not all cathode-anode pairs have the same transmission rate. Transmission rate does not change over time, but it can vary from beam-to-beam and when focusing voltages are altered. Practically, the average transmission rate among the beams is used when calculating the anode exposure required for a certain image acquisition.

The effectiveness of the tube collimators needed to be evaluated. It was found that, for the outermost beam locations, the internal collimator cuts off some of the X-ray beam inside the detector area. This cannot be changed, but was not found to significantly impact image quality. External collimation had to be designed and built to meet the standards for X-ray penetration into the chest wall. Once built, the X-ray field was observed and the collimator adjusted to the correct position.

Focal spot size was evaluated because it is an important factor for spatial resolution. Smaller focal spots reduce geometric blurring in the images⁵. Typically, mammography units have a nominal focal spot size of 0.3 mm, but regulations allow for focal spot size to be up to 2 times larger than the nominal size⁵. After the tube was built the focal spots were characterized by measuring over various focusing voltages. The tube was principally operated with the grounded focusing setting to maximize transmission rate while having an acceptably small focal spot size. Further experiments needed to be done to determine the voltages that would produce the smallest focal spot sizes in the s-DBT system. There is a level of complexity to this because not all of the cathodes operate at the same cathode voltage and not every beam has the same focal spot size.

System spatial resolution depends on the focal spot size, the detector's spatial resolution, and the image reconstruction technique. Typically, in the depth direction the reconstruction slices are 1 mm thick, but can be adjusted with the reconstruction software. The detector pixel size on the Hologic Selenia Dimensions system is 70 μm for full resolution, and 140 μm for 2×2 binning mode. In-plane spatial resolution is measured with the modulation transfer function (MTF), usually reported at 10 % of the maximum. The MTF is a measure of how accurately objects' spatial frequency gets transferred through the entire

imaging system. To be certified for clinical use, there are MTF requirements a breast imaging must meet. At a height of 4.5 cm above the detector, the MTF must be at least 13 cycles/mm perpendicular to the chest wall, and 11 cycles/mm parallel to the chest wall⁵.

3.2.4 Electronic controls integration and system summary

One of the major hurdles overcome to make s-DBT viable for clinical imaging was obtaining a reliable high-voltage cathode switching system. The current high-voltage switching system is the third unit that has been made for this purpose, and was custom built by XinRay Systems and H&P Advanced Technology (Erlangen, Germany). It is able to supply up to 3100 V to each cathode, but the feedthrough limitation of the s-DBT tube is 2500 V. It can generate current pulses of 10 ms to 250 ms. It has the ability to control up to 250 separate channels at a time, but s-DBT only requires 15 to 31. It can handle between 1 mA to 100 mA of cathode current, but the s-DBT tube is limited to 43 mA.

Due to the high voltage applied to the cathode and even higher voltage applied to the anode, there were many precautions taken for both safety and reliable operation of the system. For the anode voltage not to arc to any surrounding equipment, it had to be well insulated. The whole system underwent electrical safety testing through MET Laboratories Inc. (MET Southeast, Cary, NC) for it to be approved for patient use.

Final integration of the Argus 3.0 electronic controls with the Hologic software is diagrammed in Figure 3.12. Custom electronics had to be built by Hologic for the detector software to communicate with the s-DBT control software. The s-DBT control software was primarily programmed using LabVIEW. A pulse generator was used to synchronize detector and cathode switching-system signals. The program was designed to automatically set the

following imaging parameters, depending on compressed breast thickness: anode voltage, pulse width, and number of projections.

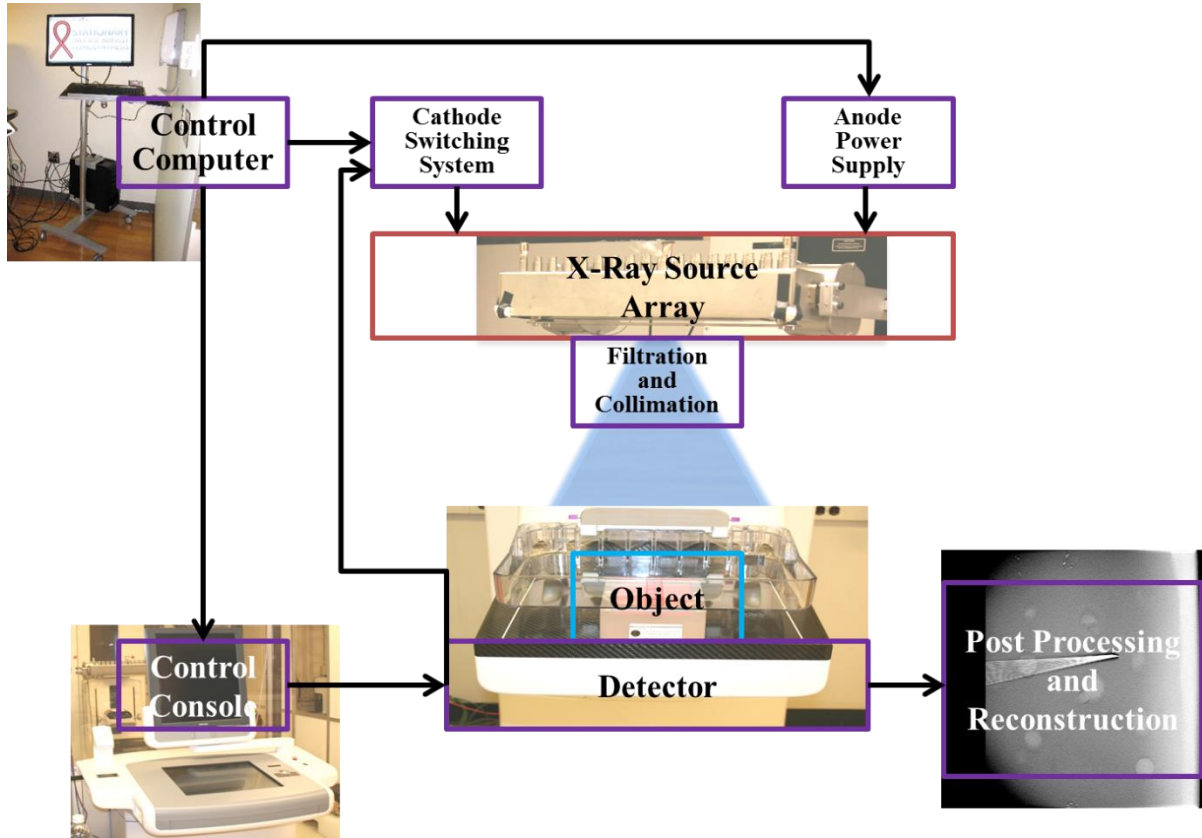


Figure 3.12 Simplified electronic communication flow diagram of the integrated system.

A summary of the key parameters of the integrated system is presented in Table 3.2.

Table 3.2 Key, integrated s-DBT system parameters.

System property	Value
SID	70 cm
Source-to-isocenter distance	65 cm
Detector size	23.3 cm × 28.5 cm
Detector pixel size, un-binned	70 μm
Gantry rotation range	-140° to +180°
Max anode kilovolt peak	45 kV
Maximum cathode current	43 mA
Maximum anode current	28 mA

System property	Value
Maximum pulse width	250 ms
Maximum cathode voltage	3 kV

3.2.5 Reconstructions

Software developed by Real Time Tomography (Villanova, PA), abbreviated RTT, called Dynamic Reconstruction and Rendering (DRR) is used to reconstruct the tomosynthesis images. Successful image reconstruction requires accurate geometry information about the location of the focal spots, acquired through the analysis of images taken of a geometry phantom. Typically, reconstructions are presented in 1 mm thick slices through the reconstructed breast volume, but 0.5 mm is also sometimes used.

3.2.6 FDA requirements

To be approved by the FDA for clinical use, a radiographic imaging system must adhere to all of the requirements in the MQSA^{5,6}. These requirements are not imposed for experimental systems, but must be met when the s-DBT system moves into commercial use.

An initial leakage radiation study was conducted to test if the s-DBT system met FDA requirements. The FDA requires that leakage radiation from a diagnostic source assembly not exceed 0.88 mGy/hr of air Kerma, or 100 mR/hr exposure. This must be measured at a distance of 1 m in a 100 cm² area where no dimension is larger than 20 cm. The X-ray tube must be operated at the maximum rated anode voltage and in pulsed mode. The initial measurements were taken with use of an ion chamber at settings of 250 ms pulse width, 25.5 mA cathode current, and approximately 28 kVp. The measured leakage radiation, presented in Table 3.3, was well below the FDA limit, but would need to be repeated at a higher anode voltage for official FDA submission.

Table 3.3 Leakage radiation results. Directions are relative to facing the system from the front, as a patient.

Beam	Approx. cathode current (mA)	Dose rate in front (mR/hr)	Dose rate to the right (mR/hr)	Dose rate behind (mR/hr)
Left-most beam	25.5	0.77	0.49	1.60
Central beam	25.5	0.78	-----	1.98
Right-most beam	25.5	0.76	0.42	1.45

3.3 Other CNT X-ray sources

At UNC there are several other X-ray sources based on CNT cathodes. The systems were built for various applications including microbeam radiation therapy⁷, micro-CT⁸, digital chest tomosynthesis⁹, cell irradiation¹⁰, and radiation therapy image guidance¹¹. There are also systems built by XinRay Systems for airport security and rectangular CT¹².

In 2006, Kawakita et al. presented a sealed, microfocus X-ray source employing arc-discharge MWNTs on a tungsten wire as the cathode. The tube contained three electrostatic focusing lenses and a copper anode. The tube pressure was 5×10^{-7} torr. A current of 1.3 mA was produced with 7 kV, imaging a leaf and showing structures of less than 30 μm in size¹³.

Wang et al., in 2008, presented a sealed cathode ray tube with a screen using a “carbon nanometer electron exit” material on a stainless steel rod as the cathode. The tube also contained gate and focusing electrodes. The pressure was 3×10^{-6} torr. The threshold field was 0.95 V/ μm , and the maximum current density produced was 1.569 A/cm²¹⁴.

Beginning in 2010, a Korean group began developing CNT X-ray sources. A CNT paste optimized with metal fillers was developed and used in screen-printed field emission cathodes¹⁵. Using this cathode, a portable, sealed, and miniature X-ray source was built with a triode configuration. It produced 150 μA , and maintained 10 mA/cm^2 for 12 hours¹⁵. In 2011, they presented a sealed Kovar and ceramic X-ray tube using the same cathode type, of 10 mm, for the s-DBT application¹⁶. The electrode structure was again triode, with a double focusing lens and a molybdenum anode. The cathode was controlled through a high voltage semiconductor switch control, with 2 % fluctuations. Using a 0.3 mm focal spot, a computer mouse was imaged at 30 kVp and 450 V on the gate electrode¹⁶. Using the same CNT paste, a pentode configuration microfocus tube was presented in 2012 with a 2 mm \times 10 mm cathode containing 0.2 mm CNT dots¹⁷. That tube was 71 mm \times 35 mm in size, sealed, and made of Kovar and ceramic. This tube employed the same double focus design as the previous tube, with a 0.3 mm focal spot. The anode was tungsten. Again, a computer mouse was imaged with a 2 s exposure at 30 kV. Current of 100 μA was produced at 400 V gate voltage¹⁷. Another sealed tube using their high temperature brazing process was presented in 2013¹⁸. The tube was 6 mm \times 38 mm in size, and was triode type. The failure mechanism was studied and determined to be current leakage to the gate. This caused charge buildup on the insulator layer and arcing from the gate to the anode. Without gate leakage, the tube could operate for 250 hours at 25 kVp¹⁸.

A sealed, miniature X-ray tube was built in 2012 by Heo et al. The tube measured 10 mm \times 50 mm, with further miniaturization planned. A CNT tip on a tungsten wire was the cathode, with a built-in focusing electrode. The anode had a tungsten-film coating, making it

a diode structure. It operated up to 70 kVp and produced 600 μA , equivalent to 0.123 A/cm^2 . They presented images of a small fish¹⁹.

Also in 2012, Ryu et al. presented a triode-configuration tube using a pumped system consisting of a cathode, gate, focus, and anode to be applied to tomosynthesis. The CNT cathode was elliptical and 2.0 mm \times 0.5 mm in size. A process for making CNT cathodes called resist-assisted patterning was described where MWNTs were grown on silicon, and then attracted together forming cones. Images of a small animal and electronics were produced with 3 s exposures at 50 kV and 0.5 mA current. The transmission rate was 70%²⁰.

In 2013, Chen et al. presented a sealed microfocus tube with a cathode, gate, and anode. The cathode was made of CNT bundles arrayed on a silicon wafer. Each bundle was 0.1 mm \times 0.8 mm and able to produce 2.0 mA, or 2.5 A/cm^2 . The gate was a copper mesh 250 μm above the cathode. The focusing electrode produced a focal spot size of 35 μm \times 39 μm . The anode was copper, covered in tungsten, with a 7° tilt. The tube was able to produce 2 mA cathode current with a TR of 57.5 %, and a gate voltage of 2.7 kV²¹.

REFERENCES

- 1 Calderón-Colón, X. *Fabrication, characterization and integration of carbon nanotube cathodes for field emission x-ray source* PhD thesis, University of North Carolina at Chapel Hill, (2009).
- 2 Qian, C. *et al.* Fabrication of small diameter few-walled carbon nanotubes with enhanced field emission property. *J Nanosci Nanotechnol* **6**, 1346-1349, doi:10.1166/Jnn.2006.140 (2006).
- 3 Sultana, S. *Electron optics simulation for designing carbon nanotube based field emission X-ray source* PhD thesis, University of North Carolina at Chapel Hill, (2010).
- 4 Strudley, C. J., Looney, P. & Young, K. C. Technical evaluation of Hologic Selenia Dimensions digital breast tomosynthesis system (NHS Cancer Screening Programmes, Public Health England, Guildford, England, 2013).
- 5 A Guide to Mammography and Other Breast Imaging Procedures. (National Council on Radiation Protection and Measurements, 2004).
- 6 Improving Breast Imaging Quality Standards. 221 (Institute of Medicine and National Research Council of the National Academies, Washington, DC, 2005).
- 7 Hadsell, M. *et al.* A first generation compact microbeam radiation therapy system based on carbon nanotube X-ray technology. *Appl Phys Lett* **103**, 183505, doi:10.1063/1.4826587 (2013).
- 8 Burk, L. M., Lee, Y. Z., Wait, J. M., Lu, J. & Zhou, O. Z. Non-contact respiration monitoring for in-vivo murine micro computed tomography: characterization and imaging applications. *Phys Med Biol* **57**, 5749-5763, doi:10.1088/0031-9155/57/18/5749 (2012).
- 9 Shan, J. *et al.* in *Medical Imaging 2013: Physics of Medical Imaging*. (eds Robert M. Nishikawa & Bruce R. Whiting) 86680E-86680E-86612 (SPIE).
- 10 Bordelon, D. E. *et al.* A nanotube based electron microbeam cellular irradiator for radiobiology research. *The Review of scientific instruments* **79**, 125102, doi:10.1063/1.3043417 (2008).
- 11 Maltz, J. S. *et al.* Fixed gantry tomosynthesis system for radiation therapy image guidance based on a multiple source x-ray tube with carbon nanotube cathodes. *Med Phys* **36**, 1624-1636, doi:<http://dx.doi.org/10.1118/1.3110067> (2009).

- 12 Gonzales, B. *et al.* in *Medical Imaging 2013: Physics of Medical Imaging*. (eds Robert M. Nishikawa & Bruce R. Whiting) 86685K-86685K-86688 (SPIE).
- 13 Kawakita, K., Hata, K., Sato, H. & Saito, Y. Development of microfocused x-ray source by using carbon nanotube field emitter. *Journal of Vacuum Science & Technology B: Microelectronics and Nanometer Structures* **24**, 950, doi:10.1116/1.2183785 (2006).
- 14 Wang, H. X. *et al.* Fabrication of field-emission cathode ray tube with a unique nanostructure carbon electron emitter. *Journal of Vacuum Science & Technology B: Microelectronics and Nanometer Structures* **26**, 698, doi:10.1116/1.2837853 (2008).
- 15 Kim, D.-J. *et al.* in *Vacuum Electron Sources Conference and Nanocarbon (IVESC), 2010 8th International*. 430-431.
- 16 Choi, S., Jeong, J.-W., Kang, J.-T., Kim, J.-W. & Song, Y.-H. in *Vacuum Nanoelectronics Conference (IVNC), 2011 24th International*. 185-186.
- 17 Jeong, J.-W., Kim, J.-W., Choi, S., Kang, J.-T. & Song, Y.-H. in *Vacuum Electron Sources Conference (IVESC), 2012 IEEE Ninth International*. 93-94.
- 18 Kang, J.-T. *et al.* in *Vacuum Nanoelectronics Conference (IVNC), 2013 26th International*. 1-2.
- 19 Heo, S. H., Kim, H. J., Ha, J. M. & Cho, S. O. A vacuum-sealed miniature X-ray tube based on carbon nanotube field emitters. *Nanoscale Res Lett* **7**, 258, doi:10.1186/1556-276X-7-258 (2012).
- 20 Ryu, J., Kang, J. & Park, K. Carbon Nanotube Electron Emitter for X-ray Imaging. *Materials* **5**, 2353-2359 (2012).
- 21 Chen, Z., Wang, Z., Hu, T., Zeng, Y. & Tang, N. in *Vacuum Electronics Conference (IVEC), 2013 IEEE 14th International*. 1-2.

CHAPTER 4: FABRICATION OF TUNGSTEN METAL GATE MESH

4.1 Introduction

The gate mesh is responsible for creating the electric field that extracts electrons from the CNT cathode. One gate mesh is welded onto the gate frame per cathode. A proper gate mesh allows longer current pulse widths to be produced for X-ray imaging. If the gate mesh breaks due to heat damage, the cathode will no longer emit electrons effectively, and X-ray production would be negatively affected. The gate mesh also impacts the focal spot size and transmission rate of the X-ray tube^{1,2}. The electron beam divergence due to the gate mesh motivated the initial development of the focusing electrodes in the CNT X-ray tubes¹.

4.1.1 Various gate mesh used in CNT X-ray sources

The original gate mesh used in the CNT X-ray tubes, developed at UNC, were made of woven tungsten wires. This mesh was first used in micro-focus X-ray tubes. To reduce focal spot size and improve electric field uniformity, a linear mesh was studied¹. A top-view of the different types are shown in Figure 4.1. The optimal pitch, defined as the center-to-center distance between wires, must limit beam divergence while not lowering transmission rate too much. Simulations showed that a 100 μm pitch is best, and produced the highest possible transmission rate¹. A linear gate mesh produced better spatial resolution than a woven mesh by its ability to create a smaller focal spot size¹.

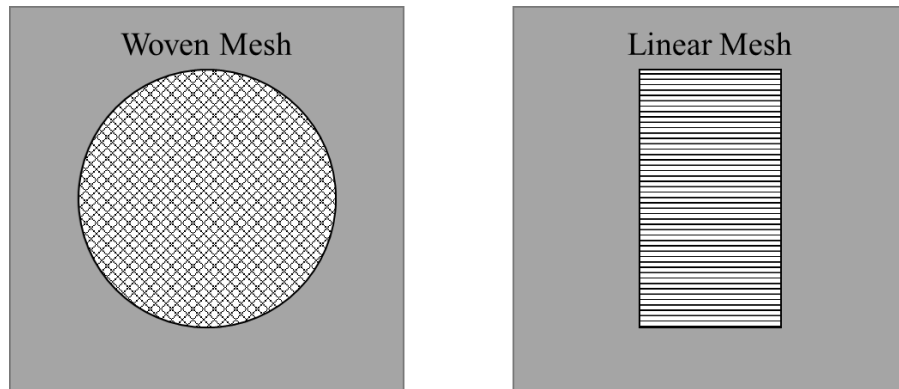


Figure 4.1 Illustration of woven and linear tungsten-wire gate mesh. Adapted with permission from Sultana, 2010.

In her dissertation, Dr. Calderòn-Colòn discussed experiments that determined the effect of the gate mesh on transmission rate and focal spot size². Three types of gate mesh, shown in Figure 4.2, were tested and compared in a micro-focus tube. One was a 2D woven tungsten-wire mesh, one was a molybdenum mesh with circular openings, and one was a tungsten gate mesh fabricated at UNC, the fabrication optimization of which being the topic of this chapter. The linear tungsten mesh created the smallest and most isotropic focal area, and allowed a transmission rate of 67 %².

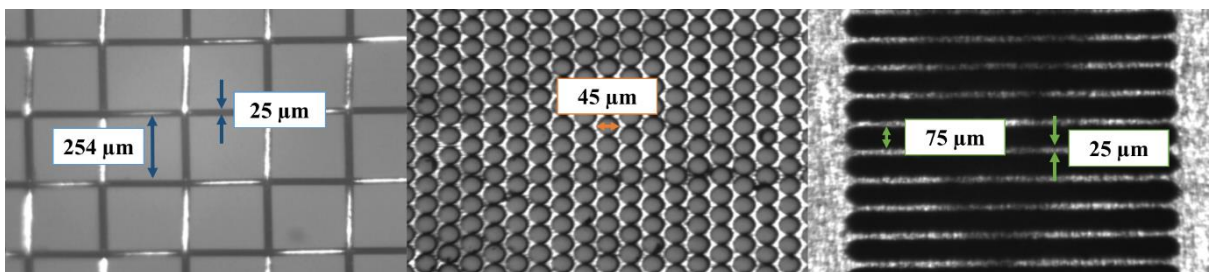


Figure 4.2 Optical microscope images. Left: Woven tungsten mesh. Middle: Molybdenum with a grid of circular openings. Right: Etched, linear tungsten mesh. Images reused with permission of Xiomara Calderòn-Colòn.

The linear tungsten gate mesh studied for the micro-focus tube was inadequate for the s-DBT application due to the high current, and high heat load requirements¹. The woven mesh was unable to withstand a 100 ms pulse, and the typical pulse used in s-DBT is 250 ms. It was necessary to produce a more robust tungsten mesh that could withstand a higher heat load. Simulations to optimize a linear mesh for s-DBT found that transmission rate lowered with less open space and thicker tungsten metal. Results found maximum transmission rate with 100 μm thick tungsten metal, 50 μm wide tungsten bars, and a 250 μm bar pitch¹. Further simulations attempting to reduce the focal spot size of the s-DBT system showed that a decrease in pitch would reduce the focal spot size by making the electric field more uniform. Initially, there was no known way to fabricate or procure such a mesh made of tungsten. Therefore, a stainless steel mesh was attempted as a substitute¹.

For s-DBT, there were many materials and configurations tested for the gate mesh. Figure 4.3 summarizes the options that were considered, some were fabricated at UNC and some were purchased. Attempting to manufacture a gate mesh for s-DBT began with etching silicon, which was found to be too brittle. Then stainless steel mesh was tested for field emission, but shown to have too low of a melting temperature for the s-DBT application. Lastly, a fabrication process for tungsten was attempted when those initial options proved inadequate (X. Calderòn-Colòn 2013, pers. comm., 28 Feb). Both straight bars and curved bars were fabricated on tungsten mesh. Curved bars were preferred because they were shown to not break as easily during field emission testing.

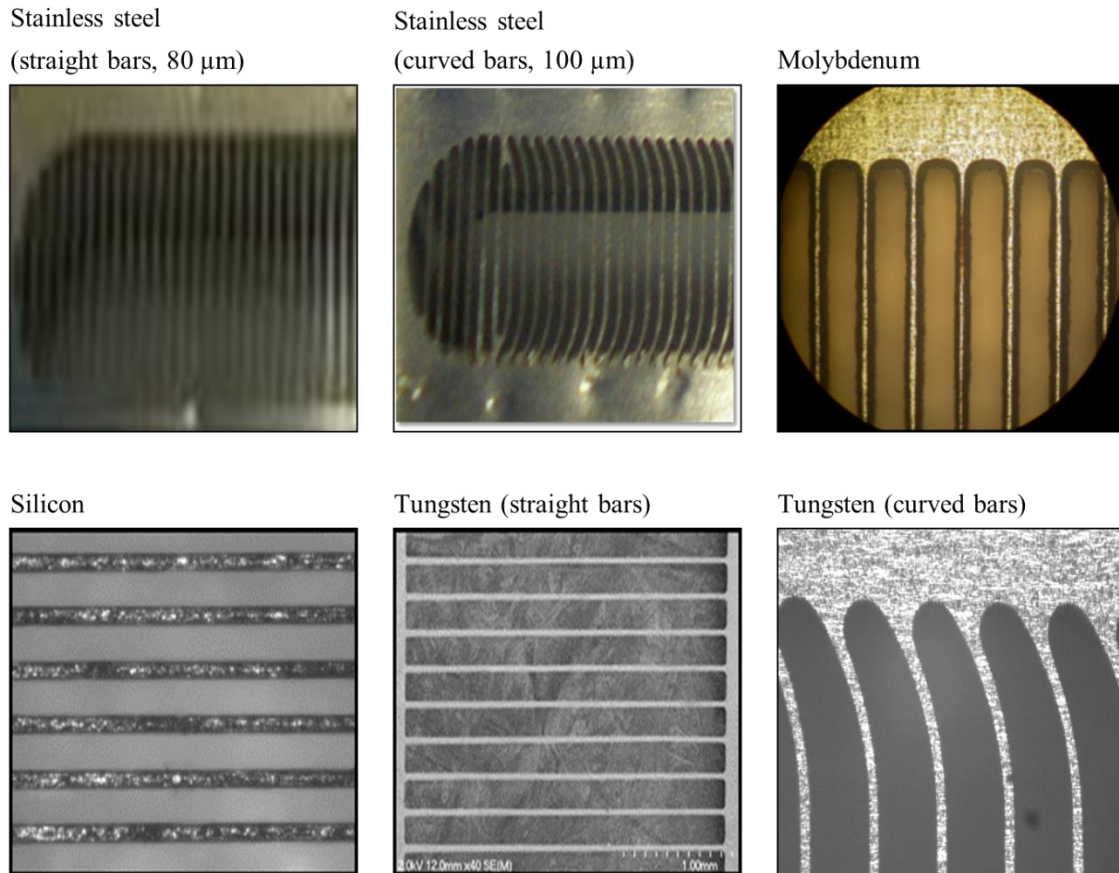


Figure 4.3 Pictures of various gate materials investigated for s-DBT. The silicon and tungsten (straight bars) images were used with permission from Xiomara Calderon-Colon. Stainless steel and molybdenum images are from XinRay Systems.

4.1.2 Deep reactive ion etching

The method chosen to fabricate the tungsten gate mesh was a combination of photolithography and deep reactive ion etching (DRIE) (X. Calderòn-Colòn 2013, pers. comm., 28 Feb), both available in the CHANL facilities at UNC. DRIE is an extension of reactive ion etching (RIE), and both etch materials by bombarding the surface with a plasma of ionized gas particles³. RIE is used to make features with a high aspect ratio, replicate any shape patterned with lithography, and create vertical walls of any shape. Etch rates range from 0.1 μm/min – 1.0 μm/min. DRIE etches deeper and more quickly, even creating

through features, with etch rates ranging from 2 $\mu\text{m}/\text{min}$ – 20 $\mu\text{m}/\text{min}$. Etch rates depend on reactor geometry, RF power scheme, specimen holder temperature, gas flow rate, and device design of the object being etched. Important design parameters include etchable area, feature size, and aspect ratio. DRIE has been shown to produce features with an aspect ratio of up to 40:1, with standard practice producing 20:1³.

There are two main process types for DRIE, cryogenic and Bosch³. Cryogenic etching uses a continuous gas flow of SF_6/O_2 at $-120\text{ }^\circ\text{C}$. Etching is prevented in the horizontal direction by the cold temperature and SiO_xF_z polymer deposits on vertical walls, so that ion bombardment primarily affects horizontal surfaces. The Bosch process, in contrast, is an alternating pulse method. Pulses of SF_6 and C_4F_8 gases are alternated to vertically etch structures by a process beginning with etching, then depositing a protective polymer, and etching again, as shown in Figure 4.4. The protective polymers are known as passivation films. They protect the side walls so that etching continues primarily in the vertical direction, or anisotropically. However, it is possible that the film thickness could get too large creating residues or re-deposition. Re-deposition of the etch product, lithography mask, or passivation film could occur. This could prevent etching of the desired pattern, or make the features smaller by re-depositing material. Over-passivation could cause etching to stop altogether. The Bosch method produces rougher walls. Depending on how the process parameters are regulated this method could also produce retrograde walls, barreling, or trenching. Roughness is a problem because it could lead to cracks, making the object weaker. Roughness can be smoothed by post-etch low-power plasma etching, wet etching, or hydrogen annealing³.

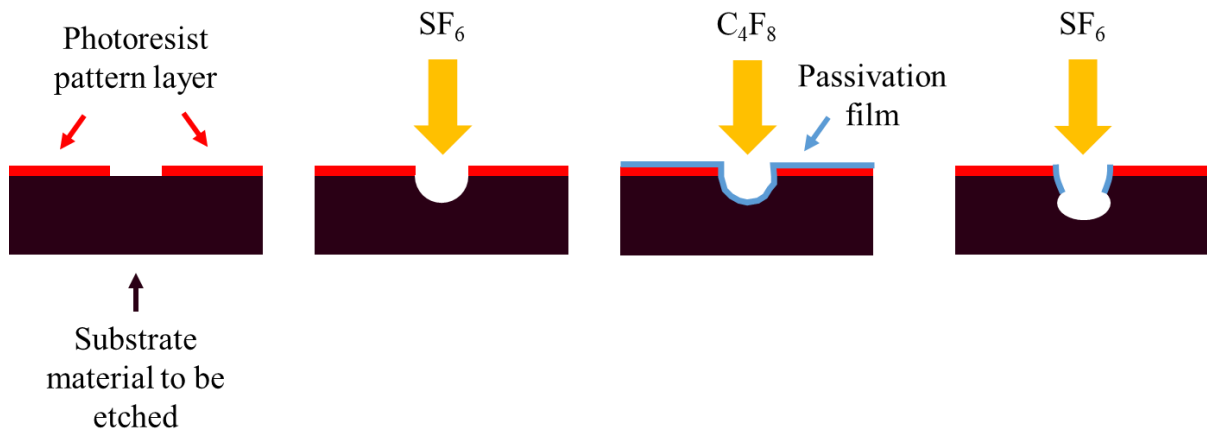


Figure 4.4 Illustration of the Bosch process. Adapted from Fransilla, 2010.

The etch rate, selectivity, and anisotropy of a DRIE process should be maximized³. These are important to etch only the pattern to the desired depth, and prevent lateral etching or undercut. Processes are dependent on the particular reactor being used. Therefore, for each reactor one must determine the optimal gas flow rates, RF power, pressure, stage temperature, and He backing pressure. Typically, etching is done on silicon. The main ions used are fluorine, chlorine, and bromine produced from SF_6 , Cl_2 , and HBr , respectively. SF_6 etches much faster than the other gases and is required for etching to larger depths. These same ions can be used for etching other materials as well³.

4.1.3 Tungsten etching alternatives

For the application of X-ray spectroscopy, tungsten films were etched into $0.2 \mu\text{m}$ period diffraction gratings using RIE⁴. The ideal gas for this application was found to be CBrF_3 ⁴. In 1992, Petri et al. showed that the etching mechanism of tungsten metal films during RIE resulted from the formation and destruction of a low-density reactive top layer⁵. The layer was approximately 5 nm thick and contained fluorine, oxygen, and tungsten atoms. It was amorphous and contained voids. The tungsten atoms in the reactive top layer were

more weakly bound than those remaining in the bulk material⁵. Li et al. studied RIE for etching sputtered tungsten films into metal gates for semiconductor transistors⁶. Lines of 25 nm were stably etched using a combination of SF₆ and N₂ gases, at flow rates of 30 sccm. RF power was 20 W, chamber pressure was 15 mTorr, and the cathode temperature was -12 °C⁶.

Wet etching is another alternative to DRIE for tungsten etching³. Wet etching is very accurate, producing smooth lines compared to DRIE, but is limited in geometry and application due to being a crystal-plane dependent process. It takes longer than DRIE, and is limited in mask material options. Advantages include simultaneous etching from both sides of the material, and being very aggressive for metals³.

Photochemical machining (PCM) is a process similar to that used for producing integrated circuits⁷. It is a type of chemical etching that employs a photoresist stencil⁸, similar to the methods already mentioned. It is typically used to manufacture metal precision parts or decorative metal pieces⁷. A downside to PCM is that it is largely isotropic, and can easily undercut the photoresist mask⁸. However, it is able to etch metal up to 2 mm in thickness. For tungsten, the aqueous etchant used is alkaline potassium ferricyanide⁸.

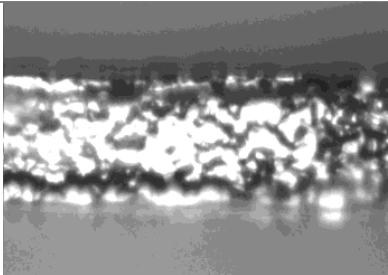
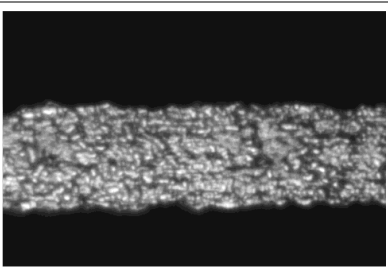
Krauss, Holstein, and Konys developed an electro-chemical machining (ECM) process capable of etching tungsten for the future application of a heat divertor in fusion power systems^{9,10}. It is a method of dissolving tungsten using an electrolyte containing a nitrate salt and ammonia. It can serve to remove microcracks as a surface finisher, or etch 3D structures into bulk tungsten material, up to 1 mm deep. The etching method was improved by using high-frequency current pulses^{9,10}.

4.2 Methods

4.2.1 Determining optimal etch process

It was determined that tungsten etching could be achieved by DRIE with either chlorine or fluorine gases (X. Calderòn-Colòn 2013, pers. comm., 28 Feb). Various combinations of gases were evaluated for etching. The chemistries evaluated were: SF₆, SF₆ + Cl₂, SF₆ + He, NF₃, NF₃ + Cl₂, CF₄ + Cl₂, CF₄ + O₂, SF₆ + C₄F₈ + O₂, and SF₆ + Ar. The temperature was also tested at 0 °C, 40 °C, and 45 °C. Lower temperatures promote anisotropy, preventing undercut, whereas higher temperatures improve selectivity. At higher temperatures, tungsten etches more quickly than silicon dioxide. The two fabrication methods that were initially most successful are summarized in Table 4.1. It was found that Method 2 was most effective for producing the gate mesh (X. Calderòn-Colòn 2013, pers. comm., 28 Feb), and therefore was the starting point for the s-DBT mesh fabrication.

Table 4.1 Initial method parameters and results used by Xiomara Calderòn-Colòn for etching tungsten gate mesh.

Parameter	Method 1	Method 2
Tungsten foil thickness	50 µm	50 µm
Photolithography (adhesion promoter / photoresist)	Omnicoat / SU-8 2010	MCC Primer 02/20 / KMPR 1010
Gases	SF ₆ + C ₄ F ₈ + O ₂	SF ₆ + Ar
RF power	1200 Watts	1200 Watts
Temperature	0 °C	0 °C
Etch rate	1.4 µm/min	~1.43 µm/min
Optical microscope image, 50x magnification (used with permission of Xiomara Calderòn-Colòn)		

4.2.2 Complete procedure for tungsten gate mesh fabrication

Tungsten metal preparation

First, the tungsten metal sheets were cut into the appropriate size for the photomask being used. For s-DBT, the tungsten foil was 50 μm thick and cut into 1" \times 2.5" rectangles.

After the tungsten was cut into the desired shape, they had to be cleaned. They were wiped with a lint free cloth to remove excess dirt. This was followed by three sonication baths, each lasting 15 min. The first bath was methyl alcohol, the second was acetone, and the third bath isopropyl alcohol. After the last sonication bath was complete, each piece was rinsed with deionized water.

Following the water rinse, each piece was blown dry with nitrogen, and laid to dry on a hot plate for 5 min. The hot plate was set to 100 $^{\circ}\text{C}$. After initial preparation, all work was completed in the CHANL clean room facility.

Spin coating

Spin coating was used to apply the adhesion promoter and photoresist layers onto the cleaned tungsten metal. Prior to spin coating it was necessary to flatten the cut pieces as much as possible, ensuring the metal would be evenly coated. The adhesion promoter used was MCC Primer 80/20 (MicroChem Corp., Newton, MA). It was applied to the metal with a pipette, then spun on at 3000 rpm for 30 s. After being coated with the adhesion promoter, the metal was immediately transferred to a hot plate set at 100 $^{\circ}\text{C}$, and baked for 1 min.

After baking, the metal pieces were then, one by one, put back onto the spin coater and coated with the photoresist. The photoresist was KMPR 1010 (MicroChem Corp., Newton, MA). It is important that no bubbles were introduced to the photoresist as it was applied to the metal surface before spin coating. The tungsten metal, once coated with the

photoresist, was spun for 5 s at 500 rpm, then 30 s at 1000 rpm. The pieces were again immediately placed on the hot plate, at same temperature, for 12 min. They were cooled to room temperature before photolithography was performed.

Photolithography

Photolithography is used to cure the photoresist according to the photomask used. The photomask design depends on whether one uses a positive photoresist or a negative photoresist. A negative photoresist will develop in the pattern that was exposed to the UV light, and a positive photoresist will develop in the pattern that was covered from UV light by the mask design⁸. KMPR 1010, used here, is a negative photoresist. The photomask was clear except for the spacing pattern in between the bars. After exposure, the bar pattern portion of the photoresist was developed, and the photoresist in between the bars could be removed.

The photomask was taped to a glass plate that was loaded into the mask aligner, Karl Suss MA6/BA6 (SUSS MicroTec Lithography GmbH, Garching, Germany). After the metal piece was aligned under the photomask, it was exposed by UV light. The settings used were: 100 μm alignment gap, hard contact, and 40 s exposure time. After exposure, the metal pieces were immediately placed on the hot plate set to 100 °C for 2 min, during which they should be observed. If the pattern becomes visible before 1 min has passed, it is indicative of overexposure.

After heating, the photoresist was developed in SU-8 developer by submersion for 2 min. The pieces were then rinsed with isopropyl alcohol. The submersion and rinse procedure must be repeated until, upon rinsing, the pattern does not appear white. Next, the pieces were rinsed with deionized water and dried with nitrogen gas.

At this point, some of the photoresist film thicknesses were measured with use of a KLA Tencor P-6 stylus profiler (KLA-Tencor Corporation, San Jose, CA) for quality assessment. It was found that the procedure produced films ranging from 22 μm – 23 μm in thickness. Uniformity across the surface was $\pm 1 \mu\text{m}$.

DRIE

The DRIE system was an Alcatel AMS 100 Deep Reactive Ion Etcher (Alcatel Micro Machining Systems, Annecy, France) with which the Bosch process was employed for etching the tungsten metal. The tungsten metal foil used was from Alfa Aesar (Ward Hill, MA). The purchased foil was 50 μm thick, but was measured at 63 μm before etching. There was a choice of two photomasks for s-DBT. One photomask had 60 μm bars, and one had 75 μm bars. Although DRIE is very anisotropic, the 75 μm bar pattern was used to produce 50 μm bars, because some lateral etching is unavoidable.

Before etching the tungsten metal, the reactor was cleaned with a seasoning process. This process removes etch products from any previous etching procedures, preventing any negative effects to the tungsten etching procedure. The seasoning procedure was done with a 6" silicon wafer in O_2 for at least 30 min.

The tungsten pieces were set onto an aluminum wafer for etching. Several pieces could be etched at once, and up to three pieces have been etched successfully at the same time. After ensuring that the metal is as flat as possible, thermal paste was sparingly placed on the four corners of the underside of the tungsten metal pieces. The amount of paste needed was just enough to ensure the corners of the metal would be held down under vacuum. After paste was applied, the pieces were pressed onto the aluminum wafer. Care was taken to ensure that the pieces did not touch one another, but were as close to the center of the wafer

as possible. To help guarantee all pieces were flattened, they could be pressed with another aluminum wafer or the wooden end of a long Q-tip. At this point, the wafer was loaded into the reactor.

Table 4.2 summarizes the optimized process parameters determined for etching the s-DBT tube’s tungsten gate mesh. Two gases were employed for the Bosch process, SF₆ and Ar. The etching pulse lasted 30 ms. Source generator power was 1200 W to maintain reasonable etching rates. The temperature was 0 °C, which was intended to help prevent photoresist burn off, but it does lower the etch rate. Maintaining higher etch rates is important to minimize lateral etching.

Table 4.2 Table summarizing the process parameters used for DRIE of tungsten gate mesh for the s-DBT X-ray tube.

DRIE process parameter	Value
SF ₆ flow rate	200 sccm
Ar flow rate	200 sccm
Pressure	4.5×10^{-3} mbar
He backing pressure	10 mbar
Source generator power	1200 W
Substrate bias high power	75 W
High power pulse on time	30 ms
Substrate bias low power	0 W
Low power pulse on time	70 ms
Position from source	150 mm
Etching time	5 min
Rest time	2 min
Temperature	0 °C

The etching step time, in Table 4.2, is 5 min. The etching was not done all at once, to prevent overheating. It is important not to over-etch the sample, discontinuing to etch once the bars have been fully “cut out”. To prevent this, the etching time interval was decreased as etching progressed. After each etching session, the substrate holder was removed and the

metal observed. Depending on the etching progress and user discretion, another 5 min step could be used or the step time could be lowered anywhere from 3 min to 30 s. After etching was complete, the aluminum wafer was removed from the deep reactive ion etcher.

Post-etch processing

The tungsten metal pieces were carefully removed from the aluminum wafer with tweezers while being careful not to break the delicate, etched bars. Any thermal paste remaining on the metal was wiped off with a lint free cloth and deionized water. Remaining photoresist on the metal was removed with N-Methylpyrrolidinone (NMP) (Thermo Fisher Scientific Inc., Waltham, MA). The tungsten was placed in NMP on a hot plate set to 100 °C. After the photoresist came off, the etched tungsten was rinsed with deionized water.

The complete tungsten metal cleaning procedure, described in the “*Tungsten metal preparation*” section above, was repeated. Following cleaning, all etched pieces were annealed in a vacuum furnace for 3 hr at 500 °C. All etched tungsten was stored in a vacuum desiccator until used.

4.3 Results

Two main parameters were important in optimizing gate mesh fabrication: power and thermal paste configuration. Mesh were fabricated at both 1000 W and 1200 W. Thermal paste was used along all four sides in large amounts or only in small amounts on the four corners of the tungsten pieces. Large amounts of thermal paste led to photoresist damage before etching was complete. In addition, 1200 W gave better results by increasing the etch rate, allowing etching to complete before the photoresist was damaged. The summary for all combinations of thermal paste configuration and power setting experiments is presented in Table 4.3. The table shows that, in addition to mesh for the s-DBT system, gate mesh were

also etched for the microbeam radiation therapy (MRT) system. The only settings producing successfully etched mesh were 1200 W and small amounts of paste on the corners (Figure 4.5). The average etch rate for the 1000 W experiments was $1.1 \pm 0.5 \mu\text{m}/\text{min}$. The average etch rate for the 1200 W experiments was $2.3 \pm 0.9 \mu\text{m}/\text{min}$. There were no successfully etched samples when all sides of the samples were covered with thermal paste. However, not 100 % of the 1200 W, corner-pasted samples were successful. The stability of the photoresist during etching also dependd on how well the photoresist was developed, and how uniform the photoresist pattern is. Factors surrounding the patterning of the photoresist are likely to blame for those unsuccessful samples. Figure 4.6 compares the appearances of a successful etch to one that was unsuccessful due to photoresist damage.

Table 4.3 Etch rates for tungsten gate mesh fabricated by DRIE.

Application	Tungsten foil thickness (μm)	Power (W)	Thermal paste configuration	Sample size	Success	Etch rate ($\mu\text{m}/\text{min}$)
s-DBT	63	1000	All sides	3	No	0.9 ± 0.3
		1200	All sides	8	No	1.0 ± 0.2
		1000	Corners only	1	Yes	1.7
		1200	Corners only	4	No	3.1 ± 0.1
				8	Yes	2.9 ± 0.6
MRT	56	1200	Corners only	3	No	3.0 ± 0.2
				8	Yes	2.4 ± 0.2

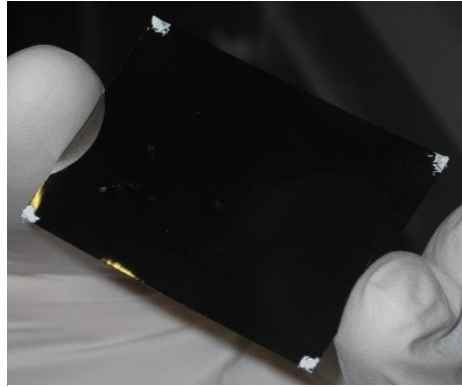


Figure 4.5 Photograph of the corner paste configuration that allowed for successful mesh etching.

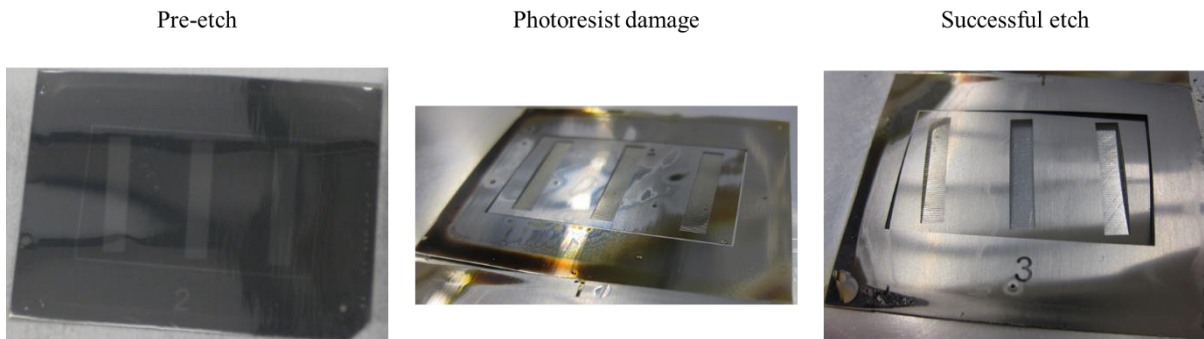


Figure 4.6 Photographs comparing the appearances between a failed sample, due to photoresist damage, to a successful one. There was some photoresist damage even on the successful sample, but it did not reach the critical area containing the tungsten bars. The top of the left-most mesh in the successful etch example was not fully etched, but the other two were.

In addition to etching successfully without photoresist damage, it was important to measure etching quality. This was quantified through bar width uniformity and size relative to the desired thickness of $50\ \mu\text{m}$. The width measurements were taken across each etched sample, including multiple mesh for the s-DBT application, as pictured in Figure 4.6. A summary of all measurements are presented in Table 4.4. The pitch was calculated by the summation of the bar width and space width. The desired space width was $200\ \mu\text{m}$, and therefore the desired pitch was $250\ \mu\text{m}$.

Table 4.4 Data summary of measurements collected on etched mesh's bar widths and space widths. Pitch was calculated by the sum of bar and space widths.

System	Sample number	Fabrication settings	Bar width (μm)	Space width (μm)	Pitch (μm)
s-DBT	1	1000 W, paste - all sides	40 ± 14		
	2	1200 W, paste - all sides	60 ± 11	206 ± 15	255.6 ± 0.5
	3	1200 W, paste - corners*	32 ± 6	216 ± 7	248 ± 2
	4	1200 W, paste - corners*	54 ± 4	194 ± 4	248 ± 3
MRT	1	1200 W, paste - corners	44 ± 8	206 ± 6	250 ± 2
	2	1200 W, paste - corners	26 ± 11	224 ± 12	250 ± 1
	3	1200 W, paste - corners	56.0 ± 0.9	195 ± 3	251 ± 2
	4	1200 W, paste - corners	36.5 ± 0.4	215 ± 4	252 ± 4
	5	1200 W, paste - corners	46 ± 5	202 ± 7	248 ± 2
Average			45 ± 13	206 ± 12	249 ± 3

* Photoresist not removed

Bar width uniformity is indicated by the standard deviations of the measurements. The average bar width was $45 \mu\text{m}$ with a standard deviation of $13 \mu\text{m}$. On average the desired bar width was achieved, but the uniformity was low. Bar width uniformity within a single mesh ranged from $1 \mu\text{m} - 10 \mu\text{m}$. Not all etched mesh were measured for bar width uniformity and accuracy. Figure 4.7 presents optical microscope images of MRT mesh samples, with the images of Sample 2 highlighting the non-uniformity issue. Two of the s-DBT mesh had not had photoresist removed, as indicated with asterisks in Table 4.4. It is possible that this could have changed the results, making the bars appear thicker. The reason for the non-uniformity is unknown. It is likely caused by non-uniform sample heating which would be affected by sample flatness, photoresist thickness, paste configuration, and fabrication settings. However, the pitch calculations were uniform and accurate. The pitch is very important for field uniformity. The mesh with thinner bars thinner would still function well in providing uniform electric fields, but would suffer from heating and likely break more easily than mesh with thicker bars.

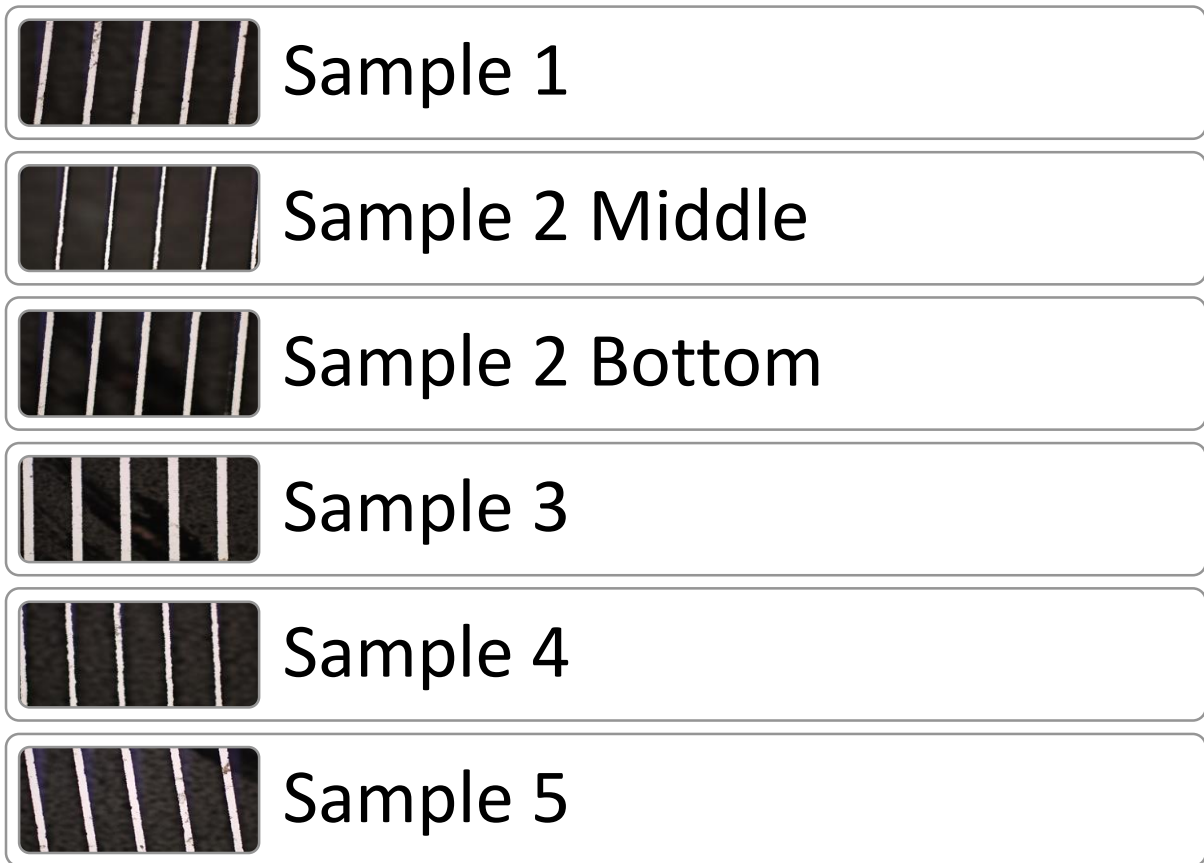


Figure 4.7 10x magnification optical microscope images of tungsten gate mesh corresponding to the MRT sample data presented in Table 4.4.

4.4 Discussion

The longer etching takes, undesired lateral etching and the chance of ruining the photoresist increases. Higher etch rates are preferred for this reason. Increasing etch rates is achieved by increasing RF power or substrate temperature. However, a lower temperature was used to protect the photoresist. There is a tradeoff between optimizing substrate temperature for fast etching and optimizing for photoresist protection. Proof of lateral etching is in the average measured bar thickness. It was $45 \pm 13 \mu\text{m}$, whereas the photomask had $75 \mu\text{m}$ bars.

There were many issues that had to be addressed during the fabrication of the tungsten gate mesh for the s-DBT system. One major issue was the photoresist damage during etching. The photoresist would begin to liftoff and then be removed altogether. Photoresist damage was prevented by optimizing the thermal paste configuration and ensuring that the tungsten metal remained flat on the aluminum wafer during etching. Too much thermal paste underneath the sample prevented etching of the tungsten while allowing time for the photoresist to sustain damage. More thermal paste was also ineffective in keeping the tungsten metal edges flat onto the aluminum wafer. The best distribution was a small amount of paste on all four corners. It was necessary that the metal be flat so that it was not necessary to use the paste to keep the metal flat on the wafer surface. If the metal was not flat, the edges that lifted up would burn, allowing damage to quickly spread across the sample.

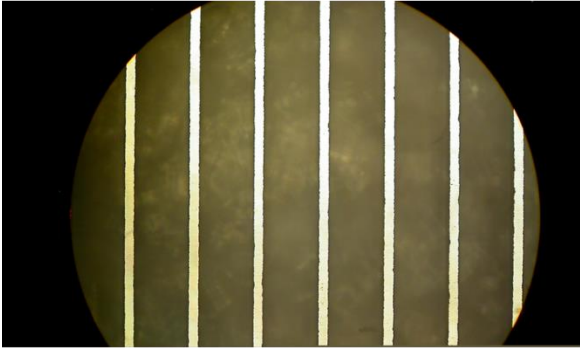
The flatness of the metal sample was necessary to not only help protect photoresist but also to help ensure bar uniformity. Bar uniformity was a constant issue in the fabrication procedure. Even successfully etched pieces suffered from low uniformity. If the tungsten metal was not flat during etching, the raised portions would heat more quickly than those in contact with the aluminum wafer. This led to edges suffering photoresist liftoff and non-uniform etching. One portion of the mesh would etch before the others and also etch more quickly. Therefore, to etch the whole sample, the bars that began to etch first would become over-etched due to lateral etching. Uniformity is improved through ensuring uniform spin coating, which required 1000 rpm even though the photoresist layer was slightly thinner than with lower rpm settings.

4.5 Conclusion

After optimization of the process parameters and fabrication methods, a reproducible technique for etching tungsten metal was developed using DRIE. The original types of gate mesh used in the CNT X-ray sources were unable to withstand a pulse width of 100 ms. Mesh fabricated by Dr. Xiomara Calderòn-Colòn were shown to have favorable performance with pulse widths of up to 228 ms at 45 mA cathode current (X. Calderòn-Colòn 2013, pers. comm., 28 Feb). This method, based on the initial work of Dr. Calderòn-Colòn, produced gate mesh that were able to withstand pulse widths of 4 s. A set of 31 individual gate mesh were welded onto a gate frame and installed in the first Argus 3.0 s-DBT X-ray tube.

The development of fabrication method was an important step in allowing the CNT X-ray technology to advance toward clinical use as part of the s-DBT system. After development of this method, mesh were purchased from Elcon Precision LLC (San Jose, CA), fabricated with a chemical wet etching method. Figure 4.8 shows that the wet-etched mesh is smoother than the DRIE mesh. A smoother surface increases the strength of the mesh, and likely leads to longer lifetime in an X-ray tube. The roughness of the DRIE mesh is worse on one side than the other because the DRIE method is a one-sided method, whereas chemical wet etching is a double-sided method. Therefore, when using the DRIE mesh it is important to place the rougher side nearer to the anode to ensure better field uniformity (X. Calderòn-Colòn 2013, pers. comm., 28 Feb). The chemical wet-etched mesh were used in the second Argus 3.0 s-DBT tube, built to be used in a clinical trial.

DRIE mesh



Wet-etched
mesh

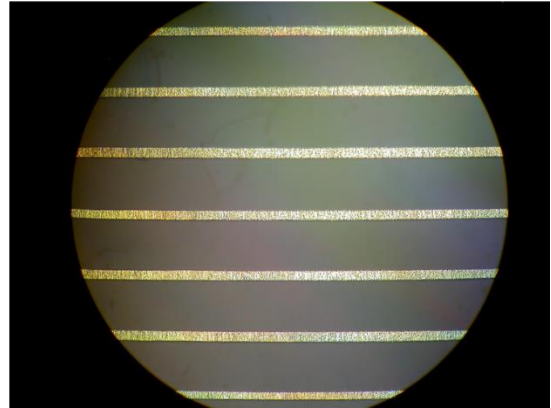


Figure 4.8 Optical microscope images comparing the surface roughness of DRIE mesh and wet-etched mesh. Images taken by Derrek Spronk.

REFERENCES

- 1 Sultana, S. *Electron optics simulation for designing carbon nanotube based field emission X-ray source* PhD thesis, University of North Carolina at Chapel Hill, (2010).
- 2 Calderón-Colón, X. *Fabrication, characterization and integration of carbon nanotube cathodes for field emission x-ray source* PhD thesis, University of North Carolina at Chapel Hill, (2009).
- 3 Franssila, S. *Deep Reactive Ion Etching, in Introduction to Microfabrication*. Second edn, (John Wiley & Sons, Ltd, 2010).
- 4 Schattenburg, M. L. Reactive-ion etching of 0.2 μm period gratings in tungsten and molybdenum using CBrF_3 . *Journal of Vacuum Science & Technology B: Microelectronics and Nanometer Structures* **3**, 272, doi:10.1116/1.583244 (1985).
- 5 Petri, R., Henry, D. & Sadeghi, N. Tungsten etching mechanisms in low-pressure SF_6 plasma. *Journal of Applied Physics* **72**, 2644, doi:10.1063/1.351565 (1992).
- 6 Li, X. *et al.* A low damage RIE process for the fabrication of compound semiconductor based transistors with sub-100nm tungsten gates. *Microelectronic Engineering* **83**, 1159-1162, doi:10.1016/j.mee.2006.01.074 (2006).
- 7 Roy, R., Allen, D. & Zamora, O. Cost of photochemical machining. *Journal of Materials Processing Technology* **149**, 460-465, doi:10.1016/j.jmatprotec.2004.01.059 (2004).
- 8 Allen, D. M. Photochemical Machining: from ‘manufacturing's best kept secret’ to a \$6 billion per annum, rapid manufacturing process. *CIRP Annals - Manufacturing Technology* **53**, 559-572, doi:10.1016/s0007-8506(07)60029-8 (2004).
- 9 Krauss, W., Holstein, N. & Konys, J. Strategies in electro-chemical machining of tungsten for divertor application. *Fusion Engineering and Design* **82**, 1799-1805, doi:10.1016/j.fusengdes.2007.06.029 (2007).
- 10 Holstein, N., Krauss, W. & Konys, J. Development of novel tungsten processing technologies for electro-chemical machining (ECM) of plasma facing components. *Fusion Engineering and Design* **86**, 1611-1615, doi:10.1016/j.fusengdes.2010.11.003 (2011).

CHAPTER 5: INITIAL PERFORMANCE OF CNT X-RAY SOURCE FOR STATIONARY DIGITAL BREAST TOMOSYNTHESIS

5.1 Argus 3.0 performance characterization

The CNT X-ray tube described in Chapter 3 underwent initial characterization of anode heat capacity, current performance of the CNT cathodes, focal spot sizes, spatial resolution, and phantom imaging. Most of the data and analysis in this section was published in Medical Physics by Qian et al. in a journal article titled “High resolution stationary digital breast tomosynthesis using distributed carbon nanotube x-ray source array”¹.

5.1.1 Anode heat capacity

During tube operation it is important that the anode temperature stays below 80 % of its melting temperature, which for tungsten is 3,695 K. A conventional mammography X-ray tube typically produces 100 mA – 200 mA tube current (anode current) and runs at an anode voltage of approximately 30 kVp. Peak power on the anode ranges between 3 kW – 6 kW. In Argus 3.0 power is distributed on the stationary tungsten anodes over the focal spot area of each cathode-anode pair. To determine the power limit of the s-DBT tungsten anodes, finite element simulations were carried out by Jing Shan using ANSYS. The anode temperature was calculated by solving the heat equation:

$$\rho c_p \frac{\partial T(\vec{x}, t)}{\partial t} = (P_{in} - P_{rad}) \cdot t - \nabla \cdot (k \nabla T(\vec{x}, t))$$

where c_p and k , respectively, are the temperature dependent heat capacity and thermal conductivity. P_{in} is the input power and P_{rad} is the output power due to blackbody radiation².

Temperature distribution on the whole anode structure was simulated for the targeted focal spot size. Power density was distributed on the anode as a Gaussian function according to the measured full width at half maximum (FWHM) of the focal spot size², in this case 0.6 mm × 0.6 mm.

As can be seen in Figure 5.1, at 28 mA anode current with a 250 ms pulse width, the temperature remained in the safe range, below 80 % of the melting temperature (T_m). The insert shows that the temperature drops off quickly, traveling out from the center of the focal spot. Transient temperatures drop quickly back to the base value after the exposure. The anode's transient temperature rises with increasing tube power, and exceeds T_m at 38 mA and 38 kVp. To operate safely at 38 mA anode current, the anode voltage needs to be reduced to approximately 28 kVp. The anode temperature is reduced to 2,811K at 38 mA, 28 kVp, the same as for the 28 mA, 38 kVp case. The combinations of 28 mA / 250 ms and 38 mA / 183 ms were selected for the simulation because each provides the necessary dose for a projection view assuming 100 mAs per tomosynthesis scan, with 15 projection views. The simulations confirm that the anodes of the s-DBT tube would be able to withstand the power requirements of breast tomosynthesis imaging.

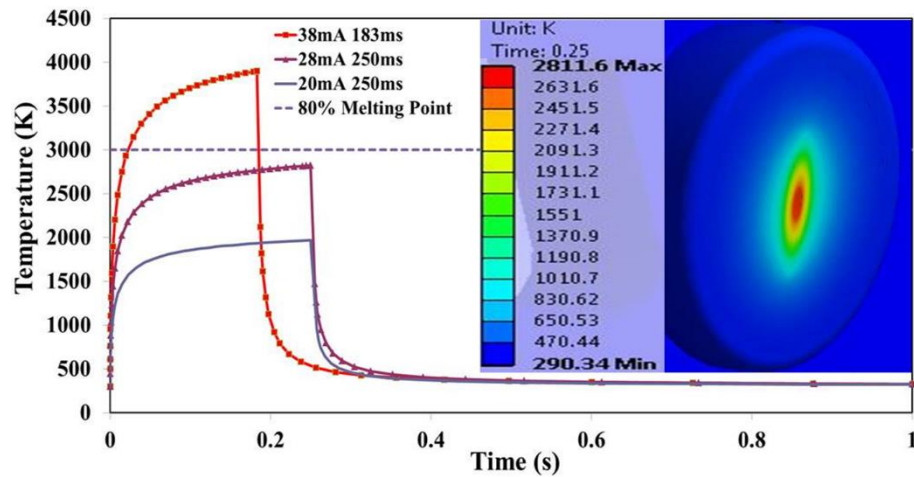


Figure 5.1 Temperature simulation results at the center of the s-DBT tungsten anode during one X-ray pulse. The settings are for various anode currents and pulse widths, all at 38 kV anode voltage. The insert is an image of the simulated anode showing the temperature distribution at the end of a pulse with settings of: 250 ms, 28 mA anode current, and 38 kV anode voltage. Reprinted with permission from Qian et al., *Med. Phys.*, 39, 2094, (2012). Copyright 2012, American Association of Physicists in Medicine.

5.1.2 Current characteristics of CNT cathodes

Emission current of the cathodes was evaluated at the anticipated operating conditions, before the X-ray tube was manufactured, using a test module that housed three X-ray sources. The test module had a similar structure to the s-DBT tube. Each source consisted of a CNT cathode, an extraction gate, focusing lenses, and a tungsten anode. Accelerated lifetime measurements were performed with pulse widths of 250 ms and 183 ms, and various duty cycles. Anode voltage was held at 35 kVp. During measurements the electric field was automatically adjusted to maintain constant cathode current.

Figure 5.2 shows the stability of the CNT cathode under the two different conditions. The first condition of 27 mA anode current, 250 ms pulse width, and 5 % duty cycle showed

no degradation over 8,000 min, equivalent to 400 min of beam-on time or ~100,000 tomosynthesis scans. The second test was performed at 38 mA anode current, 183 ms pulse width, and 0.6 % duty cycle. In this case, the focal spot size was larger than 0.6 mm × 0.6 mm. During approximately 5,000 min of measurement, the extraction voltage increased approximately 8 V per 1,000 tomosynthesis scans. These two current settings were selected for the long-term stability test because each pulse provided the dose required for one projection view of a 15-view, 100 mAs tomosynthesis scan.

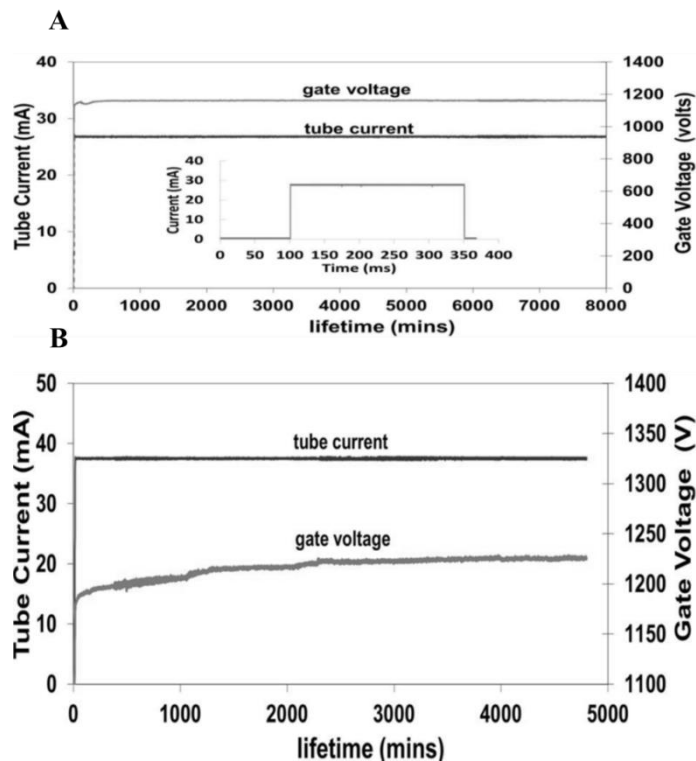


Figure 5.2 Accelerated lifetime test data using a testing module, simulating the electrode configuration of the s-DBT X-ray tube. (A) 27 mA anode current, 250 ms pulse width, 5 % duty cycle. Inset: Shows an example cathode current pulse. (B) 38 mA anode current, 183 ms pulse width, 0.6 % duty cycle. Reprinted with permission from Qian et al., *Med. Phys.*, 39, 2095, (2012). Copyright 2012, American Association of Physicists in Medicine.

The accelerated lifetime tests indicated that the CNT cathodes to be used in the s-DBT tube would be able to produce the required current needed for breast imaging. Over the

time period tested the degradation of cathode performance was negligible, indicating that many more pulses than tested in Figure 5.2 could be produced by the finished s-DBT tube.

The cathode-gate voltages of all 31 CNT cathodes required to produce 43 mA were measured in February 2011 of the sealed, completed s-DBT X-ray tube. Assuming a transmission rate of 63 %, the tube current would be 27 mA. The average cathode currents produced from all 31 beams was 42.6 ± 0.4 mA. The average voltage to produce that current was 1553 ± 144 V. The data is shown in Figure 5.3, with the units of the vertical axis –V to indicate that the cathode was held at a negative potential relative to the gate electrode. The beam with the highest voltage was Number 9 at 1954 V, and the beam with the lowest voltage was Number -14 at 1351 V. The standard deviation of all beams was 144 V, but the difference between the maximum and minimum voltages was 603 V. The numbering of the cathodes is according to position relative to the center of the X-ray tube when facing it from a patient's perspective. The leftmost cathode is labeled negative 15, or N15, and the rightmost cathode is labeled positive 15, or P15, corresponding to the numbering in Figure 5.3.

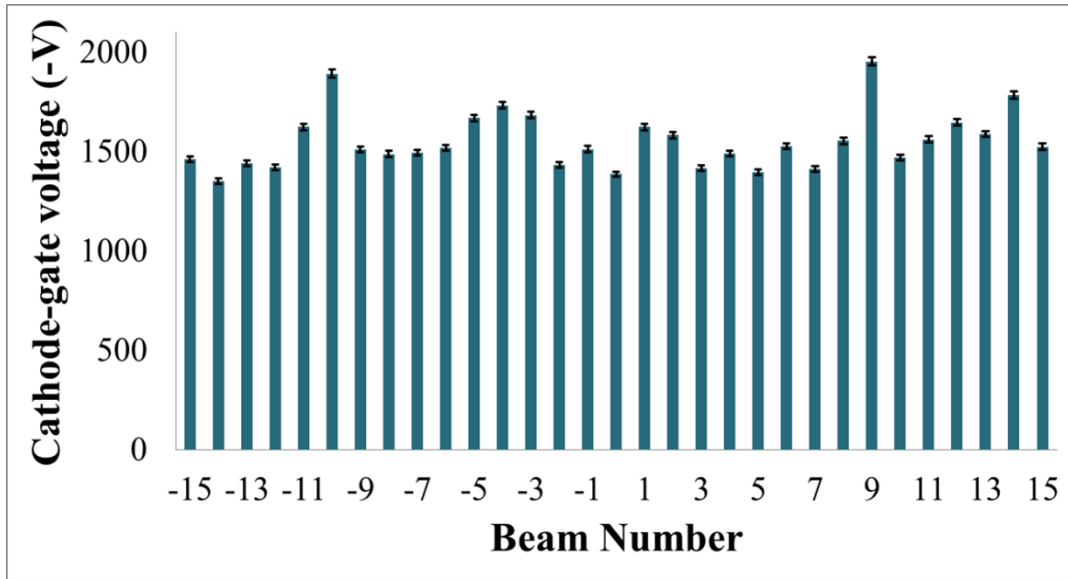


Figure 5.3 Cathode-gate voltages required to produce an average of 42.6 ± 0.4 mA for the 31 CNT cathodes in the s-DBT X-ray tube. Reprinted with permission from Qian et al., *Med. Phys.*, 39, 2096, (2012). Copyright 2012, American Association of Physicists in Medicine.

5.1.3 Focal spot sizes

The effective focal spot sizes of the X-ray sources were measured following the IEC standard³ using a gold-platinum pinhole phantom, which is 100 μm in diameter, 500 μm in length, and has a 12° opening angle. The electrical potentials applied to the two focusing electrodes were those needed to obtain the minimum focal spot size. The same focusing voltages were used for all 31 sources. The measurement was performed at 35 kV anode voltage for all 31 sources, and Figure 5.4 shows the measured focal spot sizes. The average focal spot size was 0.64 ± 0.04 mm \times 0.61 ± 0.05 mm, width \times length, at FWHM. Width direction is defined as being parallel to the X-ray source array orientation, or scanning direction. Maximum focal spot dimension in both width and length was approximately 0.7 mm, and the smallest dimension was approximately 0.5 mm.

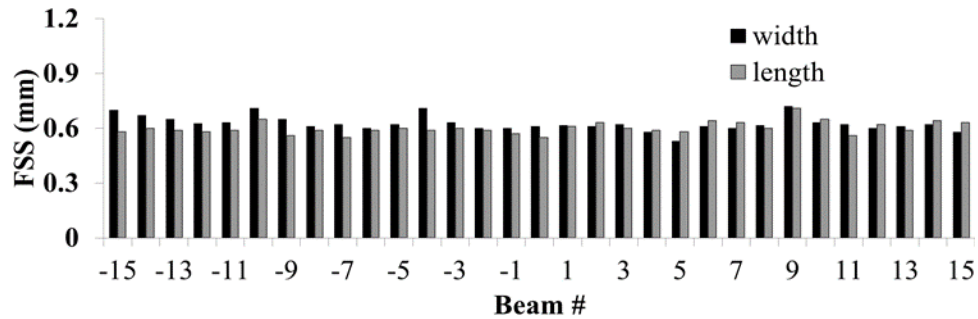


Figure 5.4 Results of focal spot size measurements using focusing settings to achieve the smallest focal spot sizes. Reprinted with permission from Qian et al., *Med. Phys.*, 39, 2096, (2012). Copyright 2012, American Association of Physicists in Medicine.

For comparison, nominal mammography focal spot sizes are either 0.3 mm or 0.1 mm, depending on the exam being performed. A nominal focal spot size corresponds to an allowed range, according to regulations. The 0.1 mm focal spot size can be up to 0.15 mm in width or length. The 0.3 mm focal spot size can be up to 0.45 mm in width and up to 0.65 mm in length⁴. The average focal spot size on the s-DBT tube would be a nominal size of 0.60 mm because the width is just over that allowed for the 0.40 mm size.

5.1.4 Spatial resolution

The modulation transfer function (MTF) of the s-DBT scanner was measured with a 50 μm diameter tungsten wire. The phantom was mounted on the compression paddle of the Hologic scanner. The wire was at a 2° angle relative to the detector edge, allowing oversampling of the line spread function⁵. The detector was operated in 2×2 binning mode with 140 μm pixel size. Images were taken at 28 kV anode voltage and 6.67 mAs/view. Fifteen projection images of the wire phantom were taken over 14° , with a magnification factor of 1.08x.

Figure 5.5 shows the measured MTF from source N07, 000 (central source), and P07. For comparison, the corresponding projection MTFs from the Hologic Selenia Dimensions

rotating gantry system were measured at viewing angles of -7° , 0° , and 7° . The spatial resolution for the rotating gantry system, measured by 10 % MTF, was 4 cycles/mm along the scanning direction and 5.4 cycles/mm perpendicular to the scanning direction. For the s-DBT system, the measured 10 % MTF for the central source was 5.1 cycles/mm along the scanning direction and 5.2 cycles/mm perpendicular to the scanning direction. The MTF degraded slightly for the off-center X-ray beams. For example, beams N07 and P07 had a 10 % MTF of 5 cycles/mm along the scanning direction. The small variation in MTF for different X-ray beams can be attributed to the oblique angle of the X-ray beam on the detector⁶.

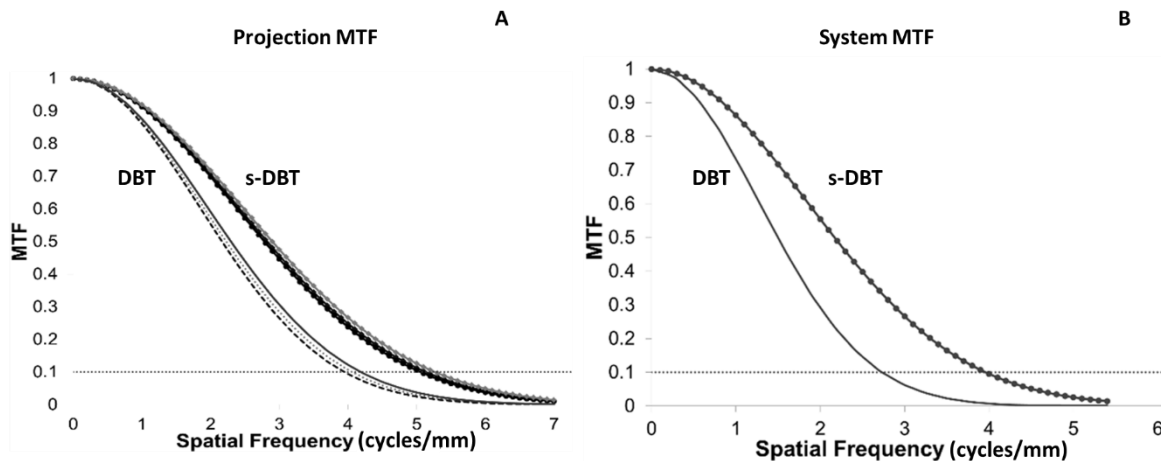


Figure 5.5 (A) The projection MTFs of the stationary and rotating gantry DBT systems along the scanning direction. (B) The system MTFs obtained using the in-focus reconstruction slice. Reprinted with permission from Qian et al., *Med. Phys.*, 39, 2097, (2012). Copyright 2012, American Association of Physicists in Medicine.

The system MTF obtained using the reconstructed in-focus slice for the two systems is plotted in Figure 5.5. The slice separation was 1 mm. The 10 % system MTF was approximately 1 cycle/mm lower than the projection MTF for the same system. This is attributed to the reconstruction process and the z-axis offset. When a reconstructed slice does

not intersect the object exactly (z-axis offset), the object will blur. It has been reported that with 0.5 mm z-offset, the system MTF can be degraded by as much as 1.5 cycles/mm ⁷.

5.1.5 Phantom imaging

Projection images of a tissue-equivalent breast phantom (Model 013, CIRS, Inc.) and an ACR Gammex 156 Mammographic Accreditation phantom were collected using both the s-DBT system and the Hologic Selenia Dimensions system. The CIRS phantom is shaped to represent a partially compressed breast approximately 5 cm thick. Embedded within the CIRS phantom are randomly positioned solid masses, and two MC clusters placed in the center layer. The ACR phantom simulates the X-ray attenuation of a 4.2 cm slab of a compressed human breast composed of 50 % adipose tissue and 50 % glandular tissue. Target objects in the ACR phantom are six nylon fibrils, five simulated microcalcification specs, and five masses. All of them are of known size, shape, and density. The projection images were reconstructed using a Hologic-provided back projection (BP) method yielding 50 slices through the phantom. The slice separation was 1 mm. The images were collected using the following parameters: 15 views over 14°, 28 kV anode voltage, 43 mA cathode current, and a total dose of 100 mAs (6.67 mAs per view).

Figure 5.6 shows three reconstructed slices from the s-DBT system of the biopsy breast phantom at depths of 1 cm, 2.5 cm, and 4 cm from the top of the phantom. The red boxes indicate where one MC cluster is located within the phantom, and the corresponding zoomed-in view of the MC cluster is shown below each slice, outlined with a red border. The diameters of the microcalcifications range between 0.2 mm – 0.5 mm. The MCs are in focus in the slice corresponding to their location in the phantom, shown in part C of Figure 5.6.

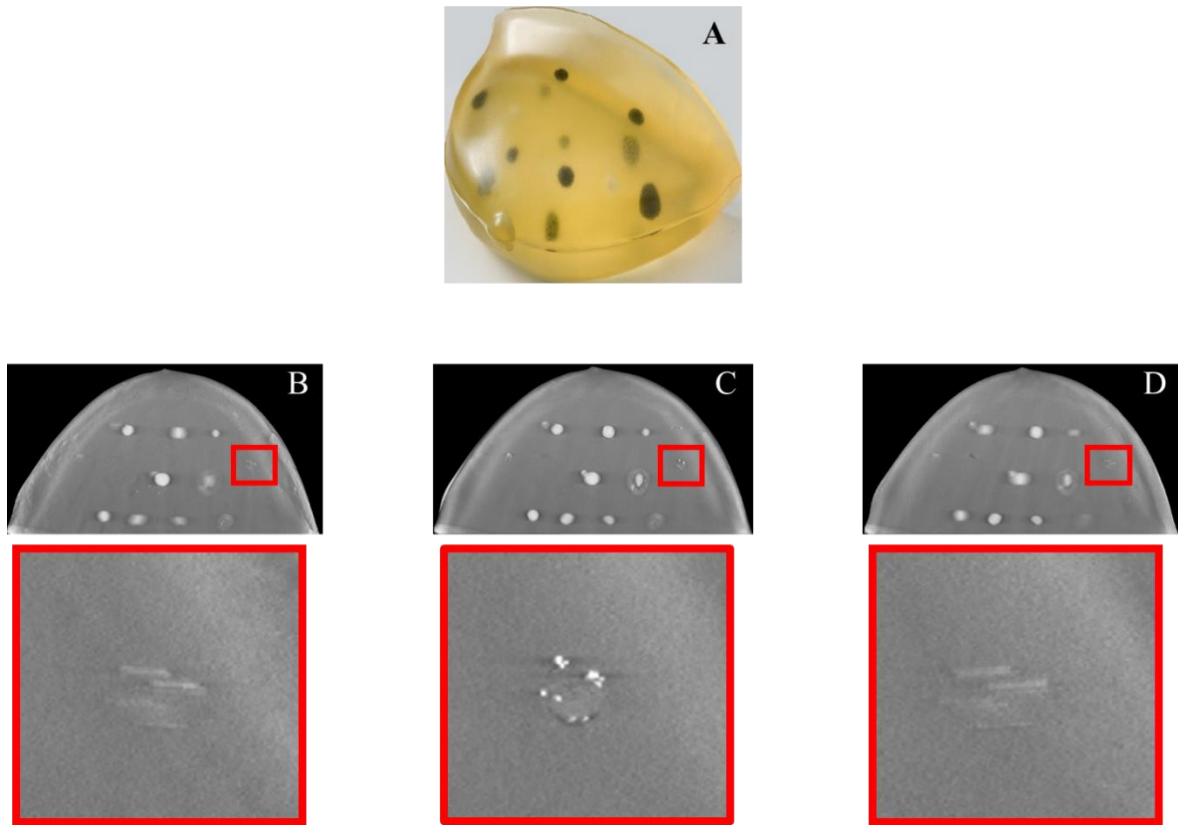


Figure 5.6 (A) Photograph of the CIRS breast biopsy phantom. (B) - (D) Reconstructed slices of the CIRS phantom from the s-DBT system. The depths of the slices are (B) 1 cm, (C) 2.5 cm, and (D) 4 cm from the phantom's surface. Reprinted with permission from Qian et al., *Med. Phys.*, 39, 2097, (2012). Copyright 2012, American Association of Physicists in Medicine.

The layout of the target objects in the Gammex 156 ACR phantom is shown in Figure 5.7, part B. Parts C through E show three slices of the phantom at depths of 0.7 cm, 1.4 cm, and 2 cm from the top. The diameters of these microcalcifications are 0.54 mm. For comparison, parts F through H and parts I through K in Figure 5.7 show focused slices of the ACR phantom reconstructed using the data collected from the s-DBT and the Hologic system, respectively. The three images from left to right in each row are the zoomed-in views of the central MC of the MC clusters 7, 8, and 9, respectively. The diameters of these three MCs are 0.54 mm, 0.4 mm, and 0.32 mm, respectively. The same magnification factor and

window level are used in displaying the two sets of data. Qualitatively, those using the s-DBT system are clearer.

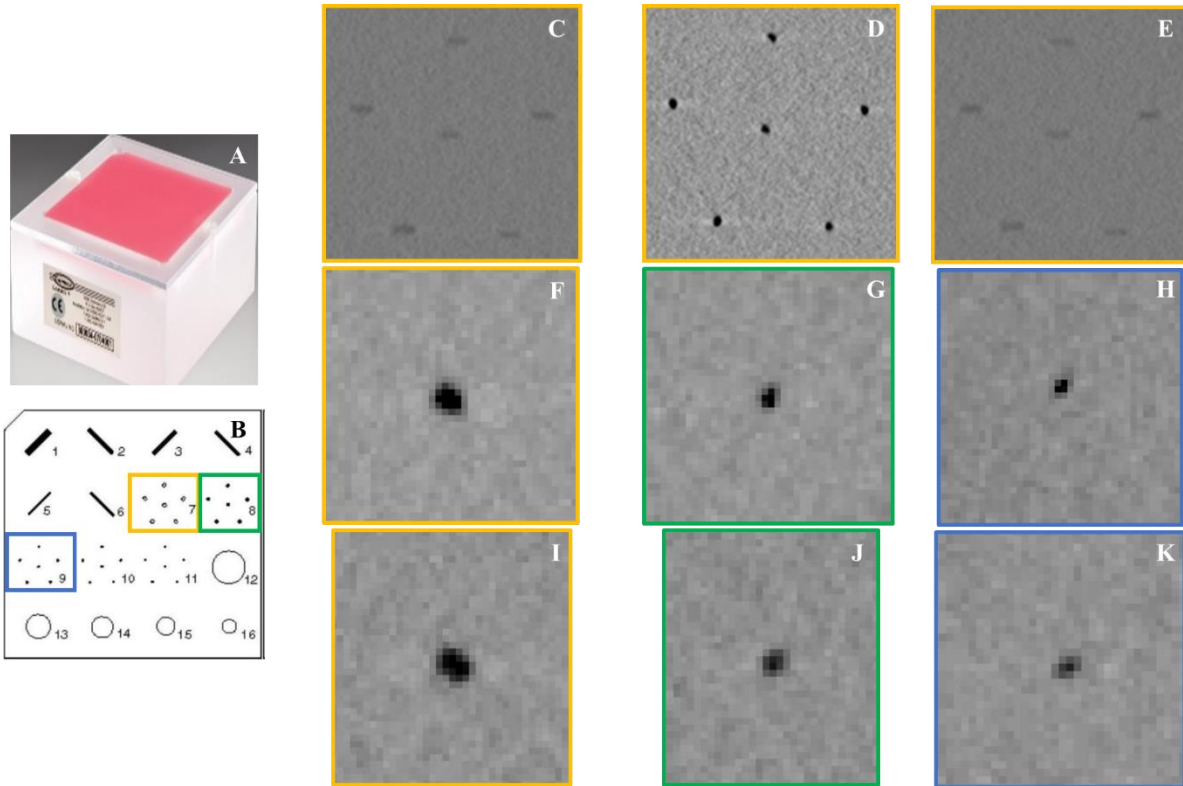


Figure 5.7 (A) Photograph of the ACR phantom. (B) Illustration of the objects imbedded within the ACR phantom. The yellow box indicates 0.54 mm specs, the green box indicates 0.4 mm specs, and the blue box indicates 0.32 mm specs. (C) - (E) s-DBT system reconstruction slices at (C) 0.7 cm, (D) 1.4 cm, and (E) 2 cm from the top of the phantom. (F) - (H) s-DBT reconstruction slices at 1.4 cm for the three MC spec sizes indicated by the colored boxes. (I) - (K) The same images as (F) - (H) for the Hologic system. Reprinted with permission from Qian et al., *Med. Phys.*, 39, 2097-98, (2012). Copyright 2012, American Association of Physicists in Medicine.

5.2 Additional tomosynthesis accelerated lifetime tests

This section of the chapter reprints of a portion of Emily Gidcumb *et al.* 2014

Nanotechnology **25** 245704.

5.2.1 Motivation and methods

In the mammography clinic, the imaging dose for breast cancer screening varies from patient to patient. On average, a tomosynthesis scan for breast thicknesses ranging 10 mm – 110 mm, requires approximately 50 mAs – 100 mAs total anode exposure⁸. Anode exposure is defined as anode current in milliamperes multiplied by the pulse length, or exposure time, in seconds. An s-DBT system exposure of 100 mAs is approximately equivalent to delivering 700 mR, or 6 mGy, entrance dose at the breast surface⁹. Using s-DBT, the dose is evenly distributed among the set of sources used, typically 15 sources over a 28° angular span. For a 15-view, 100 mAs imaging protocol, each source produces 6.67 mAs on the anode¹.

A series of tests were carried out by Dr. Bo Gao to determine the upper limit of the emission current from a CNT cathode within this context, with use of a cathode with a deposition area of dimensions 2.5 mm × 13.0 mm. This cathode is known to produce an average focal spot size of 0.6 mm × 0.6 mm at FWHM¹. Lifetime measurements were carried out in pulse mode at a frequency of 0.1 Hz with both 250 ms and 125 ms pulses, giving duty cycles of 2.5 % and 1.25 %, respectively. Two cathodes were used in these measurements. The first was used for all the 250 ms testing, performed sequentially. The second cathode was used for the 125 ms testing.

The intention of these measurements was to determine the intrinsic limitation of the CNT cathode, in terms of maximum current output. Maximum current output determines how fast the necessary X-ray dose can be delivered to a patient. Higher current allows imaging time to decrease while maintaining the same anode exposure, directly related to X-ray dose. Shorter imaging time benefits the patient by decreasing time under compression and improving image quality. For example, if the tube current, defined as the current

reaching the anode, is 27 mA, then a 250 ms exposure is needed, per view, to obtain an anode exposure of 6.67 mAs. The exposure time can be reduced to 125 ms if the tube current is increased to 54 mA.

5.2.2 Results

Figure 5.8 shows the field emission testing results for the following settings: 250 ms at 27 mA, 41 mA, 60 mA, and 80 mA cathode current. The settings correspond to current densities of 83.1 mA/cm², 126 mA/cm², 185 mA/cm², and 246 mA/cm². In addition, there was 125 ms testing at 78 mA, corresponding to a current density of 240 mA/cm². All 250 ms testing was done sequentially on one cathode, and the 125 ms testing done on a separate cathode. According to parts A through C of Figure 5.8, the cathode showed stable behavior at 27 mA, 41 mA, and 60 mA conditions. The 41 mA conditions correspond to imaging conditions used in the s-DBT system. The percentage change in electric field per 1,000 pulses for these current settings were 0.017 %, 0.054 %, and 0.159 %, respectively. These results indicate that at conditions typical of tomosynthesis imaging, the CNT cathodes could operate stably far beyond the time periods tested.

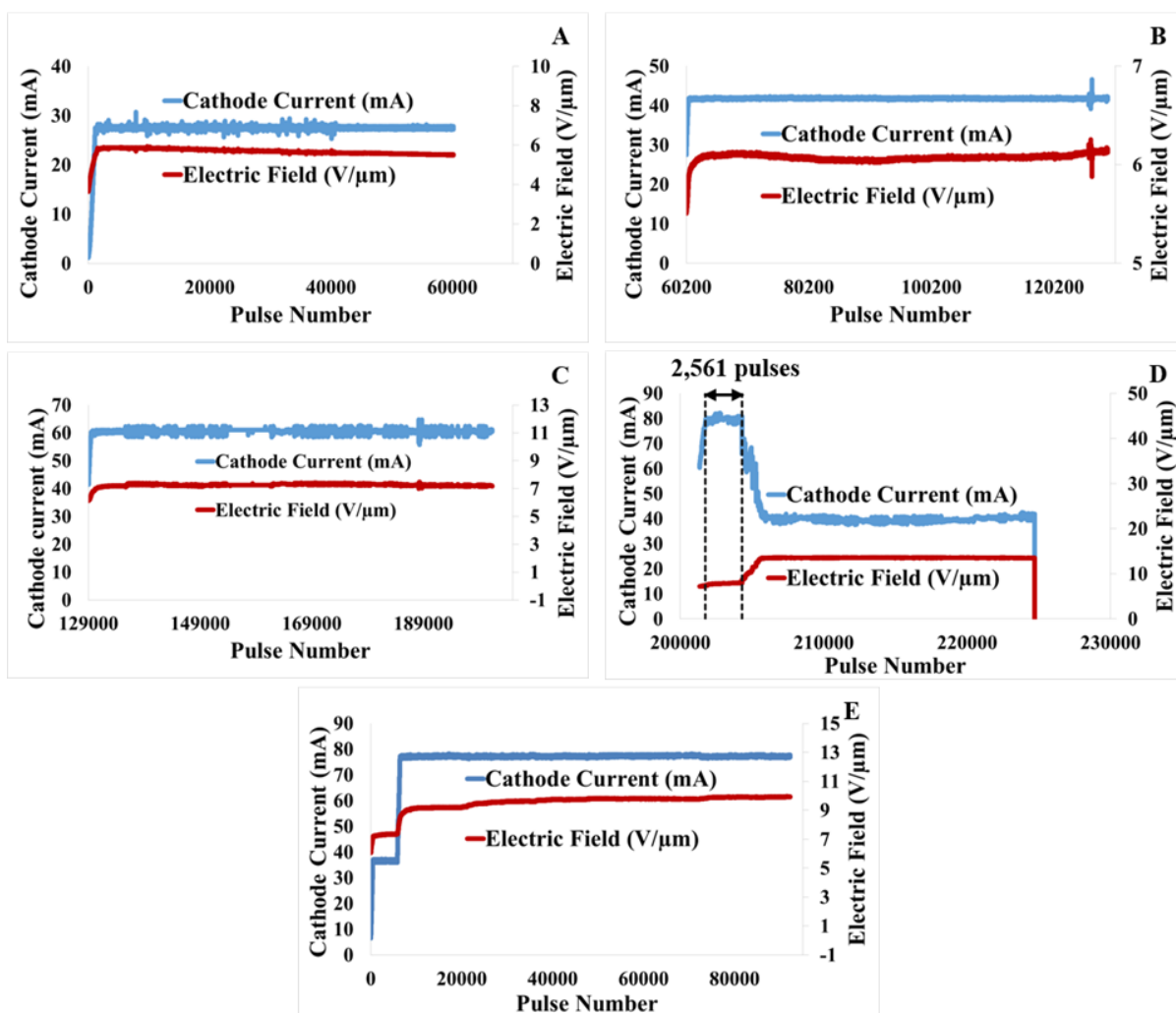


Figure 5.8 Plots of cathode current and electric field data during field emission testing with 0.1 Hz frequency. Cathode current settings were (A) 27 mA, (B) 41 mA, (C) 60 mA, (D) 80 mA, and (E) 78 mA. The experimental data for (A) through (D) was gathered sequentially on a single cathode using 250 ms pulse widths. The data in (E) was performed with a second cathode, and 125 ms pulse widths. Reprinted from Emily Gidcumb *et al.* 2014 *Nanotechnology* **25** 245704.

In part A of Figure 5.8, the trend of the electric field appears to be decreasing over time. However, the reported percentage change is positive 0.017 %. This is due to the fact that the target cathode current, 27 mA, was reached during a time of increasing electric field. For approximately 300 pulses the electric field continued to rise after reaching 27 mA. The

electric field peaked and then decreased over the majority of the experiment. The electric field at the end testing, although having decreased over time, did not reach below the electric field value reached during the initial electric field increase. This explains how the electric field was found to increase, although it appears to largely decrease over the course of the experiment.

Although 60 mA was stable, higher rates of degradation occurred. However, the higher rate of degradation could be impacted by the fact that all settings were tested sequentially on one cathode. To achieve the necessary anode exposure for a tomosynthesis scan, 60 mA in 250 ms is more than adequate. A typical tomosynthesis scan requires 100 mAs of anode exposure. Assuming a 60 % transmission rate for 30 kVp anode voltage, a series of 15 projections using 60 mA, 250 ms cathode pulses would produce 135 mAs. To achieve a 100 mAs exposure over 15 projections, a 60 mA pulse would only need to be 185 ms in duration. Data supporting the assumption of a 60 % transmission rate is presented in Section 3.3.

Parts D and E of Figure 5.8 highlight the effect of pulse width on CNT cathode degradation. The 80 mA, 250 ms test indicated significant cathode degradation by the rapid decrease in cathode current, within a fraction of the time that the other settings were tested. There was an 8.7 % degradation in only 2,561 pulses, giving a change in electric field per 1,000 pulses of 3.4 %. After this degradation occurred, the cathode current could only be maintained at approximately 40 mA, due to the voltage limit on the cathode power supply. In contrast, the 78 mA, 125 ms setting fared much better over a much longer testing period, noting that this testing was done on a separate cathode. In over 85,000 pulses there was only a 17.8 % degradation. When normalized to percent change in electric field per 1,000 pulses,

the degradation was only 0.207 %. The cathode current for 78 mA, 125 ms was stable, and lasted for a duration approximately 34 times longer than the 80 mA, 250 ms setting.

Table 5.1 shows a summary of the results for all tested conditions. Columns 1 and 2 state the current value and pulse width of each setting, respectively. The number of pulses tested, in Column 3, is the number of pulses between the first and last pulse at which the current reached $\pm 2.5\%$ of the stated current value from Column 1. The length of accelerated lifetime tested in years was calculated by assuming a 260 day work-year in which an average of 30 or 60 patients would receive an average of four images each day. In most clinical settings, 60 patients per day would be an extreme case, whereas 30 patients per day would be closer to average. In this context, each pulse tested is equivalent to one projection image that an individual cathode would produce during each image given to each patient. The term accelerated lifetime implies that the number of images a cathode could produce was tested back-to-back, instead of through the course of actual clinical use. The accelerated lifetime length reported here is not the maximum lifetime possible, but rather the portion of lifetime actually tested in these experiments. The percent change in electric field is the difference in electric field between the first and last pulse, relative to the electric field of the initial pulse, and normalized per 1,000 pulses.

Table 5.1 Testing summary and percent increases with respect to initial electric field. Reprinted from Emily Gidcumb *et al.* 2014 *Nanotechnology* **25** 245704.

Cathode current (mA)	Pulse width (ms)	Number of pulses in test	Total beam-on time (hr)	Length of accelerated lifetime tested (yr)		Percent change in electric field per 1,000 pulses (%)
				30 patients/day	60 patients/day	
27	250	59,067	4.10	1.89	0.95	0.017
41	250	40,922	2.84	1.31	0.66	0.054
60	250	71,921	4.99	2.31	1.15	0.159

Cathode current (mA)	Pulse width (ms)	Number of pulses in test	Total beam-on time (hr)	Length of accelerated lifetime tested (yr)		Percent change in electric field per 1,000 pulses (%)
				30 patients/day	60 patients/day	
80	250	2,561	0.18	0.08	0.04	3.4
78	125	85,786	2.98	2.75	1.37	0.207

Decreasing the pulse width, while maintaining the same current, decreases the heat produced due to electron bombardment with the gate material. Because the gate is so close to the cathode, the lower-temperature environment will allow the cathode to run stably for a much longer period of time. Decreasing the pulse width benefits imaging applications because it is directly related to decreasing imaging time, which is important for maintaining high image quality. Major factors impacting imaging time are the length of the X-ray pulses and the readout time of the X-ray detector. Readout time of the detector is the amount of time the detector takes per projection to read out the information it has acquired during a particular exposure. Readout time of the current Hologic Selenia Dimensions detector, for binned mode, is 180 ms⁹. Using 15 projections for a complete tomosynthesis image set, 250 ms pulses would make imaging time 6.45 s long. If instead, the pulse width could be decreased to 125 ms by using a higher cathode current, imaging time would be lowered to 4.58 seconds. Assuming a 60 % transmission rate, the 78 mA, 125 ms setting could produce 87.75 mAs in 4.58 s. This time would also decrease using an X-ray detector with a faster readout time. If the detector readout was reduced by half, to 90 ms, a 15 projection image set could be acquired in 5.10 s with 250 ms pulses and in 3.23 s with 125 ms pulses.

5.2.3 Conclusions

Typical operation of the s-DBT system is closest to the 41 mA, 250 ms experimental setting. The normalized degradation for the 41 mA, 250 ms pulse testing was 0.054 % over a

period of time equal to 1.31 yrs of actual use. This low degradation rate indicates that actual cathode lifetime at this setting would be considerably longer. It was also shown that CNT cathodes can stably perform a tomosynthesis imaging task at higher currents. The experimental setting of 78 mA with 125 ms pulses was tested for an equivalent of 2.75 yrs with a 0.207 % normalized increase in electric field. The results indicate that the cathode would continue to perform stably for much longer than the length of time tested in these experiments. The 80 mA, 250 ms pulse setting illustrated the behavior of CNT cathodes near the end of their useable lifetime. After a prolonged time of stable operation at low and high currents, the degradation rate exponentially increases. This behavior indicates that the CNTs began to rapidly degrade due to a combination of heavy use and high current demand.

These results show that, using these CNT cathodes, a breast tomosynthesis system averaging 30 patients a day could run far beyond the experimentally tested lifetime of 1 to 2 yrs. In addition, cathodes are capable of imaging at higher currents than typical breast tomosynthesis may require, with shorter pulse widths. Specifically the 78 mA, 125 ms setting could reduce imaging time by approximately 2 s compared to typical settings used by the s-DBT prototype, which typically images with 250 ms pulses. Each second decrease in imaging time decreases the chance that patient motion will negatively impact image quality.

REFERENCES

- 1 Qian, X. *et al.* High resolution stationary digital breast tomosynthesis using distributed carbon nanotube x-ray source array. *Med Phys* **39**, 2090-2099, doi:10.1118/1.3694667 (2012).
- 2 Carslaw, H. S. & Jaeger, J. C. *Conduction of heat in solids*. Second edn, (Clarendon Press, 1973).
- 3 IEC. Medical electrical equipment - X-ray tube assemblies for medical diagnosis - Characteristics of focal spots. (2005).
- 4 FDA. *Mammography Quality Standards Act Regulations*, <<http://www.fda.gov/Radiation-EmittingProducts/MammographyQualityStandardsActandProgram/Regulations/ucm110906.htm#s90012>> (2009).
- 5 Fujita, H. *et al.* A simple method for determining the modulation transfer function in digital radiography. *IEEE transactions on medical imaging* **11**, 34-39, doi:10.1109/42.126908 (1992).
- 6 Badano, A., Freed, M. & Fang, Y. Oblique incidence effect in direct x-ray detectors: A first-order approximation using a physics-based analytical model. *Med. Phys.* **38**, 2095-2098 (2011).
- 7 Ren, B. *et al.* in *Medical Imaging 2005: Physics of Medical Imaging*. 550-561 (SPIE).
- 8 Li, X., Zhang, D. & Liu, B. Workload and transmission data for the installation of a digital breast tomosynthesis system. *Med Phys* **40**, 063901, doi:10.1118/1.4803470 (2013).
- 9 Tucker, A. W., Lu, J. & Zhou, O. Dependency of image quality on system configuration parameters in a stationary digital breast tomosynthesis system. *Med Phys* **40**, 031917, doi:10.1118/1.4792296 (2013).

CHAPTER 6: LONG PULSE WIDTH FIELD EMISSION TESTING OF CATHODES

6.1 Introduction

Portions of this chapter are reprinted from Gidcumb *et al.* 2014 *Nanotechnology* **25** 245704.

6.1.1 Motivation

The motivation behind long pulse width testing of the CNT cathodes is to determine the feasibility of using the cathodes to produce 2D mammography images. Clinical applications for such a function could include image-guided needle breast biopsy, image-guided needle localization, magnification imaging, or aiding patient diagnosis through comparison to previous 2D images. In addition, current FDA approval for DBT requires the use of a combination mode where a 3D scan must be followed by a 2D image. It is a current regulatory requirement that a clinic providing DBT imaging must also have 2D imaging onsite, and for convenience should be provided by one piece of equipment as in the Hologic Selenia Dimensions system. Under current regulation requirements, to be clinically viable both functions need to be repeatable and sustainable, but until now s-DBT had not been evaluated for 2D imaging.

The challenge in 2D imaging is that the imaging dose, distributed among many cathodes in tomosynthesis, must be drawn from a single cathode. In these cases, the power demand on the CNT cathode drastically increases in comparison to the standard s-DBT practices in place. Clinically, a single mammogram exposure, of which there are four to six

in a complete imaging session, requires anywhere from 18 mAs – 500 mAs, depending on the patient and imaging system¹. For this purpose, the stability of the CNT cathode was measured for delivering pulses with an exposure of either 50 mAs or 75 mAs, which is in the lower range of typical clinical use. In addition, pulse width was considered because short exposure times are desired to minimize motion blur. The pulse widths tested in these experiments were 4 s, 3 s, and 2 s.

6.1.2 Different types of nanotubes

Two different types of CNT cathodes were tested. The first type contained small-diameter, multi-walled carbon nanotubes synthesized by the chemical vapor deposition method², referred to as few-wall nanotubes (FWNTs), identical to those in the prototype s-DBT system. The morphology of a FWNT cathode can be seen in the SEM image in part A of Figure 6.1. The diameter of the nanotubes ranges from 2 nm – 8 nm, and the nanotube lengths range from 2 μm – 6 μm . The defect density of the CNT samples deposited on the cathodes is relatively low, with an I_D / I_G ratio between 0.2 – 0.3. An example of Raman spectroscopy data for these CNTs is shown in part B of Figure 6.1.

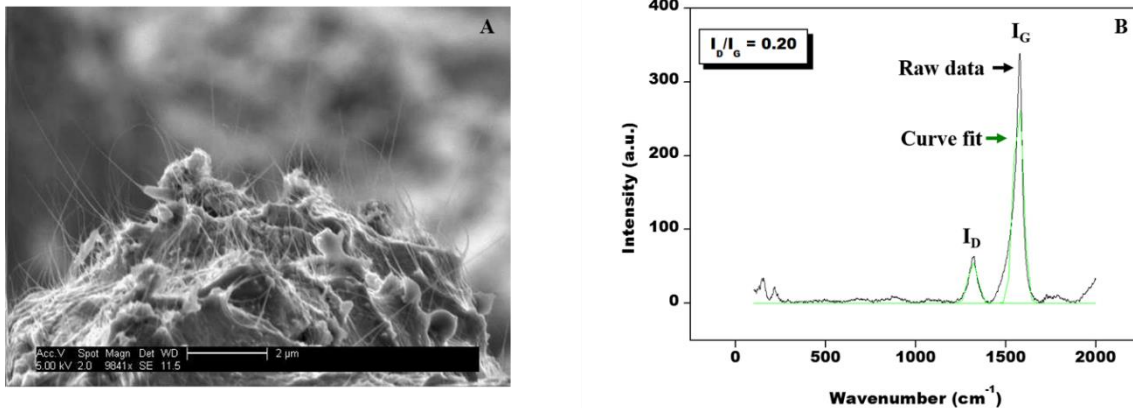


Figure 6.1 (A) SEM image of a CNT cathode. (B) Raman spectroscopy data of a CNT sample representative of those deposited on the FWNT cathodes tested throughout this study. Data provided by Dr. Bo Gao. Reprinted from Gidcumb *et al.* 2014 *Nanotechnology* **25** 245704.

In addition, a cathode containing multi-wall nanotubes (MWNTs) produced through arc discharge was tested to compare to the “traditional” cathodes. Other than the type of emitter, the cathodes were identical. It is hypothesized that the MWNTs would be more stable under harsher tube conditions due to better crystallinity as a result of their manufacturing process. Arc discharge occurs at greater than 3,000 °C, whereas CVD is performed at approximately 1,000 °C. The higher temperature is the source of increased crystallinity.

A study in collaboration with Ai Leen Koh and Robert Sinclair at Stanford University compared the oxidation resistance of the two types of CNTs with an aberration-corrected environmental transmission electron microscope (ETEM)³. The nanotube samples were exposed to oxygen at various temperatures while in the ETEM, and directly imaged afterwards. The CVD-grown tubes typically had 1 to 6 layers, with outer diameters of 2 nm – 11 nm. The arc-discharge tubes had 4 to 34 walls and diameters of 6 nm – 31 nm. Example TEM images of the studied samples can be seen in Figure 6.2. It was found that without

oxygen exposure there was no change in nanotube structure up to 520 °C. Then the samples were exposed to 1.5 mbar of oxygen while being heated to 520 °C. It was found that the CVD FWNTs sustained partial removal of outer graphene layers at 400 °C and above. Arc-discharge MWNTs with greater than six walls were unaffected in oxygen at all temperatures³. These initial results imply that because the arc-discharge MWNTs have more walls, they may be more resistant to oxidation effects compared to CVD FWNTs.

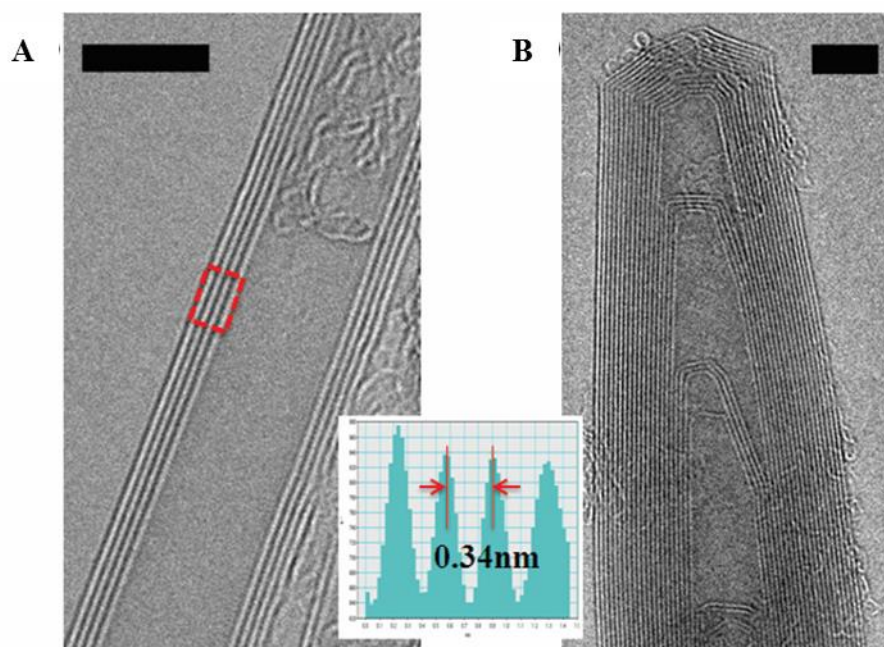


Figure 6.2 (A) High-magnification TEM images of (A) CVD-grown CNTs and (B) arc-discharge CNTs. Scale bar represents 5 nm. Reprinted with permission from Koh et al., ACS Nano, 7, 2567, (2013). Copyright 2013 American Chemical Society.

6.1.3 Differences in nanotube fabrication

6.1.3.1 FWNTs with thermal CVD

The general chemical vapor deposition (CVD) method involves heating a transition metal catalyst to a high temperature while hydrocarbon gas flows in for a set period of time⁴.

The three main components of the process are the choice of hydrocarbon gas, catalyst material, and growth temperature. The growth temperature usually ranges between 550 °C to 750 °C. The growth of the nanotube nucleates on the catalyst particles. Initially, hydrocarbon molecules become dissociated at the catalyst particles until the particles are saturated. Once a particle is saturated, carbon atoms precipitate at the catalyst site and form a carbon nanotube⁴.

The specific CVD method used to produce the FWNTs studied here uses a MgO catalyst support and a Fe/Mo catalyst². The catalyst was prepared by glycine combustion followed by annealing. The hydrocarbon source was methane. The reaction time was 10 min – 30 min².

6.1.3.2 MWNTs with arc discharge

The arc-discharge setup requires a solid anode and cathode made of carbon, surrounded by a helium gas environment⁴. Large currents passed from the anode to the cathode create a helium plasma. The plasma then evaporates carbon atoms from the carbon electrodes. MWNTs can be selectively produced by optimizing gas pressure and arcing current. Generally, the tubes are on the order of 10 µm in length and have diameters ranging from 5 nm to 30 nm. MWNTs produced by arc discharge are much straighter than those produced with CVD, indicating a higher level of crystallinity⁴.

6.2 Methods

The CNT cathodes were fabricated by electrophoretic deposition of a composite film of pre-formed CNTs and inorganic binders on a conducting substrate, followed by heat treatment⁵. Cathodes deposited both with CVD FWNTs and arc-discharge MWNTs were tested. The field emission properties of the CNT cathodes were evaluated using a testing

vacuum chamber housing 3 X-ray sources. The sources are similar in structure to those in the s-DBT X-ray tube, each consisting of: a CNT cathode, an extraction gate electrode, an Einzel-type series of electrostatic focusing lenses^{6,7}, and a tungsten anode. The tests were performed with the base vacuum pressure, the pressure when the electron beam is off, in the 10^{-8} torr – 10^{-9} torr range. The peak pressure during the emission pulses was maintained below 1×10^{-6} torr. A schematic of the experimental set up is shown in Figure 6.3.

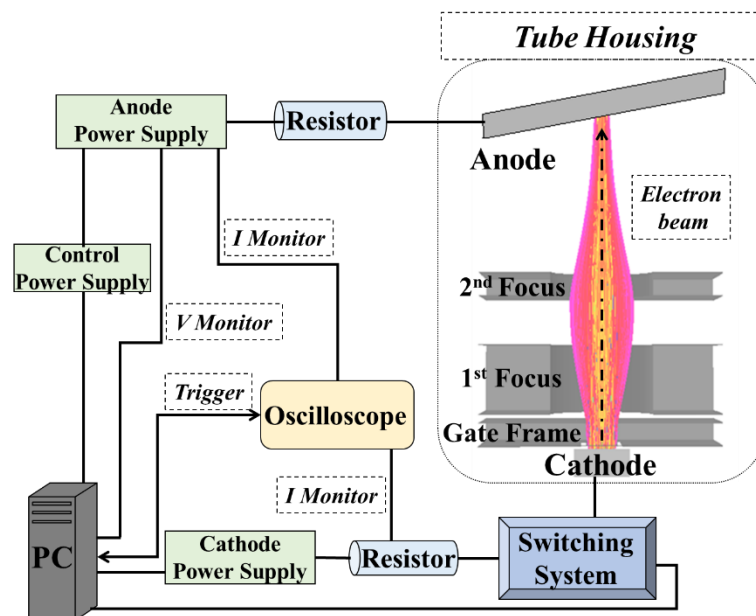


Figure 6.3 Illustration of the experimental setup, not drawn to scale. The tube housing contained three cathode-anode pairs, an example of only one is shown here. Reprinted from Gidcumb *et al.* 2014 *Nanotechnology* **25** 245704.

The field emission measurements were conducted using a setup mimicking the geometry of the prototype s-DBT system. The CNT deposition area dimensions were $2.5 \text{ mm} \times 13 \text{ mm}$, or 0.325 cm^2 . The gate electrode was comprised of three tungsten mesh, having $50 \text{ }\mu\text{m}$ bars spaced by $200 \text{ }\mu\text{m}$, welded onto a metal gate frame. The gate electrode was grounded, and negative voltage was applied to the cathode. The gate electrode was

approximately 120 μm above the cathode surface in the FWNT setup, but approximately 275 μm in the MWNT setup. The gate-cathode distance is difficult to measure and make consistent at each post of the plates; therefore, it is not considered accurate. The MWNT setup distances more accurately reflect those in the prototype s-DBT system.

The focusing electrodes were also grounded, with the lower focusing electrode, F1, 0.762 mm above the gate. The upper focusing electrode, F2, was 1.178 mm above F1. The tungsten anode had a 10° angle (16° in the s-DBT system). The anode in the testing chamber was not identical to those in the s-DBT system. It was much larger and held by stainless steel, whereas the s-DBT tube anodes are set in copper.

Data was taken over a range of anode voltages, 10 kV – 35 kV. For the FWNT setup, anode current was only measured up to 20 kV due to the voltage limitations of the current probe. Using these measurements, a transmission rate was calculated and used to determine the anode current at higher anode voltages. The current probe used was a Tektronix TCP312A with the TCPA300 Current Probe Amplifier (Tektronix, Beaverton, OR 97707).

Transmission rate is defined as the percentage of cathode current that reaches the anode. Figure 6.3 includes an illustration of the electrode structure for each cathode–anode pair, with a simulated electron beam trajectory shown going through the electrodes. After the electrons are produced from the CNTs, they must pass through three electrodes before reaching the anode: gate, 1st focus (F1), and 2nd focus (F2). Upon reaching each electrode, some of the original cathode current is lost. Therefore, only a portion of the created cathode current reaches the anode to produce X-rays. Anode current is defined as the remaining cathode current that reached the anode, and can be estimated if the cathode current and transmission rate are known from previous measurements.

Throughout the experiment many parameters were measured simultaneously using LabVIEW. Cathode and anode voltages were directly measured from the power supplies. Current was measured for both the anode and cathode from the pulse shapes as detected with an oscilloscope and then recorded in LabVIEW. It was possible to record the pulse shape and the average current over the pulse. During the FWNT experiments, only cathode pulse shapes were periodically recorded, but in the MWNT experiments only anode pulse shapes were recorded. In addition, the pressure was constantly monitored, but only recorded via LabVIEW in the MWNT experiments.

Anode exposure was determined differently between the FWNT and MWNT testing. During FWNT testing the anode current was not measured directly over 20 kV. Therefore, transmission rates up to 20 kV were used to estimate the anode current and anode exposure, assuming a square pulse. The MWNT experiments had a more exact measurement protocol. Every anode pulse shape was read into LabVIEW. The current was integrated over the pulse shape, after high frequency noise was filtered out, more accurately calculating exposure using the true, slightly inclined, pulse shape.

The cathodes were turned on and off using a Cyttec switching system controlled through an NI-DAQ in LabVIEW. Duty cycle never increased over 2 %. There was 90 k Ω resistance between the anode power supply and the anode electrode. The true anode voltage is less than that applied. Some voltage dropped across the resistors when there was current on the anode.

The testing chamber was assembled twice, once with three FWNT cathodes and again with three MWNT cathodes. Each time the chamber was opened to atmosphere the tube had

to be conditioned. After initial conditioning, the cathodes were slowly “ramped up” to the target values.

After tube conditioning, initial I-V curves were taken, followed by field emission testing. The first target was 50 mAs in 4 s, at either 30 kV or 35 kV anode voltage. In addition, the FWNT cathode was tested to 75 mAs in 4 s at 35 kV. After 4 s testing was completed, and shown to be stable, the pulse width was lowered to 3 s, and finally to 2 s. As this was a feasibility test, lifetimes for each setting were not measured in this sequential testing.

During all testing, the base pressure was approximately 5×10^{-9} torr for the FWNT experiments and 1×10^{-8} torr for the MWNT experiments. The peak pressure during emission did not exceed 1×10^{-6} torr for the FWNT testing and stayed below 5×10^{-7} torr for MWNT testing.

Total beam on time for all experimentation on the FWNT cathode was 67.03 min, but only 30.21 min for the MWNT cathode. This difference was due to the difference in time spent gradually increasing current toward the target levels.

Finally, SEM and optical microscope images were taken to evaluate the cathodes and gate mesh. SEM images were taken before and after testing for both types of cathodes.

Optical microscope images were taken of the tungsten gate mesh after testing was completed.

6.3 Results

6.3.1 Initial I-V curves

Before feasibility testing began, initial I-V curve characterization was done and is plotted in Figure 6.4. The turn-on field measured for these cathodes was less than $3 \text{ V}/\mu\text{m}$, defining the turn-on field as that needed to produce $10^{-6} \text{ A}/\text{cm}^2$. Both I-V curves reached a

maximum current of 40 mA, with a density of 123 mA/cm², which was more than enough for the testing requirements. Applied fields at 1 mA, 10 mA, and 40 mA are given in Table 6.1. The I-V curves show that the MWNT cathode required lower applied fields to produce the same current as the FWNT cathode. However, because the gap distance measurements were inaccurate, the comparison between the exact electric field values of the two cathodes is not particularly meaningful. Other experiments have shown MWNT cathodes require approximately 1.5 V/μm higher applied field to produce 40 mA, compared to FWNT cathodes. Lower turn-on fields can indicate better field emitters. What is shown is that both cathodes were able to produce the same currents at reasonable applied fields.

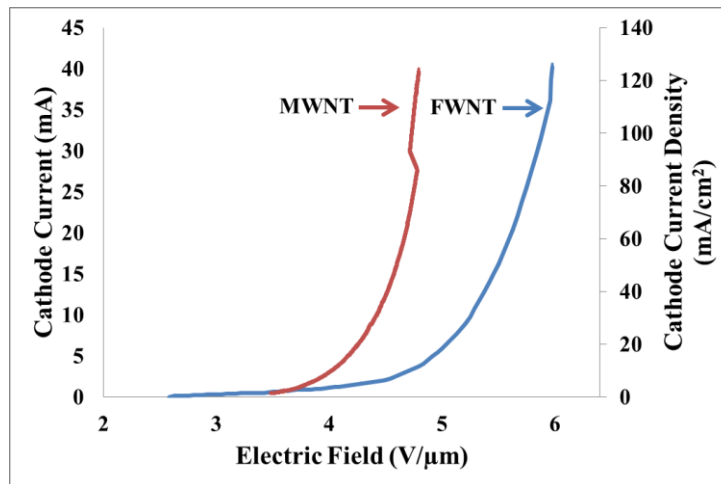


Figure 6.4 I-V curves for both the MWNT and FWNT cathode. Both current and current density are shown plotted versus electric field. FWNT data reprinted from Gidcumb *et al.* 2014 *Nanotechnology* **25** 245704.

Table 6.1 Electric field values at various cathode currents corresponding to the initial I-V curves. Results conflict with other experiments due to uncertainty in gate-cathode distances in these experiments.

Cathode	Electric field @ 1 mA (V/μm)	Electric field @ 10 mA (V/μm)	Electric field @ 40 mA (V/μm)
FWNT	3.7	5.2	6.0

Cathode	Electric field @ 1 mA (V/ μ m)	Electric field @ 10 mA (V/ μ m)	Electric field @ 40 mA (V/ μ m)
MWNT	3.7	4.4	4.8

6.3.2 FWNT results

6.3.2.1 4 s pulses

There were two targets for the 4 s pulse width testing, 50 mAs and 75 mAs of anode exposure. Field emission testing was done consecutively on the same cathode, as can be seen in Figure 6.5. Parts A and B present data on the 50 mAs experiment, and parts C and D present data on the 75 mAs experiment. The results are plotted versus pulse number, with each pulse being 4 s long, an example is plotted in the insets of parts A and C of Figure 6.5. Cathode current and cathode voltage were directly measured. The anode exposure was calculated by multiplying the pulse width by the anode current. Anode current was directly measured only for anode voltages ranging from 10 kV – 20 kV. An average transmission rate of $55.4 \pm 0.4\%$ was calculated for pulses with an estimated anode exposure within 50.0 ± 2.5 mAs. For data taken at 25 kV – 35 kV, this transmission rate was used to estimate the anode current. Parts A and B of Figure 6.5 indicate what data corresponds to the various anode voltages. All data for the 75 mAs experiments, in parts C and D, were taken at 35 kV. All of the data was taken using a duty cycle of 1.25 %, except the 10 kV data which was taken at 1.5 % duty cycle. The applied electric field values were calculated for all experiments by dividing the measured cathode voltage by the gate-cathode distance.

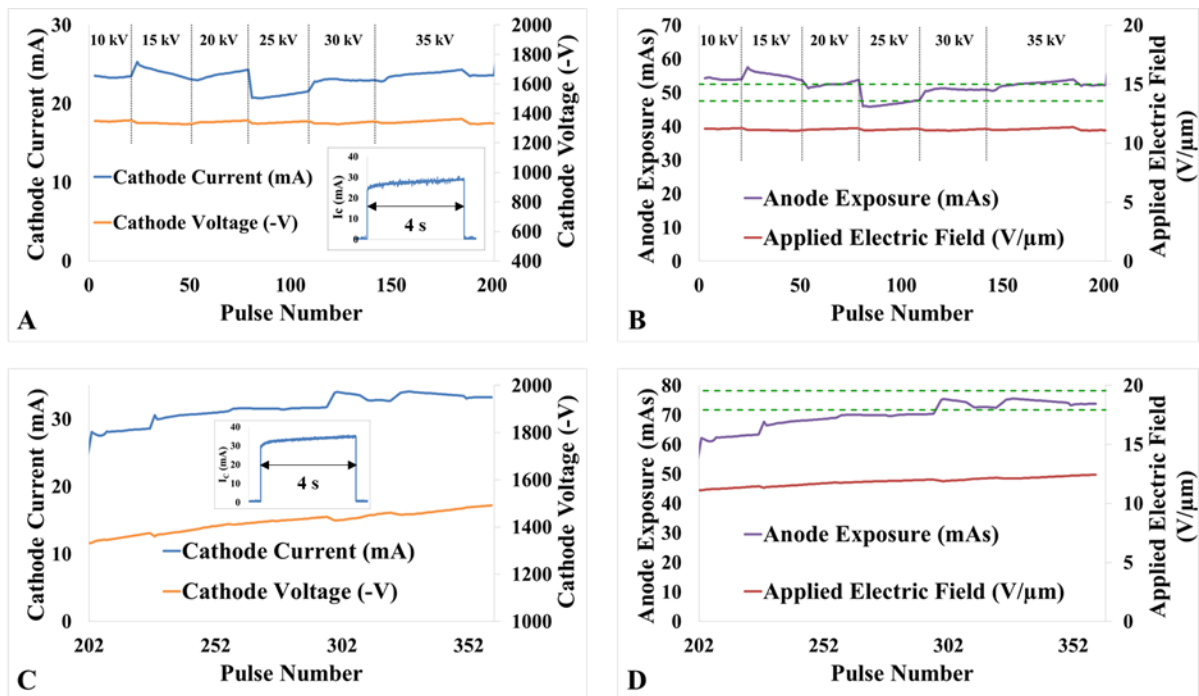


Figure 6.5 FWNT field emission results for the 4 s pulse width testing, for both 50 mAs and 75 mAs targets. (A) and (B) plot different quantities for the same pulses; same for (C) and (D). (A) Raw cathode current and voltage data for the 50 mAs target. Inset: One, 4 s pulse of cathode current averaging 27.6 mA, producing 61 mAs. (B) Calculated anode exposure and electric field data for the 50 mAs testing. The green lines demarcate the region considered the target exposure region. The vertical dotted lines in (A) and (B) indicate when anode voltage changed during the experiments. (C) Cathode current and voltage data for the 75 mAs testing. Inset: One, 4 s pulse of 33.5 mA cathode current, equaling 74 mAs. (D) Calculated anode exposure and electric field data for the 75 mAs testing, also with green dotted lines indicating the target region. All data in (C) and (D) was taken at 35 kV. Cathode current and applied electric field data, as well as the inset in (A) are reprinted from Gidcumb *et al.* 2014 *Nanotechnology* **25** 245704.

Pulses were considered to meet the target anode exposure if calculated value was within 5% of target value, the range is demarcated on parts B and D of Figure 6.5. For 50 mAs this meant pulses valuing 50.00 ± 2.50 mAs, and for 75 mAs it meant 75.00 ± 3.75 mAs. The cathode current for the 73 pulses reaching the 50 mAs target averaged 23.2 ± 0.5 mA, giving an average current density of 71.3 mA/cm^2 . The average anode exposure was 51 ± 1 mAs. The average current for 58 target pulses in the 75 mAs experiment was 33.5 ± 0.4

mA, corresponding to an average density of 103.1 mA/cm^2 . The average anode exposure was $74 \pm 1 \text{ mAs}$. The increase in cathode voltage between the first pulse the last pulse reaching the target during each experiment was calculated. For the 50 mAs experiment, the cathode voltage difference -7 V. For the 75 mAs experiment, the difference was 64 V.

The 4 s, 50 mAs testing on this FWNT cathode, here named FW 1, was the first long pulse-width testing that had been done on the CNT cathodes. It was unknown how the cathodes would perform. Therefore, measurements began at a lower anode voltage than the target setting. This allowed the cathode, and the chamber setup, to be conditioned slowly and gauge the cathode's performance over incremental increases in anode voltage. For the FWNT testing, which was done first, 35 kV was chosen as the target operating anode voltage. However, the MWNT testing was done at a lower, 30 kV value. The range of energies used in breast imaging is typically 25 kVp – 45 kVp, depending on breast thickness⁸. The targeted values chosen for these experiments reflect middle-range anode energies for breast imaging.

The duty cycle settings were chosen to preserve cathode performance. A lower duty cycle allows the cathode to cool down between pulses, whereas a higher duty cycle allows the experiment to progress more quickly. Throughout these experiments, it was desired to balance those two factors in determining the duty cycle. In this initial setting, the duty cycle began at 1.5 % and was then lowered to 1.25 %. At that time it was unknown if the cathode performance was sensitive to the duty cycle or not. Taking a conservative approach, a lower duty cycle was used in the initial experiments.

The data in parts A and B of Figure 6.5 have a disjointed appearance around the points where anode voltage changed. Anode voltage was changed when initiating a new experimental run. The new run did not always begin at the same voltage that the previous run

had at the end. Once a run began, the cathode voltage was either increased or decreased by a specified amount until the target current was achieved. This explains why the anode exposure values appear to move in and out of the target region. The LabVIEW program was attempting to regulate the current, but did so over many pulses.

The 4 s, 75 mAs testing shown in parts C and D of Figure 6.5 were done to see how much current the cathode could output with a 4 s pulse, to increase the dose created by the X-ray tube. The goal was to increase the amount of dose possible per unit of time. After this setting was shown feasible, instead of increasing current further over 4 s pulses, the pulse width was decreased. That is why testing continued at lower pulse widths, and also why the 75 mAs target was not repeated in the MWNT experiments. In comparing the 4 s, 50 mAs results to the 4 s, 75 mAs results, it can be seen that higher cathode voltages were required to produce higher anode exposure levels, as expected. The cathode needed to produce an additional current of approximately 10 mA to increase the anode exposure by 15 mAs.

The insets in parts A and C of Figure 6.5 show sample pulses of cathode current. All pulses shown are not horizontal but have a positive slope. As the cathode emits current over time, the gate mesh above increases in temperature. As the gate's temperature increases, the metal bars sag slightly causing the cathode-gate distance to decrease. As the distance decreases, the field strength increases and more current can be drawn from the cathode, causing the current during the pulse to increase over time.

6.3.2.2 3 s pulses

After the 50 mAs and 75 mAs targets were reached with 4 s pulses, pulse width was lowered to 3 s, with a target of 50 mAs. All 3 s data was taken at 35 kV, with a duty cycle of 1.25 % (Figure 6.6). The 3 s data are counted starting at 1 although they were emitted from

the same cathode having produced the data in Figure 6.5, which shows that 361, 4 s pulses were emitted. As for the 4 s data, the cathode current and voltage were directly measured. All anode currents and anode exposures were calculated from the transmission rate measured at the lower voltage data from Figure 6.5.

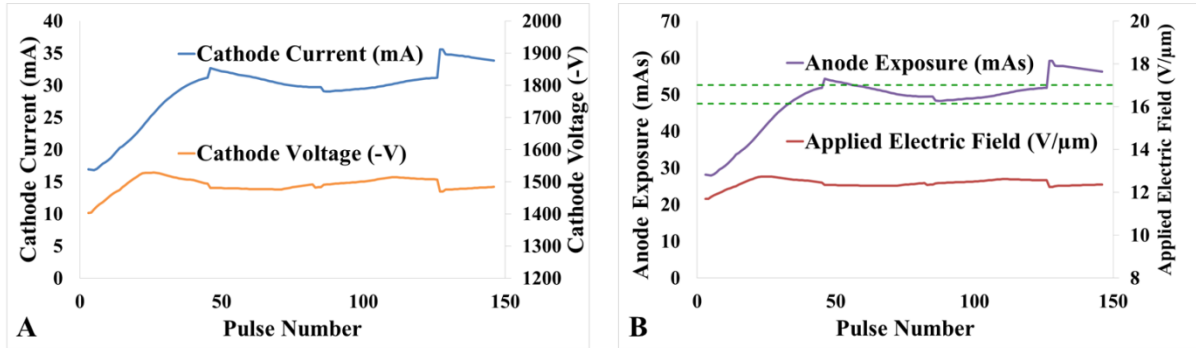


Figure 6.6 Field emission data for the FWNT cathode producing 3 s pulse widths with a target of 50 mAs. (A) Plots of measured cathode current and cathode voltage. (B) Plots of calculated anode exposure and applied electric field, with the target exposure region outlined with green dotted lines.

The average current for the 83 target pulses was 30.2 ± 0.7 mA, corresponding to an average density of 92.8 mA/cm^2 . The average anode exposure was 50 ± 1 mAs. The cathode voltage difference between the last and first target pulses was -7 V. The total number of 3 s pulses produced by the cathode was 146.

With the exception of the first approximately 20 pulses, and pulses 80 to 110, the cathode current did not increase with cathode voltage. After pulse 20, cathode current continued to rise and cathode voltage peaked and then began to decrease. This behavior is not consistent with the theory of field emission. Therefore, there must have been an error in the current and voltage measurements made with LabVIEW. It is unknown what the error was. Most likely, it lies in the cathode voltage measurements. The cathodes had resistors in series with them. The data produced by the control program automatically accounted for the voltage

drop across the resistors, according to the cathode current for each pulse. The uncorrected voltage data was not recorded. It is likely that the error was in the cathode voltage correction calculation. It is unknown why this error occurred and why it was not consistent. This error is also present in portions of the data in Figure 6.5, parts A and B of Figure 6.7, Figure 6.9, and Figure 6.10. In some cases the voltage changes are large, and in some the voltage changes are relatively small, as in the last 20 pulses of Figure 6.6.

Because the field emission I-V relationship is exponential, as shown in Figure 6.4, it is possible that the current was in an unstable region. In other words, the same cathode current, calculated by an average over a long pulse, could be produced over a range of voltages. This could account for some of the discrepancies on the scale of tens of volts, but would not likely account for a change of 50 V to 100 V, as was present in some dramatic cases (i.e. part A in Figure 6.7, Figure 6.9, and Figure 6.10). All control parameters for each recorded pulse were not saved, and it is impossible to know precisely the cause of these voltage changes.

6.3.2.3 2 s pulses

After the 3 s experiments were concluded, pulse width was lowered to 2 s. The target was 50 mAs and the results are shown in Figure 6.7. All 2 s data was taken at 35 kV, but two different duty cycles were used. The first 123 pulses were produced with a duty cycle of 1.25 %, but this was lowered to 0.83 % in hopes of preserving the cathode, as it was showing signs of degradation. The cathode was unable to reach the 50 mAs target and a second cathode was tested to attempt to reach the 50 mAs goal, shown in parts C and D of Figure 6.7. This second cathode was already in the chamber during all of the experiments. The data on the second cathode was taken at 35 kV as well, with a duty cycle of 1.0 %.

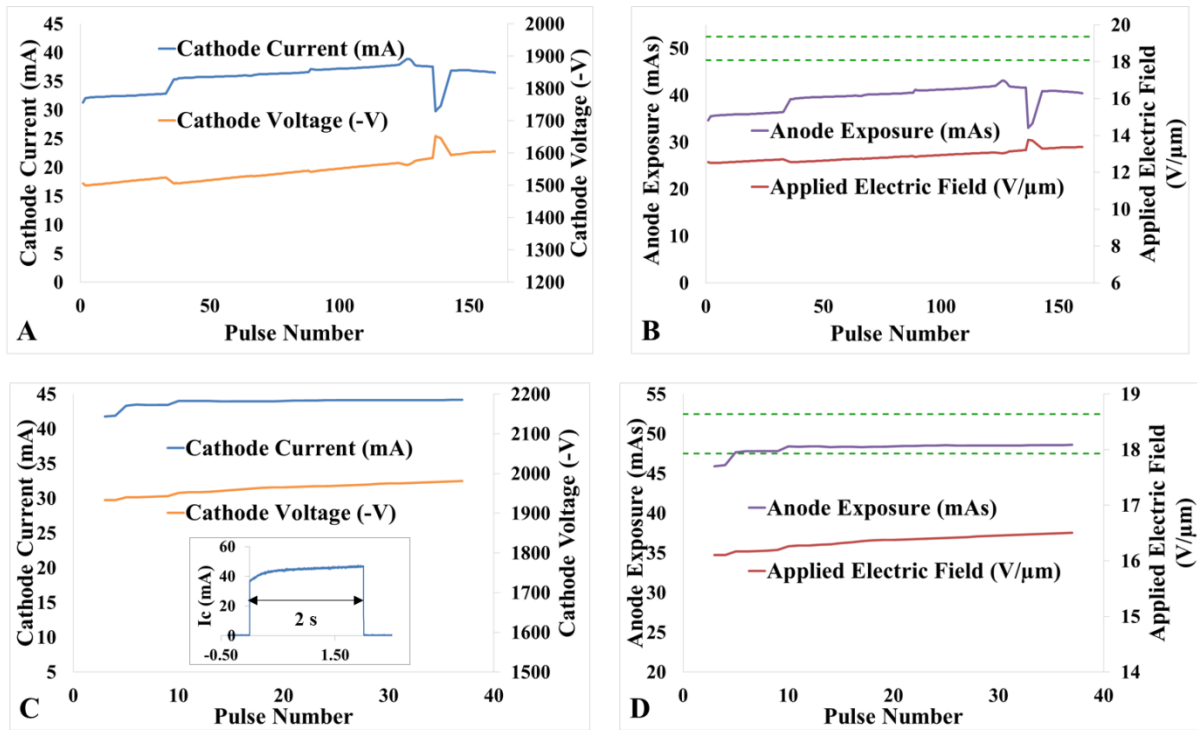


Figure 6.7 Field emission results for 2 s pulses. All data was taken at 35 kV. (A) and (B) show the results for cathode 1 (FW 1); (C) and (D) show the results for cathode 2 (FW 2). An example 2 s pulse is shown in the inset of (C). The pulse had an average current of 44.5 mA, equaling an exposure of 49 mAs. It can be seen that the anode exposure in (B) never reached the target region, outlined by the green dotted lines.

Cathode 1 (FW 1) was the cathode that produced all of the 4 s and 3 s data. None of its 160, 2 s pulses were able to reach the 50 mAs target. The average anode exposure of the 160 pulses was 40 ± 2 mAs. The cathode voltage increase over those pulses was 99 V. The second cathode used, FW 2, successfully reached the target range. FW 2 had previously undergone conditioning, with I-V curves taken, and was ramped up to 2 s pulses starting at 100 ms pulses. Average current for the 33 pulses reaching the 50 mAs target range was 44.0 ± 0.2 mA, corresponding to an average density of 135.3 mA/cm^2 . The average anode exposure was 48.3 ± 0.3 mAs. The cathode voltage difference between the last and first target pulses was 0 V. The total number of 2 s pulses produced by the cathode was 37.

The inability of FW 1 to reach the 50 mAs target indicated emitter failures on the cathode. Data was taken after this (not shown) with 500 ms pulses that showed the cathode was unable to produce more than 40 mA. After the heavy testing, there was damage to a significant number of CNT field emitters, preventing it from producing higher levels of current.

6.3.3 MWNT results

After the FWNT testing was completed, the chamber was opened and three MWNT cathodes were installed and conditioned. The same experiments were completed, except for the 4 s, 75 mAs experiment. The 50 mAs target was attempted using 4 s, 3 s, and 2 s pulses. When the testing chamber was reloaded with new cathodes, data acquisition changes were also made. The anode current was no longer measured with a current probe, and instead measured directly through LabVIEW from the back of the anode power supply. Therefore, anode current was a directly measured quantity. Anode exposure was calculated by integrating each anode pulse shape read in from the oscilloscope with LabVIEW. The applied electric field was calculated by dividing the cathode voltage by the gate-cathode distance, which was larger than in the FWNT setup.

6.3.3.1 4 s pulses

Results for the 4 s pulse data is shown in Figure 6.8. As in Figure 6.5, this data was taken at different anode voltages. This was done in order to condition the cathode, with 30 kV being the maximum goal. When not labeled, the data was taken at 30 kV. The duty cycle was 1 % through pulse 197, 1.25 % through pulse 204, 1.5 % through pulse 211, and 1.75 % through pulse 220. For reference, the 30 kV data begins at pulse 71. Part A in Figure 6.8 shows the measured cathode current, anode current, and cathode voltage for each acquired

pulse. Part B in Figure 6.8 shows the anode exposure calculated with LabVIEW per pulse, and the corresponding calculated applied electric field. The example pulse, shown in the inset of part B in Figure 6.8, is an anode current pulse calculated to have produced 50 mAs.

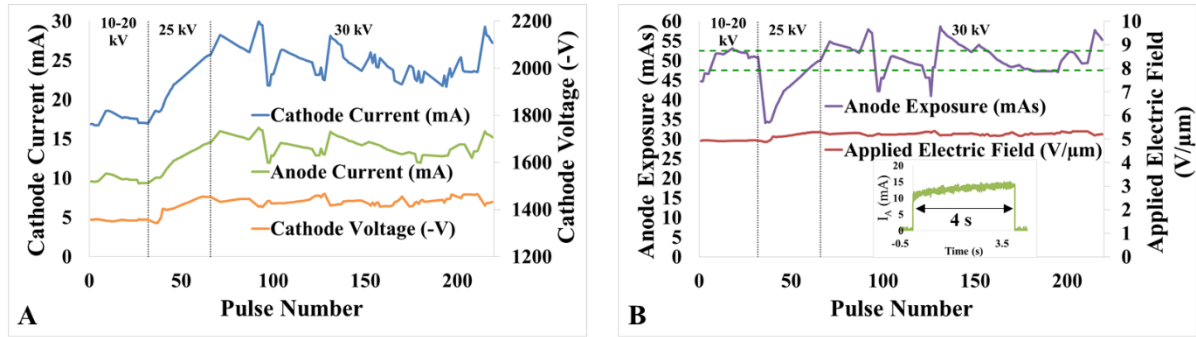


Figure 6.8 Field emission data for 4 s pulses produced from the MWNT cathode. The data was taken at various anode voltages, as indicated by the vertical dotted black lines. (A) Cathode current and voltage, and anode current measurements. (B) Anode exposure and applied electric field calculations, with the target exposure region outlined with green horizontal lines. The inset in (B) shows an anode current pulse 4 s long, averaging 13.7 mA, totaling 50 mAs.

The average current for the 79 pulses reaching 50 mAs was 23 ± 3 mA, corresponding to an average density of 71 mA/cm^2 . The average anode exposure was 50 ± 1 mAs. The cathode voltage increase between the last and first target pulses was 113 V. The total number of 4 s pulses produced by the cathode was 220.

6.3.3.2 3 s pulses

Following the 4 s experiment was the 3 s pulse, done sequentially on the same MWNT cathode. All data was taken at 30 kV. The duty cycle was 1.75 % through pulse 27, and 1.5 % after that. The results are presented in Figure 6.9.

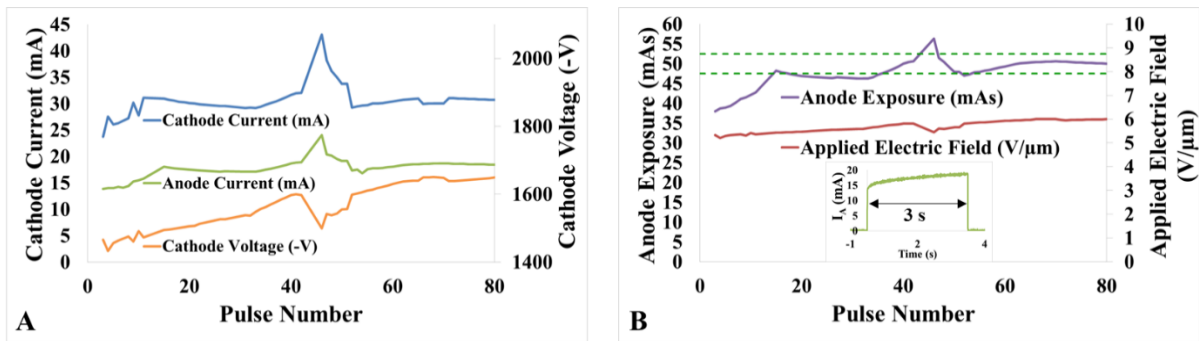


Figure 6.9 Field emission results for the 3 s experiments done with the MWNT cathode. (A) Cathode and anode current data, as well as cathode voltage data. (B) Calculated anode exposure and applied electric field data. Inset: A 3 s anode-current pulse averaging 18.3 mA, equaling 50 mAs.

The average current for 42 pulses reaching the 50 mAs target was 31 ± 2 mA, corresponding to an average density of 96 mA/cm^2 . The average anode exposure was 50 ± 1 mAs. The cathode voltage increase between the last and first target pulses was 155 V. The total number of 3 s pulses produced by the cathode was 82.

6.3.3.3 2 s pulses

The last field emission measurements done, on the same MWNT cathode, were 2 s pulses with a goal of 50 mAs. All data was taken at 30 kV. A 1.5 % duty cycle was used for the first 12 pulses, the rest done at 1.0 % duty cycle. The results are shown in Figure 6.10. Unlike the FWNT testing, the same MWNT cathode was able to meet the 50 mAs target for all tested pulse widths.

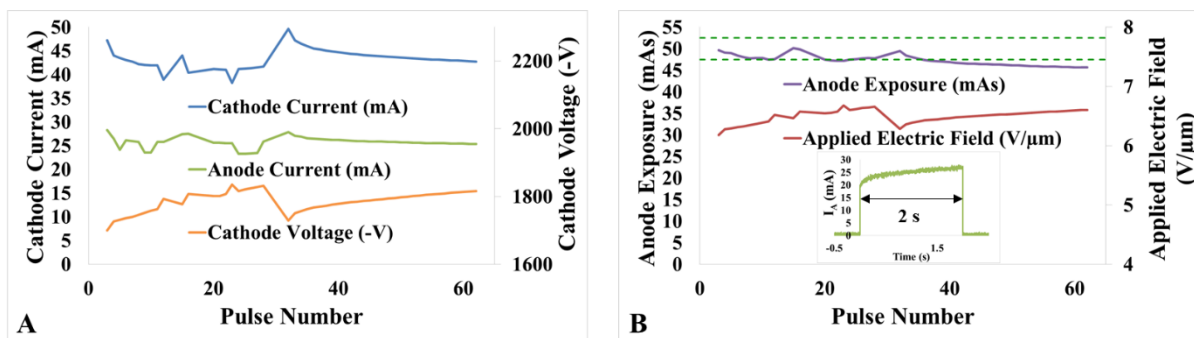


Figure 6.10 Field emission results for the 2 s, 50 mAs testing done with a MWNT cathode. (A) Measured cathode current, anode current, and cathode voltage data for each pulse. (B) Calculated anode exposure and applied electric field for each pulse. Inset: An example 2 s pulse with an average anode current of 24.2 mA, totaling an exposure of 49 mAs.

The average current for the 22 target-range pulses was 43 ± 3 mA, corresponding to an average density of 133 mA/cm^2 . The average anode exposure was 48.3 ± 0.8 mAs. The cathode voltage increase between the last and first target pulses was 62 V. The total number of 2 s pulses produced by the cathode was 63.

Table 6.2 summarizes the data from both MWNT and FWNT experiments. The first column identifies the cathodes. MW refers to the MWNT cathode tested. The average cathode current and exposure, presented in Columns 5 and 7, were calculated with the values from the “target pulses”, equal to the number of pulses in Column 4. The number of target pulses is not equal to the total number of pulses shown in the figures because not all pulses fell within the target range. The target range is the 5 % window around the anode exposure target, outlined by the green dotted lines in the data plots. The current density was calculated from the average cathode current and the cathode deposition area.

Table 6.2 Summary of all field emission measurements on both cathode types.

Cathode	Pulse width (s)	Anode exposure target (mAs)	Number of pulses	Average cathode current (mA)	Current density (mA/cm ²)	Average anode exposure (mAs)
FW 1	4	50	73	23.2 ± 0.5	71.3	51 ± 1
FW 1	4	75	58	33.5 ± 0.4	103.1	74 ± 1
FW 1	3	50	83	30.2 ± 0.7	92.8	50 ± 1
FW 1	2	50	0	0	0	40 ± 2
FW 2	2	50	33	44.0 ± 0.2	135.3	48.4 ± 0.3
MW	4	50	79	23 ± 3	71	50 ± 1
MW	3	50	42	31 ± 2	96	50 ± 1
MW	2	50	22	43 ± 3	133	48.3 ± 0.9

Although the number of pulses listed for FW 1 for 2 s pulses is 0, a calculated average anode exposure is reported. The average anode exposure in Table 6.2 was calculated over all the recorded pulses, although they did not reach the target, to show what exposure achieved by the cathode.

It can be seen from both the FWNT and MWNT results that as pulse width decreased, average cathode current and current density increased to achieve the anode exposure value of 50 mAs, as expected. In addition, the cathode currents required to produce the needed anode exposure were consistent between the FWNT and MWNT results.

The standard deviation of the MWNT average cathode currents is larger than that for the FWNT cathodes. Between the two experiments the LabVIEW control program was altered significantly. The measurement methods and the feedback loop programming were changed. This resulted in higher current fluctuations when attempting to hold cathode current constant. This is also noticeable through the “noisier” appearance of the MWNT plots, versus the FWNT plots.

6.3.4 SEM images of cathodes

All SEM images of the FWNT cathodes were taken after use in the vacuum testing chamber for field emission experiments. In contrast, the MWNT cathode was imaged before and after use in the chamber. All cathode imaging was done for profile and top views of the cathode surface. Profile views help to identify CNT emitters protruding perpendicular to the surface. Surface views serve to show the density of the deposited CNTs on the cathode, and could identify damage the cathode may have suffered.

6.3.4.1 FWNT cathodes

Figure 6.11 shows example SEM images taken of cathode FW 1 after it was removed from the vacuum testing chamber. It was easy to find areas of remaining emitters on the cathode, for both side and top views. However, the top views did show a lower CNT density than typically observed on unused cathodes. This finding supports that the cathode suffered emitter loss, resulting in its inability to achieve the 2 s, 50 mAs target.

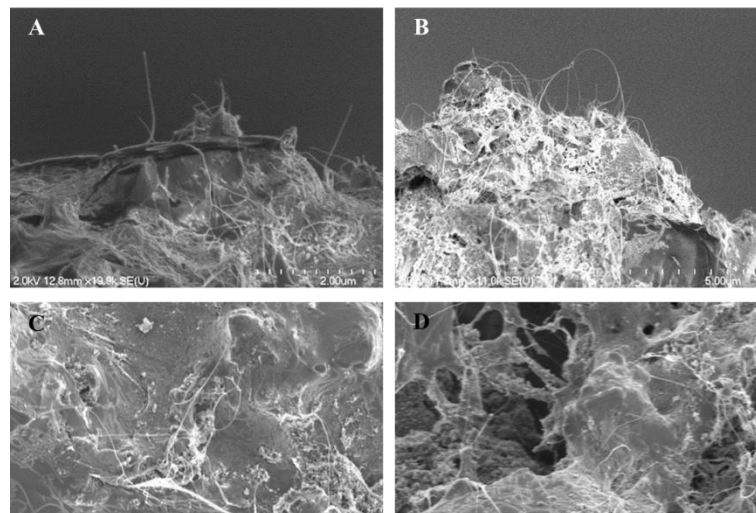


Figure 6.11 SEM images of cathode FW 1 after use in field emission experiments. (A) and (B) are profile images, where the SEM sample was tilted approximately 90°. (C) and (D) are top-view images, looking straight on the cathode surface.

Although cathode FW 2 was conditioned and used in the 2 s, 50 mAs experiments, it can represent an unused cathode, or one lightly used. Figure 6.12 shows SEM images of cathode FW 2 in which there is a higher density of CNTs visible in both profile and top views. In particular, part C of Figure 6.12 shows a very high density of nanotubes, unmatched in the areas observed on cathode FW 1. Upon comparing the images of cathodes FW 1 and FW 2, it appears that the sequential long-pulse testing on FW 1 led to much more damage than the testing of only the 2 s setting on FW 2.

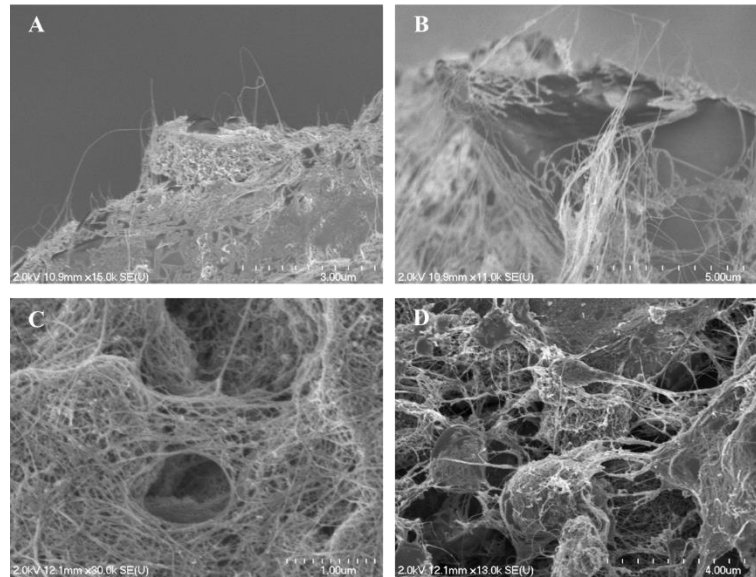


Figure 6.12 SEM images of cathode FW 2 after being removed from the testing chamber, where it underwent conditioning and 2 s pulse testing. (A) and (B) are profile views, and (C) and (D) are top views.

Figure 6.13 shows SEM images of the third FWNT cathode that resided in the chamber during field emission testing but was unused except for some conditioning and initial I-V curves. In taking top-view images it was easy to find regions of high nanotube density. However, it was difficult to find emitters protruding perpendicular to the surface in the side-view images, even though the cathode was covered with many nanotubes. This could

either indicate not finding good areas during imaging, or improper activation of the cathode before being placed in the vacuum chamber. What was most striking in the images, was the surface damage imaged in part D of Figure 6.13. Damage of this sort was not found on any other cathodes.

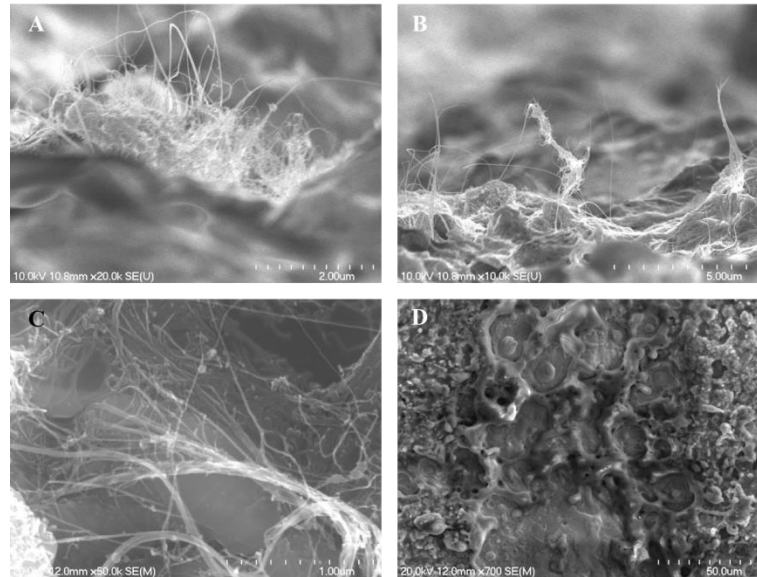


Figure 6.13 SEM images of the third FWNT cathode in the testing chamber that only underwent conditioning. (A) and (B) are side-view images. (C) and (D) are top-view images. (D) is a low magnification image showing unusual pock marks or melting.

To attempt to determine a cause for this damage, energy-dispersive X-ray spectroscopy (EDS) was done on the damaged area, shown in Figure 6.14. The elements detected in the highest weight percentage were oxygen, zinc, molybdenum, and carbon. These are elements that are involved in creating the cathodes, and were also found on two other analyzed portions of the cathode. However, this damaged portion was the only area that showed the presence of tungsten, albeit a small one. The weight percentage of tungsten over the indicated area was only 0.56 %. It is possible that the tungsten M-shell peaks simply

overlapped with the zinc K-shell peaks, and is not actually present. Another possibility is that the tungsten gate mesh could have been damaged at that location and deposited some material there.

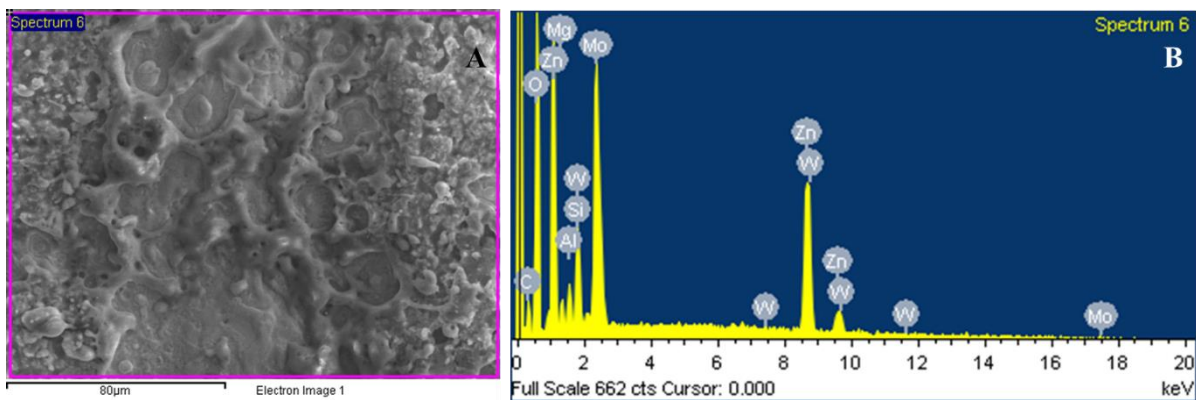


Figure 6.14 (A) SEM image of surface damage of the third FWNT cathode. Pink outline indicates where the EDS spectrum was taken. The scale bar represents 80 μm . (B) EDS spectrum from the area in (A), taken at 20 kV and 12 mm working distance.

6.3.4.2 MWNT cathode

Figure 6.15 shows SEM images of the MWNT cathode taken before it was used in the vacuum testing chamber. The top-view images in parts C and D were ultra-high resolution images taken at a working distance of 6.5 mm. During imaging of the cathode profile, it was very easy to identify areas of good CNT emitters. In comparison to the images of the FWNT cathodes, the MWNTs were more rigid and straight in appearance. They also did not appear to group or clump together to the same degree as the FWNTs.

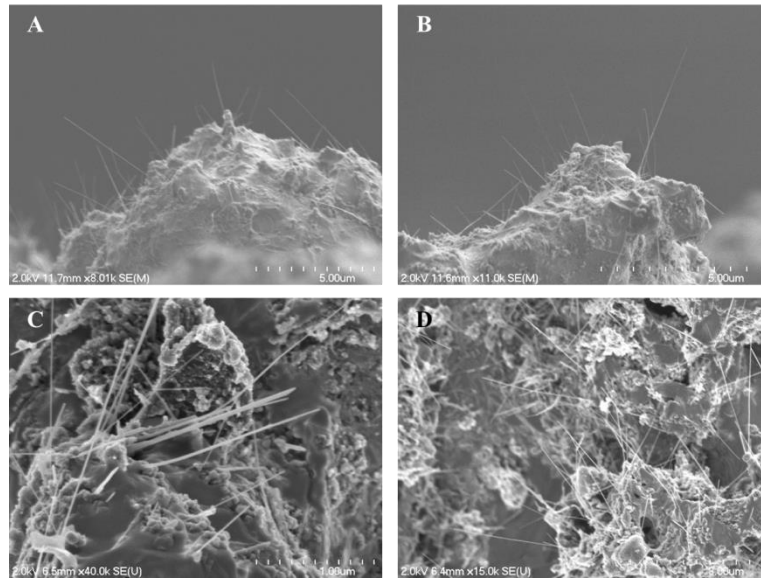


Figure 6.15 SEM images of the MWNT cathode before it was used for field emission measurements. (A) and (B) are profile views. (C) and (D) are top views. The scale bar in (D) is 3 μm .

After field emission testing the cathode was imaged again, and the results are shown in Figure 6.16. Both the top and side views showed plenty of carbon nanotubes, with many that could contribute to field emission. When the MWNT field emission measurements were completed, the cathode was no longer able to emit high amounts of current. However, the SEM images did not indicate heave emitter damage. The other two unused MWNT cathodes in the chamber were also imaged and found to have no damage, and plenty of carbon nanotubes.

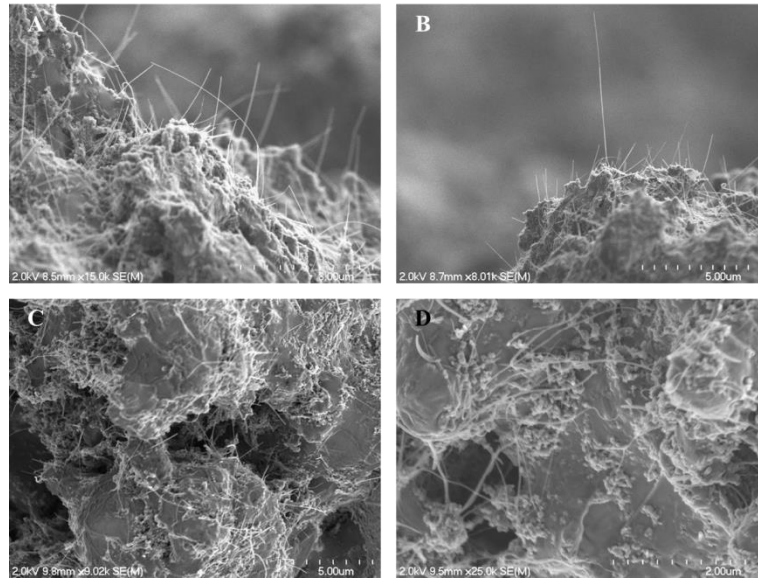


Figure 6.16 SEM images of the MWNT cathode after it was used for field emission measurements. (A) and (B) are profile views. (C) and (D) are top views.

6.3.5 Optical microscope images of gate mesh

All of the optical microscope images were taken after mesh removal from the vacuum chamber. The damage experienced by the gate mesh was a result of the field emission measurements, mostly through heating and ion bombardment. The images shown are samples of the range of damage found along the entire mesh.

6.3.5.1 FWNT cathodes' gate mesh

Figure 6.17 shows sample images taken of the gate mesh above cathode FW 1. Part A shows a portion of the gate mesh that had no visible damage, and the bars remained straight and parallel to one another. Part B shows a region where a bar had been warped from heat. Part C shows surface pitting with a rough appearance, as well as a clean break. It is possible that this break was a mechanical break made while putting the chamber together. It is also possible that a micro-crack formed during fabrication was exacerbated by the heat load,

causing the bar to break cleanly. Part D shows a higher level of pitting and surface damage of the tungsten bars. Parts E and F are higher magnification images of different bars where extreme pitting and melting occurred. This damage seems to be a combination of melting from high temperatures and pitting from electron bombardment from the cathode.

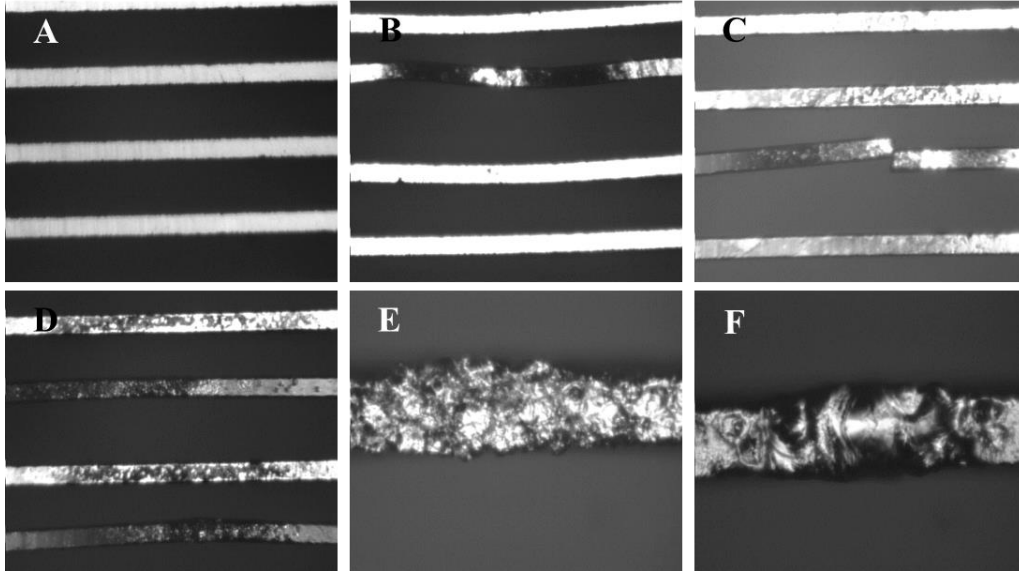


Figure 6.17 Optical microscope images of the gate mesh above cathode FW 1 during field emission measurements.

The gate mesh above cathode FW 2 was used much less and fared much better. The images of that mesh are shown in Figure 6.18. Part A shows bars that retained their original shape, but have some visible micro-cracks. Part B shows an area of slight melting and warping. This type of damage was the most extensive found.

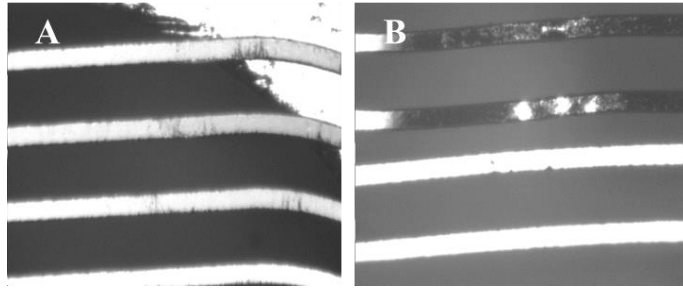


Figure 6.18 Optical microscope images of the gate mesh above cathode FW 2.

The last set of images are those of the FWNT cathode that went largely unused during the field emission measurements, but showed an area of severe surface damage in SEM images (Figure 6.13). Corresponding gate mesh images are shown in Figure 6.19. As can be seen in parts A and B, most of the gate mesh was intact, with only slight bending and surface pitting. However, parts C and D show low and high magnification images of one location that had a complete bar break and melted at the ends. It appears that one end of the melted bar break was below the other, creating a closer point to the cathode than anywhere else on the gate mesh. This, combined with the SEM and EDS data, indicates that the severe damage on that spot of the cathode was likely due to this gate mesh damage.

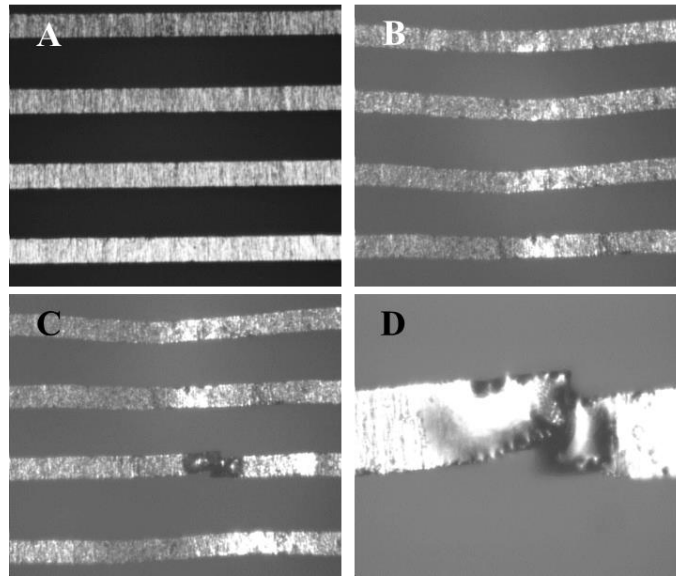


Figure 6.19 Optical microscope images of the gate mesh above the third FWNT cathode in the testing chamber, only used during conditioning.

6.3.5.2 MWNT cathode's gate mesh

Figure 6.20 shows images of the gate mesh above the MWNT cathode used in field emission measurements, after it was removed from the vacuum chamber. The other two gate mesh were imaged (not shown) and found to have experienced no damage apart from slight surface erosion. Part A is representative of the majority of the gate mesh. Some bars were not of uniform thickness, but were not severely warped or pitted. Parts B through D, however, show several bars that were broken in one region of the gate mesh. Some of the bars were not merely broken, but portions had been completely removed. The severe gate mesh damage is likely the cause of the poor cathode performance toward the end of the field emission experiments. This explains how the SEM images of the MWNT cathode showed no damage, but the performance of the cathode was poor. For cathodes to function properly, the gate mesh must be intact.

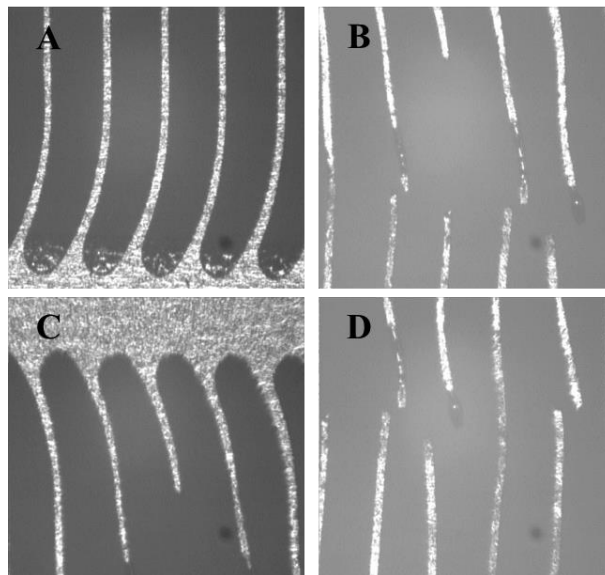


Figure 6.20 Optical microscope images of the gate mesh above the MWNT cathode used in field emission experiments.

6.4 Discussion

The field emission tests showed that it was possible with both FWNT and MWNT cathodes to produce an anode exposure of 50 mAs within a 2 s pulse. The goal of these experiments was to test the feasibility of producing 2D mammogram images with the CNT cathodes in the present iteration of the s-DBT X-ray tube. In addition, another type of cathode was tested—the MWNT cathode. Because the goal was feasibility, not stability, it is difficult to use these results to determine whether one type of nanotube is more suitable for 2D imaging than the other. The oxidation results presented by Koh et al. suggested that the MWNTs survive better in an oxygenated environment than the FWNTs. The field emission results showed that one FWNT cathode failed to meet all of the target conditions, whereas a single MWNT was able to. However, a direct comparison is unwise because the cathodes were conditioned and ramped up for varying amounts of time, and the number of pulses

taken at each setting were inconsistent between the experiments. The FW 1 cathode was used approximately twice as long as the MWNT. The cathodes were also at different distances from the gate, with the MWNT cathodes being farther away, although exact distance measurements were inaccurate. A larger distance would result in higher voltages needed to extract the same current, increasing the power demand on the cathode and degrading it more quickly. It was also shown that the gate mesh performance impacted field emission performance, independently of the characteristics of the nanotubes themselves.

In terms of relevance for breast imaging, it was shown that CNT cathodes are capable of producing enough current for a 50 mAs image within 2 s. For practical use, this time would need to lower to at least 1 s, only be achievable by increasing anode current to 50 mA, assuming a 50 mAs anode exposure. That would require at least 83 mA of cathode current, assuming a 60 % transmission rate.

The transmission rate of the FWNT testing was only 55.4 ± 0.4 %, measured at low anode voltages. The average transmission rate for all MWNT testing, over all 1,218 pulses including conditioning, was 58 ± 4 %. There have been 2 s-DBT tubes built. For typical operation, the transmission rate among all beams in both tubes is approximately 61 %. Therefore, a 60 % transmission rate assumption is reasonable. The testing chamber measurements tended to have a lower transmission rate than the actual s-DBT tubes have.

It has not been tested whether the cathodes can produce 83 mA in a 1 s pulse. As presented in Chapter 5, FWNT cathodes were able to produce 80 mA in 250 ms pulses, which would only produce 1/4 of the required 50 mAs anode exposure. From the short pulse-width data, it is clear that higher current is possible. What is unknown is if the emitters would survive at a pulse width lengthened to 1 s. One possibility for extracting more current from

the cathodes might be to decrease the gate-cathode distance, increasing the field at the nanotube tips.

Another factor for 2D imaging consideration is the heat load on the anode. 50 mA of current at 40 kVp would generate 2,000 W of power on the anode which could be detrimental to the tungsten anode. The feasibility of this would require further study or a redesign of the anode. These experiments have also shown that the heat load capability of the gate mesh is an important part of the field emission capabilities of the tube. If the gate mesh breaks down, even with an intact cathode, high currents will not be produced.

The testing done on the cathodes was very close to the requirements for a 2D mammography image, but only for thinner breasts of compressed thicknesses of 1 cm – 2 cm⁹. The target anode exposure used in this study, 50 mAs, is in the middle to low range of exposures needed for mammography imaging. Clinically, it would be necessary to have the capability of higher currents. Very thick breasts could require several hundred mAs for an acceptable screening image. In addition, the pulse widths tested were too long to be practical for imaging in a clinical setting. The pulse would need to be approximately 1 s long. Assuming a target exposure of 300 mAs, and that 80 mA could be produced from the CNT cathodes, a pulse width of 3.75 s would be required. If higher currents were possible, the heat capacity of the gate mesh and anode would have to be increased as well.

6.5 Conclusion

The feasibility of using FWNT and MWNT cathodes for 2D radiography of thinner breasts within 2 s – 4 s was illustrated. However, 2 s – 4 s is much longer than the current imaging time for 2D mammography. To image thicker breasts, 3.75 s may be the quickest that the required dose could be produced from the current s-DBT CNT cathodes. To add 2D

functionality to the s-DBT system useful for all patients in a clinical setting, the cathodes would need to match current output in a time similar to thermionic X-ray sources, at most 1.5 s. Adding 2D functionality would expand the prototype s-DBT systems' clinical appeal for imaging and intervention applications. However, it seems that the current design is not feasible for producing the dose needed to screen a wide range of patients. More realistic applications would be a 2D scout image for positioning procedures, automatic exposure control measurements, or a low-quality 2D image accompanying a DBT scan for comparing previous 2D images in the patients' medical record.

The feasibility results did not give definitive evidence that one type of nanotube cathode would perform better than the other. Further testing would be required and need to be conducted as a lifetime test, not sequential testing on a single cathode, as in this study. To definitively prove usefulness in 2D imaging, it would be necessary to image phantoms and measure image quality of the technique. Exact dose measurements would need to be conducted to ensure anode exposure translates into enough dose to produce images of acceptable quality.

REFERENCES

- 1 Hendrick, R. E. *et al.* Comparison of acquisition parameters and breast dose in digital mammography and screen-film mammography in the American College of Radiology Imaging Network digital mammographic imaging screening trial. *AJR. American journal of roentgenology* **194**, 362-369, doi:10.2214/AJR.08.2114 (2010).
- 2 Qian, C. *et al.* Fabrication of small diameter few-walled carbon nanotubes with enhanced field emission property. *J Nanosci Nanotechnol* **6**, 1346-1349, doi:10.1166/Jnn.2006.140 (2006).
- 3 Koh, A. L., Gidcumb, E., Zhou, O. & Sinclair, R. Observations of carbon nanotube oxidation in an aberration-corrected environmental transmission electron microscope. *ACS Nano* **7**, 2566-2572, doi:10.1021/nn305949h (2013).
- 4 Dresselhaus, M. S., Dresselhaus, G. & Avouris, P. in *Topics in Applied Physics* Vol. 80 (eds Claus E. Ascheron & Hans J. Kolsch) (Springer-Verlag Berlin Heidelberg, Germany, 2001).
- 5 Oh, S. J., Zhang, J., Cheng, Y., Shimoda, H. & Zhou, O. Liquid-phase fabrication of patterned carbon nanotube field emission cathodes. *Appl. Phys. Lett.* **87**, 3738 (2004).
- 6 Qian, X. *et al.* Design and characterization of a spatially distributed multibeam field emission x-ray source for stationary digital breast tomosynthesis. *Med Phys* **36**, 4389-4399 (2009).
- 7 Liu, Z. *et al.* Carbon nanotube based microfocus field emission x-ray source for microcomputed tomography. *Appl. Phys. Lett.* **89**, 103111-103113 (2006).
- 8 Li, X., Zhang, D. & Liu, B. Workload and transmission data for the installation of a digital breast tomosynthesis system. *Med Phys* **40**, 063901, doi:10.1118/1.4803470 (2013).
- 9 Hologic. *Selenia Dimensions Quality Control Manual* (Catalogue No. MAN-01965, Hologic, USA, 2011).

CHAPTER 7: s-DBT SYSTEM PERFORMANCE

The purpose of this chapter is to outline the performance and study results obtained with the two s-DBT X-ray systems.

7.1 Optimization study results

This section is a summary of the work done by Tucker et al.¹ to determine the s-DBT system configuration parameters that produce the highest spatial resolution. The data was taken on the s-DBT system in the laboratory.

7.1.1 Artifact spread function

Artifact spread function (ASF) is a quantity used to measure the z-axis spatial resolution in tomosynthesis imaging. The z-axis direction is perpendicular to the detector plane. In tomosynthesis imaging, objects are focused on their particular focal planes, but are blurred across other planes. The ASF measures the extent of a particular object's artifact across all focal planes. In this case, the region of interest (ROI) was a 0.54 mm aluminum oxide spec within the ACR phantom, shown in Figure 5.7. The distance between focal planes was 0.5 mm. Figure 7.1 shows the ASF results found using either 14° or 28° angular coverage. The raw ASF at different focal planes was calculated from the maximum intensity in the ROI by

$$ASF(z) = \frac{|\max(\text{signal}(z)) - \mu_{bkg}(z)|}{\mu_{bkg}(z)}$$

where z is the focal plane location, and $\mu_{bkg}(z)$ is the average background pixel value of the ROI. The data was fit to a Gaussian, and the FWHM measured.

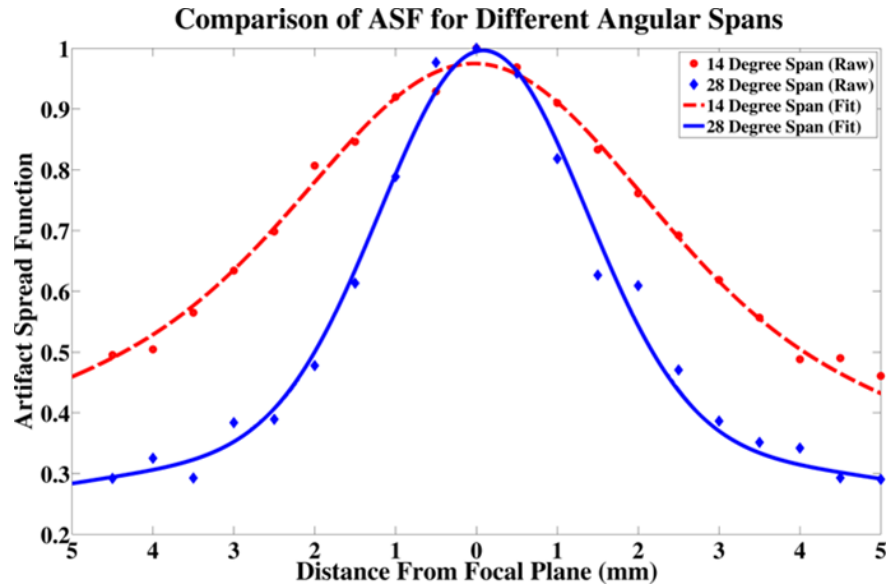


Figure 7.1 Plot of the ASF of a 14° angular span (red) and of a 28° angular span (blue). Number of projection images and total entrance dose were held constant. Reprinted with permission from Tucker et al., Med. Phys., 40, 031917-8, (2013). Copyright 2013, American Association of Physicists in Medicine.

When the angular span increased from 14° to 28°, the FWHM of the ASF data decreased by approximately 50 % from 7.80 mm to 4.08 mm. The ASF decreases with increasing angular coverage, as can be seen in Figure 7.2, because more information is collected in the projection images. Decreasing ASF is desirable because it reduces image clutter from out of focus objects.

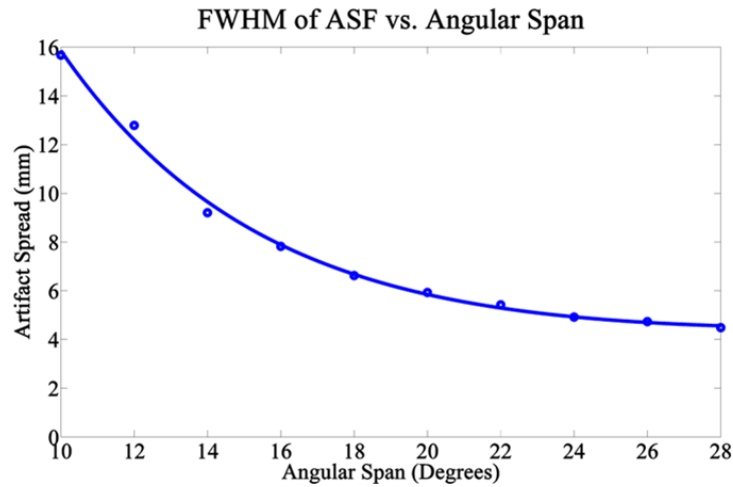


Figure 7.2 FWHM of ASF data at various angular spans. Reprinted with permission from Tucker et al., *Med. Phys.*, 40, 031917-8, (2013). Copyright 2013, American Association of Physicists in Medicine.

7.1.2 Modulation transfer function

The spatial resolution in the x and y directions (in the detector plane) of the system is measured through the modulation transfer function (MTF) in units of cycles/mm. System MTF depends on both the X-ray focal spot size and the detector pixel size. It was measured by imaging a 50 μm tungsten wire placed at an angle with respect to the chest wall, and then reconstructed from each projection. The line spread function (LSF) was sampled along the wire on the in-focus plane. The LSF samples were combined, taking into account the angle of the wire, fitted to a Gaussian, and transformed with the Fourier transform to produce the MTF. The 10 % value was quoted for the in-plane spatial resolution. Figure 7.3 presents system MTF results measured from a reconstruction of 15 projections over a 28° angular span. Using 70 μm pixels the MTF was 5.15 ± 0.05 cycles/mm, and with 140 μm pixels it was 4.20 ± 0.03 . At the smaller pixel size, MTF increased by 25 %, indicating greater spatial resolution.

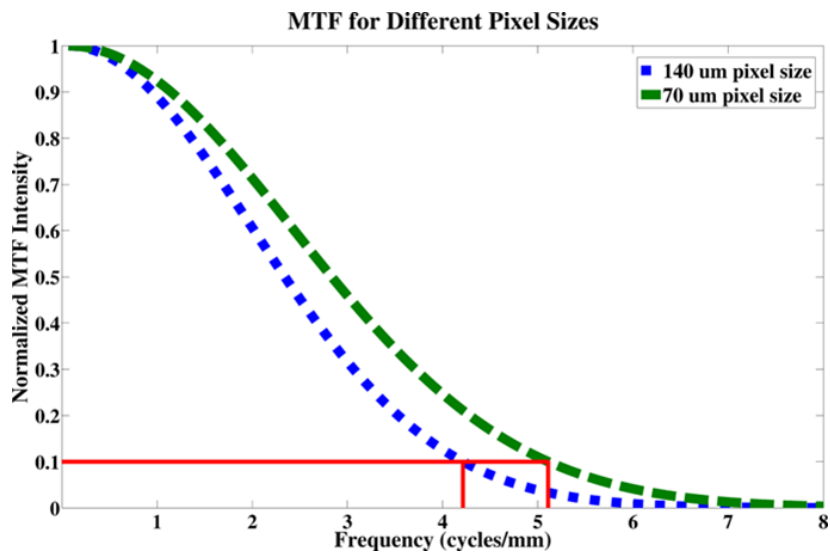


Figure 7.3 MTF of the s-DBT system for two different detector pixel sizes. Reprinted with permission from Tucker et al., Med. Phys., 40, 031917-8, (2013). Copyright 2013, American Association of Physicists in Medicine.

The best spatial resolution for the s-DBT system was achieved using 15 projections over an angular span of 28° and a detector pixel size of $70 \mu\text{m}$.

7.2 System operation over time

Portions of this section are reprinted from Gidcumb *et al.* 2014 *Nanotechnology* **25** 245704.

Long-term stability of the CNT cathodes was measured by analyzing the prototype s-DBT system's cathode voltage increases over a two-year timespan. Increases in the cathode voltage required to extract the same current indicates cathode degradation. Typically, all cathodes used in the s-DBT tube were run at approximately 39 mA. Therefore, the cathode voltages required to produce 39 ± 1 mA of current were recorded over time. This was done for all 31 CNT cathodes over a two-year period, during which the device was heavily used

for tomosynthesis imaging and characterization, with the cathodes assigned even numbers having been used most.

In addition to cathode voltage increases, transmission rate measurements were made over time. This was done to verify the overall stability of tube performance. The measurements were taken with both focusing electrodes grounded, minimizing current loss to the focusing electrodes. Most imaging with the s-DBT system is done with focusing electrodes grounded, so this measurement reflects the transmission rate available during typical imaging. The time points for these measurements were September 2011 and June 2013. The 2011 data had an anode voltage of 15 kV, 35 mA cathode current, and 295 ms pulse widths. The 2013 data had an anode voltage of 30 kV, two cathode current settings of 10 mA and 40 mA, and 250 ms pulse widths.

7.2.1 Cathode voltage over time

Figure 7.4 plots the measured cathode voltage required to emit 39 mA of cathode current from each of the 31 cathodes in the prototype s-DBT system. The measurements were done at two time points. The first was December 2010 and the second was November 2012, giving almost two years' time between when these measurements were taken. During that time, the system was used heavily for imaging, but not all beams were necessarily fired for each use.

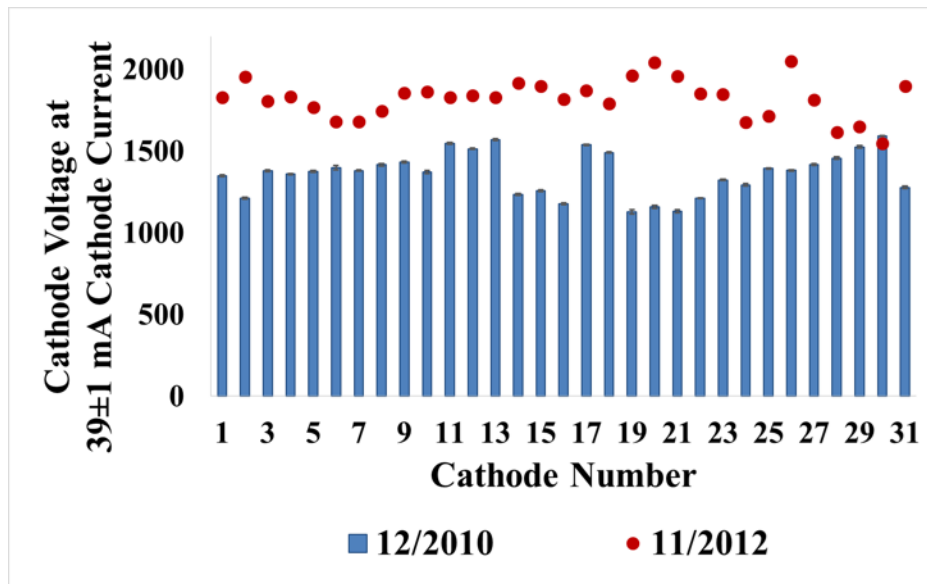


Figure 7.4 Cathode voltages required to produce approximately 39 mA cathode current, for each of the 31 s-DBT system cathodes, at two different points measured in Dec. 2010 and Nov. 2012. This data demonstrates that all 31 cathodes in a working s-DBT tube can reliably operate for several years. Dec. 2010 data provided by Derrek Spronk. Reprinted from Gidcumb *et al.* 2014 *Nanotechnology* **25** 245704.

Almost every beam showed an increase in the cathode voltage required to emit 39 mA of current over the two-year time period. This increase was due to degradation of the cathodes whereby the best CNT emitters were lost over time. To employ the other emitters required an increasingly strong electric field to be applied.

The original data, taken in December 2010, averaged 1,400 V applied between the cathode and the gate for all 31 cathodes, with a standard deviation of 130 V. Two years later, the average voltage to emit 39 mA was 1,800 V, with a standard deviation of 120 V. The measurements were made using a multi-pixel electronic control system in learning mode, using 250 μ s pulses. Typical imaging operation uses 250 ms pulses. From experience there is a ± 10 V discrepancy between learning curve values and operating values (J. Shan 2014, pers. comm.).

Cathode 30 showed a decrease of approximately 45 ± 8 V in the cathode voltage required to produce 39 mA of current. This indicates that either this cathode, under relatively heavy use, did not degrade as the others did, or even improved. Improvement is possible since individual cathodes perform differently over time. However, it is unlikely that the cathode improved over such a long time period. It is more likely an error occurred during the measurement of the initial cathode voltage.

The s-DBT tube is equipped with 31 cathodes, but in general, imaging protocols only call for groups of 15 beams to be used. The two groups generally used are the even numbered beams and the odd numbered beams. The numbering of the beams follows those used in the x-axis of Figure 7.4, where the odd numbers make up the odd beam group, and the same for the even beam group. Evaluating the degradation of even beams versus odd beams showed a similar average percent increases relative to the original voltage. On average, even beams' voltage increased 36 % with a standard deviation of 21 %. Odd beams increased, on average, 34 % with a standard deviation of 19 %. Even though the odd beams were used less regularly, their degradation matched pace with the more heavily used even beams. This indicates that cathodes undergo passive degradation from being in a chamber with other cathodes due to increased ion bombardment during momentary pressure increases during neighboring cathodes' field emission pulses. This is supported by general experience in the laboratory.

7.2.2 Transmission rate over time

Figure 7.5 and Table 7.1 show the results of transmission rate measurements of the s-DBT tube over time. Figure 7.5 plots the transmission rate of the 31 cathodes at two time points. The earliest time point is approximately 10 months after the initial time point of the

cathode voltage measurements in Figure 7.4. The data taken during September 2011 included each cathode. The data from June 2013 only includes the cathodes given even number identifiers.

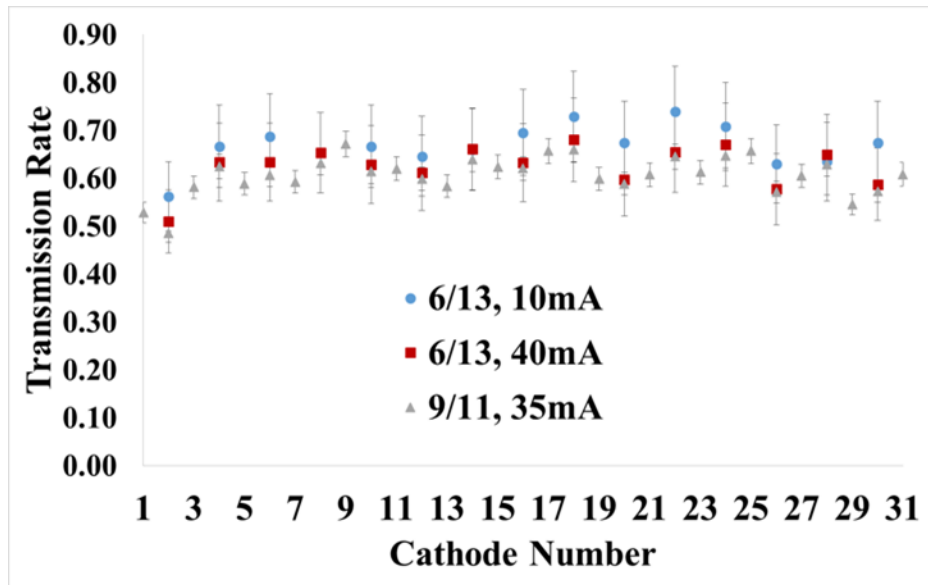


Figure 7.5 Plot of the transmission rate, in fraction form, for each cathode in the s-DBT prototype X-ray tube at various dates. The legend entry contains the date the data was taken in month and year, followed by the cathode current. Sept. 2011 data provided by Andrew Tucker. Reprinted from Gidcumb *et al.* 2014 *Nanotechnology* **25** 245704.

Table 7.1 Transmission rate data summary. Reprinted from Gidcumb *et al.* 2014 *Nanotechnology* **25** 245704.

Date (month/year)	Anode voltage (kV)	Cathode current (mA)	Pulse width (ms)	Average transmission rate (%)	Standard deviation (%)
6/13	30	10	250	67	4
6/13	30	40	250	63	4
9/11	15	35	295	61	4

Table 7.1 lists all settings used for each measurement, including anode voltage and pulse width. The average transmission rate and standard deviation were for all beams measured in that data set; 15 for the earliest date, and 31 for the later date. In 2011, the

average transmission rate for all cathodes was 61 %, and in 2013 it was 67 % and 63 % for the 10 mA and 40 mA data, respectively. The average transmission rate over time was unchanged, taking into account the standard deviation of the data sets, equal to 4%. The 10 mA data was barely within the average range of the higher current settings, implying a higher transmission rate is available at lower currents.

7.2.3 Summary

Among all 31 cathodes, there was an average increase of 400 V over two years, during which the system was heavily used and continues to be used to this day. The transmission rate data taken two years apart were consistent, taking into account the standard deviation among all 31 beams. This indicates a constant correlation between cathode current produced and usable anode current for X-ray production over time. In addition, the constant transmission rate reveals no failure or significant change in the extraction gate mesh, or any other part of the electrode assembly. Over the lifetime of the prototype s-DBT system, both cathode performance and transmission rate were stable and consistent.

7.3 Specimen study results

An imaging trial was conducted in which surgical breast specimens were imaged with the s-DBT system. The images taken with the s-DBT system were compared to magnification 2D imaging² and CTM DBT imaging³. Surgical breast specimens were imaged after being removed from the patient to verify that the entire lesion was removed, and that the margin around the lesion was adequate. Typically, the specimens are placed in a plastic specimen container with a location grid inside, and then imaged with a 1.8x magnification stand on a FFDM system. Imaging the specimens in 3D could improve visualization of the removed lesions and verify if the margins around the lesions are adequate. The lesions of interest are

typically masses with spiculated or obscure borders and areas containing malignant or suspicious microcalcifications.

7.3.1 Lesion characterization versus 2D imaging

The initial breast specimen study set out to show whether s-DBT would result in improved image quality and reader confidence versus 2D magnification imaging for assessing surgical breast specimens. The specimens were imaged on the s-DBT system and a GE Senograph 2D mammography system. The study recruited a total of 39 patients. The specimens were imaged using 26 kVp anode voltage. The anode exposure in 2D imaging varied depending on specimen size. 3D imaging protocol with the s-DBT system used 15 projections over 28° and 95 mAs of total anode exposure. The projections images were reconstructed using the RTT software, with 0.5 mm slice spacing. Only the lesion focal plane was observed by the reader.

The study had one reader to assess the images for malignancy and margin clearance. Malignancy was scored 1 to 5, with 5 being highly malignant. For margin assessment, the margin was positive if the lesion reached the specimen edges and negative if the lesion was fully contained within the specimen. A rating for margin assessment confidence was given ranging from -3 to +3, depending on whether the reader was more confident in the 2D image or the 3D image, respectively. Figure 7.6 shows a side-by-side comparison between a 3D reconstructed slice and a 2D magnification image. The s-DBT image shows sharper lesion margins than the 2D image, because overlap from surrounding tissue was removed.

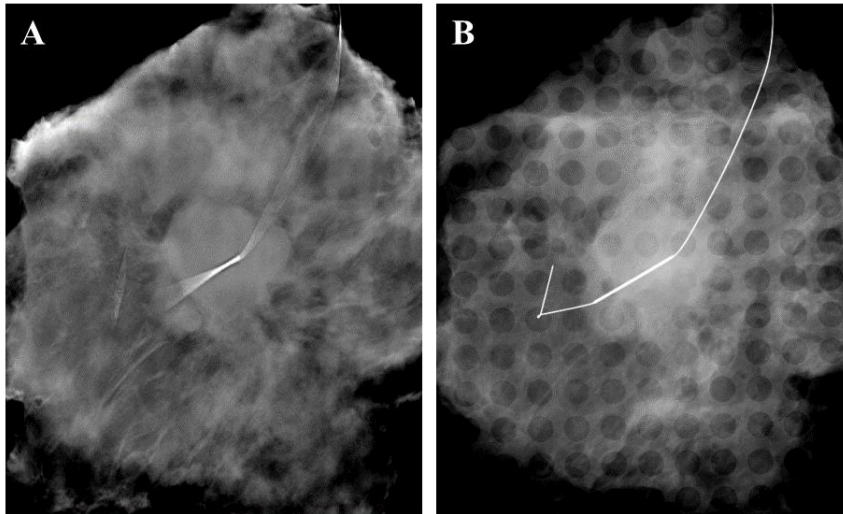


Figure 7.6 (A) Reconstructed slice from the s-DBT system of a breast specimen with a suspicious mass. (B) 2D magnification image of the same breast specimen. Reprinted with permission from SPIE. Tucker et al., Comparison of the diagnostic accuracy of stationary digital breast tomosynthesis to digital mammography with respect to lesion characterization in breast tissue biopsy specimens: a preliminary study, Proc. of SPIE, Vol. 8668, 2013.

All images were read twice, once with the 2D image presented first, and once with the s-DBT reconstructed slice presented first. The modality presented first was given a malignancy score. After both modalities were viewed first, the s-DBT margin confidence was given. Twenty specimens were viewed with the 2D image presented first, and 13 were scored correctly (65%) compared to histological results. The average confidence score for s-DBT margins was 0.74 ± 1.59 . Twenty-one specimens were viewed with the s-DBT slice shown first, and 15 were scored correctly (71%). The s-DBT margin confidence was -0.20 ± 1.40 . These results indicate that the s-DBT method produced equivalent results to the magnification 2D imaging, but with only one reader the results are not conclusive.

After these results were published, three more readers were recruited for this comparison study, and 50 total specimen images were read. The full results have not yet been published. In addition to inconclusive results, the study design inherently favors the 2D

modality. The 2D modality employs 1.8x magnification and a smaller focal spot size, designed to enhance lesion visibility. The s-DBT, and other DBT, systems are not optimized for specimen imaging in this way. Even so, initial results show the possibility of s-DBT being a viable option for specimen imaging.

7.3.2 Microcalcification visibility versus CTM DBT

Twenty-three of the specimen samples recruited through the previous study, with known breast lesions of BI-RADS 4 or 5, were also imaged on the Hologic Selenia Dimensions DBT system, employing continuous tube motion (CTM). Past studies showed that CTM DBT when added to 2D imaging improved the sensitivity and specificity of mass detection versus 2D imaging alone, but the improvement was not shown for microcalcification (MC) imaging⁴. It was hypothesized that MC imaging could be improved with s-DBT due to the increased spatial resolution in comparison with the CTM DBT systems. The MTF of the s-DBT system has been measured to be 5.15 cycles/mm compared to 2.8 cycles/mm for the CTM system^{1,5}.

Both sets of images from the two systems were reconstructed with the RTT software. From the 23 specimens, 12 individual MCs were selected from 5 specimens for image analysis. The chosen MCs were clearly visible with both modalities. MCs were analyzed on in-focus slices to calculate the area for in-plane sharpness, and ASF for z-axis sharpness. It was assumed that smaller area indicates a more accurate image. The area was estimated by multiplying pixel size by the number of pixels in the MC, the latter determined by a 50 % threshold of the maximum pixel intensity. The FWHM of the ASF of each MC was calculated as described in Section 7.1.1.

Figure 7.7 shows an example of an MC chosen for analysis. Parts C and D show that s-DBT increases sharpness of the MCs in comparison with the CTM system. In addition, the angular span of the s-DBT system was greater, allowing increased artifact removal from the out-of-plane MCs, in this particular cluster.

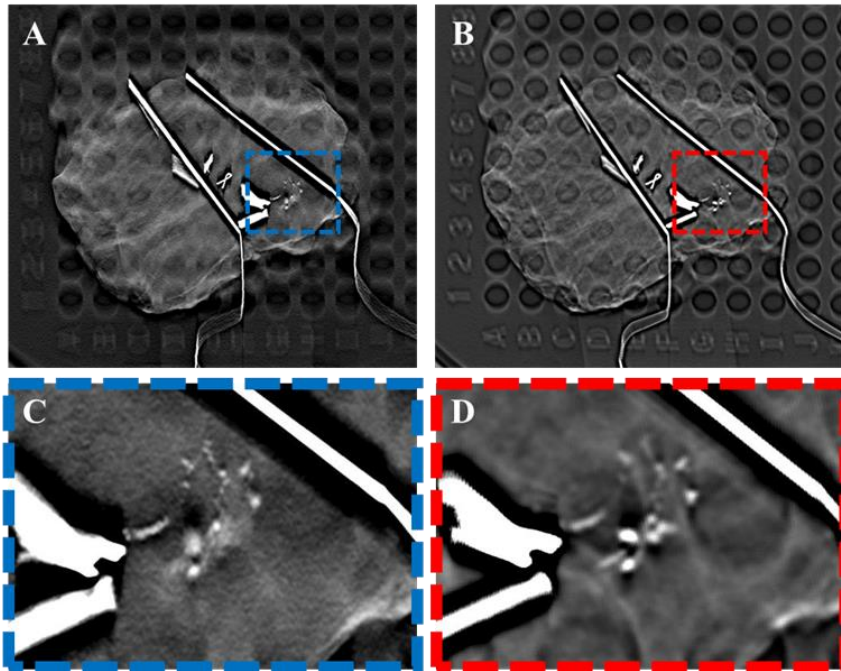


Figure 7.7 (A) Reconstruction slice of a specimen with a large cluster of MCs using the s-DBT system. (B) The same cluster imaged with the CTM DBT system. (C) Zoomed-in area of the MC cluster as indicated by the blue box in (A). (D) Zoomed-in area of the same MC cluster imaged with the CTM DBT system. Reprinted with permission from SPIE. Tucker et al., Increased microcalcification visibility in lumpectomy specimens using a stationary digital breast tomosynthesis system, Proc. of SPIE, 2014.

In total, 12 microcalcifications were analyzed for sharpness. Figure 7.8 shows images of the first 6, and analysis results for all 12 are listed in Table 7.2. Visual inspection of Figure 7.8 shows that the MCs are smaller in the s-DBT images. This is shown in Table 7.2 through the percentage decrease in area of each MC in the s-DBT images, compared to the CTM

DBT images. The average decrease was 29 ± 13 %. This result was expected due to the higher spatial resolution of the s-DBT system and confirms that higher spatial resolution leads to increased sharpness of MCs. In analyzing the ASF data, the s-DBT system reduced the FWHM by an average 2.0 ± 0.7 mm, over all 12 MCs. In addition to better in-plane spatial resolution, s-DBT increased sharpness in the z-axis direction as well.

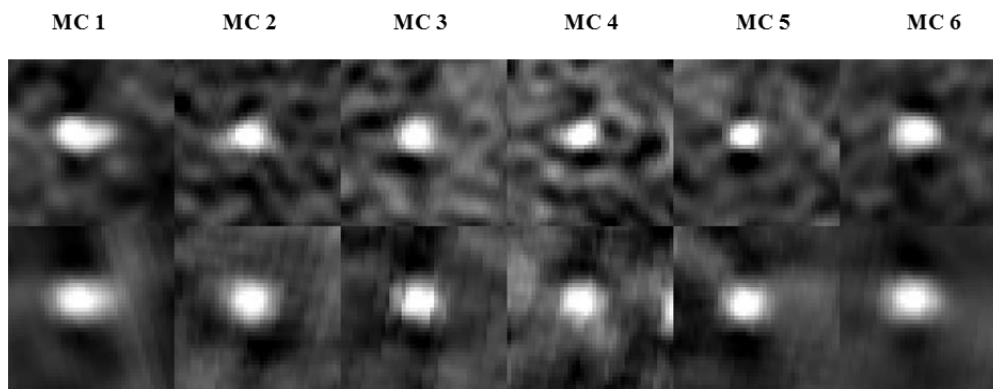


Figure 7.8 Regions of interests around the first 6 chosen MCs. The s-DBT images are in the top row, and the CTM DBT images are in the bottom row. Reprinted with permission from SPIE. Tucker et al., Increased microcalcification visibility in lumpectomy specimens using a stationary digital breast tomosynthesis system, Proc. of SPIE, 2014.

Table 7.2 MC area and FWHM of the ASF for each of the 12 MCs, for both imaging modalities. DBT refers to the CTM DBT system. Reprinted with permission from SPIE. Tucker et al., Increased microcalcification visibility in lumpectomy specimens using a stationary digital breast tomosynthesis system, Proc. of SPIE, 2014.

MC number	s-DBT area (mm ²)	DBT area (mm ²)	Percent area decrease for s-DBT	FWHM of ASF (s-DBT) (mm)	FWHM of ASF (DBT) (mm)
1	3.60	4.09	11.98	3.5	5.0
2	2.33	3.66	36.34	2.5	4.5
3	2.79	3.05	8.52	2.0	4.0
4	1.69	2.79	39.43	1.5	5.0
5	1.74	3.08	43.51	1.5	4.0
6	2.96	3.59	17.55	2.5	4.0
7	1.70	2.74	37.96	1.5	3.5

MC number	s-DBT area (mm ²)	DBT area (mm ²)	Percent area decrease for s-DBT	FWHM of ASF (s-DBT) (mm)	FWHM of ASF (DBT) (mm)
8	2.21	3.69	40.11	1.5	4.0
9	2.10	3.69	43.09	2.5	4.0
10	2.43	3.21	24.30	3.5	4.5
11	2.50	3.10	19.35	3.5	5.0
12	2.82	3.76	25.00	2.5	5.0

Comparison of MC images between s-DBT and CTM DBT showed that increased sharpness increases visibility as well, as in Figure 7.7. Increased sharpness is due to the decreased effective focal spot size of the s-DBT system, because it is not enlarged through motion, as in the CTM system. Sharpness in the depth direction was increased due to a larger angular span in the s-DBT projections. The 15 s-DBT projections were taken over 28° compared to 15° for the 15 CTM projections. A larger angular span increases resolution across more of the frequency domain.

7.4 Patient images

The s-DBT technology is currently being evaluated by an Institutional Review Board-approved patient trial at N.C. Cancer Hospital¹⁰ (Chapel Hill, NC). At this point, 9 patients have been imaged for the trial. Images of the first patient are shown in Figure 7.9 and Figure 7.10. Figure 7.9 shows CC slices at different heights, and Figure 7.10 shows the MLO view. The goal of the study is to recruit a total of 100 patients.

¹⁰ U.S. National Library of Medicine. (January 2013). Comparison of Stationary Breast Tomosynthesis and 2-D Digital Mammography in Patients With Known Breast Lesions. *ClinicalTrials.gov*. Retrieved November 4, 2013. From clinicaltrials.gov/ct2/show/NCT01773850.

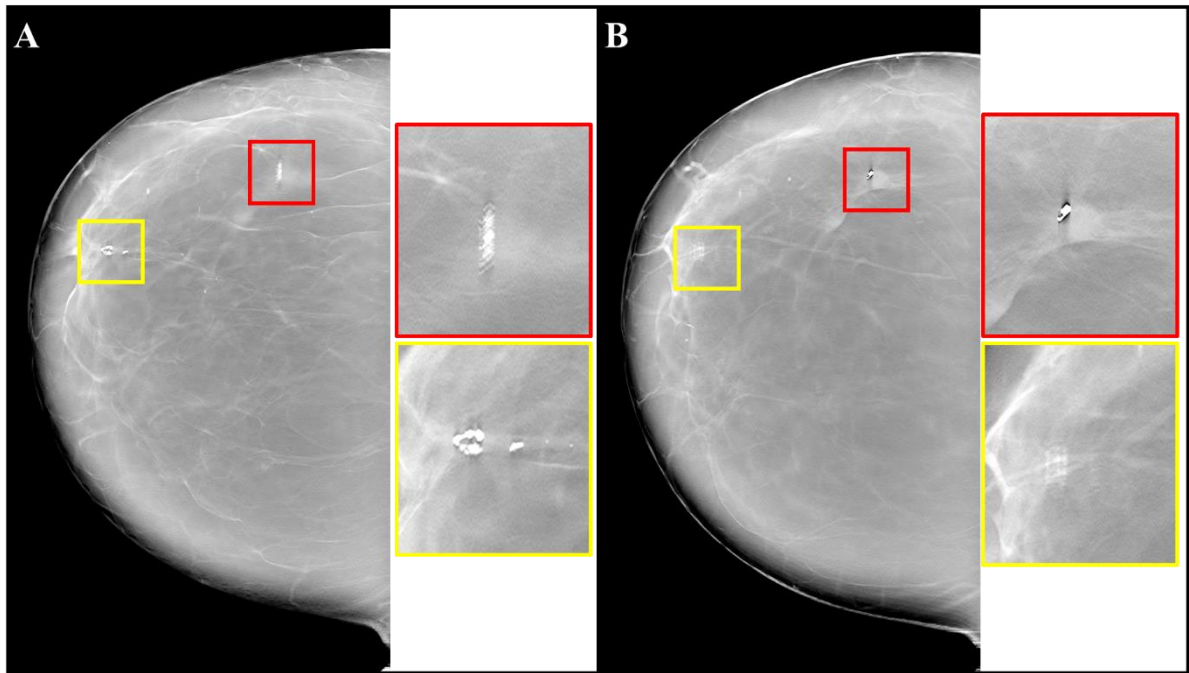


Figure 7.9 Reconstructed CC image slices of Patient 1 at heights of (A) 13.5 mm and (B) 26.5 mm. The red and yellow boxes illustrate different objects coming into focus at different heights. The red box shows a mass marked by a metal biopsy clip, and the yellow box shows a microcalcification cluster. Total exposure was 91 mAs over 15 projections, with a peak voltage of 34 kVp.

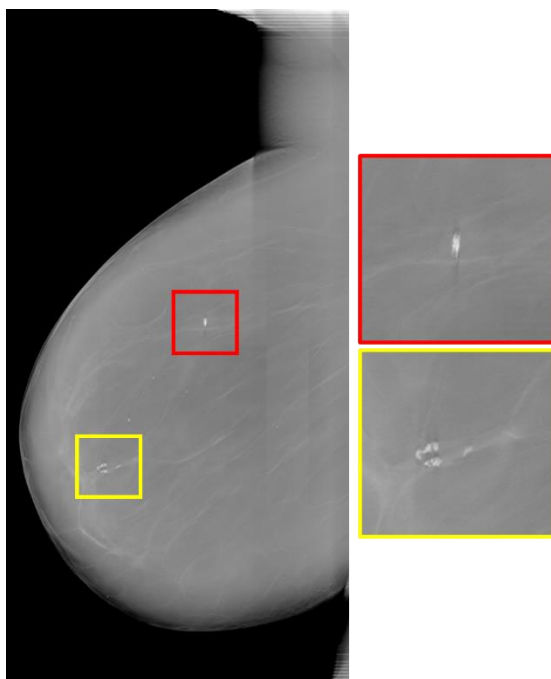


Figure 7.10 A reconstructed MLO slice from Patient 1, at 16.5 mm, with the same areas highlighted in yellow and red as in Figure 7.9. Total exposure was 97 mAs over 15 projections, with a peak voltage of 38 kVp.

REFERENCES

- 1 Tucker, A. W., Lu, J. & Zhou, O. Dependency of image quality on system configuration parameters in a stationary digital breast tomosynthesis system. *Med Phys* **40**, 031917, doi:10.1118/1.4792296 (2013).
- 2 Tucker, A. W. *et al.* in *Medical Imaging 2013: Physics of Medical Imaging*. (eds Robert M. Nishikawa, Bruce R. Whiting, & Christoph Hoeschen) 86685Q-86685Q-86688 (SPIE, 2013).
- 3 Tucker, A. W. *et al.* in *Medical Imaging 2014: Physics of Medical Imaging*. (eds Bruce R. Whiting & Christoph Hoeschen) 903316 (SPIE).
- 4 Michell, M. J. *et al.* A comparison of the accuracy of film-screen mammography, full-field digital mammography, and digital breast tomosynthesis. *Clin Radiol* **67**, 976-981, doi:10.1016/j.crad.2012.03.009 (2012).
- 5 Qian, X. *et al.* High resolution stationary digital breast tomosynthesis using distributed carbon nanotube x-ray source array. *Med Phys* **39**, 2090-2099, doi:10.1118/1.3694667 (2012).

CHAPTER 8: FOCUSING VOLTAGE OPTIMIZATION

8.1 Introduction

8.1.1 Focal spot size and the focusing electrodes

The focal spot size of an X-ray tube is an important factor in determining the spatial resolution of a system. Focal spot size of the s-DBT tube is affected by the cathode deposition area, gate mesh design, focusing electrodes, the anode, and distances between electrodes. The focusing electrodes were designed to reduce the electron beam divergence after it passes through the gate mesh. The focusing electrodes are electrostatic lenses that manipulate ion beam trajectories, similar to the way optical lenses focus light¹. The electric field created by the lenses changes the path of the ions. The divergent ions, in this case electrons, are focused into a finite focal spot size, but suffer from spherical aberration and aberration due to space charge effects. The s-DBT tube design employs two focusing lenses above the gate electrode. The first lens, F1, pre-focuses the divergent electrons after moving through the gate mesh, and primarily determines the focal spot size. The second lens, F2, acts to move the focal plane along the vertical direction depending on the size of the aperture (Figure 8.1). However, the effects of the two lenses are not entirely independent. Employing the focal lenses can decrease transmission rate by blocking the more divergent electrons. This is especially true if the electron's kinetic energy is increased, making the electrons more difficult to focus¹.

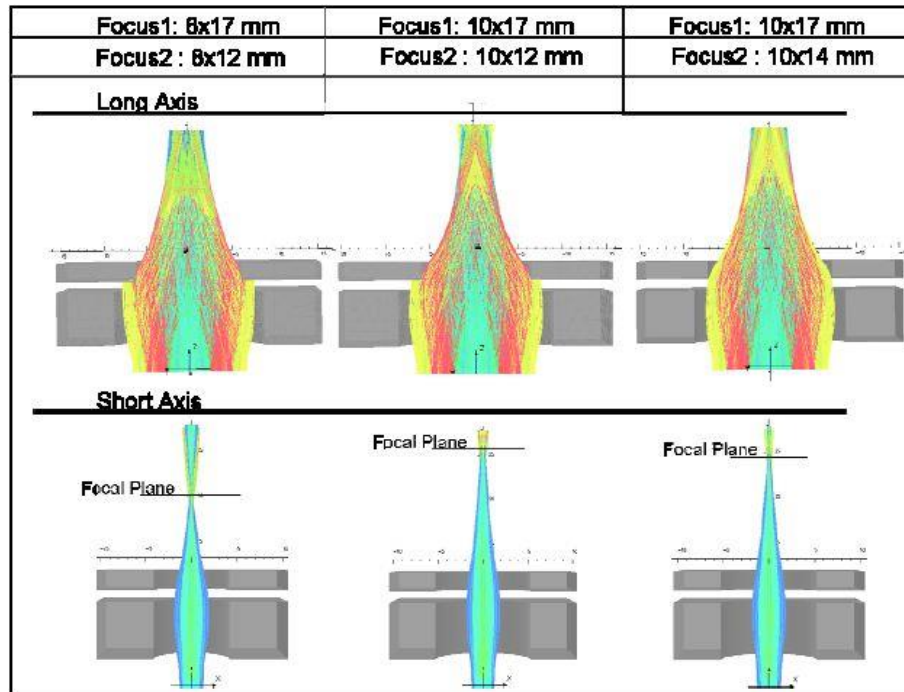


Figure 8.1 Representative beam profile exhibiting shift in focal plane along the axial direction with change in Focus 2 aperture. Figure reprinted with permission from S. Sultana, PhD thesis, 2010¹.

The focusing structure design, described in Chapter 3 (Figure 3.4) was designed to produce a focal spot size of $0.3 \text{ mm} \times 0.5 \text{ mm}$ (long \times short)¹. Long and short refers to the long and short dimensions of the CNT cathode, respectively. The dimensions in the short direction were limited by the 1.2 cm spacing between the cathodes in the s-DBT tube. Elliptical openings were found to be best in focusing electrons produced from s-DBT's larger cathodes. Initial study of the focusing structure in a testing chamber, using a woven gate mesh, showed that the focal spot size was $0.6 \text{ mm} \times 1.2 \text{ mm}$ (long \times short). The mesh was not the only difference during that test from the final design. The electrodes had slightly different parameters during that experiment, and are listed in Table 8.1¹.

Table 8.1 Dimensions for initial testing chamber focal spot size measurements. The long side dimension is listed first. The electrodes had elliptical apertures. Reused with permission from S. Sultana, PhD thesis, 2010.

	Gate electrode	Focus 1 electrode	Focus 2 electrode
Dimensions (mm)	15 × 5	15 × 5	10 × 5

Further optimization was completed leading to the final design, almost identical to that shown in Figure 3.4. The main differences between the optimized design determined by Dr. Sultana and the structure in the s-DBT tube are the distances from the anode to Focus 2 and from Focus 2 to Focus 1. The optimized design gave an anode-Focus 2 distance of 15 mm and a Focus 2-Focus 1 distance of 4.238 mm¹. The increase in the anode-Focus 2 distance in the final design has the effect of increasing the focal spot size from that measured in Dr. Sultana's study. Experimental data on the final design resulted in the smallest focal spot size of 0.5 mm × 0.6 mm (long × short). The settings were 20 mA cathode current, 30 kV anode voltage, 1000 V_{Rel} on Focus 1, and 1200 V_{Rel} on Focus 2. The focusing voltages were relative to the applied cathode voltage¹. The optimized design decreased the focal spot size in both directions, with respect to the initial results found with the dimensions listed in Table 8.1. The minimum focal spot sizes for all 31 cathodes in the first s-DBT tube were 0.64 ± 0.04 mm × 0.61 ± 0.05 mm (short × long)². Those reported values correspond to the FWHM. When the width at 20 % maximum was measured, the sizes increased to 0.98 ± 0.06 mm × 0.93 ± 0.07 mm (short × long). The cathode current was 43 mA, and anode voltage was 40 kV. The voltages applied to the power supplies were 1000 V on Focus 1 and -1000 V on Focus 2. The voltages relative to the cathode voltage are unknown.

Another way to describe the two directions is the scanning and non-scanning direction, which are equivalent to the short and long convention used up to this point. The

scanning direction is also called the y-direction on the detector, and the non-scanning the x-direction on the detector. These conventions are illustrated in Figure 8.2.

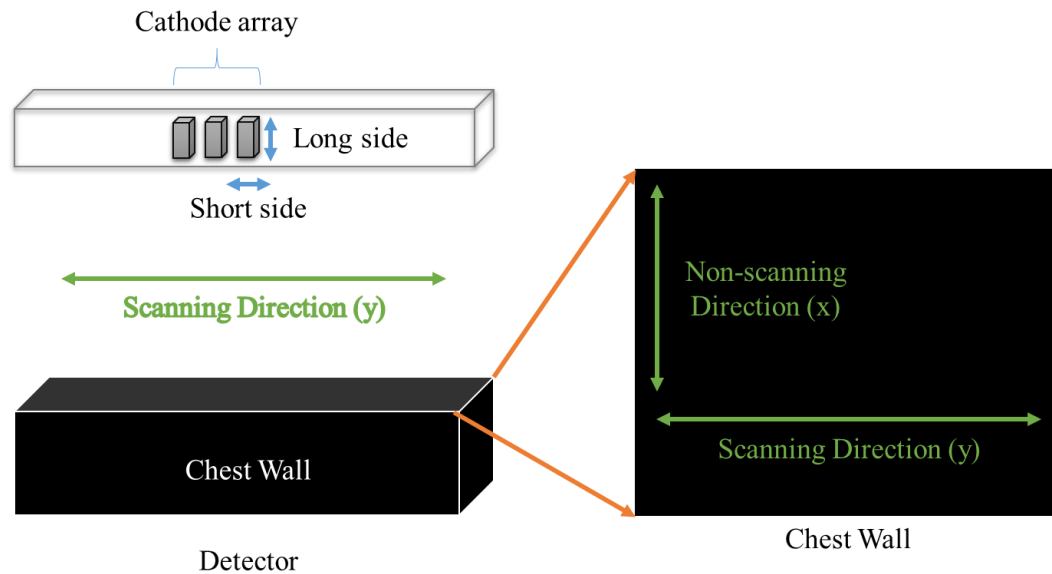


Figure 8.2 Illustration showing directional naming conventions. The short and long side of the cathode gave rise to the terms short and long side of the focal spot size. The short side corresponds to the scanning direction, and the long side corresponds to the non-scanning direction. The right side of the picture is a top-view of the detector plane.

8.1.2 Modulation transfer function

A measure of spatial resolution that incorporates the influence of the imaged object, the X-ray beam characteristics, the detector response, and image processing is known as the modulation transfer function (MTF)³. Modulation is defined as the output contrast of an object divided by the input contrast of the object⁴. Modulation depends on the object's size, or its spatial frequency. Objects of higher spatial frequency, or smaller size, have lower output contrasts. The MTF plots the modulation transfer intensity versus spatial frequency in

cycles/mm. The MTF is calculated from the magnitude of the Fourier transform of a normalized line spread function (LSF) as

$$MTF(f) = |FT\{LSF(x)\}|$$

where f is spatial frequency, x is distance, and FT stands for Fourier transform. A wider LSF leads to a narrower MTF, indicating a system with poorer spatial resolution⁴. The figure of merit for spatial resolution is the spatial frequency at which the MTF lowers to 50 % or 10 % of the maximum.

The LSF is derived from imaging either a point, a line or slit, or an edge. The goal is to produce an impulse response from the imaging system. When using a pinhole phantom, a point spread function (PSF) is produced which can be thought of as linear collection of many LSFs⁴. Imaging an edge gives an edge spread function (ESF), and this method is used when scattering plays a large role in spatial resolution⁴. An ESF is differentiated to obtain the corresponding LSF⁵. An LSF is produced directly from imaging a thin wire or slit.

MTF is important in breast imaging because measuring system sharpness is required for testing system performance and assuring quality standards are met⁶. As more digital systems are used, MTF has become a more common way to measure system performance. Previously, line pair phantoms were used more commonly, giving spatial resolution in line pairs per millimeter instead of cycles per millimeter. A study by Marshall and Bosmans showed the MTF of the Siemens Inspiration and Selenia Dimensions DBT systems decreased with increasing height above the detector surface. It was also shown that the wire method is more reliable for measuring the MTF of DBT systems. At the detector surface the 50 % system MTFs, including focal spot and detector MTFs, were given for both systems. A comparison between these results and past wire-method measurements on the s-DBT and

other DBT systems are shown in Table 8.2 and Table 8.3. The 10 % MTF values reported in Table 8.2 were estimated from data presented in the Marshall and Bosmans paper⁶. The s-DBT data in Table 8.2 and the data in Table 8.3 were taken at a different height than the data presented from Marshall and Bosmans, and cannot be considered an exact comparison.

Table 8.2 10 % MTF results from various DBT systems using the wire method. The MTF values are system values given from reconstructed images. Pixel sizes vary due to different detector binning and reconstructions between the systems. Siemens and Hologic data are for 0 mm above detector surface.

	Siemens Inspiration ⁶	Hologic Selenia Dimensions ⁶	s-DBT ⁷	
10 % MTF scanning direction (cycles/mm)	2.8	4.2	5.2	4.2
10 % MTF non-scanning direction (cycles/mm)	4.6	5.3		
Reconstructed pixel size (μm)	85	91	70	140

Table 8.3 10 % MTF results comparing Hologic Selenia Dimensions and s-DBT. The MTF values are from central projection images, and do not incorporate effects of the reconstruction. Pixel sizes are identical.

	Hologic Selenia Dimensions ²	s-DBT ²
10 % MTF scanning direction (cycles/mm)	4.0	5.1
10 % MTF non-scanning direction (cycles/mm)	5.4	5.2
Projection pixel size (μm)	140	140

The data in these tables are intended to give an example of what typical MTF values are for commercial DBT systems, and also compare those to measurements done so far on the s-DBT system. The reconstruction MTF data, Table 8.2, shows that s-DBT is comparable to the Hologic Selenia Dimensions system when using binned mode, but improves when the pixel size is lowered for full resolution projection images. The central projection data in Table 8.3, all taken at UNC, suggests that s-DBT has improved spatial resolution in the scanning direction and comparable spatial resolution in the non-scanning direction with

respect to the Hologic system. A comparison between the s-DBT data in the two tables also shows that reconstruction causes system MTF to drop relative to the projection MTF of the same system by approximately 1 cycle/mm.

8.2 Purpose

Past MTF measurements on the s-DBT system were done with the focusing electrodes grounded to the tube housing. Normal s-DBT operation has been conducted with both focusing electrodes grounded to preserve transmission rate, at the sacrifice of improved focal spot size. As shown in Table 8.2 and Table 8.3, s-DBT was able to produce higher 10 % MTF values than other DBT systems, with focusing grounded. The goal of this work was to research what further spatial resolution improvements could be for the s-DBT system if focusing voltages were applied, and to determine the tradeoff in loss of transmission rate.

8.3 Methods

8.3.1 Experimental setup and MTF measurement

The phantom used to measure MTF was a cross-wire tungsten wire phantom, with 50 μm wire thickness. Two strands of wire were strung perpendicular to one another across a stainless steel frame. The phantom was taped to the underside of a breast compression paddle, as shown in Figure 8.3. For each image, the compression paddle height was set to 4.5 cm with a pressure of 8 lbs to 9 lbs. The compression force was against the base of an ACR phantom, allowing the compression paddle to be held parallel to the detector surface. The source-to-image receptor distance (SID) was 70 cm, and the source-to-object distance (SOD) was 63.9 cm. The SOD was calculated by

$$\begin{aligned} SOD = SID & - \text{detector cover-to-detector distance} \\ & - \text{tungsten wire-to-detector cover distance} \end{aligned}$$

where the detector cover-to-detector distance was 2.5 cm and the tungsten wire-to-detector cover distance was 3.6 cm. Magnification was calculated as SID divided by SOD, and was 1.095 for all results presented here.



Figure 8.3 Photos of the experimental setup. (A) Top-view of the MTF cross-wire phantom attached to the breast compression paddle. A line pair phantom is also present. (B) Side-view of the setup showing the display on the gantry, used for relocating the paddle after each image. (C) Front-view showing the phantom suspended below the compression paddle. (D) ACR phantom, after the top and wax insert were removed, was used to level the compression paddle so that it was parallel to the detector surface.

An example of an X-ray image produced from this setup is shown in Figure 8.4. A line-pair phantom was imaged, though not used in data analysis. The two perpendicular tungsten wires can be seen. The blue box outlines the wire and region used to measure MTF in the y-direction (MTF_y), which is the scanning direction. The other wire, with the orange box, was used to measure MTF in the x-direction (MTF_x), or non-scanning direction. It is difficult to see from the image, but the MTF phantom is not aligned perfectly to the chest-wall side of the image. There is a slight angle, done intentionally to prevent aliasing of the wire on the detector.

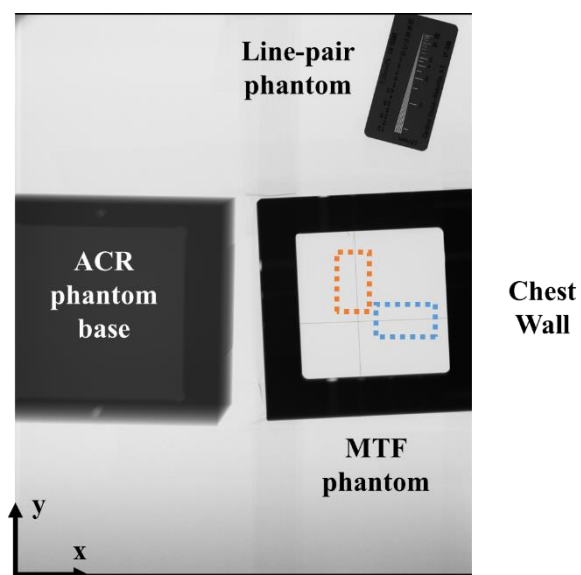


Figure 8.4 Example image taken during the experiments, with each item labeled. The chest wall side of the image is the right side, and the x and y coordinates have been labeled according to the conventions of Figure 8.2. The orange box shows the region of wire used to measure MTF in the x-direction, and the blue box is that for MTF in the y-direction.

All images were taken using a cathode current of 43 mA, anode voltage of 30 kV, and a pulse width of 235 ms. The detector was set to full resolution mode, so the pixel size of the projection images was 70 μm . For each setting, cathode current, cathode voltage, and anode current were recorded with an oscilloscope. Both projection and reconstruction data sets were taken. Projection data was taken using beam P11 only, and reconstruction data was taken with the odd-numbered beams, excluding P13 and N13. The reconstructions consisted of 15 projections covering an angular span of 28° , with a slice separation of 0.5 mm. The reconstructed images were analyzed at 1.4x magnification, giving a pixel size of 0.0459 mm. The in-focus plane was at a slice depth of 37.0 mm.

The method used to calculate MTF from the wire phantom was a slant-angle oversampling method^{8,9}. After the image or image set was acquired, images were corrected using blank and dark images. After correction, sets were reconstructed using software from Real Time Tomography (RTT). The wire ROI was selected in either the y or x direction, as in Figure 8.4, on the projection image or in-focus plane, for reconstructions. Within the selected ROI, the wire was sampled many times, creating a series of LSFs along its length. The sampled LSFs were corrected for the wire angle and combined into one, oversampled LSF, as shown in part A of Figure 8.5. The FT of the LSF produced the MTF curve, shown in part B of Figure 8.5. The 10 % value was recorded as the figure of merit. Each image was analyzed five times to obtain an average value for each image at each setting.

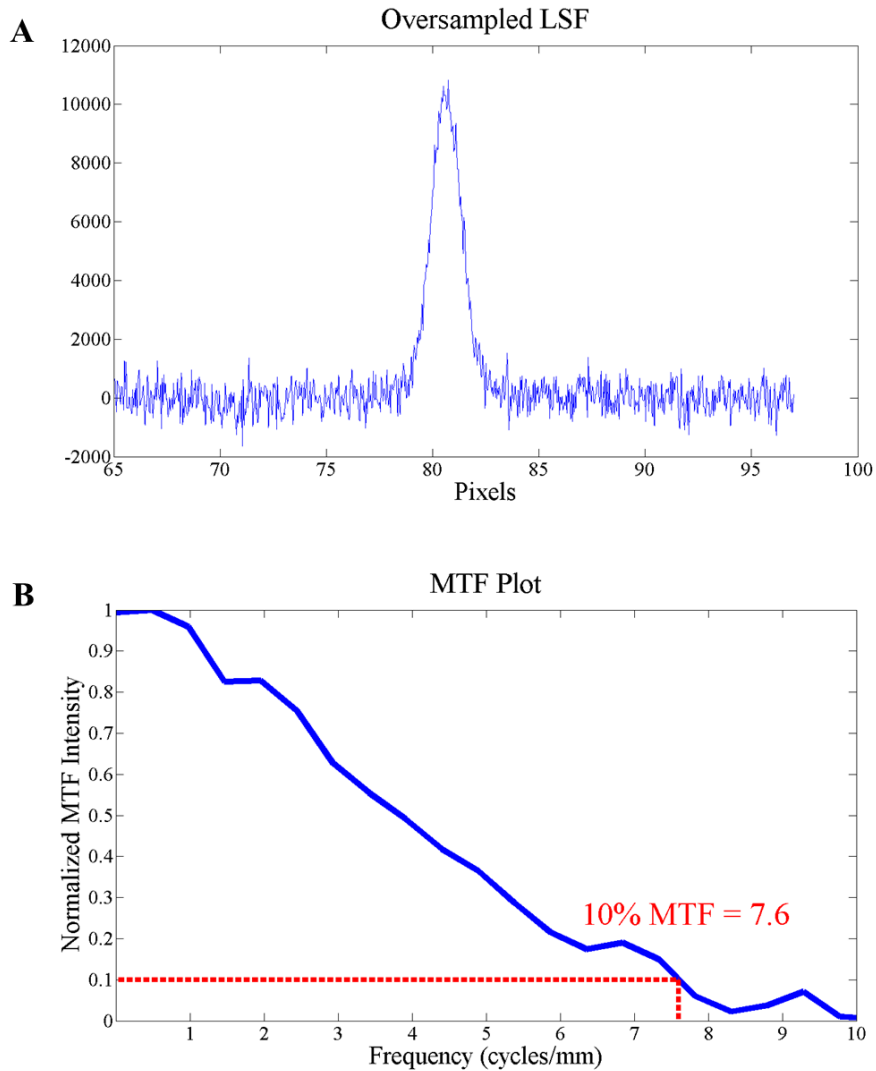


Figure 8.5 Example data analysis of the image shown in Figure 8.4 from beam P11 for MTF in the x-direction. (A) The resultant oversampled LSF produced from many LSFs along the wire ROI and adjusted for wire angle. (B) MTF resulting from the FT of the oversampled LSF in (A), with a 10 % value of 7.6 cycles/mm.

8.3.2 Tested range of focusing voltages

Initial I-V characteristics of each beam indicated that beam P11 was closest to the average voltage among all 15 beams to produce 43 mA of cathode current. Therefore, beam P11 was used to narrow down the voltage ranges that would be tested for all 15 beams

constituting the reconstruction image sets. Then, the reconstructed image sets were evaluated to determine the optimal focusing setting that, on average, produced the best spatial resolution for all 15 beams. Fifteen more beams in the tube were not evaluated because they were not intended for clinical imaging use at the time of these experiments.

There are two possible ways to refer to the focusing voltages applied to the electrodes, the applied voltage or the relative voltage. The applied focusing voltage is the value set on the front panel of the power supplies for each electrode. Another way to quote the voltage is the relative focusing voltage, with respect to cathode voltage. That method was useful for past CNT X-ray tubes in which the cathode was grounded instead of the gate, as is the case in the s-DBT tube. This is more complicated because when the cathode voltage changes, i.e. for different currents or different cathodes being used, relative focusing voltages change. The gate lies between the cathode and focusing electrodes. Because the gate is grounded, the electric field created by the focusing electrodes is shielded from the effect of the cathode voltage. The electric field created by the focusing electrodes is affected more by the gate and anode potentials. Therefore, it is more useful to quote applied focusing voltages versus relative focusing voltages.

However, the relative voltages will be discussed, in case their calculation would be desired. The relative voltage is $V_{Rel} = V_{Appl} - V_{Cath}$, where V_{Appl} is the voltage applied to the focusing power supply and V_{Cath} is the cathode voltage. Table 8.4 shows an example of this calculation with both focusing electrodes grounded. When grounded, the focusing electrodes are at the same potential as the gate. Table 8.4 refers to 3 cathode groupings. The first is beam P11 alone, the beam chosen to do the initial measurements. The other two refer to the 15-beam setup for use in the clinical trial. The difference is the time when the averages

were calculated, either before or during these experiments. The second measurement includes the standard deviation among all 15 beams. The importance of these values is that they provided the basis of the voltage range tested.

Table 8.4 Relative focusing voltages when both F1 and F2 grounded. Cathode voltages are reported for 43 mA cathode current. Note: $V_{\text{Appl, F1}} = V_{\text{Appl, F2}}$, and $V_{\text{Rel, F1}} = V_{\text{Rel, F2}}$.

Beam configuration	$V_{\text{Cath @ 43 mA}}$ (V)	V_{Appl} (V)	V_{Rel} (V)
Beam P11	-1120	0	1120
Initial I-V 15-beam average	-1139	0	1139
Measured 15-beam average	-1140 ± 50	0	1140 ± 50

The range of settings chosen, listed in Table 8.5, were based on simulation testing done by Dr. Sultana¹, which were with respect to gate-cathode voltage. Figure 8.6 plots all settings tested using beam P11. The grounded setting has been outlined in orange for a point of reference. The settings tested using a full 15-beam set are outlined in purple, with the grounded setting also tested for comparison. It can be seen in Figure 8.6 that the region surrounding the purple-outlined markers was sampled more heavily, with 100 V increments, than the rest of the tested region.

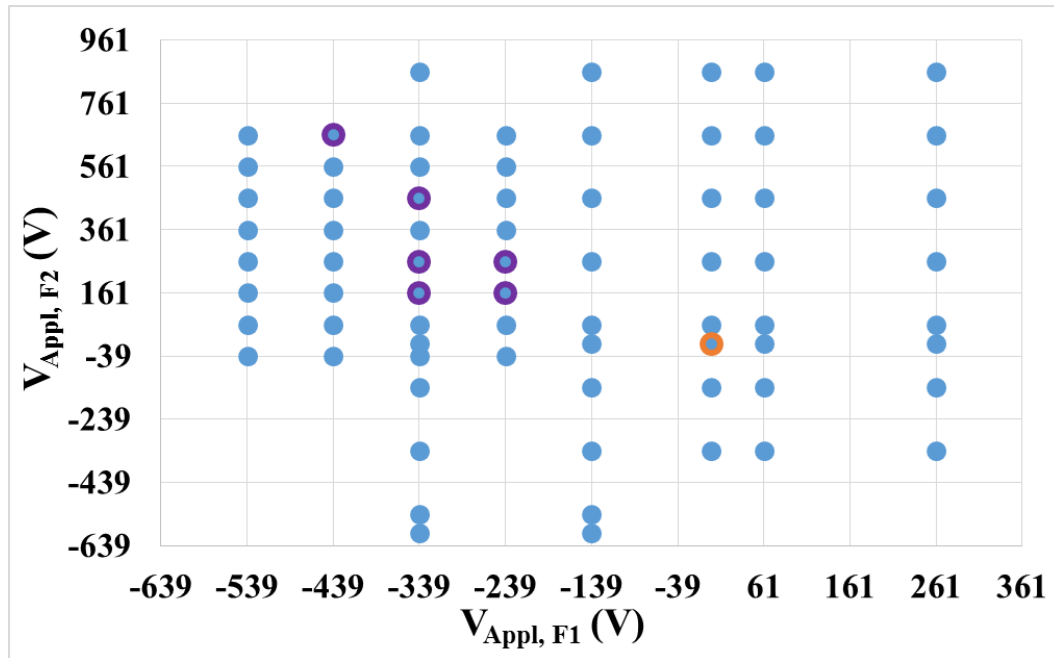


Figure 8.6 Plot of all applied focusing settings tested using beam P11 to narrow down an area to test the 15-beam set. The point outlined in orange is the grounded setting. The purple-outlined points were selected for testing all 15 beams.

Table 8.5 Tested ranges corresponding to Figure 8.6, for both the applied and relative focusing voltages. The relative values, as noted in the table, are in reference to the initial I-V data of the 15 beams.

Voltage range	F1 (V)	F2 (V)
V_{Appl}	-539 – 261	-600 – 861
V_{Rel} (Initial I-V 15-beam average)	600 – 1400	539 – 1700

8.3.3 Transmission rate measurements

The transmission rate for each setting was measured. The anode current was monitored from the back of a Spellman SL50P2000 power supply, and measured with a Tektronix oscilloscope, model TDS3014C. The Spellman power supply has a monitoring accuracy of ± 0.01 V, less than the oscilloscope accuracy of $\pm 2\%$, approximately ± 0.1 V in this case.

Cathode current was measured with the same oscilloscope but monitored from the ECS,

which has an error of ± 1 mA. The uncertainty of the transmission rate measurements was approximately 2 % for all readings. For the system transmission rates the stated error is the standard deviation among all 15 beams, larger than the 2 % error for the individual measurements.

8.4 Results

8.4.1 One-beam projection data using cathode P11

Cathode P11, the eleventh cathode to the right of the central cathode when facing the tube, was used to test a wide range of focusing voltage combinations. The MTF phantom projection for each setting was analyzed in both the x (non-scanning) and y (scanning) directions. Each direction was measured five times, with the average and standard deviation calculated. The averages in each direction were used to calculate the MTF product, to be used as a figure of merit for each setting, as follows:

$$MTF \text{ product} = \overline{MTF}_X \times \overline{MTF}_Y.$$

MTF product is in units of (cycles/mm)², and \overline{MTF}_X and \overline{MTF}_Y are 10 % of maximum MTF in their respective in-plane directions. Error in the MTF product was calculated with the standard deviations of the MTF values in each direction:

$$\delta MTF \text{ Product} = |MTF \text{ Product}| \sqrt{\left(\frac{\delta \overline{MTF}_X}{|\overline{MTF}_X|}\right)^2 + \left(\frac{\delta \overline{MTF}_Y}{|\overline{MTF}_Y|}\right)^2}.$$

$\delta \overline{MTF}_X$ is the standard deviation in the x-direction, and $\delta \overline{MTF}_Y$ is the standard deviation in the y-direction¹⁰. MTF product was chosen as the figure of merit to incorporate the effect of the MTF in each direction into a single parameter.

Figure 8.7 displays the MTF product results for all settings shown in Figure 8.6, plotted versus $V_{\text{App1, F2}}$ values and grouped by $V_{\text{App1, F1}}$ values. For $V_{\text{App1, F1}}$ values going from -539 V to -339 V, MTF product increased for all $V_{\text{App1, F2}}$ values. At more positive $V_{\text{App1, F1}}$,

MTF product decreased for most $V_{\text{App1, F2}}$ values. There is are peak ranges of -200 V to -300 V for $V_{\text{App1, F1}}$, and 100 V to 300 V for $V_{\text{App1, F2}}$. At some more negative $V_{\text{App1, F2}}$ values, the MTF product falls to 0. The image quality was so bad that the MTF could not be calculated for those settings.

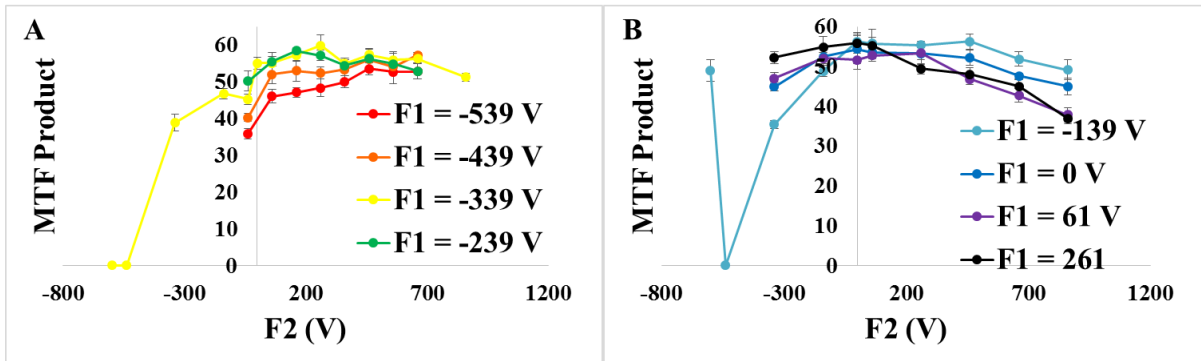


Figure 8.7 MTF product results for all settings from P11 images. MTF product is in $(\text{cycles/mm})^2$ and plotted versus V_{App1} on F2. (A) Results for the most negative V_{App1} settings on F1. (B) Results for more positive settings on F1. Results were separated for better data visualization.

To better visualize the trends over the focusing voltage ranges, the data was plotted using the curve fitting tool in Matlab. The data was fit using the interpolant setting with the nearest neighbor method. The results are presented in Figure 8.8. Part A plots the MTF product, part B plots MTF_X , and part C plots MTF_Y . The peak area for MTF product was around the brightest yellow area in part A. The peaks of MTF_X and MTF_Y are not in that same region. MTF_X peaks in the area where both focusing voltages are positive, and MTF_Y peaks in the area closer to the MTF product results. MTF_Y is worse in the areas where MTF_X is best, so the net benefit trends towards MTF_Y 's best values.

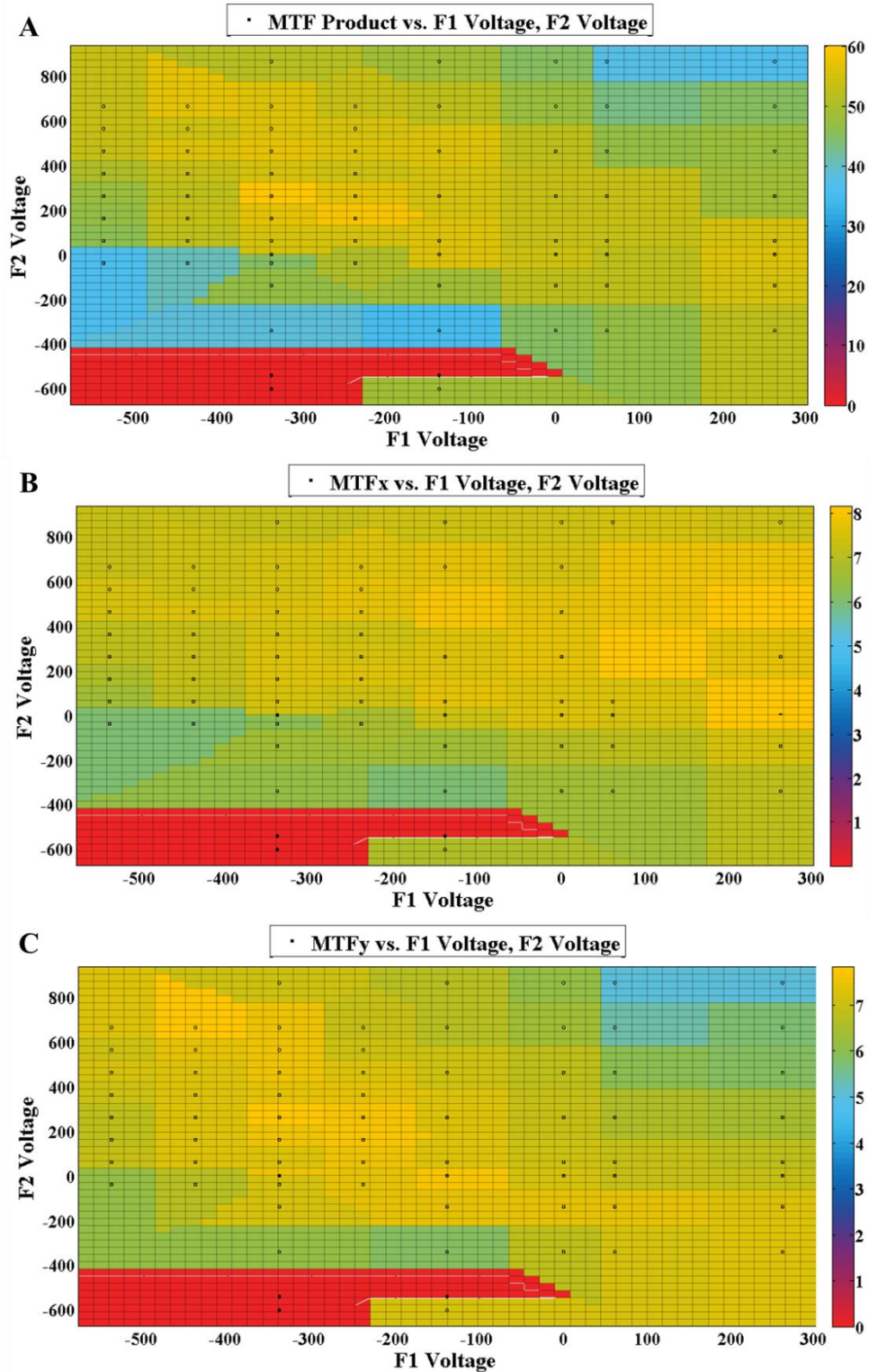


Figure 8.8 Color figures giving 2D distribution of MTF magnitudes over applied focusing voltages. (A) MTF product results. (B) X-direction only. (C) Y-direction only. Color bars to the right provide scaling information.

Transmission rate results for all focusing voltage combinations are displayed in Figure 8.9. In the MTF product optimal focusing voltage range, the transmission rate decreased relative to the grounded setting, but is very consistent. Transmission rate increased in the lower positive range of $V_{\text{App1, F2}}$ values, and as $V_{\text{App1, F2}}$ became more positive. When $V_{\text{App1, F2}}$ became increasingly negative, transmission rate dropped dramatically.

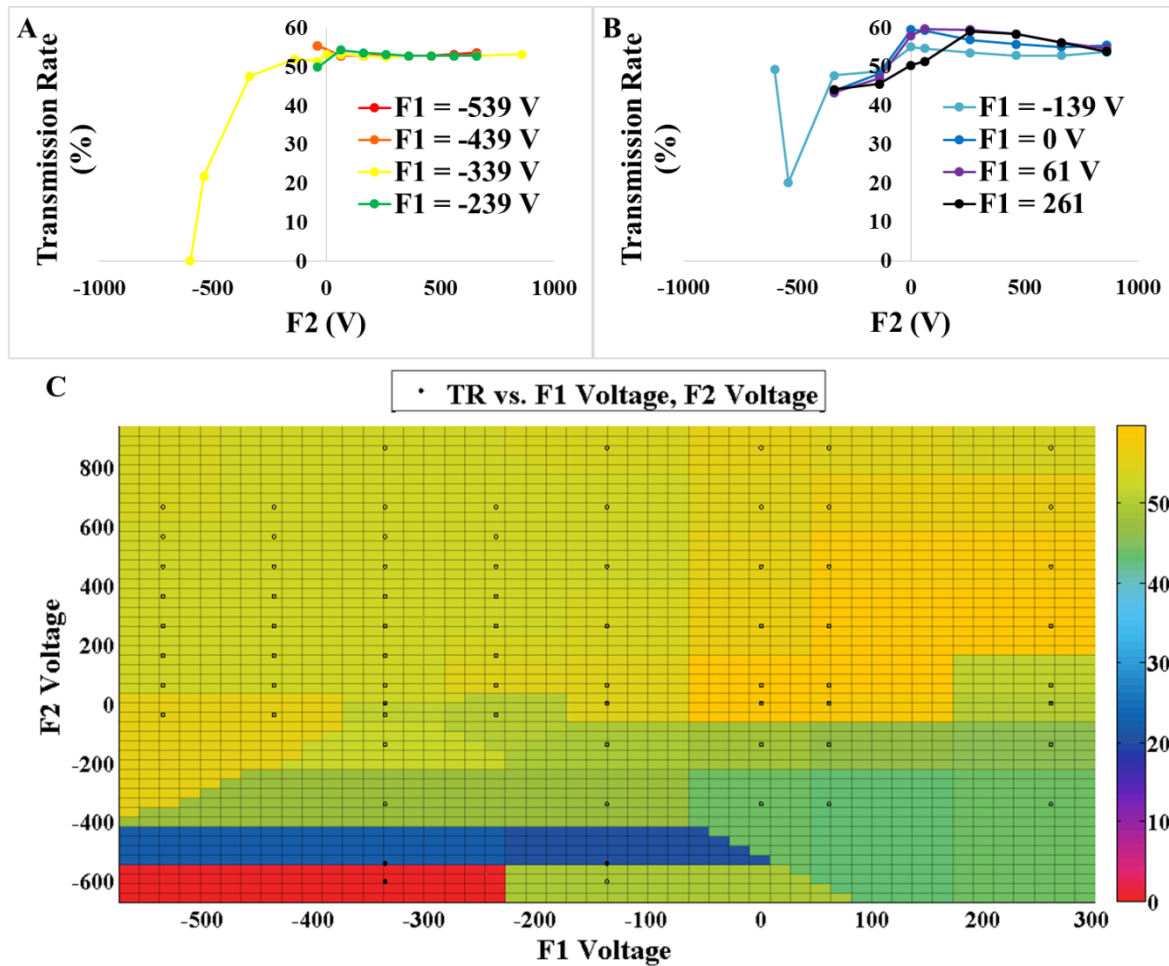


Figure 8.9 Transmission rate results for beam P11 at all tested focusing voltages. (A) and (B) separate the results according to more negative and positive V_{App1} settings on F1, respectively. (C) 2D color distribution of TR results, with the magnitude scale bar to the right.

Because the loss of transmission rate was uniform and within 10 % of the grounded setting in the peak MTF product region, the full 15-beam settings were determined from the highest MTF product values only. The top 6 values were chosen, with the addition of the grounded setting for comparison. Details of those settings are listed in Table 8.6. The percent difference from the grounded setting were calculated to determine the best settings because typical tube operation uses grounded focusing electrodes. The maximum improvement in MTF product was 10 %, achieved with setting $V_{\text{Appl, F1}} = -339 \text{ V}$, $V_{\text{Appl, F2}} = 261 \text{ V}$. The increase was primarily due to an increase of MTF in the y-direction. This setting had the largest drop in transmission rate of 7 %, which is a 12 % percentage drop. All settings improved with respect to the grounded setting in the y-direction, but two settings decreased in MTF_x : settings $V_{\text{Appl, F1}} = -439 \text{ V}$, $V_{\text{Appl, F2}} = 661 \text{ V}$ and $V_{\text{Appl, F1}} = -239 \text{ V}$, $V_{\text{Appl, F2}} = 261 \text{ V}$.

Table 8.6 Results from P11 of the best settings, chosen for 15-projection imaging. Ground refers to the setting $F1 = F2 = 0 \text{ V}$, where F1 and F2 refers to the electrode on which the voltage is applied.

F1 (V)	F2 (V)	MTF_x (cycles/mm)	MTF_y (cycles/mm)	MTF product (cycles/mm)²	Percent difference from ground (%)	TR (%)	Percent difference from ground (%)
-439	661	7.36 ± 0.09	7.77 ± 0.04	57.2 ± 0.8	5	53	-10
-339	161	7.6 ± 0.2	7.6 ± 0.1	57 ± 2	5	53	-11
-339	261	7.7 ± 0.2	7.8 ± 0.3	60 ± 3	10	52	-12
-339	461	7.6 ± 0.1	7.6 ± 0.1	57 ± 1	5	53	-11
-239	161	7.61 ± 0.04	7.7 ± 0.1	58.4 ± 0.8	7	54	-10
-239	261	7.48 ± 0.03	7.6 ± 0.2	57 ± 1	5	53	-10
0	0	7.6 ± 0.4	7.2 ± 0.3	54 ± 4	0	59	0

8.4.2 Fifteen-beam projection and reconstruction data

This section reports the results when applying the 7 settings listed in Table 8.6 to a 15-beam configuration. The beams tested were the odd numbered beams, except for P13 and N13, and including the central beam.

8.4.2.1 Transmission rates

The transmission rate for each cathode was measured during projection acquisition for each setting. Table 8.7 displays the average transmission rate and the standard deviation among the 15 cathodes. All settings had the same transmission rate, 54 %, except for ground which was 62 %.

Table 8.7 Transmission rate results for 15-beam imaging and the percentage difference from the grounded setting. TR error is the standard deviation between all 15 beams.

F1 (V)	F2 (V)	TR (%)	Percent difference from ground (%)
-439	661	54 ± 3	-12
-339	161	54 ± 3	-12
-339	261	54 ± 3	-13
-339	461	54 ± 3	-12
-239	161	54 ± 3	-12
-239	261	54 ± 3	-12
0	0	62 ± 3	0

8.4.2.2 Projection results

The results in this section are from the individual projections, not the reconstructed image volume. Each cathode's projection image was measured 5 times and averaged. The result for each setting is the average of all 15 cathodes' projection averages. The spatial resolution from the projection images does not include effects from the geometry calibration or reconstruction method used. It is only the result of source and detector characteristics.

Table 8.8 gives results for the MTF in each direction, and Table 8.9 gives results for the MTF product, all compared to the grounded setting.

Table 8.8 gives MTF_X and MTF_Y averages for all cathodes and the standard deviation. In comparison to the grounded setting, all settings maintained or increased spatial resolution in both directions, except for a drop of 2 % in the x-direction with $V_{App1, F1} = -439$ V, $V_{App1, F2} = 661$ V. Overall, the spatial resolution in the y-direction improved more than that in the x-direction. For the grounded setting, the x-direction MTF was higher than the y-direction. The focusing settings made the focal spot more isotropic, increasing the spatial resolution in the y-direction and becoming more equal to the x-direction.

Table 8.8 MTF results in both directions for the 15-beam imaging and percentage difference from the grounded setting. Error is the standard deviation in the measurement between all 15 beams.

F1 (V)	F2 (V)	MTF_X (cycles/mm)	Percent difference from ground (%)	MTF_Y (cycles/mm)	Percent difference from ground (%)
-439	661	7.2 ± 0.3	-2.3	7.3 ± 0.2	4.9
-339	161	7.4 ± 0.3	0.1	7.6 ± 0.3	8.9
-339	261	7.5 ± 0.4	2.1	7.6 ± 0.3	9.1
-339	461	7.4 ± 0.4	0.5	7.4 ± 0.2	6.8
-239	161	7.4 ± 0.3	0.9	7.5 ± 0.2	7.8
-239	261	7.5 ± 0.2	1.7	7.4 ± 0.2	6.4
0	0	7.4 ± 0.4	0	6.9 ± 0.3	0

Improvement of MTF product (Table 8.9) with respect to the grounded setting follows a similar trend to the P11-only results, with setting $V_{App1, F1} = -339$ V, $V_{App1, F2} = 261$ V improving the most, at 12 %. Overall, MTF product was increased for each setting compared to the grounded setting.

Table 8.9 MTF product results for 15-beam imaging and the percentage difference from the grounded setting. Error was calculated from the standard deviation in the MTF measurements, in each direction.

F1 (V)	F2 (V)	MTF product (cycles/mm)²	Percent difference from ground (%)
-439	661	52 ± 3	3
-339	161	56 ± 4	9
-339	261	57 ± 5	12
-339	461	55 ± 3	7
-239	161	56 ± 3	9
-239	261	55 ± 3	8
0	0	51 ± 3	0

Figure 8.10 details the projection average results according to individual cathodes. The voltage settings in the legend are identified with an “N” representing a negative voltage and a “P” representing a positive voltage, with the voltage for F1 being listed first. Overall, it can be seen that the positive cathodes had lower MTF products than the negative cathodes. However, beam N15 was the worst performing beam, overall. P15 performed worse for most of the settings compared to ground. Also, it was the only cathode with worse spatial resolution in the y-direction. Several beams worsened in the x-direction for various settings but improved overall. The discrepancy between the two sides of the tube may be caused from misalignment of the two halves of the anode assembly, or misalignment of individual cathodes.

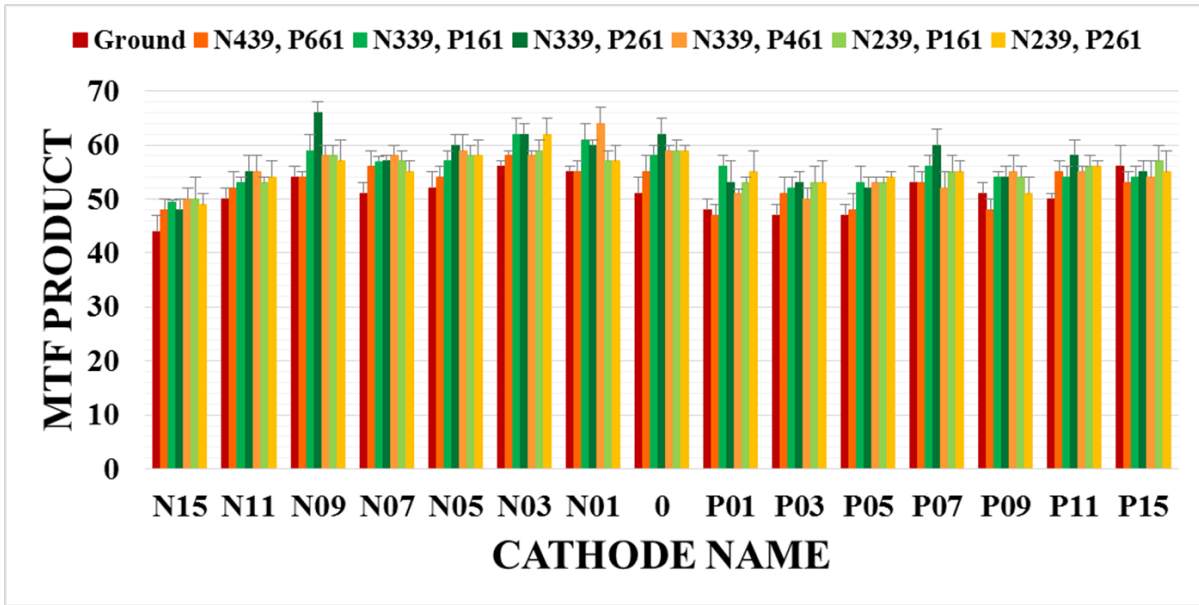


Figure 8.10 MTF product results. Results for each cathode/projection are given for each setting. Coloring from green to red indicates the settings with the highest to the lowest all-beam average MTF product.

8.4.2.3 Reconstruction results

The 15 projections were reconstructed into a 3D image volume, and the MTF was measured on the in-focus plane. These results are called reconstruction results, but they can also be referred to as the system MTF, because it incorporates all aspects of the imaging system. MTF product results for the optimal setting, $V_{\text{Appl}, F1} = -339 \text{ V}$, $V_{\text{Appl}, F2} = 261 \text{ V}$, are shown in Table 8.10, and the results in the x and y directions are shown in Table 8.11. The results for the grounded setting are also listed, for comparison. The optimal setting showed a percentage improvement of 9 % in MTF product, compared to the grounded setting.

Table 8.10 In-focus plane, reconstructed MTF product results and percentage difference from the grounded setting. Error was calculated from the standard deviation in the MTF measurements in each direction.

F1 (V)	F2 (V)	MTF product (cycles/mm)²	Percent difference from ground (%)
-339	261	27 ± 2	9
0	0	24.6 ± 0.5	0

It can be seen in Table 8.11 that improvement was achieved in the x-direction, but a decrease in spatial resolution was observed in the y-direction. This trend is opposite to the results of the P11 and 15-beam projection average data. The results for the grounded setting are in agreement with the s-DBT system MTF results from earlier studies, presented in Table 8.2 and Table 8.3.

Table 8.11 In-focus plane, reconstructed MTF results for each direction, and percentage difference from the grounded setting. Error is the standard deviation in the MTF measurements.

F1 (V)	F2 (V)	MTF_x (cycles/mm)	Percent difference from ground (%)	MTF_y (cycles/mm)	Percent difference from ground (%)
-339	261	5.6 ± 0.3	20	4.8 ± 0.2	-9.0
0	0	4.69 ± 0.03	0	5.2 ± 0.1	0

8.5 Discussion

8.5.1 Trends over focusing voltages

Simulation results of focal spot size variation in the optimal range of focusing voltages, done by Dr. Sultana¹ and reflected in Figure 8.11, showed that focal spot size was dependent on $V_{\text{Appl, F2}}$ only. Just outside the optimal range, the focal spot size was smaller with more negative $V_{\text{Appl, F1}}$ values. However, only three values of $V_{\text{Appl, F1}}$ were simulated. The experimental results shown in this chapter indicate that there is an optimal focusing

voltage for F1, as well as for F2. Note that spatial resolution increases when focal spot size decreases, which is why the simulated data is optimal at the lowest point whereas the experimental data is optimal at the highest point. Also, the focusing voltages in Figure 8.11 are relative to the gate voltage of 1250 V. The V_{Appl} is the stated value minus 1250 V, revealing that the simulated values are within the same range as the experimentally tested values.

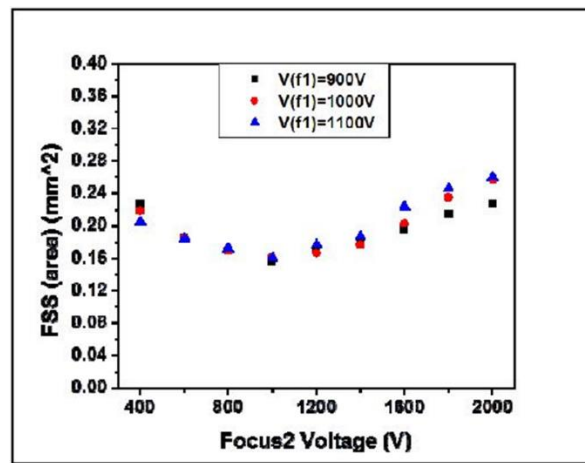


Figure 8.11 Simulation results showing FSS area to be weakly dependent on F1 voltage. Anode voltage was 30 kV, gate voltage was 1250 V producing 20 mA. Data reprinted with permission from Shabana Sultana¹.

Since the trend in the x and y directions differ between the reconstruction MTF results and the projection average results, it is likely due to an aspect of image reconstruction. There could be errors in the geometry calibration method or something inherent to the reconstruction method. The same methods were used when calculating system MTF in previous studies, which is why the values agree.

8.5.2 Optimal focusing settings and focal spot size

According to simulation results in Figure 8.11, the smallest FSS area was achieved when $V_{\text{Rel, F2}} = 1000\text{V}$ and with $V_{\text{Rel, F1}} = 900\text{ V, } 1000\text{ V, or } 1100\text{ V}$. Subtracting the gate voltage, they correspond to $V_{\text{Appl, F2}} = -250\text{ V}$ and $V_{\text{Appl, F1}} = -350\text{ V, } -250\text{ V, or } -150\text{ V}$. Taking into account the P11 data, the projection average data, and the reconstruction data, the best setting from these experiments was $V_{\text{Appl, F2}} = 261\text{ V}$ and $V_{\text{Appl, F1}} = -339\text{ V}$. The F1 voltage is in agreement with simulation, and the F2 voltage is approximately 500 V higher than simulation results. Table 8.9 illustrates that altering the voltages by 100 – 200 V does not significantly alter MTF product results. It is more reasonable that there is an optimal range of $V_{\text{Appl, F2}} = 100 - 400\text{ V}$ and $V_{\text{Appl, F1}} = -400 - -200\text{ V}$, over which the spatial resolution does not vary significantly.

Even so, the simulation results differ in terms of optimal $V_{\text{Appl, F2}}$. There are some differences that could be the cause of this. The simulations were completed at 20 mA, the cathode was grounded, and distances between electrodes were slightly different than the final design. In experiment, cathode current was 43 mA and the gate was grounded. These differences could account for the slight shift in optimal focusing voltages.

Experimentally, the smallest focal spot size measured using testing chamber setups and the first prototype s-DBT system was approximately 0.6 mm in both directions. However, the optimal focusing result in these studies suggest a larger focal spot size, according to a simulation program written by Dr. Andrew Tucker. The program takes inputs of focal spot size (FSS), detector pixel size, source-to-image receptor distance (SID), and object-to-detector distance (ODD). It then simulates the MTF curve for a projection image, as shown in Figure 8.12. The figure shows the simulated results for a focal spot size of 0.6

mm. The 10 % MTF value was 10.27 cycles/mm. This result is much higher than the projection MTF measurements from the optimal focusing setting ($V_{\text{Appl, F2}} = 261 \text{ V}$, $V_{\text{Appl, F1}} = -339 \text{ V}$), at 7.5 cycles/mm in the x-direction and 7.6 cycles/mm in the y-direction. Through trial and error it was found that a focal spot size of 0.985 mm produces a 10 % MTF of 7.55 cycles/mm. It is possible that the s-DBT used in these experiments is not able to produce the same focal spot size as the previous setups, or there may be untested focusing voltages which would peak at higher MTF values than the peak found in these experiments.

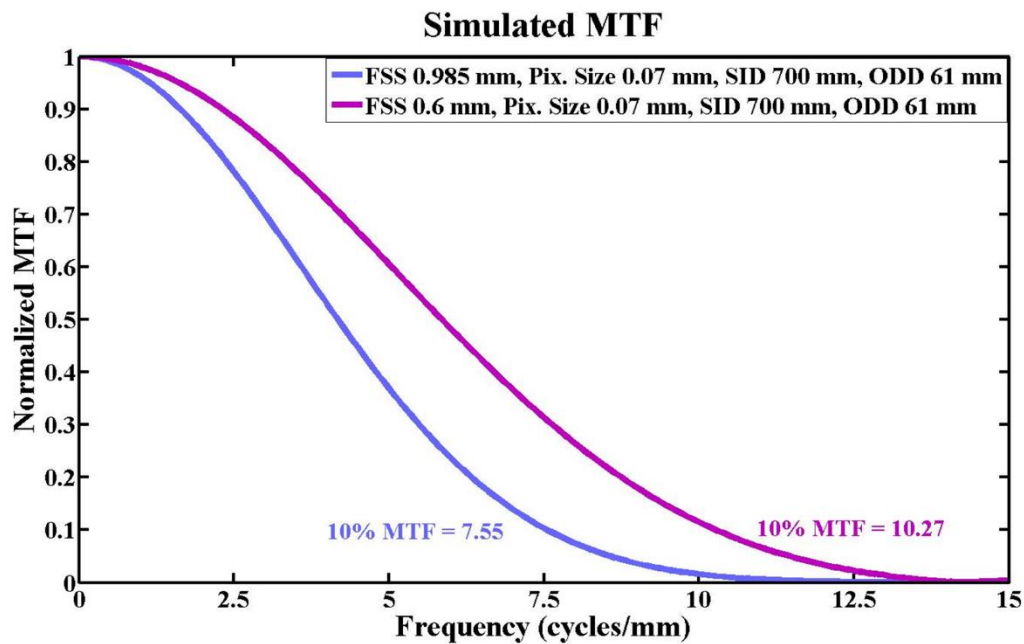


Figure 8.12 Simulation of projection MTF curves based on focal spot size. The blue curve results from a focal spot of 0.985 mm, and the purple curve corresponds to a focal spot size of 0.6 mm. All other settings are the same, and are the parameters used in these experiments. The 10 % MTF results are displayed next to their respective curves.

8.5.3 Transmission rate tradeoff

With every setting that improves spatial resolution, the transmission rate decreased. It is likely that when voltage is applied to the focusing electrodes more current is drawn

through the focusing electrodes, or more electrons are directed back toward the gate electrode. When averaged over all 15 cathodes, each setting had the same loss in transmission rate. The grounded setting had a transmission rate of 62 %, but the settings with focusing voltages applied had transmission rates of 54 %. To maintain proper image quality, this signal loss would have to be compensated for by increasing cathode current, increasing pulse width, increasing anode voltage, and/or adding more projections to the image sequence. Increasing pulse width or the number of projections would also increase the image acquisition time, increasing the chance for patient motion blur and increasing patient discomfort.

The clinical system currently has limitations in maximum pulse width, maximum cathode current, and number of allowed projections. Currently, the system is limited to 250 ms pulse widths, 43 mA cathode current, and 15 projections. The requirements determined for imaging in the clinical trial have been summarized into a technique table, also known as an AEC table, shown in Table 8.12. The maximum thickness that can be imaged is limited by the pulse width limitations of the ECS control electronics, and a maximum anode voltage of 40 kV. The required imaging exposure was determined based on the technique table of a commercial DBT system, and adjusted for the differences in dose rate of the s-DBT tube. The acquisition time is based on the maximum cathode current of 43 mA, the number of projections, and the total exposure.

Table 8.12 Table displaying the number of projections, pulse width, and exposure required for imaging different compressed breast thicknesses. The total acquisition time assumes a detector integration time of 0.1 s.

Thickness (mm)	Anode voltage (kV)	Number of projections	Pulse width (ms)	Total exposure (mAs)	Total acquisition time (s)
10	29	9	178	41	2.40
15	29	9	203	47	2.63
20	29	13	156	52	3.23
25	29	13	185	62	3.61
30	29	13	208	70	3.90
35	29	15	213	82	4.60
40	35	15	158	61	3.78
45	35	15	183	71	4.15
50	35	15	215	83	4.63
55	39	15	201	78	4.42
60	39	15	232	90	4.88

Practically, the drop in transmission rate due to the focusing electrodes would require changes to be made to the technique table, Table 8.12. To produce the same total exposure in the same total acquisition time, the cathode current would need to be increased from 43 mA to 48 mA. CNT cathodes are capable of achieving this increase, however the control electronics are not able to allow that much cathode current at this point. If instead the cathode current was kept at 43 mA and the pulse width was increased, the total acquisition time would increase between 0.18 s – 0.39 s for thicknesses of 10 mm – 60 mm. However, due to pulse width limitations of the control electronics, the maximum thickness that could be imaged would be 55 mm, down from 60 mm.

8.6 Conclusion

The results from cathode P11 and the averaged projection results from 15 cathodes shows that applying voltage to the focusing electrodes, rather than grounding them, can

increase the spatial resolution of the s-DBT tube. However, there is a loss in transmission rate which must be compensated for to maintain the same level of image quality. Overall, it appeared that most improvement in spatial resolution could be achieved using setting $V_{\text{App1, F2}} = 261 \text{ V}$ and $V_{\text{App1, F1}} = -339 \text{ V}$.

Employing the focusing voltages in the clinical s-DBT system would require altering the technique table, and would most likely limit the breast thicknesses that could be imaged. Otherwise, the control electronics would need to be adjusted in order to compensate for the required increase in cathode current. The ideal situation would be having a focusing voltage switching system able to customize the optimal focusing voltages for each cathode. The loss of transmission rate can be accommodated if the necessary changes to the electronics and system operation procedures could be made.

Further study should be done to see if the increase in spatial resolution is noticeable on phantom images. This would need to be evaluated through a reader study that would assess increased lesion visibility and diagnostic confidence. Spatial resolution increases could also be evaluated by a decrease in the size of imaged microcalcifications. If the optimal voltages found here are used on a different combination of cathodes, the improvement in spatial resolution would need verification because of variations among different cathodes and X-ray tubes.

REFERENCES

- 1 Sultana, S. *Electron optics simulation for designing carbon nanotube based field emission X-ray source* PhD thesis, University of North Carolina at Chapel Hill, (2010).
- 2 Qian, X. *et al.* High resolution stationary digital breast tomosynthesis using distributed carbon nanotube x-ray source array. *Med Phys* **39**, 2090-2099, doi:10.1118/1.3694667 (2012).
- 3 Giger, M. L. & Doi, K. Investigation of basic imaging properties in digital radiography. I. Modulation transfer function. *Med Phys* **11**, 287-295, doi:<http://dx.doi.org/10.1118/1.595629> (1984).
- 4 Bushberg, J. T., Seibert, J. A., Leidholdt, E. M. & Boone, J. M. *The Essential Physics of Medical Imaging*. 2nd edn, (Lippincott Williams & Wilkins, 2002).
- 5 Koutalonis, M. *et al.* Monte Carlo studies on the influence of focal spot size and intensity distribution on spatial resolution in magnification mammography. *Phys Med Biol* **53**, 1369-1384, doi:10.1088/0031-9155/53/5/013 (2008).
- 6 Marshall, N. W. & Bosmans, H. Measurements of system sharpness for two digital breast tomosynthesis systems. *Phys Med Biol* **57**, 7629-7650, doi:10.1088/0031-9155/57/22/7629 (2012).
- 7 Tucker, A. W., Lu, J. & Zhou, O. Dependency of image quality on system configuration parameters in a stationary digital breast tomosynthesis system. *Med Phys* **40**, 031917, doi:10.1118/1.4792296 (2013).
- 8 Fujita, H. *et al.* A simple method for determining the modulation transfer function in digital radiography. *IEEE transactions on medical imaging* **11**, 34-39, doi:10.1109/42.126908 (1992).
- 9 Kwan, A. L., Boone, J. M., Yang, K. & Huang, S. Y. Evaluation of the spatial resolution characteristics of a cone-beam breast CT scanner. *Med Phys* **34**, 275-281, doi:<http://dx.doi.org/10.1118/1.2400830> (2007).
- 10 Taylor, J. R. *An introduction to error analysis: the study of uncertainties in physical measurements*. Second edn, (University Science Books, 1997).

CHAPTER 9: CONCLUSIONS AND FUTURE DIRECTIONS

9.1 Conclusions

This work presented the development and performance of the third-generation s-DBT system developed at UNC. Overall development and characterization of the X-ray tube, and entire imaging system has been completed and described. Three specific areas of focus in this work included fabrication of a tungsten gate mesh, performance characterization of the carbon nanotube cathodes, and improving the system spatial resolution with the focusing electrodes. Fabrication of the gate mesh led to increased capabilities of the tube and improved stability of X-ray tube performance. This research confirmed that the CNT cathodes are not a limiting factor in delivering the necessary dose required for breast imaging. Focusing electrodes were employed to further increase the spatial resolution of the s-DBT tube, already improved over commercial DBT systems employing continuous tube motion.

Development of a tungsten gate mesh fabrication procedure was an important step in allowing CNT X-ray technology to advance toward clinical use in the s-DBT system. After optimization of the process parameters and fabrication methods, a reproducible technique for etching tungsten metal was developed using DRIE. This method, based on the initial work of Dr. Calderòn-Colòn, produced gate mesh that were able to withstand pulse widths of 4 s. A set of 31 individual gate mesh were welded onto the gate frame and installed in the first

Argus 3.0 s-DBT X-ray tube. Purchased, chemical wet-etched mesh were used in the second Argus 3.0 s-DBT tube, built for use in the clinical trial.

The robustness of carbon nanotube cathodes for the application of imaging breast cancer has been confirmed through lifetime measurements performed by Dr. Bo Gao, feasibility studies of performing 2D mammography with two types of nanotubes, and tracking tube performance over several years. These results show that, using CNT cathodes, a breast tomosynthesis system imaging 30 patients a day could run far beyond the experimentally tested lifetime of one to two years. The cathodes were capable of imaging at higher currents than typical breast tomosynthesis may require, with shorter pulse widths.

Adding 2D functionality would expand the prototype s-DBT systems' clinical appeal for imaging and intervention applications. However, it seems that the current design would not be feasible to produce the dose needed to screen a wide range of patients. More realistic applications would be 2D scout imaging for positioning procedures, automatic exposure control measurements, or low-quality 2D imaging accompanying a DBT scan to compare to previous 2D images in the patients' medical record. Feasibility results did not give definitive evidence that one type of nanotube cathode would perform better than another. But, along with initial ETEM study results, they do suggest MWNT cathodes may perform better long term. Further testing would be required to confirm this.

CNT cathodes have shown stability and robustness for the task of digital breast tomosynthesis imaging. Among all 31 cathodes in the first tube, there was an average increase of only 400 V, and consistent transmission rates over two years, during which the system was heavily used and continues to be used to this day. Constant transmission rate

indicates that there was no failure or significant change in the extraction gate mesh or any part of the electrode assembly.

Results from the focusing voltage optimization study showed that the spatial resolution of the s-DBT tube can be increased by applying voltage on the electrodes rather than grounding them. The improvement averaged to approximately 10 %. However, there is a loss in transmission rate which must be compensated for to maintain the same level of image quality. Practically, employing the focusing voltages would require some adjustment to the current s-DBT system.

9.2 Future directions

The first patient clinical trial of the s-DBT system began in December 2013. Evaluation of the s-DBT technology through a clinical trial will be instrumental in the future development and commercialization of the system. It is hoped that the clinical trial will show the s-DBT system improves the diagnosis and detection of breast cancer over current commercial DBT systems. If that is the case, further improvements in the system's functionality would only add to the usefulness of the technology. The system could be adapted for needle localization or biopsy procedures. Studying the feasibility of a dedicated cathode for 2D projections could be explored. Dual energy tomosynthesis imaging and scatter reduction are also avenues being explored to further the technology's capabilities.

To increase the applicability of the system to clinical use, the current production of the cathodes should be increased. This would allow the system to effectively image patients over a wider range of breast thicknesses. Doing this would affect the electronics needed to control the system, as well as other components of the tube such as the anode and gate mesh. Extra heat produced from more current must be compensated for so that those components would

not be permanently damaged during operation. Also, if the spatial resolution is to be further increased through a decrease in focal spot size, even more heat will be imparted to the anode. Employing focusing or reducing cathode size would both aid in increasing spatial resolution. Current cathode size is more than capable of tomosynthesis imaging. A reduction in cathode size could produce a smaller focal spot while being able to produce the necessary current required for imaging. Typical methods for dissipating the added heat would be cooling the anode with oil or rotation, with rotation being the more conventional solution.

Seriously evaluating a switch to MWNT cathodes could show an increased lifetime of the cathodes. It is likely that the MWNT cathodes would degrade less quickly if a higher-current regime was employed in the future. Continuing ETEM studies and lifetime studies of these cathodes could show a switch is warranted. This simple improvement in the CNT cathodes could expand the functionality of the tube and extend its lifetime.